Localised corrosion of AA2024.

O'Driscoll, Susanne

Localised Corrosion of AA2024

Susanne O'Driscoll

University of Wales Swansea

Thesis Submitted for the Degree of
Doctor of Philosophy (Ph.D.)

August 2003.

Acknowledgements:

Firstly I would like to thank Dr Neil M^{c}Murray for all his help throughout my Ph.D., and Dr Dave Worsley for keeping Neil sane, and helping me when Neil was busy. Many thanks to Dr Geraint Williams for all his help with the Kelvin probe (and the crosswords). To Peter and Alan for all their hard work with imaging, and many funny jokes.

A special thanks to Dr Peter Morgan at BAE Systems, Filton for his guidance (and samples), and to all those who helped and supported me during my visits, especially Chris and Mike.

To all past and present corrosion lab rats, thanks for the many laughs required to keep me sane in times of trouble. Too many to list, but a special mention for Maz and Ben for the years of support and company during Christmas shopping. Justin thank you so much for your computer genius, which saved me many hours of very painful computer work.

To the Morris family for being so understanding in times of trouble, and Ceri for her proof reading skills.

To the O'Driscoll/Olmo family for all your support throughout my education, I love you all very much.

Lastly, and most definitely most, to my other half Gavin. Thank you for everything, I only hope I can return all the love and support you have given me over these past years.

If you are reading this page chances are I owe you many thanks

Sue.

Abstract:

Novel electrochemical techniques, Scanning Vibrating Electrode (SVET) and Scanning Kelvin Probe (SKP), have been used to characterise pitting and filiform corrosion characteristics of aerospace alloy 2024-T3/T351. They have also been used to semi-quantify the inhibition efficiencies of chromate and trivalent Rare Earth Metal (REM) salts (cerium, lanthanum, and yttrium), both in solution and in coatings. It is shown that after long periods (hours) of immersion in 3.5% aqueous NaCl stable pitting occurs, these pits are believed to be in the form of interconnected tunnels, emerging at various points on the surface. It is also shown that chromate is the most effective inhibitor of those tested, both in solution and in coatings.

The role of S phase intermetallic particles on the pitting corrosion of the alloy has also been investigated using SVET, and secondary and back-scatter electron microscopy. It is shown that the pitting corrosion rate exhibited by the alloy increases with the increase of fractional surface area occupied by precipitate. It is also shown that, when a non-uniform distribution of intermetallic particles is present, the maximum density of stable corrosion pits coincides with the minimum surface density of intermetallic particles.

Table of Symbols:

Symbol	Quantity	Units
κ	Conductivity	$\Omega^{-1}m^{-1}$
ρ	Density	gcm^{-3}
ω	Frequency	Hz
ε	Dielectric constant	N/A
$\phi_{(a,z)}$	Fraction of i detected by integration of jz over a rectangular area of length 2X and breadth 2Y	N/A
$\phi_{(R,z)}$	Fraction of i detected by integration of $jz_{(r,z)}$ over a circular area of constant z and radius R	N/A
ε_0	Permittivity of a vacuum	Fm^{-1}
η_a	Anodic polarisation	V
η_c	Cathodic polarisation	V
ΔV	Volta potential	V
A	Area of cross section	m^2
C	Capacitance	F
d	Diameter of pit	cm
D	Distance between plates	m
E	Potential	V
E_{corr}	Corrosion potential	V
F	Faraday constant = 96487	$C\ mol^{-1}$
F_0	Normal field strength	Vm^{-1}
G	Calibration factor of SVET	$Am^{-2}V^{-1}$
h	Height of SVET probe over surface during scan	m
I	Integrated current	A
i	Current	A
i_a	Total anodic current present for each scan	A
j	Current density	Am^{-2}
J(t)	Time dependant, area averaged corrosion current density	Am^{-2}
J_{corr}	Anodic current density	Am^{-2}
Q	Charge	C
r	$(x^2+y^2)^{1/2}$	m
t	Time	s
teal	Total equivalent aluminium loss	gm^{-2}
Th	Threshold current density above which integration is performed	Am^{-2}
tm	Time of immersion	s
x	Position or distance in x direction	m
y	Position or distance in y direction	m
z	Position or distance in z direction	m

Contents:

Chapter 1.

Chapter 1: Introduction.

1.1: Aluminium and its Alloys.

1.1.1: Introduction.

In its pure form aluminium is a lightweight, silver-white, ductile and malleable metal. Aluminium is mostly extracted from the mineral bauxite, which contains approximately 25 percent aluminium[1]. It is the third most abundant element, and is the most abundant metal in the Earth's crust[2]. Pure aluminium is an excellent thermal and electrical conductor, magnetically neutral, and when highly polished reflects well beyond the visible spectrum at both shorter and longer wavelengths[2]. On contact with air the surface oxidises to form a thin, compact and strongly adherent aluminium oxide film, which then acts as a protective layer against further corrosive attack. This, so called passive behaviour, results in pure aluminium having a high corrosion resistance[1], despite the large thermodynamic driving force for oxidation indicated by its position in the electrochemical series, shown in table 1.6. These and other properties make aluminium highly desirable within modern industry.

However, in its pure state aluminium is a relatively soft metal and tends to lose strength over time[1]. To produce the required strong properties, aluminium is alloyed with varying quantities of heavy metals such as copper, zinc or nickel. Thus producing a relatively light alloy with good mechanical properties. A side effect of the alloying is the reduced corrosion resistance of the alloy compared to the pure metal[1].

The chief alloying constituents added to aluminium are copper, magnesium, silicon, manganese, nickel and zinc. Each type of alloy is then given a designation to

indicate its major alloying element. All are used to increase the strength of pure aluminium[1]. Table 1.1 shows the designations for wrought aluminium alloys[3].

Table 1.1: Showing the designations for wrought aluminium alloys[3].

Major alloying element	**Designated number**
None (99%+ Aluminium)	1XXX
Copper	2XXX
Manganese	3XXX
Silicon	4XXX
Magnesium	5XXX
Magnesium + Silicon	6XXX
Zinc	7XXX
Lithium	8XXX

When the aluminium has been alloyed with the elements, the desired properties may be derived from one of two types of treatment; those which derive their properties from work hardening, and those which depend on solution heat treatment and age hardening.

The 1000, 3000 and 5000 series alloys have their properties adjusted by cold work, usually by cold rolling. The exact properties gained by this process depends on the degree of cold work and whether any annealing or stabilising thermal treatment follows[3]. However, as these alloy types are not the subject of this thesis the exact types of treatment shall not be described further. The 2000, 4000, 6000, 7000 and 8000 series alloys are produced through solution heat treatment and age hardening. It is possible to achieve a wide range properties due to the wide choice of alloy compositions, solution heat treatment temperatures and times, quench rates from temperature, choice of artificial ageing treatment and degree to which the final

product has been deformed[3]. To define the treatments used a system of standard designations is used. These are based upon the letter T and are followed by a number to describe the various conditions. Table 1.2 shows the definitions of these designations, and table 1.3 shows the characteristics of some common alloys and how and where they are most commonly used.

Table 1.2: Definition of heat treatment designations for aluminium and aluminium alloys[3].

Term	Description
T1	Cooled from an elevated temperature shaping process, and naturally aged to a substantially stable condition. This designation applies to products which are not cold worked after cooling from an elevated temperature shaping process, or in which the effect of cold work in flattening or straightening has no effect on mechanical properties.
T2	Cooled from an elevated temperature shaping process, cold worked and naturally aged to a substantially stable condition. This designation applies to products which are cold worked to improve strength after cooling from an elevated temperature shaping process, or in which the effect of cold work in flattening or straightening does have an effect on mechanical properties.
T3	Solution heat treated, cold worked and naturally aged to a substantially stable condition. This designation applies to products which are cold worked to improve strength after solution heat treatment, or in which the effect of cold work in flattening or straightening does have an effect on mechanical properties.
T4	Solution heat treated and naturally aged to a substantially stable condition. This designation applies to products which are not cold worked after solution heat treatment, or in which the effect of cold work in flattening or straightening does not have an effect on mechanical properties.
T5	Cooled from an elevated temperature shaping process and then artificially aged. This designation applies to products which are not cold worked after

	cooling from an elevated temperature shaping process, or in which the effect of cold work in flattening or straightening does not have an effect on mechanical properties.
T6	Solution heat treated and then artificially aged. This designation applies to products which are not cold worked after solution heat treatment, or in which the effect of cold work in flattening or straightening does not have an effect on mechanical properties.
T7	Solution heat treated and overaged/stabilised. This designation applies to products which are artificially aged after solution heat treatment to carry them beyond a point of maximum strength to provide control of some significant characteristic other than mechanical properties.

Table 1.3: Some common aluminium alloys, their characteristics and common uses[3].

Alloy	Characteristics	Common uses
1050/1200	Good formability, weldability and corrosion resistance	Food and chemical industry
2014	Heat treatable. High strength. Non-weldable. Poor corrosion resistance.	Airframes.
3103/3003	Non-heat treatable. Medium strength work hardening alloy. Good weldability, formability and corrosion resistance.	Vehicle panelling, structures exposed to marine atmospheres.
5251/5052	Non-heat treatable. Medium strength work hardening alloy. Good weldability, formability and corrosion resistance.	Vehicle panelling, structures exposed to marine atmospheres.
5454#	Non-heat treatable. Used at temperatures 65-200°C. Good weldability and corrosion resistance.	Pressure vessel and road tankers. Transport of ammonium nitrate, petroleum. Chemical plants.
5083#/5182	Non-heat treatable. Good weldability and corrosion resistance. Very resistant to sea water, industrial atmospheres.	Pressure vessels and road transport applications below 65°C. Ship

		structures.
6063#	Heat treatable. Medium strength alloy. Good weldability and corrosion resistance. Used for intricate profiles.	Architectural extrusions, window frames, irrigation pipes.
6061#/6082#	Heat treatable. Medium strength alloy. Good weldability and corrosion resistance.	Stressed structural members, bridges, cranes, beer barrels, roof trusses.
6005	Heat treatable. Properties very similar to 6082. Preferable as air quenchable, therefore has less distortion problems.	Thin walled wide extrusions.
7020	Heat treatable. Age hardens naturally therefore will recover properties in heat affected zone after welding. Susceptible to stress corrosion. Good ballistic deterrent properties.	Armoured vehicles, military bridges, motor cycle and bicycle frames.
7075	Heat treatable. Very high strength. Non-weldable. Poor corrosion resistance.	Airframes.

= most commonly used alloys

1.1.2: Precipitate growth.

The process known as age hardening or precipitation hardening[4,5] may be used in the production of aluminium alloys to produce a fine uniform dispersion of hard precipitate particles within a softer more ductile matrix. Ideally the matrix formed will be coherent, as this produces a widespread disruption of the matrix lattice, so the movement of the crystallographic dislocations is impeded even if they merely pass close to the particle. However, if the precipitates formed are incoherent, the matrix lattice is unperturbed and the movement of dislocations is impeded only if these impinge directly on the particle. It is the reduction in dislocation mobility which

reduces susceptibility to plastic deformation, and coherent precipitates therefore produce a significantly greater hardening effect than do incoherent precipitates. Figure 1.1a[5] shows how the matrix lattice remains unperturbed in the vicinity of an incoherent precipitate, and figure 1.1b shows how a coherent precipitate disrupts the surrounding matrix lattice.

Al-Cu binary alloys:

The composition Al-4%Cu presents a classical example of an age-hardenable alloy system. Figure 1.2[4,5] shows the aluminium rich end of the Al-Cu phase diagram. Here the α phase is a solid solution of Cu in Al and exhibits a FCC crystal structure. The θ phase is the hard, brittle, intermetallic compound Al_2Cu which exhibits a body centred tetragonal crystal structure, incoherent with α. These are the only stable, equilibrium, phases available and it may therefore be understood that any formation of coherent precipitates must involve metastable, non-equilibrium, phases. These additional phases are termed transition phases and arise as kinetic intermediates in the precipitation of θ from supersaturated α. The process through which they are produced involves three steps.

Step 1 – Solution treatment. The alloy is held above the solvus temperature (500°C) until all the θ phase dissolves to produce homogeneous solid solution α. The temperatures actually employed lie between the solvus and the eutectic temperatures (500 - 548°C) to avoid microconstituent melting and loss of homogeneity at temperatures above the eutectic.

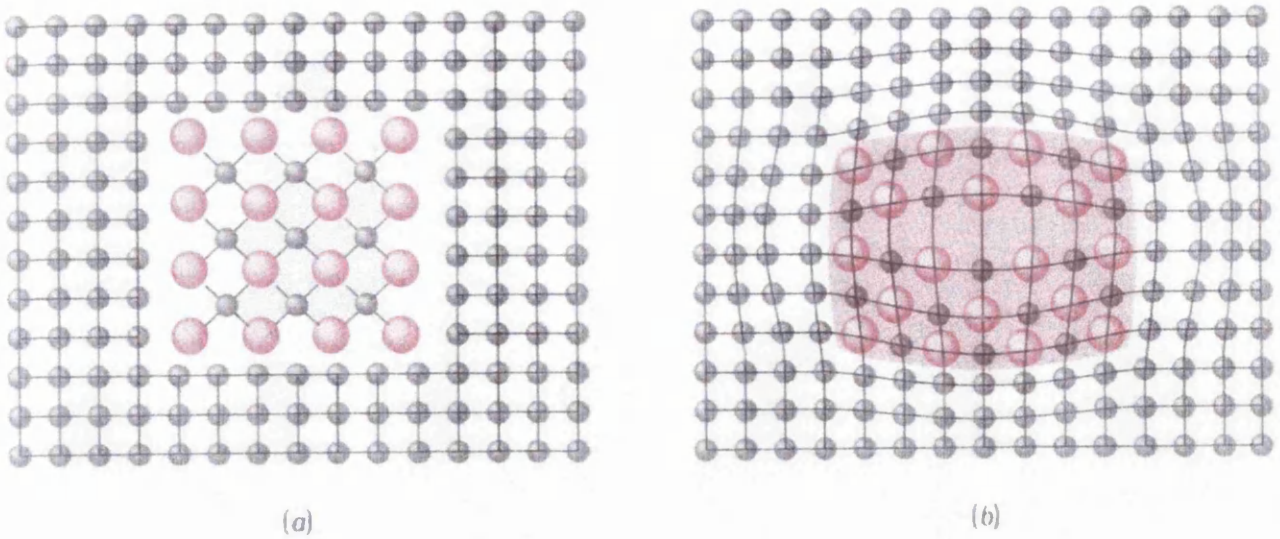

Figure 1.1: a) A non-coherent precipitate has no relationship with the crystal structure of the surrounding matrix. b) A coherent precipitate forms so that there is a definite relationship between the precipitates and the matrix's crystal structure[1].

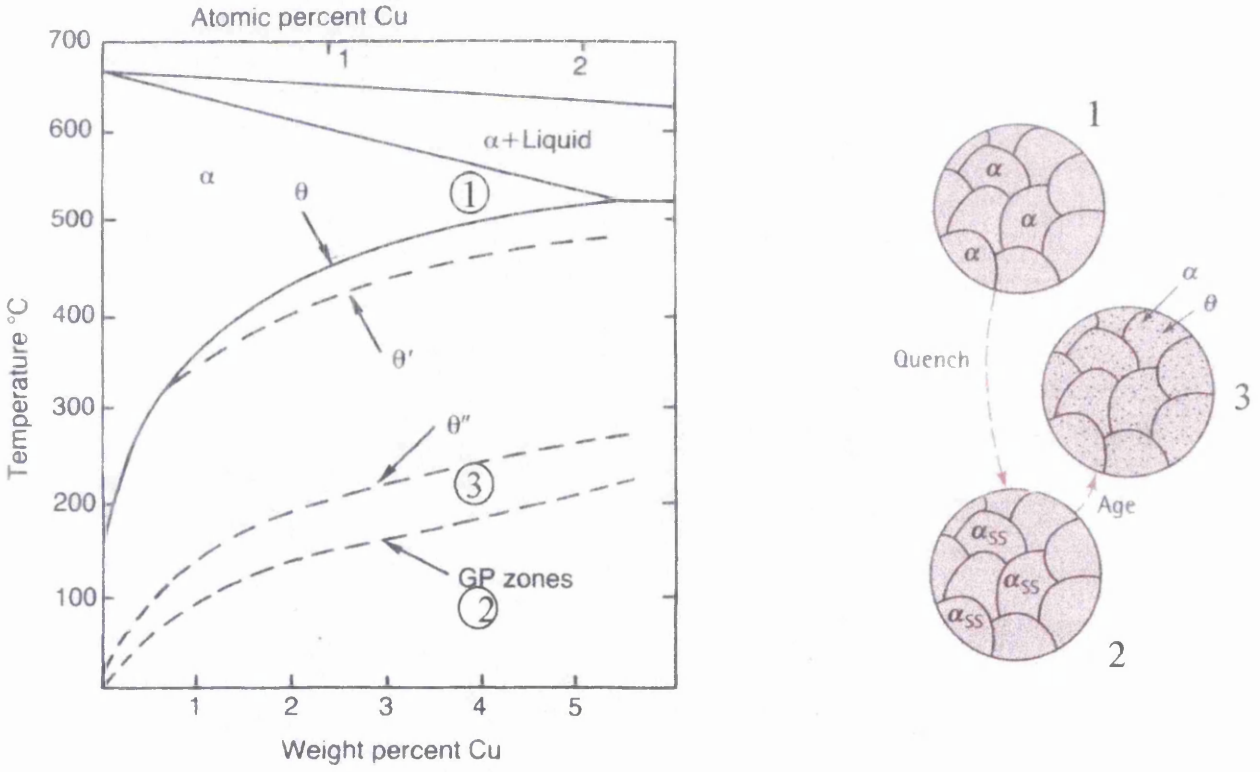

Figure 1.2: The aluminium- rich end of the aluminium-copper phase diagram showing the three steps in the age-hardening heat treatment and the microstructures that are produced[4,5].

Step 2 – Quench. The solution treated alloy is rapidly cooled or quenched to room temperature or below. Atoms have insufficient time to diffuse to potential nucleation sites with the consequence that θ phase does not form. However, the structure now consists of a supersaturated solid solution α_{ss} with a thermodynamic driving force for θ precipitation.

Step 3 – Age. Finally the alloy is reheated below the solvus temperature, typically to temperatures less than 190 °C. Copper atoms can now diffuse to nucleation sites and precipitate particles grow. If ageing is allowed to continue for long enough the equilibrium α plus θ structure will ultimately be produced. However, higher strengths may be achieved by stopping the ageing process (by cooling to room temperature) before equilibrium is attained, thereby retaining coherent transition phases. During the ageing process transition phases form successively as intermediates in a so-called precipitation sequence. The precipitation sequence for Al-4%Cu is as follows:

$$\alpha_{ss} \longrightarrow \text{GP zones (discs)} \longrightarrow \theta\text{" (discs)} \longrightarrow \theta\text{' (plates)} \longrightarrow \theta\ (CuAl_2) \qquad (1)$$

where GP (Guinier – Preston) zones are copper rich clusters fully coherent with the matrix. The θ" precipitates are typically <10nm thick and <100nm diameter and exhibit as distorted tetragonal unit cell which is essentially a distorted FCC structure fully coherent with the matrix. θ' is also tetragonal with an approximate composition $CuAl_2$ and forms precipitates up to 1 μm in diameter, semi-coherent with the matrix. The final θ precipitates may be >1μm in diameter and exhibit the body centred tetragonal unit cell, completely incoherent with the α matrix. The alloy is considered to be optimally aged and exhibits maximum strength when only GP zones and θ" plus

θ' transition phases are present in the final structure. Once significant quantities of the stable θ phase precipitate, alloy strength begins to decrease and the alloy is said to be overaged. The θ phase still provides some dispersion strengthening but as θ particles increase in size, the strengthening effect diminishes.

Al-Cu-Mg ternary alloys:

Ternary aluminium alloys containing both Cu and Mg exhibit age hardening properties like the Al-4%Cu binary system[6]. Furthermore, age hardening is brought about by a similar process of solution treatment, quenching and ageing. The precipitation sequence (1) may occur as before, ultimately producing the equilibrium $CuAl_2$ θ phase. However, a second precipitation sequence (2) also occurs, ultimately producing a face centred orthorhombic S phase with the composition Al_2CuMg. As in the case of θ the equilibrium S phase particles are completely incoherent with the FCC α matrix.

$$\alpha_{ss} \longrightarrow \text{GPB zones (cylinders)} \longrightarrow S'' \longrightarrow S' \longrightarrow S\ (Al_2CuMg) \qquad (2)$$

Strengthening of optimally aged Al-Cu-Mg alloys is associated with the presence of fully coherent Guinier-Preston-Bagaryatsky (GPB) zones (Cu/Mg clusters) which are reported to be 1-2 nm in diameter and 4 nm long. Additional strengthening arises from the presence of finely dispersed metastable precipitates. In pseudo-binary alloys (Cu:Mg ~ 2.2:1) these are principally S' (Al_2CuMg) particles, whereas both S' and θ'($CuAl_2$) particles are observed in alloys with a higher Cu:Mg weight ratio. The existence of S" is still a matter of dispute, however large stresses are thought to be

associated with its coherence. The aluminium corner of the aluminium-copper-magnesium phase diagram is shown in figure 1.3[6].

Al-Cu-Mg alloys containing Fe, Mn and Si:

A complete and accurate diagram for the alloy system Al-Cu-Fe-Mg-Mn-Si is not available[7]. However, a large number of iron, manganese and silicon containing phases are known to form in addition to those described previously[7]. Not all of these additional phases will necessarily form for all alloy compositions and all may not exist in mutual thermodynamic equilibrium. Phases which may exist in equilibrium with S-phase Al_2CuMg include: β-phase $FeAl_3$, $MnAl_6$, $(CuFe)Al_6$, Cu_2FeAl_7, $CuMg_4Al_6$, $(FeMn)Al_6$, $Cu_2Mn_3Al_{20}$ and Mg_2Si. An approximately equal number of phases are possible which may not exist in equilibrium with S-phase Al_2CuMg – the most noteworthy of which is $(CuFeMn)Al_6$.

Commercial 2024-T3:

Second phase (intermetallic) particles in commercial 2.0 mm thick 2024-T3 alloy sheet stock have been characterised with respect to geometry using a combination of optical and scanning electron microscopy (SEM), and with respect to chemical composition using electron microprobe analysis (EPMA)[8]. The alloy sample was sectioned in short, transverse and longitudinal planes – with respect to the original rolling direction. The distribution of particles and particle types was found to be uniform throughout. Furthermore, no significant geometrical differences were detected between particle populations imaged on different orthogonal planes. Table 1.4 summarises geometrical characteristics for all three orthogonal planes, as determined by optical image analysis of particles of diameter > 0.2 μm.

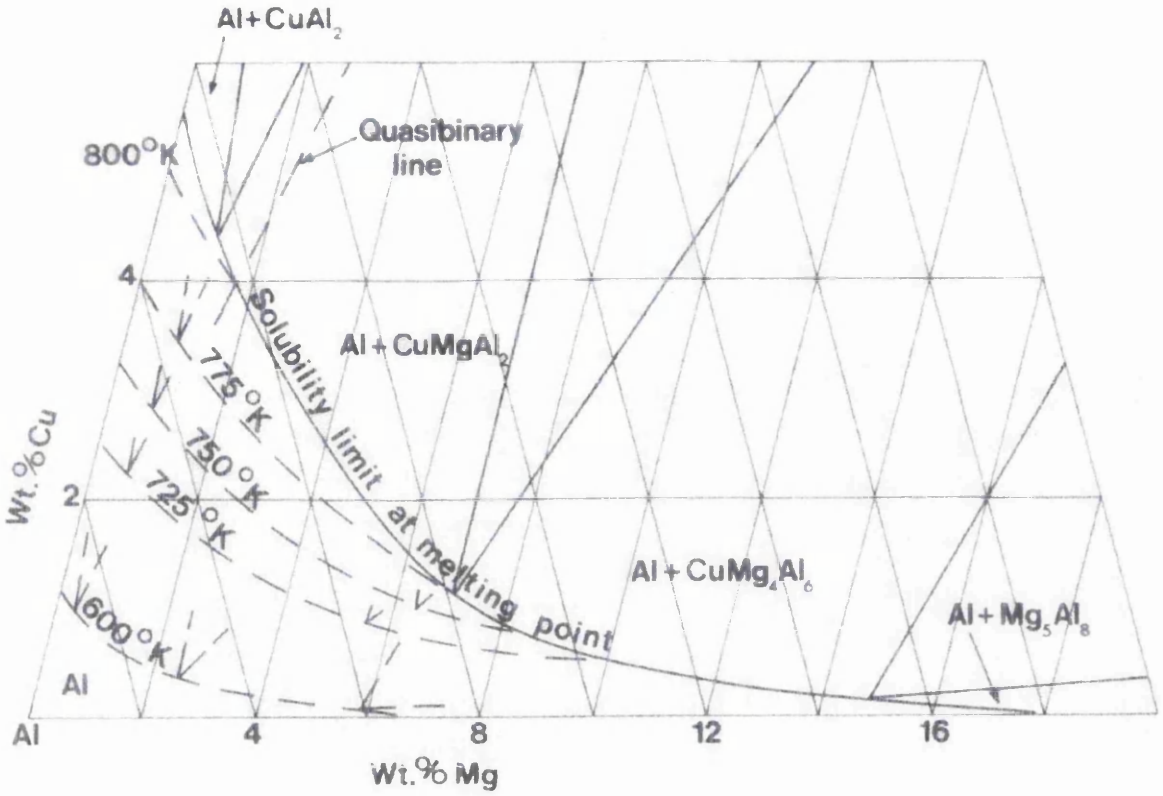

Figure 1.3: Aluminium corner of the aluminium-copper-magnesium phase distribution in the solid and solid solubilities at various temperatures[6].

Table 1.4: Geometrical characteristics of second phase particles in 2024-T3.

orientation	Mean diameter (μm)	Aspect ratio	Number analysed
short	4.09 ± 2.6	1.60 ± 0.4	196
transverse	3.97 ± 2.9	1.76 ± 0.5	232
longitudinal	3.77 ± 2.8	1.87 ± 0.7	224

As shown in Table 1.5 the S-phase (Al_2CuMg) predominates. No θ-phase (Al_2Cu) was detected in the size range studied. It is interesting that $Al_6(Cu,Fe,Mn)$ was identified as the second most abundant particle type, as this cannot exist in equilibrium with the majority S-phase[7]. The $(Al,Cu)_6Mn$ particles may be thought of as corresponding (roughly) to the $Cu_2Mn_3Al_{20}$ phase [7]. The S-phase particles were found to be rounded (spherical or globular) in shape, whereas particles containing Fe and/or Mn were angular (irregular) in shape.

Table 1.5: Particle distributions by chemical type

Particle type	Number %	Area %
Al_2CuMg	61.3	2.69
$Al_6(Cu,Fe,Mn)$	12.3	0.83
Al_7Cu_2Fe	5.2	0.17
$(Al,Cu)_6Mn$	4.3	0.11
indeterminate	16.9	0.37

1.2: Corrosion.

Corrosion is the environmental degradation of materials. The consequences of corrosion can be catastrophic both in financial and human terms. It can lead to enormous financial damage for modern industrial societies. Estimates show that between 2.1% and 5% of the gross national product is lost through corrosion[9,10,11]. Some past incidences of human loss through corrosion include the 170,000 tonne ship Derbyshire in 1980 with all 44 crew members on board. After the incident, there was much speculation that the ship had suffered a major structural failure as a result of corrosion fatigue[11]. On 15 December 1967, 46 people lost their lives, when Point Pleasant Bridge in Ohio collapsed. The cause of the disaster was found to be a stress corrosion crack 2.5 mm deep in the head end of an eyebar[11]. In the modern age, where bigger is better, the potential for even greater loss of life through corrosion is very high. Hence much research is being carried out to minimise the risk of corrosion on modern structures.

1.2.1: Introduction.

There are many mechanisms of metal corrosion that depend upon the nature of the surrounding environment, and the metal present. However corrosion can be divided into two main groups, these are chemical and electrochemical. Gaseous corrosion and corrosion in non - electrolytes are both examples of chemical corrosion. Atmospheric corrosion, soil corrosion and corrosion in electrolytic solutions are all forms of electrochemical corrosion. The effects of these forms of corrosion can vary; some of the most common are uniform or general corrosion, local corrosion, intercrystalline corrosion and pitting corrosion[12]. In this project the types of corrosion observed are localised pitting corrosion, due to a bare metal being submerged in an electrolytic

solution, and filiform corrosion due to a coated metal being exposed to chloride ions at high humidity.

Electrochemical Reactions:

An electrolyte is defined as an aqueous solution capable of conducting an electric current. Most metals corrode severely when in contact with electrolytic solutions. Various theories have been put forward to explain this phenomenon, which are explained more in-depth elsewhere[11,12]. However, what follows is a brief outline of electrochemical corrosion.

Electrochemical reactions, such as those which occur in electrolytic solutions, are characterised by the donating or receiving of electrons. When anodic reactions take place there is an emission of electrons, which results in the oxidisation of the surface metal atoms which form aqueous metal ions.

$$M_{(s)} \rightarrow M^{n+}_{(aq)} + ne^- \qquad [1.1]$$

However, a cathodic reaction is when the consumption of electrons takes place. This may involve either hydrogen evolution as shown in equation 1.2,

$$2H^+_{(aq)} + 2e^- \rightarrow H_{2(g)} \qquad [1.2]$$

Alternatively, as is more usual in aerobic conditions around neutral pH, it may involve the reduction of dissolved oxygen as shown in equation 1.3.

$$O_{2(aq)} + 2H_2O + 4e^- \rightarrow 4OH^-_{(aq)} \qquad [1.3]$$

These anodic and cathodic reactions happen at the same time, causing the corroding metal to act as a polyelectrode. A polyelectrode is defined as a system where two or more couples that are not in thermodynamic equilibrium act simultaneously at a single electrode surface[13,14,15]. It is known that the couples acting at a polyelectrode surface are independent of each other, and that the total current flowing into any external circuit will be the algebraic sum of the individual currents due to the individual couples[16]. From this it can be seen that if there is no external circuit the sum of the individual currents is zero, so under conditions of free corrosion,

$$\sum i_{anodic} = -\sum i_{cathodic} = i_{corrosion} \qquad [1.4]$$

i_{anodic} represents the partial current due to any anodic process, $i_{cathodic}$ represents the partial current due to any cathodic process and $i_{corrosion}$ is the rate of corrosion expressed in terms of current. As electrochemical currents are dependent on potential, this equation constrains the corroding metal to adopt a unique potential, this is known as free corrosion potential, E_{corr}[17,70].

Equations 1.5 and 1.6 show the mathematical relationship between current i, and potential E, which was first defined by Tafel[18].

$$i_{anodic} \propto \exp(E) \qquad [1.5]$$

and

$$i_{cathodic} \propto \exp(-E) \qquad [1.6]$$

From these equations it can be seen that a graph of E against log i for each electrode process would give a straight line (known as a Tefal plot).

Figure 1.4 shows an Evans diagram for a simple corrosion process for a metal in contact with an electrolyte[11]. This is produced by graphically combining Tefal

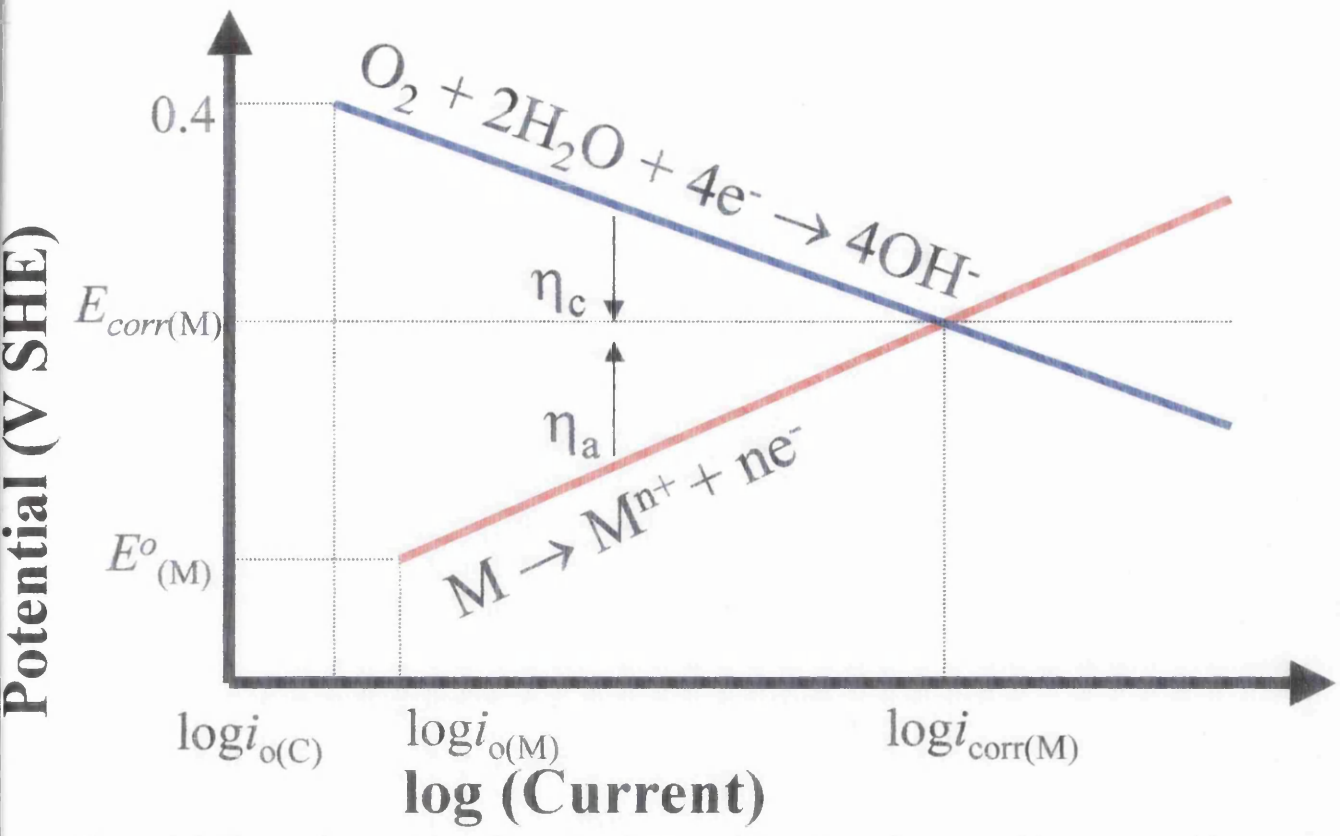

Figure 1.4: Evans diagram showing a simple corrosion process for a metal in contact with an aerated electrolyte[11].

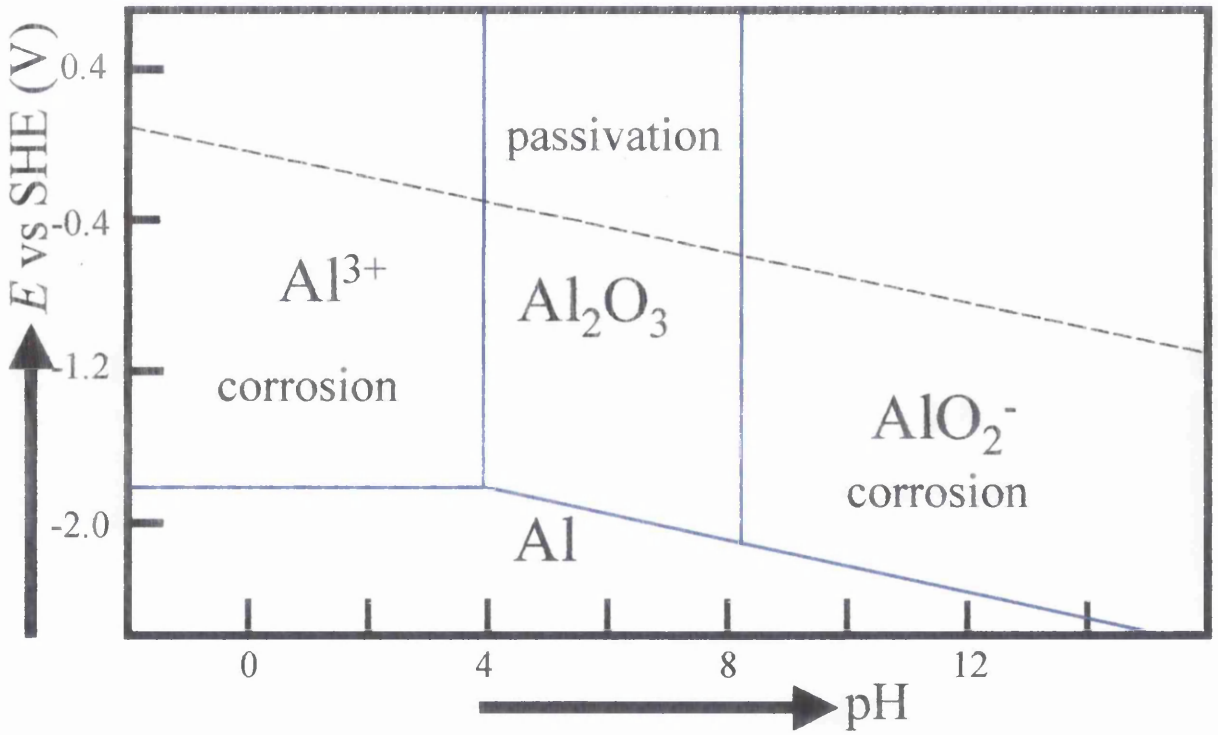

Figure 1.5: Pourbaix diagram of the system Al/H_2O (25°C). The dashed line indicates the potential -pH dependence of the reaction $2H^+ + 2e^- \longrightarrow H_2$[10].

plots for the individual electrode processes. As the anodic reaction (red line in figure 1.4) proceeds metal ions enter the solution thus leaving the metal with an excess of electrons in this area, which then flow to a cathodic site. Hence, as corrosion continues the anode becomes less negative and its potential is shifted upwards by an amount η_a, the anodic polarisation. Conversely, the cathodic site becomes more negative (blue line in figure 1.4) and its potential is shifted downwards by an amount η_c, the cathodic polarisation. Where these Tafel plots intersect the anodic and cathodic currents are zero. As stated in equation 1.4 this point defines the free corrosion current, $i_{corrosion}$. Subsequently the free corrosion potential, E_{corr} may also be obtained from the Evans diagram[11].

It is possible to determine the stability of a metal with respect to the pH of the electrolyte, as well as the potential. These plots are called Pourbaix diagrams, figure 1.5 shows such a diagram for aluminium exposed to water[10]. A metal is deemed to be corroding when the concentration of its ions in solution is $\geq 10^{-6}$ M[11]. If the concentrations of ions is less than this value then the metal is deemed to be in a condition of immunity. However, as described in section 1.1.1 pure aluminium oxidises very quickly at neutral pH to leave a thin protective layer. This is described as passivation. As can be seen from figure 1.5, for pure aluminium to corrode the electrolyte has to have an extreme pH (4>pH>9). However, as described in section 1.1 pure aluminium is very rarely used within industry, and alloying elements are added to improve mechanical properties. These additions to pure aluminium greatly change its corrosion characteristics for the worse.

1.2.2: Surface pitting corrosion.

Pitting corrosion is a highly localised form of corrosion which results in small holes in the metal[10,19]. Pitting corrosion usually occurs on metals that are protected by a thin surface film, and it is thought that pits initiate at imperfections or weak areas of the film. However, all surface defects do not result in stable pitting events. Scratching the surface of aluminium does damage the protective oxide layer, but does not always lead to pitting[10].

Pitting is most usually associated with the presence of aggressive ions, such as chloride, initiating corrosion by the break down of passive oxide films on metal surfaces through the formation of soluble metal complexes. Rapid metal dissolution then occurs within the pit whilst cathodic oxygen reduction occurs on the adjacent surface. The pitting process is autocatalytic, i.e. once started it is self sustaining. Metal cations formed in the pit attract the migration of charge balancing chloride ions, in addition the metal cations also tend to undergo hydrolysis, so reducing pH; both chloride ions and low pH stimulate metallic dissolution and act to prevent repassivation. A schematic diagram of a stable pit can be seen in figure 1.6[20].

1.2.3: Pitting corrosion of aluminium-copper alloys.

In general, the susceptibility of aluminium-copper alloys to corrosion increases with copper content. This effect has been attributed to the formation of galvanic cells at microstructural elements (copper-rich intermetallic particles *vs.* matrix or Cu-depleted grain boundary zones) or by the enhanced electrocatalytic activity (for cathodic oxygen reduction) at those intermetallics or at otherwise copper-enriched regions on the alloy surface[29,21,22,23,24,25,26]. Furthermore, it has long been known that the electrochemical heterogeneity of AA2024-T3 makes this alloy susceptible to pitting

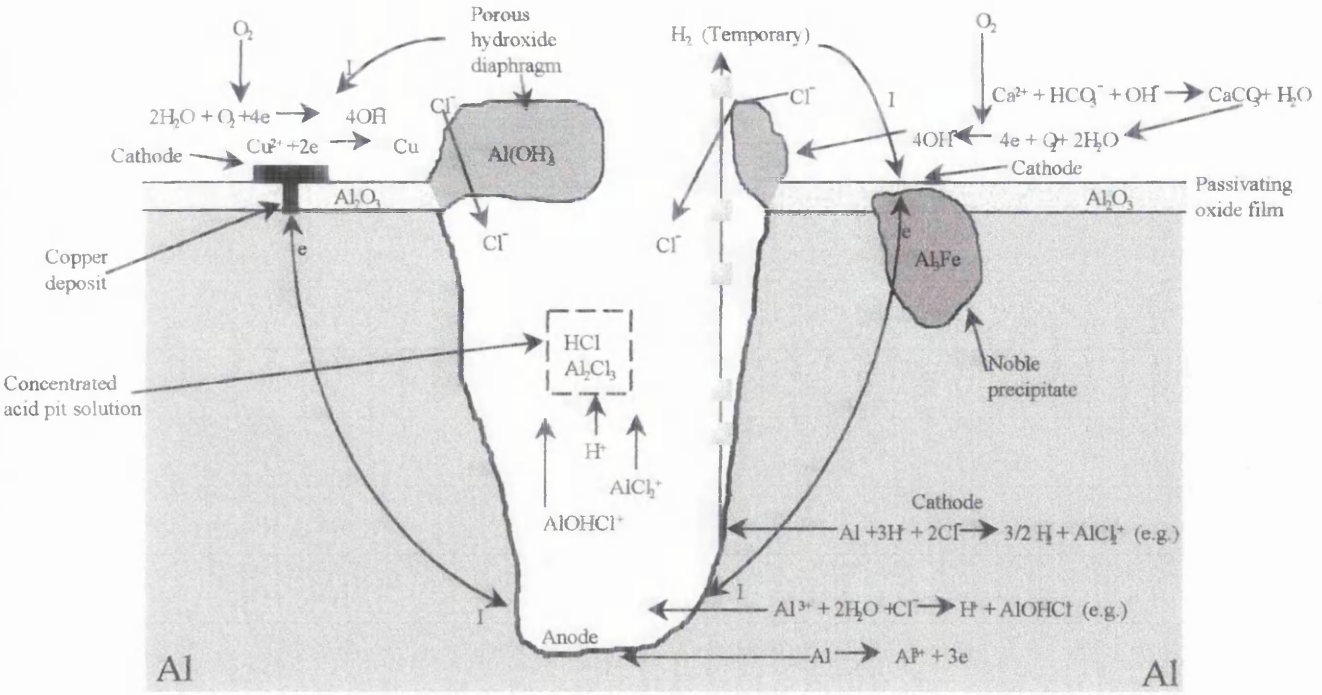

Figure 1.6: Schematic diagram of stable pit[20].

corrosion, intergranular corrosion and stress-corrosion cracking in aqueous chloride electrolytes[27,28,29]. It has been found that Al-Cu-Fe-Mn phases will be noble with respect to the α aluminium matrix and will therefore tend to act as sites of cathodic oxygen reduction[26]. Conversely, the S-phase Al_2MgCu particles are predicted to be more active than the α matrix and these are generally regarded as being sites of preferential anodic attack[26]. It is therefore evident that the onset of corrosion in AA2024-T3 is likely to be highly localised in nature. However, this picture is further complicated by observation that once corrosion has commenced copper becomes redistributed at the alloy surface, producing large localised changes in electrocatalytic activity with respect to cathodic oxygen reduction.

The role of precipitate particles:

Much work has been carried out on the effects of precipitate particles on the initiation of pitting corrosion on AA2024 exposed to aggressive aqueous electrolytes, such as those containing chloride ions[8,26,30,31,32,33]. Initiation most probably occurs either through a purely anodic process of selective dissolution in the case of S-phase Al_2CuMg particles[26,30] or through a cathodically mediated peripheral pitting of the α matrix in the case of dealloyed S-phase particles[8,31,32,33] and, possibly, Al-Cu-Fe-Mn particles[25]. However, the transient pits formed through such events are very much smaller, and orders of magnitude more numerous, than the stable, acid-filled pits observable in heavily corroded AA2024-T3. The question of whether alloy microstructure and the distribution of intermetallic particles can influence the transition from transient to stable pitting, and thereby determine the location and number density of stable pits remains substantially unaddressed. However, here are some possible theories.

If, for example, the transition from transient to stable pitting is a purely stochastic process then, under circumstances where the surface distribution of intermetallic particles is non-uniform, we would expect the maximum number density of stable pits to occur in those areas exhibiting the maximum number density of intermetallic particles (see figure 1.7a). If, on the other hand, the cathodic copper deposits formed through S-phase dealloying[8,34,35,36,37] and/or through cathodically mediated matrix dealloying[34,38,39,40,41] could influence the transition from transient to stable pitting the expected location of stable pits would depend upon the predominating mode of influence. Thus, if the predominant mode of influence is galvanic, the maximum probability of a transition to stable pitting will coincide with the minimisation of effective current pathlengths in solution, and the maximum number density of stable pits is once again predicted to occur in those areas exhibiting the maximum number (or possibly area) density of intermetallic particles. Conversely, if the predominant mode of influence is chemical, via solution pH, then the maximum number density of stable pits is predicted to occur in those areas exhibiting the minimum number (or possibly area) density of intermetallic particles (see figure 1.7b). This is because it is reasonable to expect that, all else being equal, the establishment and maintenance of an acidic micro-environment within the growing pit will become more difficult as external solution pH increases.

1.2.4: Filiform corrosion.

Filiform corrosion (FFC), first accurately described in 1944,[42] is an atmospheric corrosion phenomenon affecting organic coated metals. It is characterised by "thread-like" tracks of corrosion product deposits beneath the coating. There have been extensive studies on organic coated aluminium, steel and magnesium surfaces[43,44],

a)

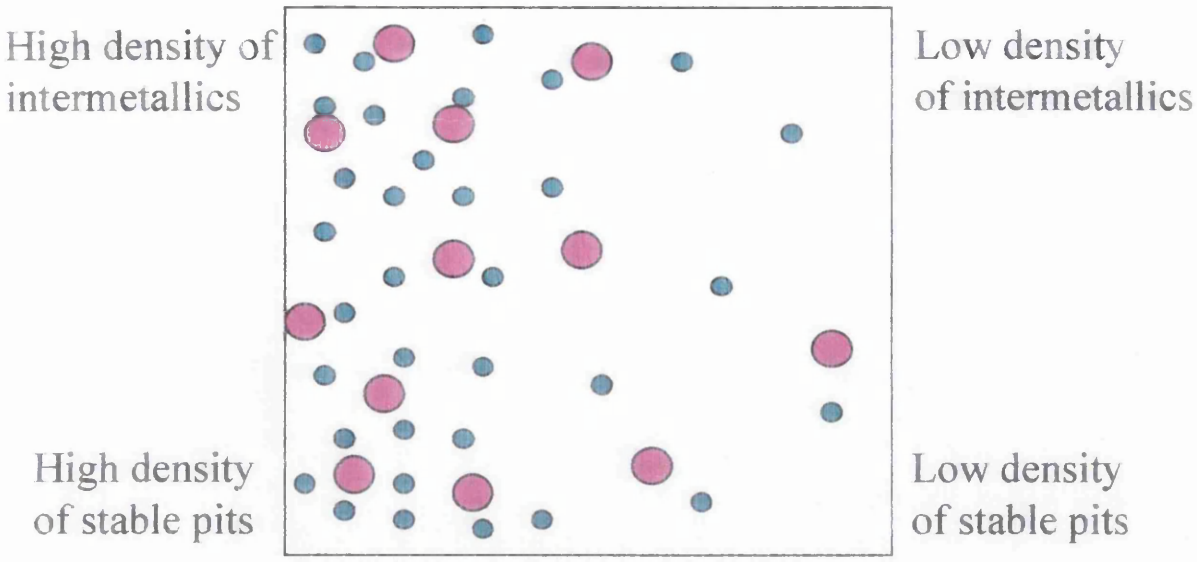

b)

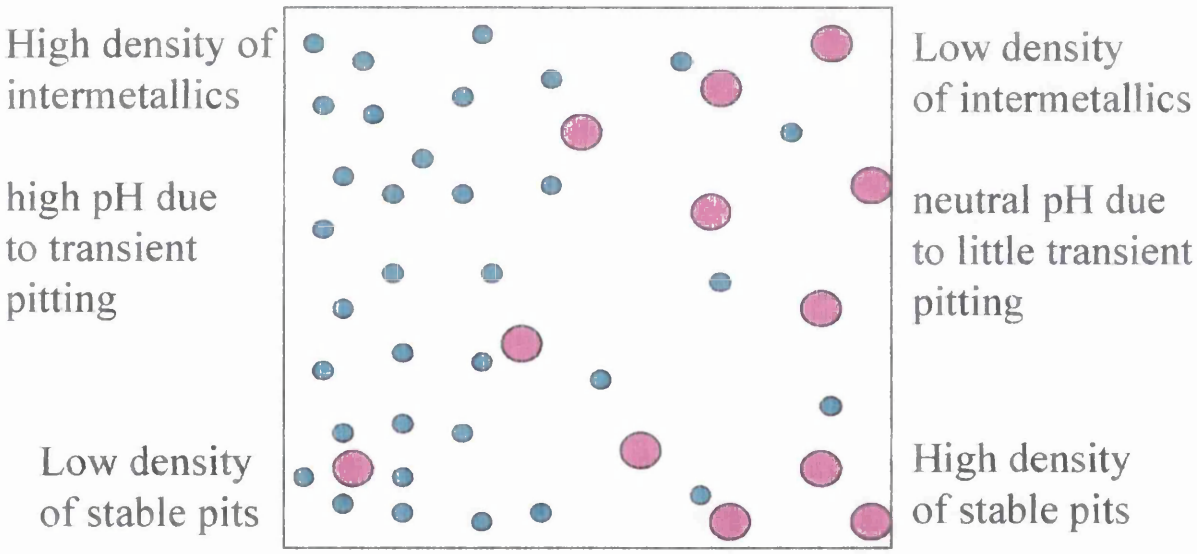

Figure 1.7: Schematic diagram showing how intermetallic distribution may influence distribution of stable pitting events, if the transition from transient to stable pitting is

a) a purely stochastic transition, or predominant mode of influence is galvanic,

b) predominant mode of influence is chemical.

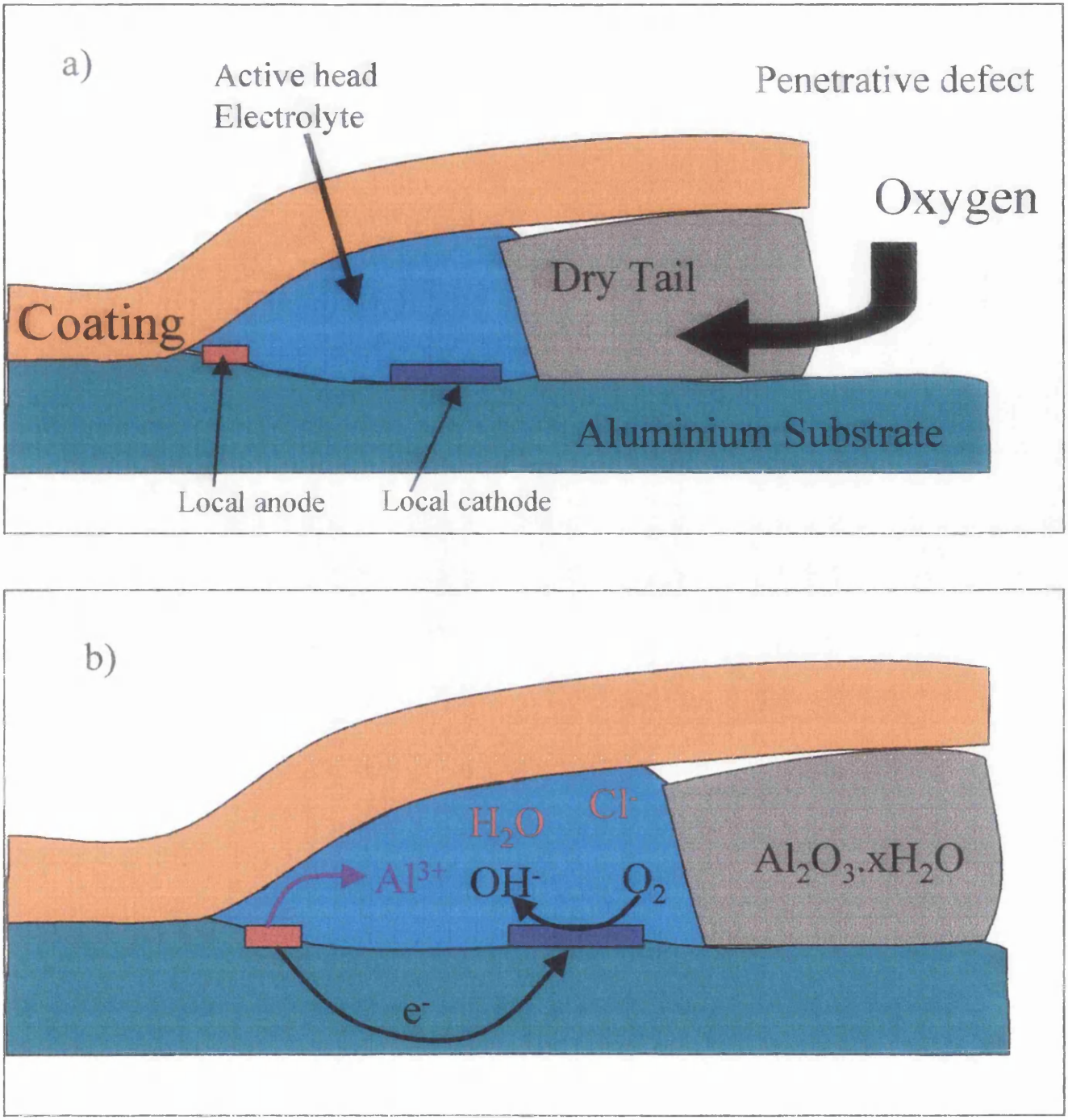

Figure 1.8: Schematic diagram of filiform cross section.

a) showing position of local anode and cathode in electrolyte filled head

b) showing movement of electrons in substrate, and Al^{3+} in solution.

which have shown that for FFC to occur, oxygen, aggressive ions such as chloride (Cl^-), and a high relative humidity must all be present. Corrosion filaments, each comprising an electrolyte filled "head" and a "tail" of dry corrosion product, propagate from penetrative defects in the organic coating and may attain a length of several centimetres. A schematic diagram of a filament can be seen in figure 1.8. The exact mechanism of FFC remains unclear but it is generally believed that filament advance involves anodic undercutting of the organic coating driven by differential aeration, which arises in turn from mass transport of atmospheric O_2 through the filament-tail.[43,44,45,46,47,48] .Aggressive anions (Cl^-) and water tend to be conserved in the filament-head electrolyte, and filaments may continue to propagate for long periods of time (years)[43,44].

1.3: Corrosion Protection.

1.3.1: Introduction.

As can be seen in section 1.2 corrosion can come at a high price, both in monetary and human terms. It is possible to reduce the effects of corrosion in many ways, what follows is a brief outline of some of these methods.

Barrier coatings:

Barrier coatings are probably the easiest form of corrosion prevention. They work by stopping the electrolyte from coming into contact with the metallic surface, thus preventing the initiation of corrosion cells. Typical barrier coatings are vitreous enamels, paints, plastic laminates and less reactive metals[49] (e.g. gold). However these coatings are only effective when the metals surface is completely covered, even

the smallest scratches or defects in the coating will allow corrosion to start. Hence, this method of corrosion protection is generally only used for relatively inexpensive easily replaced items (e.g. bicycles, domestic outhouses, white goods).

Sacrificial protection:

This form of protection utilises the fact that some metals will corrode in preference to others. Table 1.6 shows the standard reduction potentials of commonly used metals. This value is a thermodynamic measure of how easy a metal is to extract from its ore and also consequently how easily it will corrode.

Table 1.6: Standard reduction potentials[11].

Electrode Reaction	**E°/V**
$Au^{+} + e^{-} = Au$	+1.68
$Pt^{2+} + 2e^{-} = Pt$	+1.20
$Hg^{2+} + 2e^{-} = Hg$	+0.85
$Ag^{+} + e^{-} = Ag$	+0.80
$Cu^{2+} + 2e^{-} = Cu$	+0.34
$2H^{+} + 2e^{-} = H_2$	0.00
$Pb^{2+} + 2e^{-} = Pb$	-0.13
$Sn^{2+} + 2e^{-} = Sn$	-0.14
$Ni^{2+} + 2e^{-} = Ni$	-0.25
$Cd^{2+} + 2e^{-} = Cd$	-0.40
$Fe^{2+} + 2e^{-} = Fe$	-0.44
$Cr^{3+} + 3e^{-} = Cr$	-0.71
$Zn^{2+} + 2e^{-} = Zn$	-0.76

$Al^{3+} + 3e^- = Al$	-1.67
$Mg^{2+} + 2e^- = Mg$	-2.34
$Na^+ + e^- = Na$	-2.71
$Ca^{2+} + 2e^- = Ca$	-2.87
$K^+ + e^- = K$	-2.92

From this series it can be seen that the most stable metals have the most positive electrode potentials (e.g. gold), and conversely the least stable metals, which corrode rapidly, have the most negative electrode potentials (e.g. sodium).

This fact can be used to protect an item, and is most commonly used today in the form of galvanised steel. A galvanised steel surface comprises a thin zinc layer laid on an iron surface. The zinc is a more electroactive metal and corrodes in preference to the iron by galvanic action when iron is exposed. Thus the zinc sacrifices itself to protect the iron. However, because it involves adding a great deal more weight to a product, this method is unsuitable for aerospace applications.

1.3.2: Anodic inhibitors.

A corrosion inhibitor can be defined as a substance which, when added in small concentrations to an environment, effectively reduces the rate of corrosion of a metal exposed to that environment[50].

Anodic inhibitors act by increasing the polarisation of the anode by reacting with ions of the corroding metal. This may produce either a thin passive film, or a salt layer of limited solubility, which coat the anode. Figure 1.9 shows an Evans diagram where an anodic inhibitor has been added to the system. The solid red line shows the initial anodic polarisation and the dashed red line represents the anodic

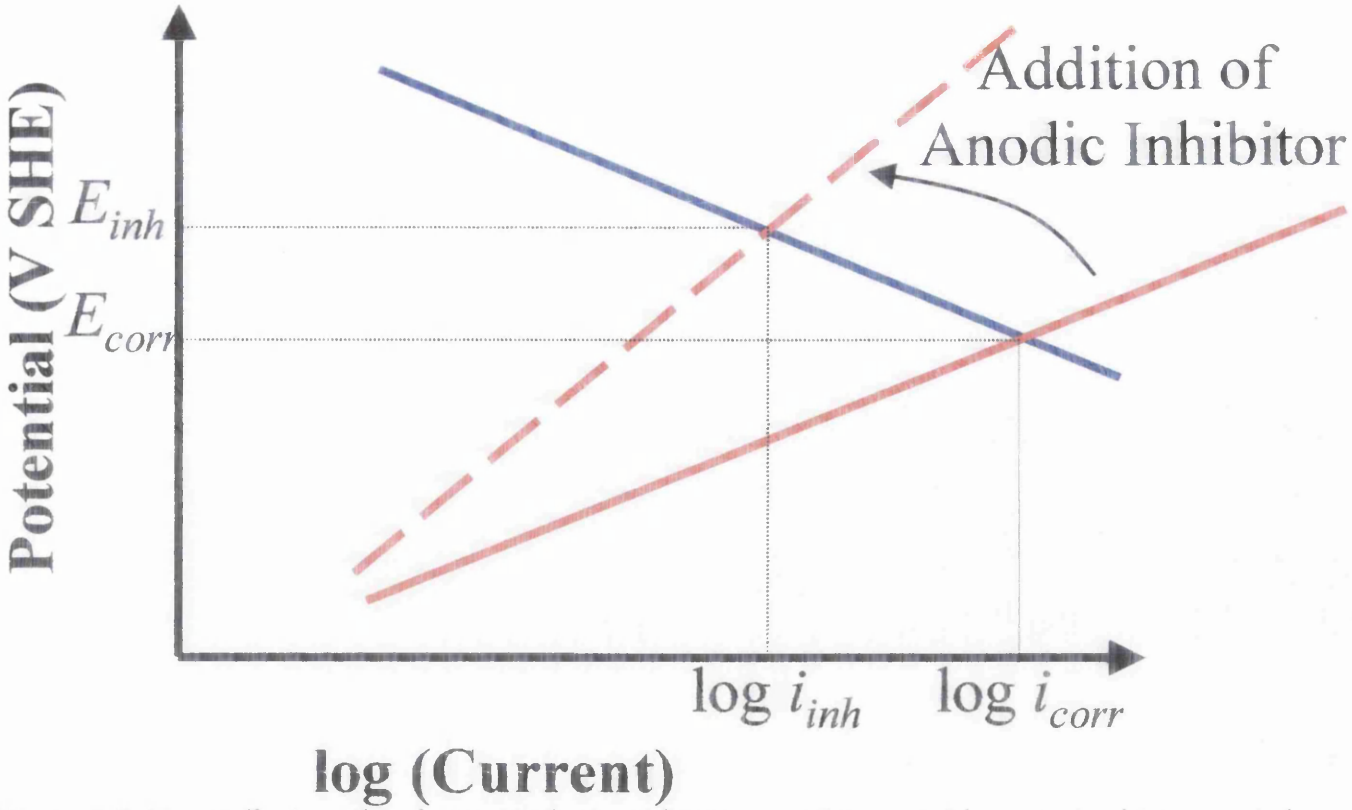

Figure 1.9: Evans diagram showing a simple corrosion process for a metal in contact with an aerated electrolyte. Dotted red line shows how anodic reaction changes when anodic inhibitor is added to the system.

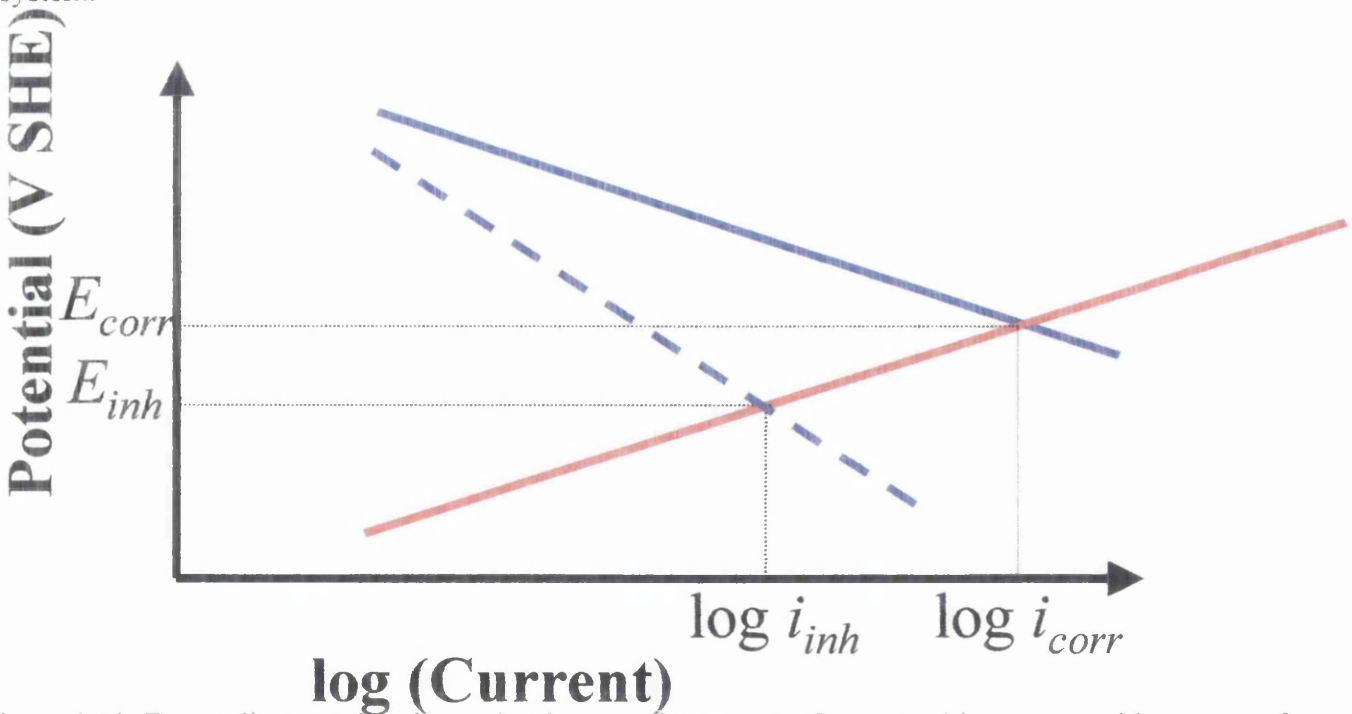

Figure 1.10: Evans diagram showing a simple corrosion process for a metal in contact with an aerated electrolyte. Dotted blue line shows how cathodic reaction changes when cathodic inhibitor is added to the system.

polarisation after the anodic inhibitor has been added. It can be seen from figure 1.9 that the corrosion current is decreased, however this is accompanied by an increase in the free corrosion potential[11,50]. Thus, if there is insufficient anodic inhibition to suppress all the corrosion in the system, the increased free corrosion potential will increase the thermodynamic driving force for corrosion. This will result in any remaining active sites experiencing an increased level of corrosion[49].

1.3.3: Cathodic inhibitors.

Figure 1.10 shows an Evans diagram for a simple corrosion process for a metal in contact with an aerated electrolyte as in figure 1.9. The dashed blue line indicates how the cathodic polarisation of the metal increases when a cathodic inhibitor is added to the system. As for the anodic inhibitor, this decreases the corrosion current, however in this case the free corrosion potential is also reduced. Hence, unlike for anodic inhibitors, even too little cathodic inhibitor added to a system will reduce corrosion activity because the thermodynamic driving force for corrosion is decreased[11,49].

1.3.4: Chromate containing inhibitors.

The use of chromates as corrosion inhibiting pigments in paints was first suggested in 1907[51] and now chromates are the most common corrosion inhibiting paint pigments[52]. Chromates are widely used in conversion coatings and paint pigments. The chromate ion is one of the most effective aqueous corrosion inhibitors for a wide range of metals including aluminium, zinc, steel and magnesium[52]. Chromates inhibit corrosion by forming a protective mixed chromium/metal oxide film (typically 0.1–1μm thick). The film forms as a result of the electrochemical reduction of the

chromate ion[52]. Chromate has proved itself to be a very effective inhibitor, and recently work has been carried out to quantify its effectiveness for comparison reasons[49,52, 53,54,58]. However, recently it has been found that chromates are toxic[55] and highly carcinogenic[56] which has resulted in increasing pressure for the development of more environmentally acceptable alternatives[57,58].

1.3.5: Rare Earth Metal (REM) salt containing inhibitors.

Due to the recent demands to reduce the usage of chromates as corrosion inhibitors, researchers have been looking for more environmentally friendly alternatives. One possible approach is Rare Earth Metal (REM) cations (i.e. cerium Ce^{3+}, Lanthanum La^{3+} and Yttrium Y^{3+}). REM salts act as cathodic precipitation inhibitors, they react with the hydroxyl ions generated by the oxygen reduction reaction to precipitate insoluble compounds on the cathodic site. This covers the cathodic sites thus stopping the electrolyte and oxygen reaching the surface.

Recently there has been much research into the effectiveness of REM salts as corrosion inhibitors[59,60,61,62,63,64] in particular cerium[59,60,61,62,63,65,66] and yttrium[59,61,63]. The rare earth metal salts have been found to successfully inhibit corrosion on various metallic surfaces including mild steel[67], stainless steel[68], zinc[69], zinc coated steel[69] and aluminium aerospace alloys[60,61,62,63,64,65].

1.4: Scanning Vibrating Electrode Technique (SVET).

1.4.1: Introduction.

The Scanning Vibrating Electrode Technique (SVET), is a scanning technique capable of estimating components of current density in solution near a corroding surface which may be related to the local corrosion rate. The SVET relies on

measurement of potential gradients in solution, which arise as a consequence of the ionic current flux generated by local corrosion cells. In corrosion studies, the potential gradient and hence current flux component measured by SVET is typically that lying normal to the corroding surface.

1.4.2: Theory.

When a metallic surface is freely corroding in contact with a conductive electrolyte, the circuit between the local anode and cathode is completed by electronic conduction through the bulk metal. The electronic resistivity of metals is sufficiently low that no significant potential differences arise in the metallic phase, therefore the metal surface itself may be considered as a plane of constant potential. However, aqueous solutions of electrolyte exhibit ionic conductivity and typically have much higher resistivity than metals. Consequently, the passage of ionic current through the electrolyte produces significant ohmic potential gradients, which may be described in terms of lines of iso-potential lying normal to the lines of ionic current flux, as shown in figure 1.11[70].

The distribution of potential and ionic current in solution can theoretically be determined from the Laplace equation (1.7),

$$\nabla^2 E = 0 \qquad [1.7]$$

where E is the electrical potential, and from Ohm's Law,

$$i = -\kappa \cdot \nabla E \qquad [1.8]$$

Where i is current and κ is the solution conductivity.

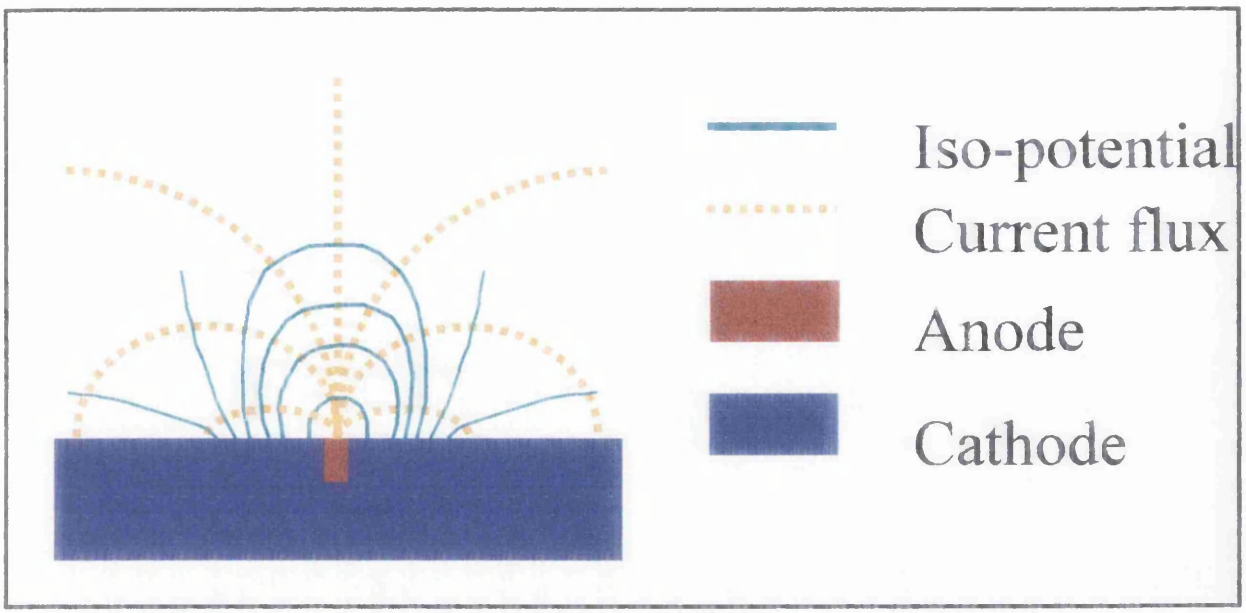

Figure 1.11: Diagram of the distribution of ionic current and thus lines of iso-potential in an electrolytic solution above a metal sample, which consists of a localised anodic pit surrounded by a distributed cathode[70].

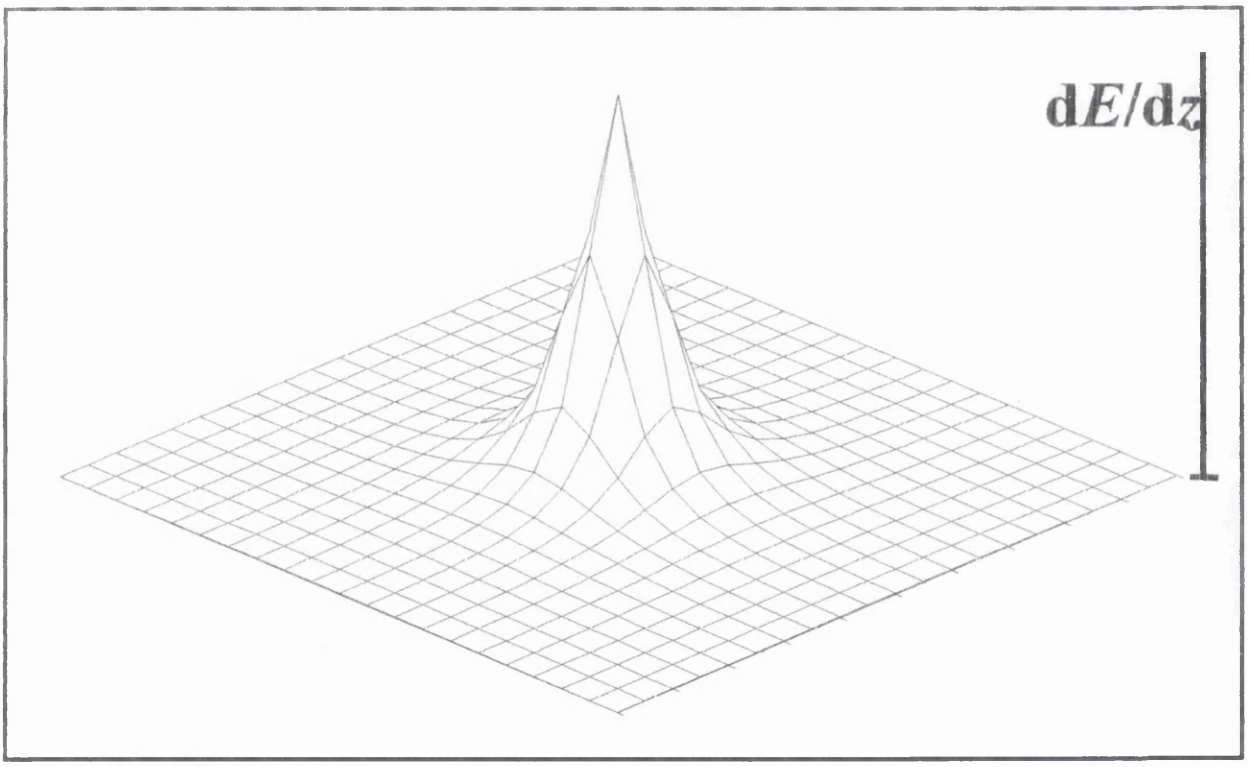

Figure 1.12: Surface plot showing the theoretical distribution of the vertical component of potential gradient above a point current source set in an insulating plane, where the quantity is calculated at a height (z) equivalent to 0.08 times the length of the x and y axes shown.

A general solution to this problem is not possible and, analytical solutions are non-trivial only in the simplest of cases. An analytical solution is possible for a point current source i, situated at height $z = 0$ on a non-conducting x,y plane with the current drain at infinity[71]. For this case it may be shown that the potential at any point (x,y,z) in solution is inversely proportional to the distance from the source and, is given by[72]

$$E = \frac{i}{2\pi\kappa\sqrt{(x^2 + y^2 + z^2)}} \qquad [1.9]$$

The normal field strength (F_0), measured by vibrating the SVET probe perpendicular to the surface, is given by[72]

$$F_0 = \frac{dE}{dz} = -\frac{iz}{2\pi\kappa\,(x^2 + y^2 + z^2)^{1.5}} \qquad [1.10]$$

The distribution of normal field strength in solution across a plane of constant height above a point current source is shown graphically in figure 1.12, which shows the characteristically peak shape centred about the current source.

The maximum field strength ($F_{0(max)}$) at height z occurs directly above the origin (x=0, y=0) and is given by

$$F_{0(\max)} = -\frac{i}{2\pi\kappa z^2} \qquad [1.11]$$

The inverse square relationship between $F_{0(max)}$ and the probe height z makes the control of probe height critical in SVET measurements of highly localised current

sources resembling point sources. Consequently when such measurements are being performed the probe should be kept at as constant a height above the samples as possible.

The theoretical spatial resolution of the SVET at any particular scan height may be characterised in terms of the signal peak-width at half maximum (whm) above a point current source, in as much as it would be difficult to resolve two point current sources that were closer together than the value of whm. If we define a parameter r as the distance on the (x,y) plane from the point current source such that

$$r = (x^2+y^2)^{0.5} \qquad [1.12]$$

then the value of r for which the value of F_o falls to half its maximum value (i.e. $0.5F_{0(max)}$) is obtained by combining equations (1.10) and (1.12).

$$0.5\,F_{0\,(\max)} = -\frac{iz}{2\pi\kappa\,(r^2+z^2)^{1.5}} \qquad [1.13]$$

The ratio of equations (1.11) and (1.13) then gives

$$r = z\,(2^{2/3}-1)^{0.5} \qquad [1.14]$$

and since the width of the SVET response peak is twice the value of r

$$\text{whm} = 2r = 1.533z \qquad [1.15]$$

Model studies[72] of the SVET have verified the relationships given by equation (1.15) for point current sources. Similar studies have demonstrated the ability of the SVET to accurately determine normal current density distributions above equi-potential disc and equi-current disc current sources[72]. It has also been shown that the variation in normal current density above any electrode may be modelled by substituting the true surface current distribution with an array of point current sources[72]. From this it can

be suggested that SVET data can be used to completely characterise the surface current density distribution of a locally corroding surface[72].

1.5: Scanning Kelvin Probe (SKP).

1.5.1: Introduction.

The Scanning Kelvin Probe (SKP), is a scanning technique used in investigating atmospheric corrosion affecting metallic surfaces, as pioneered by Stratmann and others[73,74,75,76]. The SKP is one of the most sensitive measuring procedures in surface physics and is a well established means of determining metallic work functions. The SKP can also be used to electrochemically map the localised corrosion phenomena occurring beneath thin electrolyte films and beneath intact polymer coatings[70].

1.5.2: Theory.

A schematic diagram illustrating the Kelvin Probe technique can be seen in figure 1.13. The tip of the probe electrode and the metal sample surface under study constitute the two plates of a parallel plate capacitor. The non-conducting medium (typically air, or a mixture of air gap and insulating polymer) in the space between the plates constitutes the capacitor dielectric. The capacitance (C) of a parallel plate capacitor is given by[70],

$$C = \frac{\varepsilon \varepsilon_0 A}{D} \qquad [1.16]$$

Where D is the distance between the plates, A the plate area, ε_0 the permittivity of a vacuum, and ε the dielectric constant of the capacitor dielectric.

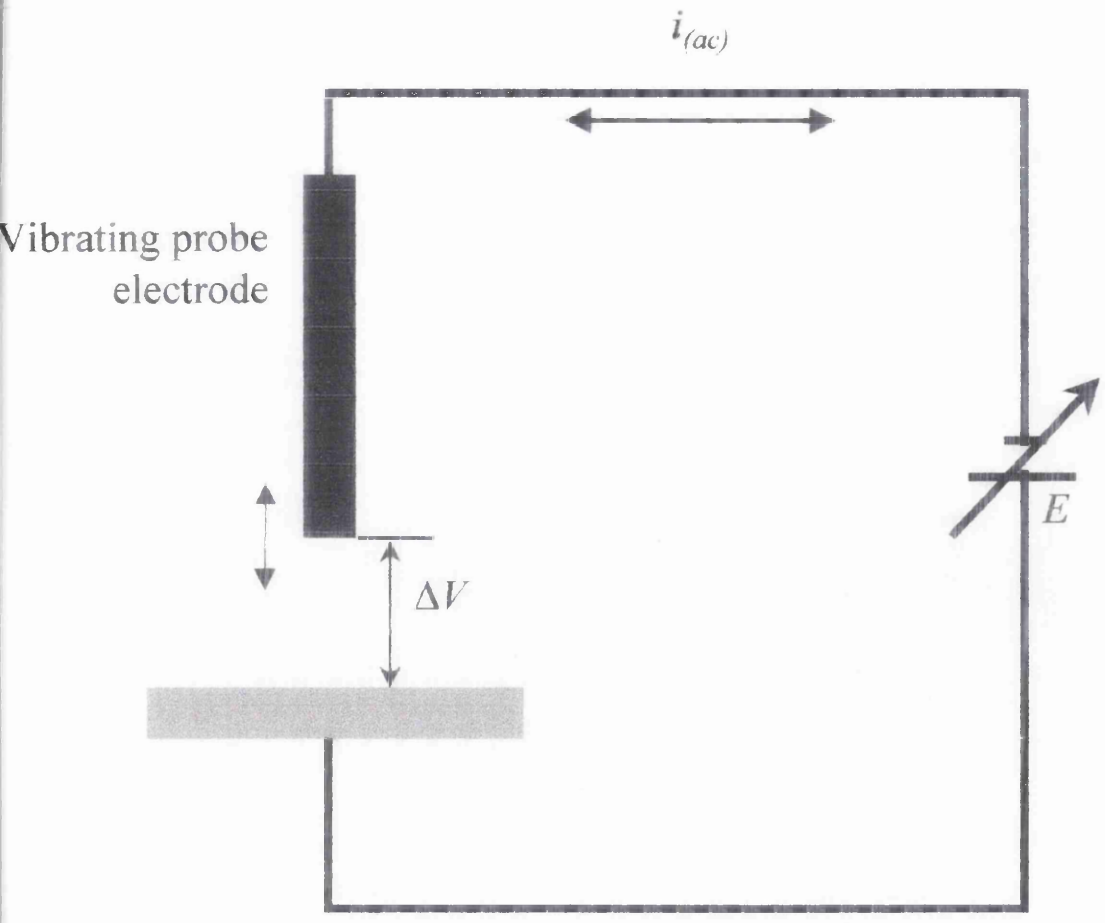

Figure 1.13: Schematic diagram illustrating the Kelvin probe for measuring surface (Volta) potential, where ΔV = Volta potential difference, E = experimentally applied bias potential and $i_{(ac)}$ = current flow in external circuit due to Volta potential difference.

The probe electrode is vibrated in a sinusoidal fashion relative to the sample surface, at a frequency ω such that the plate separation, D, varies with time, t, according to,

$$D = D_0 + D_1 \sin(\omega t) \qquad [1.17]$$

where D_0 is the mean plate separation, and D_1 is the amplitude of vibration. From this it can be seen that the probe vibration produces a periodic fluctuation in the capacitance. Also, if any Volta potential difference (ΔV) exists between the probe and the sample surface an alternating current (i) will flow in the external circuit, this will be given by,

$$i = \frac{dQ}{dt} = \Delta V \frac{dC}{dt} \qquad [1.18]$$

where Q is the electric charge on the capacitor plates. Substituting equations (1.16) and (1.17) into (1.18) gives,

$$i = -\varepsilon\varepsilon_0 A \Delta V \frac{D_1 \omega \cos(\omega t)}{[D_0 + D_1 \sin(\omega t)]^2} \qquad [1.19]$$

which for cases where $D_0 >> D_1$ the relationship simplifies to,

$$i = -\varepsilon\varepsilon_0 A \Delta V \frac{D_1 \omega \cos(\omega t)}{D_0^{\,2}} \qquad [1.20]$$

It may also be shown that the maximum signal current (i_{max}) is obtained when,

$$D_1 = \frac{D_0}{(2)^{-(1/2)}} \qquad [1.21]$$

Which may be written as,

$$D_0 = \frac{D_{min}}{1 - (\frac{1}{2^{(-1/2)}})} \qquad [1.22]$$

Where $D_{min} = D_0 - D_1$ = minimum distance between plates.

The Kelvin probe signal current is not directly used to infer the open circuit value of ΔV. This is instead obtained indirectly by adjusting the value of the externally applied DC bias voltage, E, such that the signal current becomes zero, i.e. the null current condition. Under these circumstances,

$$E = E_{i=0} = -\Delta V \qquad [1.23]$$

$E_{i=0}$ is the experimentally measured quantity, so the Kelvin Probe potential, E_{kp}, will be defined as being equal to - $E_{i=0}$, and which is wherefore equivalent to the Volta potential difference ΔV as determined by the Kelvin probe[70].

The exact meaning of E_{kp} is dependant on the conditions under which the measurement is made. If the conditions consist of a pristine metal surface placed in a perfect vacuum then the value of E_{kp} will be equal to the difference in work functions of the metals composing the probe and the sample. However, when the experimental conditions vary from these ideals, such as measurements taken in air and therefore in the presence of oxide films, E_{kp} is likely to deviate from the expected values based purely on metallic work functions[73]. Even further differences in E_{kp} are likely when other factors such as atmospheric humidity as a consequence of water absorption and the hydration of any surface oxide layer are taken into account[73].

When the metal surface is covered in a thin layer of a conducting electrolyte the interpretation of E_{kp} is more complex. Under these conditions the probe is directly above the electrolytic film, not the metallic surface, so the relevant Volta potential difference is not that existing between the probe and the metallic surface, but that existing between the probe and the outer surface of the electrolyte film. Electrolyte film potentials are subject to influences from a number of sources including electrical double layer effects at the metal-solution interface, and the presence of potential gradient in the solution resulting from the passage of ionic currents between localised corrosion sites[73]. However, it has been shown that if the electrolyte film is thicker than the electrical double layer and no ionic currents are flowing in solution then[73],

$$E_{kp} = E_{corr} + constant \qquad [1.24]$$

Where E_{corr} is the free corrosion potential of the metal relative to a real or hypothetical reference electrode immersed in the electrolyte film immediately over the point of measurement[70]. A significant advantage of the Kelvin probe technique is that since E_{kp} is measured under null current conditions, the measurement does not electrically perturb the sample-solution interface. Also the measurement is indifferent to the nature of the dielectric overlaying the metal or the electrolyte surface, hence E_{kp} measurements may be carried out with samples coated with, for example, an insulating polymer film.

1.6: Reference:

[1] S. Wernick and R. Pinner, Surface treatment of aluminium, Robert Draper Ltd, **1**, 3 (1971).
[2] Chambers Science and Technology Dictionary, (Ed. P. M. B. Walker) W & R Chambers Ltd, 27 (1991).
[3] R. Woodward, www.azom.com, (Ed. S. Harmer).
[4] A. Porter and K. E. Easterling, *Metals and Alloys*, Chapman and Hall, (1992).
[5] D. R. Askland, *The Science and Engineering of Materials*, Chapman and Hall, (1996).
[6] L. F. Mondolfo, *Aluminium Alloys: Structure and Properties*, ,Butterworth Markam, Ontario, CN, 497 (1976).
[7] L. F. Mondolfo, *Aluminium Alloys: Structure and Properties*, ,Butterworth Markam, Ontario, CN, 688 (1976).
[8] R. G. Buchheit, R. P. Grant, P. F. Hlava and G. L. Zender, *J. Electrochem. Soc.*, **144,** 2621 (1997).
[9] H. H. Strehblow, *"Corrosion"*, Corrosion and Environmental Degradation, (Ed. M. Schutze) Wiley-Vch, **1**, 5 (2000).
[10] M. Spoelstra, Filiform Corrosion of Anodised Aluminium Alloys, ISBN 90-901-3375-5, (1999).
[11] K. R. Trethewey and J. Chamberlain, Corrosion for Science and Engineering, Longman (1988).
[12] G. T. Bakhvalov and A. V. Turkovskaya, Corrosion and Protection of Metals (Ed. G Isserlis) Pergomon Press (1965).
[13] R. Parsons, Pure Appl. Chem., **37**, 512 (1974).
[14] J. M. O'Bockris, Modern Aspects of Electrochemistry (Ed. J. M. O'Bockris and B. E. Conway) Butterworths: London, Chap 4 (1954).
[15] P. Van Rysselburg, Electrochem. Acta, **9**, 1343 (1964).
[16] C. Wagner and W. Traud, Z. Electrochem., **44**, 391 (1938).
[17] L. Kiss, Kinetics of Electrochemical Metal Dissolution, Elsevier, 11 (1988).
[18] J. Tafel, Z. Physik. Chem., **50**, 641 (1905).
[19] M. Huisert, Electrochemical Characterisation of Filiform Corrosion on Aluminium Rolled Products, ISBN 90-407-2236-6, (2001).
[20] R. T. Foley, Corrosion NACE, **42**, 277 (1986).
[21] R. Ambat and E. S. Dwarakadasa, *J. Appl. Electrochem.*, **24,** 911 (1994).
[22] K. SugimotoK. Hoshino, M. Kageyama, S. Kageyama and Y. Sawada, *Corros. Sci.*, **15,** 709 (1975).
[23] T. J. Warner, M. P. Schmitt, F. Sommer and D. Bellot, *Z. Metallkd.*, **86,** 494 (1995).
[24] C. Blanc, B. Lavelle and G. Mankowski, *Corros. Sci.*, **39,** 495 (1997).
[25] J. O. Park, C. H. Paik, Y. H. Huang and R. C. Alkire, *J. Electrochem. Soc.*, **146,** 517 (1999).
[26] P. Leblanc and G. S. Frankel, *J. Electrochem. Soc.*, **149, B**239 (2002).
[27] L. Muller and J. R. Galvele, *Corros. Sci.*, **17,** 179 (1977).
[28] J. Galvele and S. M. DeMicheli, *Corros. Sci.*, **10,** 795 (1970).
[29] K. Urishino and K. Sugimoto, *Corros. Sci.*, **19,** 225 (1979).
[30] T. Suter and R. C. Alkire, *J. Electrochem. Soc.*, **148,** B36 (2001).
[31] K. Nisancioglu and H. Holtan, *Corros. Sci.*, **19,** 537 (1979).
[32] R. P. Wei, C.-M. Liao and R. O. C. Ming, *Metall. Mater. Trans.*, A **29A**, 1153

(1998).
[33] K. Shimizu, K. Kobayashi, G. E. Thompson and G. C. Wood, *Corros. Sci.*, **34,** 1475 (1993).
[34] M. B. Vukmirovik, N. Dimitrov and K. Sieradszki, *J. Electrochem. Soc.*, **149,** B428 (2002).
[35] N. Dimitrov, J. A. Mann, M. B. Vukmirovik, and K. Sieradszki, *J. Electrochem. Soc.*, **147,** 3283 (2000).
[36] R. G. Buchheit, M. A. Matrinez and L. P. Montes, *J. Electrochem. Soc.*, **147,** 119 (2000).
[37] N. Dimitrov, J. A. Mann and K. Sieradski, *J. Electrochem. Soc.*, **146,** 98 (1999).
[38] T. J. R. Leclere and R. G. Newman, *J. Electrochem. Soc.*, **149,** B52 (2002).
[39] H. H. Ulig, Corrosion Handbook, 1st. edn. P. 53, Wiley, New York (1948).
[40] P. Hulser and F. Beck, *Aluminium*, **67,** 999 (1991).
[41] P. Hulser, U. A. Kruger and F. Beck, *Corros. Sci.*, **38,** 47 (1996).
[42] C. F. Sharman, *Nature*, **153**, 621 (1944).
[43] R. T. Ruggieri and T. R. Beck, *Corrosion*, **39**, 452 (1983).
[44] A. Bauista, *Prog. Org. Coatings*, **28**, 49 (1996).
[45] G. Grundmeier, W. Schmidt and M. Stratmann, *Electrochim. Acta*, **45,** 2515 (2000)
[46] N. Le Bozec, D. Persson, A. Nazarova and D. Thierry, *J. Electrochem., Soc.*, **149,** B403 (2002).
[47] W. Schmidt and M Stratmann, *Corrosion Sci.*, **40**, 1441 (1998).
[48] J. H. W. de Wit, Electrochim. Acta, 46, (2001), 3641.
[49] S. Powell, Scanning Electrochemical Techniques for Monitoring Localised Corrosion in Organically Coated Galvanised Steels, Eng.D. thesis, University of Wales Swansea, (1999).
[50] D. Harrop, Chemical Inhibitors for Corrosion Control in Proceedings of the Industrial Division of the RSC and Institution of Corrosion Science and Technology, University of Manchester, (Ed. B. G. Clubley), 1 (1990).
[51] A. S. Cushman, Proc. ASTM, **3**, 211 (1907).
[52] B. R. W. Hinton, Corrosion Prevention and Chromates, the End of an Era?, Metal Finishing, 55 (1999).
[53] H. N. McMurray, G. Williams and S. O'Driscoll, *Corrosion and Corrosion Protection*, (Ed. J. D. Sinclair, R. P. Frankenthal, E. Kalman and W. Plieth), Electrochemical Society Proceedings, **2001-22**, 891 (2001).
[54] J. H. Osborne, *et al*, Progress in Organic Coatings, **41**, 217 (2001).
[55] U.S. Public Health Service, *Toxicological Profile for Chromium, Report No ATSDR/TP 88/10*, Agency for toxic substances, U.S. Public Health Service, Washington D.C., (1989).
[56] U.S Environmental Protection Agency, "Health Assessment Document for Chromium", *Final Report*, EPA-600/8-83-014F, 21 (1984).
[57] G. Pallos and G. Wallwork, *Corrosion*, **38**, 305 (1982).
[58] H.N. McMurray, S.M. Powell and D.A. Worsley, *Corrosion*, **55**, 1040 (1999).
H.N. McMurray, S.M. Powell and D.A. Worsley, *Corrosion 99 NACE International Conference Proceedings*, San Antonio, Texas, paper 211, (1999).
[59] B. R. W. Hinton, Corrosion 89, NACE International, New Orleans, Louisiana, Paper 170 (1989).
[60] A. J. Aldykewicz jr, H. S. Isaacs and A. J. Davenport, J. Electrochemical Society, **142**, 3342 (1995).

[61] B. R. W. Hinton, *et al.*, Corrosion Australasia, 12 (1985).
[62] B. R. W. Hinton, Journal of Alloys and Compounds, **180**, 15 (1992).
[63] D. R. Arnott, B. R. W. Hinton and N. E. Ryan, Corrosion Science, **45**, 11 (1989).
[64] M. Bethencourt, *et al.*, Corrosion Science, **40**, 1803 (1998).
[65] D. R. Arnott, *et al.*, Applications of Surface Science, **22/23**, 236 (1985).
[66] A. J. Aldykewicz jr, A. J. Davenport and H. S. Isaacs, J. Electrochemical Society, **143**, 147 (1996).
[67] B. R. W. Hinton, Journal of Alloys and Compounds, **180**, 15 (1990).
[68] S. Bernal, *et al.*, Journal of Alloys and Compounds, **225**, 638 (1995).
[69] B. R. W. Hinton and L. Wilson, Corrosion Science, **29**, 967 (1989).
[70] H. N. McMurray and D. A. Worsley, "*Scanning Electrochemical Techniques for the Study of Localised Metallic Corrosion*", Research in Chemical Kinetics, (Ed. R. G. Compton and G. Hancock) Blackwell Science Ltd, **4**, 149 (1997).
[71] C. Kasper, *Trans. Electrochem. Soc.* **77**, 353 (1940).
[72] H. S. Isaacs, *Journal of the Electrochemical Society*, **138**, 723 (1991).
[73] S. Yee, R. A. Oriani and M. Stratmann, *Journal of the Electrochemical Society*, **138**, 55 (1991).
[74] M. Stratmann and H. Streckel, *Corrosion Science*, **30**, 681 (1990).
[75] M. Stratmann, H. Streckel and R. Feser, *Corrosion Science*, **32**, 467 (1991).
[76] M. Stratmann, M. Wolpers, H. Streckel and R. Feser, *Ber. Busenges. Phys. Chem.*, **95**, 1365 (1991).

Chapter 2.

Chapter 2: Experimental apparatus, calibration and quantification.

2.1: Scanning Vibrating Electrode Technique (SVET).

2.1.1: Integration of normal current density data.

If we consider a point current source (i) set in a insulating surface with the current drain at infinity, the potential (E) at any point in solution defined by a set of Cartesian co-ordinates (x,y,z) with the origin at the point source and the insulating surface lying in the x,y plane will be given by equation 1.9. The potential gradient ($\partial E/\partial z$) normal to the x,y plane may then obtain by partial differentiation of equation 1.9 with respect to z.[1,2], and is given by equation 1.10.

From equation 1.8 (Ohms law) the potential gradient $\partial E/\partial z$ will be related to the component of current density along the z axis (jz) by

$$\frac{\partial E}{\partial z} = \frac{jz}{\kappa} \qquad [2.1]$$

where κ is the solution conductivity. Thus, from equations 1.10 and 2.1 we may write

$$jz_{(x,y,z)} = \frac{i.z}{2.\pi(x^2+y^2+z^2)^{1.5}} \qquad [2.2]$$

If, for reasons of symmetry, we let $r^2 = x^2 + y^2$, equation 2.2 may be rewritten as

$$jz_{(r,z)} = \frac{i.z}{2.\pi(r^2+z^2)^{1.5}} \qquad [2.3]$$

The area integral of jz about the origin may then be obtained by writing the infinitesimal increment in area as $2.\pi.r.dr$. Thus,

$$\int_0^R jz_{(r,z)} \cdot dr = i \int_0^R \frac{z.r}{(r^2 + z^2)^{1.5}} \cdot dr \qquad [2.4]$$

which yields

$$i\,\phi_{(R,z)} = i\left(1 - \frac{z}{(R^2 + z^2)^{0.5}}\right) \qquad [2.5]$$

where $\phi_{(R,z)}$ is the fraction of i detected by integration of $jz_{(r,z)}$ over a circular area of constant z and radius R, concentric with the point source. It may be shown from equation 2.5 that, for any finite value of z, $\phi_{(R,z)} \longrightarrow 1$ as $R \longrightarrow \infty$. Furthermore, it may be shown that $\phi_{(R,z)} = 0.5$ for $R = \sqrt{3}\ z$, *i.e.* half the point source current may be detected by integration of $jz_{(r,z)}$ up to a radius 1.732 times z. Figure 2.1a shows $\phi_{(R,z)}$ as a function of dimensionless R, for various values of dimensionless z, plotted according to equation 2.5.

However, in practical SVET measurements the probe is scanned in a rectilinear, and not a circular, fashion. It is therefore desirable to carry out the integration of jz values over a square or rectangular area. Under these circumstances the appropriate area integral is obtained from equation 2.2, *i.e.*

$$\int_{-Y}^{Y}\int_{-X}^{X} jz_{(x,y,z)}\,dxdy = \int_{-Y}^{Y}\int_{-X}^{X} \frac{i.z}{2.\pi(x^2 + y^2 + z^2)^{1.5}}\,dxdy \qquad [2.6]$$

Which yields,

$$i.\phi_{(X,Y,z)} = \left(\frac{2.i}{\pi}\right).\arctan\left(\frac{X.Y}{z.(X^2 + Y^2 + z^2)^{0.5}}\right) \qquad [2.7]$$

Where $\phi_{(X,Y,z)}$ is the fraction of i detected by integration of jz over a rectangular area of length $2X$ and breadth $2Y$, concentric with the point source. When integration is performed over a square area of side $2a$ equation 2.7 simplifies to give

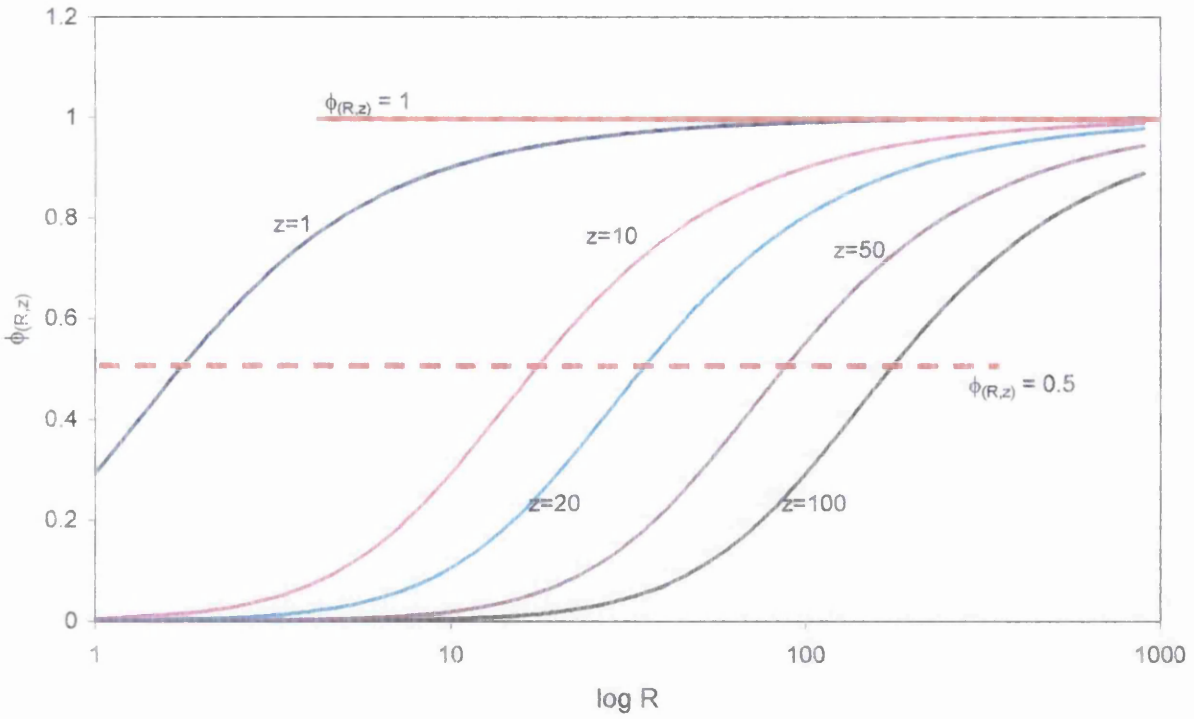

Figure 2.1a: Plot showing how $\phi(R,z)$ varies as a function of dimensionless R, for various values of dimensionless z, plotted according to equation 2.5 (Red line indicated the value at which all current is detected).

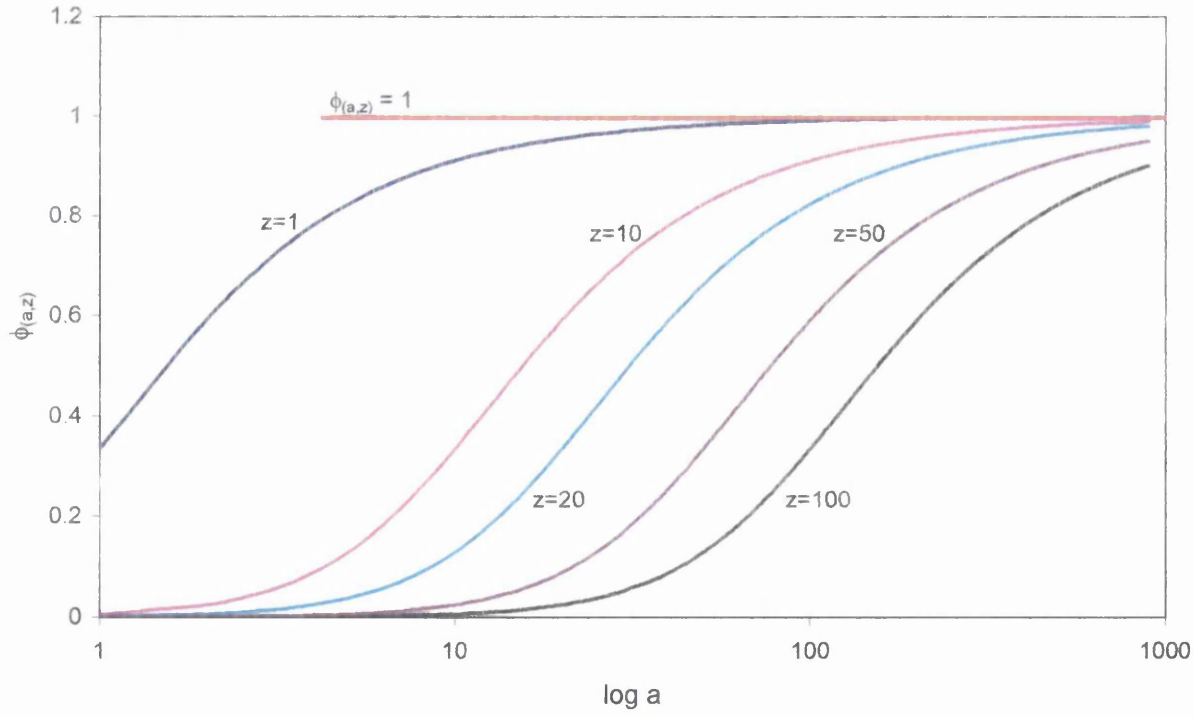

Figure 2.1b: Plot showing how $\phi(a,z)$ varies as a function of dimensionless a, for various values of dimensionless z, plotted according to equation 2.8 (Red line indicated the value at which all current is detected.)

$$i.\phi_{(a,z)} = \left(\frac{2.i}{\pi}\right).\arctan\left(\frac{a^2}{z.(2.a^2+z^2)^{0.5}}\right) \qquad [2.8]$$

Using equation 2.6 it may be shown that the fraction of i detected, $\phi_{(a,z)}$, $\longrightarrow 1$ as a/z $\longrightarrow \infty$, also that $\phi_{(a,z)} = 0.5$, 0.9 and 0.99 when $a = 1.555 \cdot z$, $9 \cdot z$ and $90 \cdot z$, respectively. Figure 2.1b shows $\phi_{(a,z)}$ as a function of dimensionless a, for various values of dimensionless z, plotted according to equation 2.8[3].

2.1.2: Apparatus.

A schematic diagram of the SVET equipment used can be seen in figure 2.2a. The sample to be scanned is placed on a Perspex table (a schematic diagram in figure 2.3) in a tank of electrolyte. The height and orientation of the sample table is adjustable via screw threads, making it possible to level the sample. The micro-computer (IBM compatible, Pentium II™ processor supplied by Mertec Ltd) is used to control the lock-in amplifier (Perkin Elmer model 7505) parameters such as sensitivity, frequency and drive voltage before each scan (control shown as a black line on figure 2.2a). The computer is also used to control the motor drivers (L25 Paragon drives supplied by Time and Precision Ltd) which move the tri-axial micro-manipulator (x-y platform: model XY4505CR-GBS compact table, z-axis: model UP2505P motorised ballslide, for mechanical details see table 2.1[4], supplied by Time and Precision Ltd) (green line on figure 2.2a). An optical picture of the SVET equipment used can be seen in figure 2.2b.

The blue line in figure 2.2a shows the path of the vibrator drive voltage, which is sent from the lock-in amplifier to an external amplifier (gain ten), and then to the

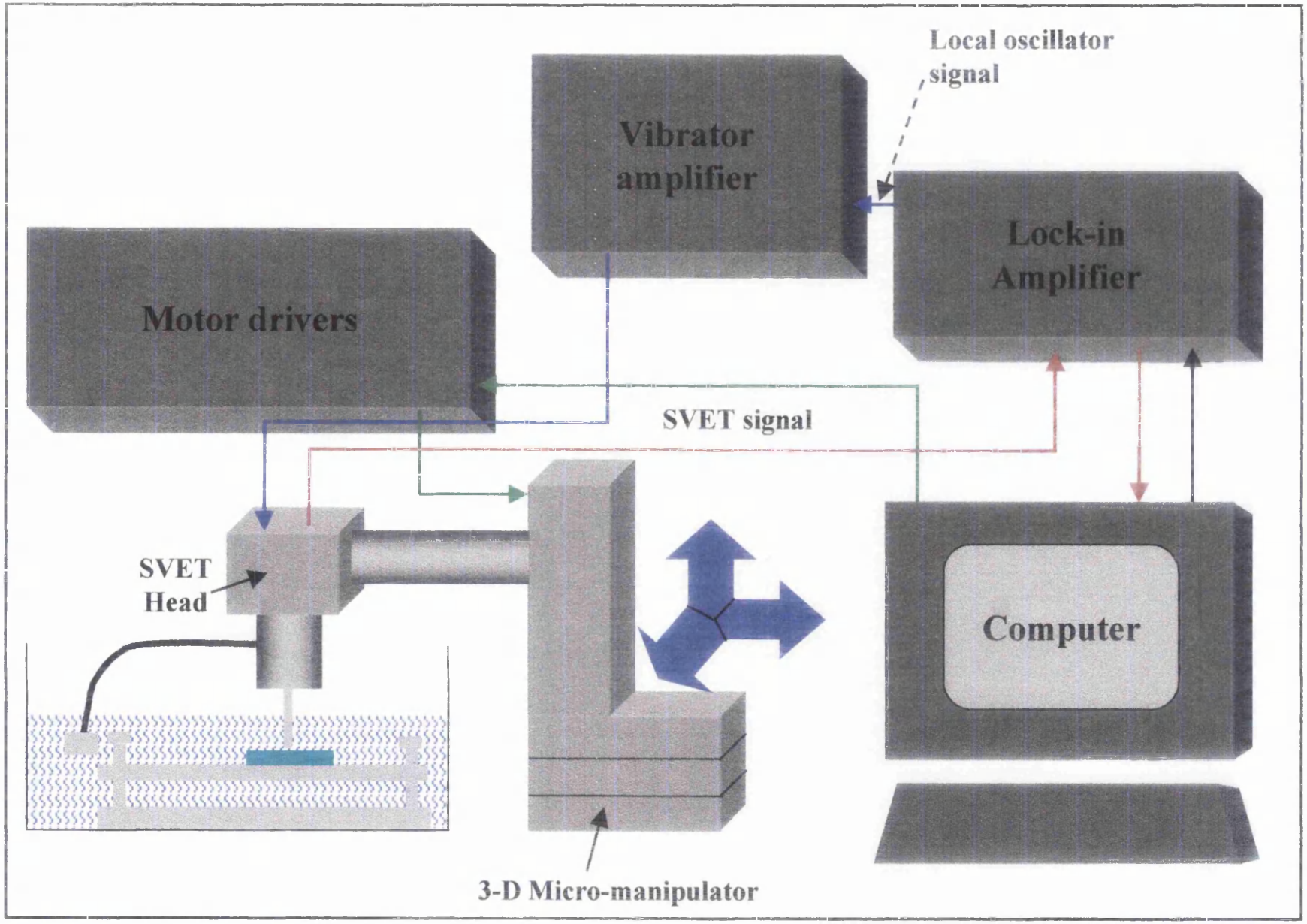

Figure 2.2a: A schematic diagram of the SVET apparatus.

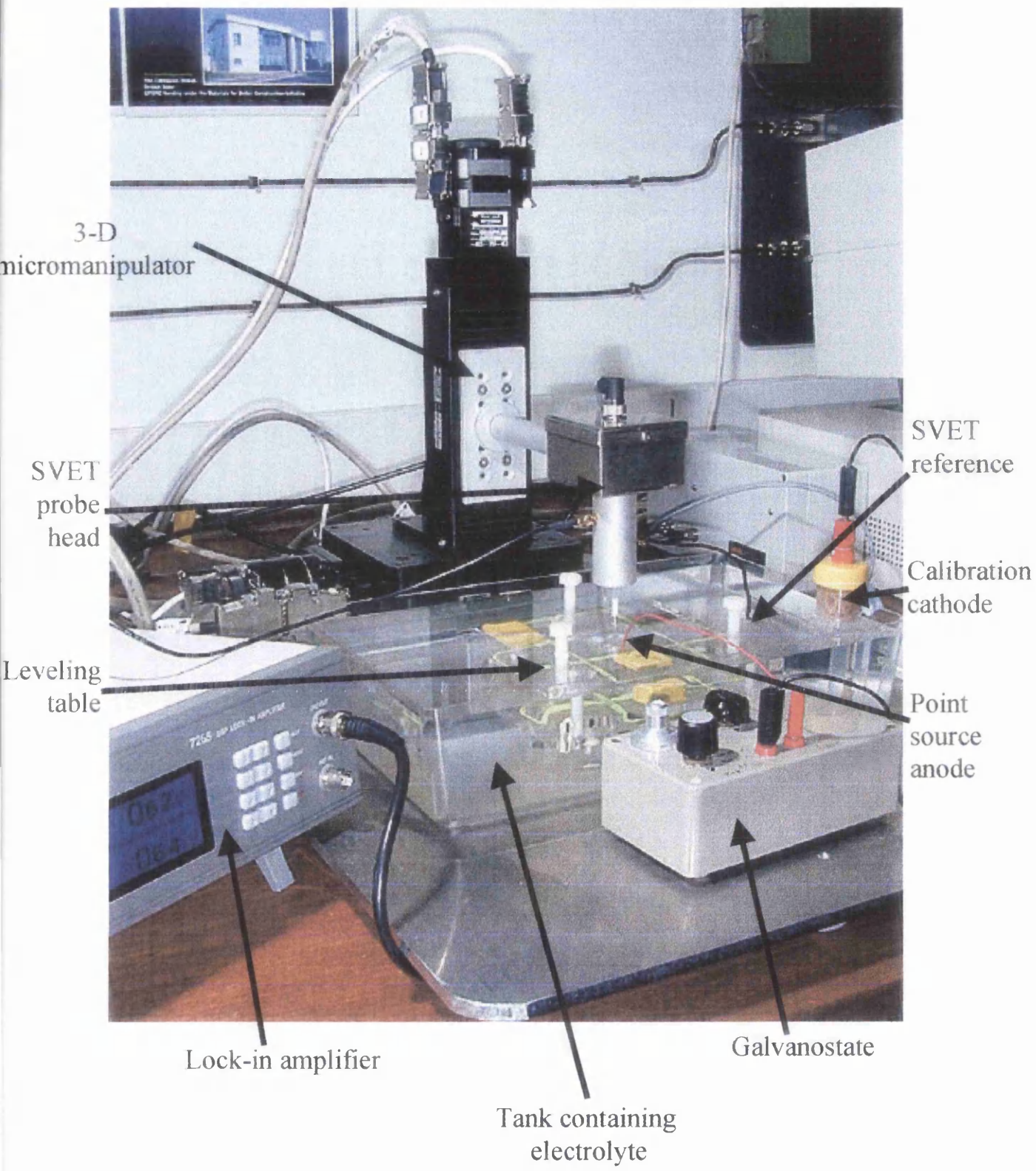

Figure 2.2b: Optical picture of SVET equipment used throughout, as set-up for point source calibration.

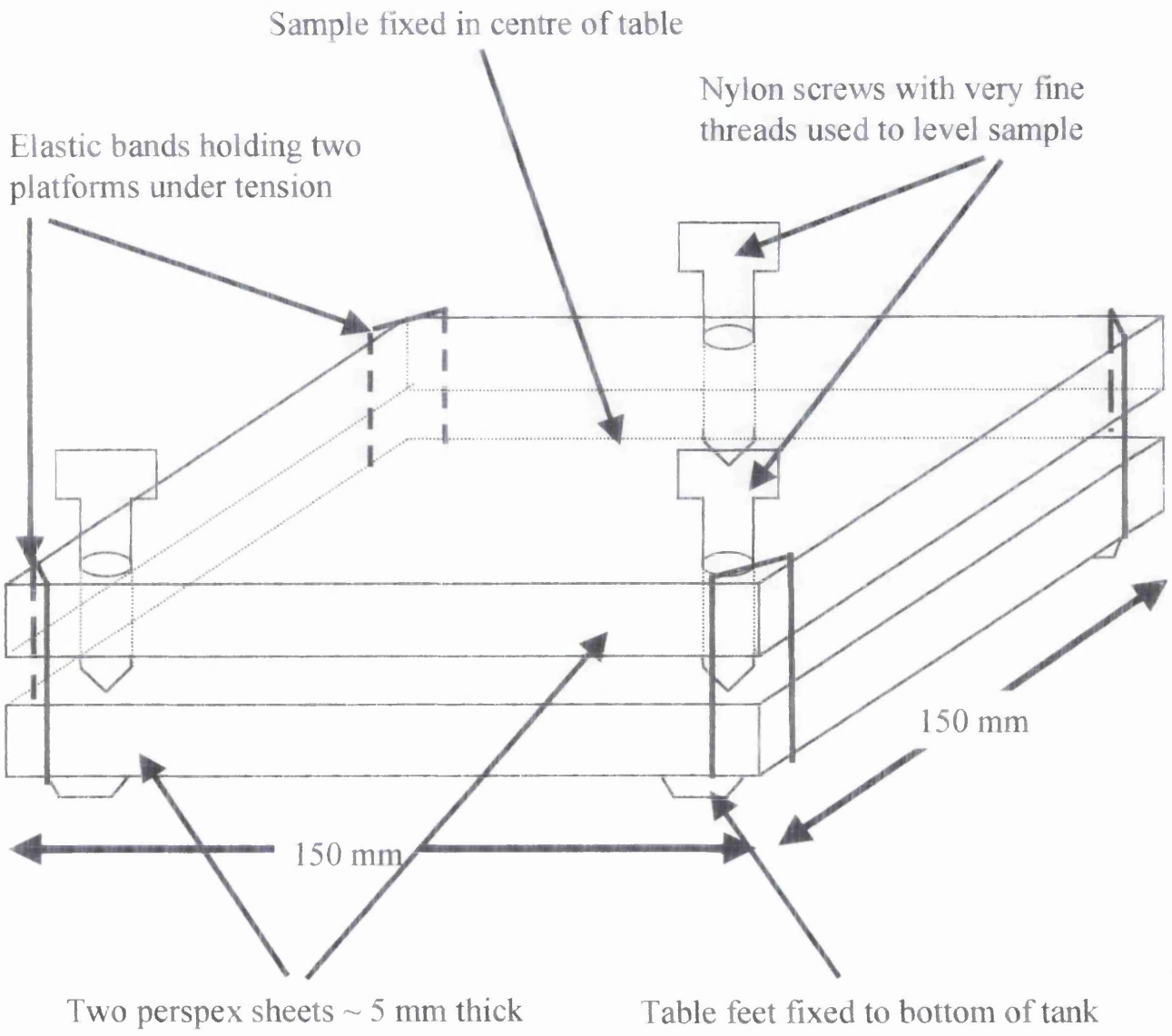

Figure 2.3: Schematic diagram of SVET leveling table.

SVET head, where it is used to drive the probe electrode, via a 8Ω 1 watt moving coil loudspeaker (see SVET head design figure 2.4). The signal picked up by the probe electrode is detected using the lock-in amplifier. The lock-in only detects signals at the drive frequency, thus greatly reducing experimental noise (see red line on figure 2.2a). The r.m.s value of the detected signal voltage is digitised in the lock-in amplifier and recorded by the micro computer.

Table 2.1: Table showing the mechanical details available for the tri-axial micro-manipulator[4].

	***z*-axis**	***x*-*y* platform**
Usable travel	50mm	50x50mm
Linear accuracy	-	2μm
Repeatability	-	2μm
Maximum load	8.0kg	55kg
Resolution	Depends on drivers used	2.5μm
Flatness	-	<0.02mm / 50mm travel
Straightness	-	<0.02mm / 50mm travel

The SVET head is set on an aluminium arm attached to a tri-axial micro-manipulator which is controlled via the micro-computer. This makes it possible to control the position of the probe head in three dimensions (x,y,z). The SVET head incorporates a mu-metal screen to minimise electro-magnetic flux leakage from the loud speaker. Any drive flux leakage may generate potential gradients in solution through ac eddy current induction. These potential gradients will alternate at the same frequency as the SVET signal and may therefore be detected by the lock-in amplifier.

The Mu-metal box enclosing the loud speaker acts as both a magnetic screen and Faraday cage (see figure 2.4). To further minimise interference from the loudspeaker, the distance between the speaker and signal detection area was maximised. The probe tip is mounted on the end of a hollow glass push rod (length ~ 80mm) which is directly connected to the loud speaker. The glass push rod passes through a small hole in a cylinder of solid aluminium which provides electrostatic screening as well as stabilising the glass rod to eliminate any x,y motion in the tip. The tip is then vibrated perpendicular to the plane of scan, at the experimental frequency (140Hz), amplitude of vibration ~ 40μm, by the loud speaker via the glass rod. The probe tip itself consists of a 125μm platinum wire set in a glass sheath, total tip diameter ~ 200μm. The end is ground flat so the tip acts as a 125μm diameter planar electrode (see figure 2.5a and 2.5b).

2.1.3: SVET Calibration.

Introduction:

If the SVET tip is vibrating with a peak to peak amplitude Δz, and detects a peak to peak ac potential amplitude ΔE_z then $\Delta E_z/\Delta z \rightarrow \partial E_z/\partial z$ as $\Delta z \rightarrow 0$. Thus for small values of Δz equation 2.1 may be written as

$$\frac{\Delta E_z}{\Delta z} = \frac{jz}{\kappa} \qquad [2.9]$$

Where Δz is the mechanical amplitude of probe vibration.

Rearranging equation 2.9 gives

$$jz = \Delta E \cdot G \qquad [2.10]$$

Where G is a calibration factor given by $\kappa/\Delta z$.

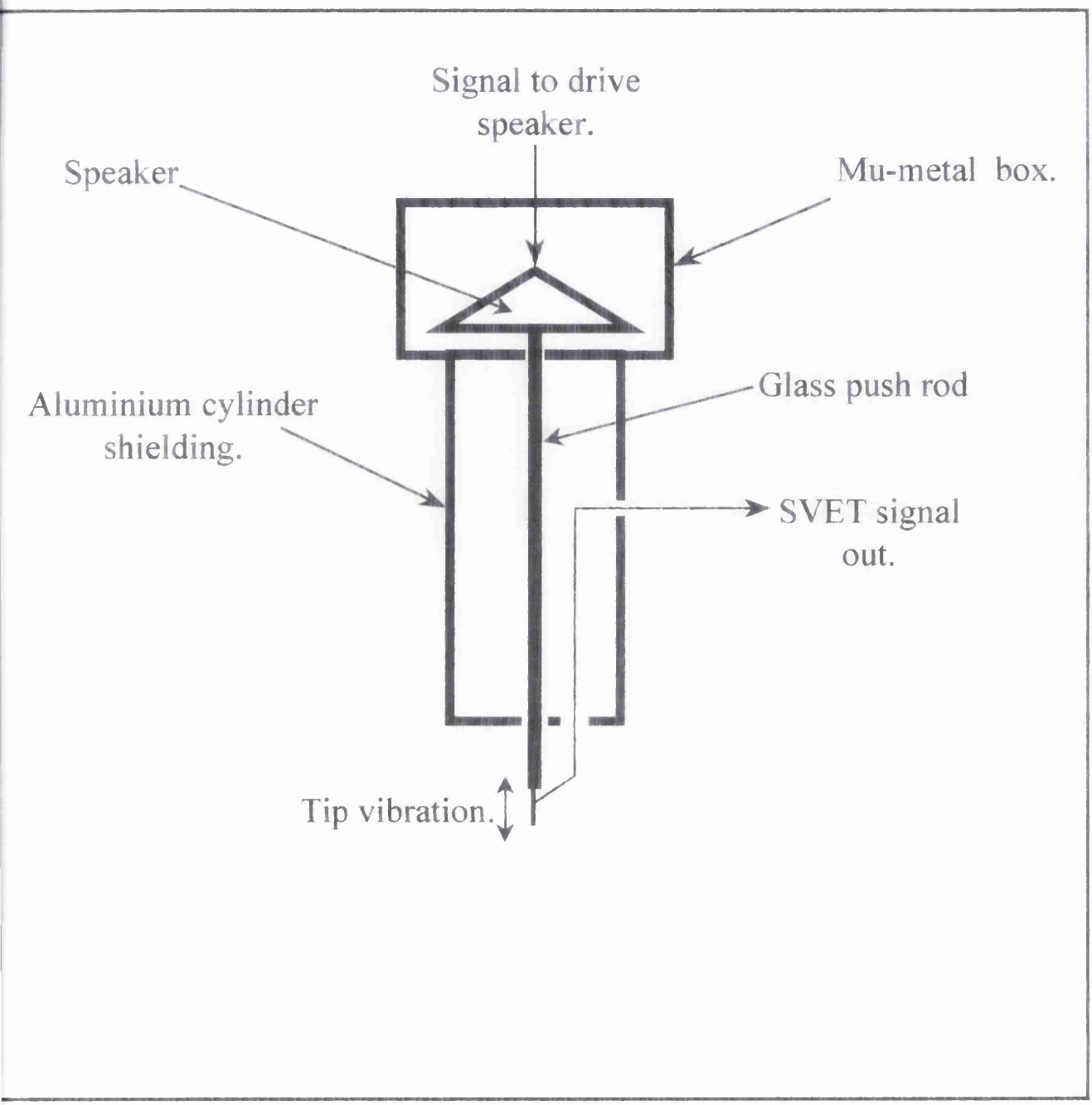

Figure 2.4: Schematic diagram of SVET head design.

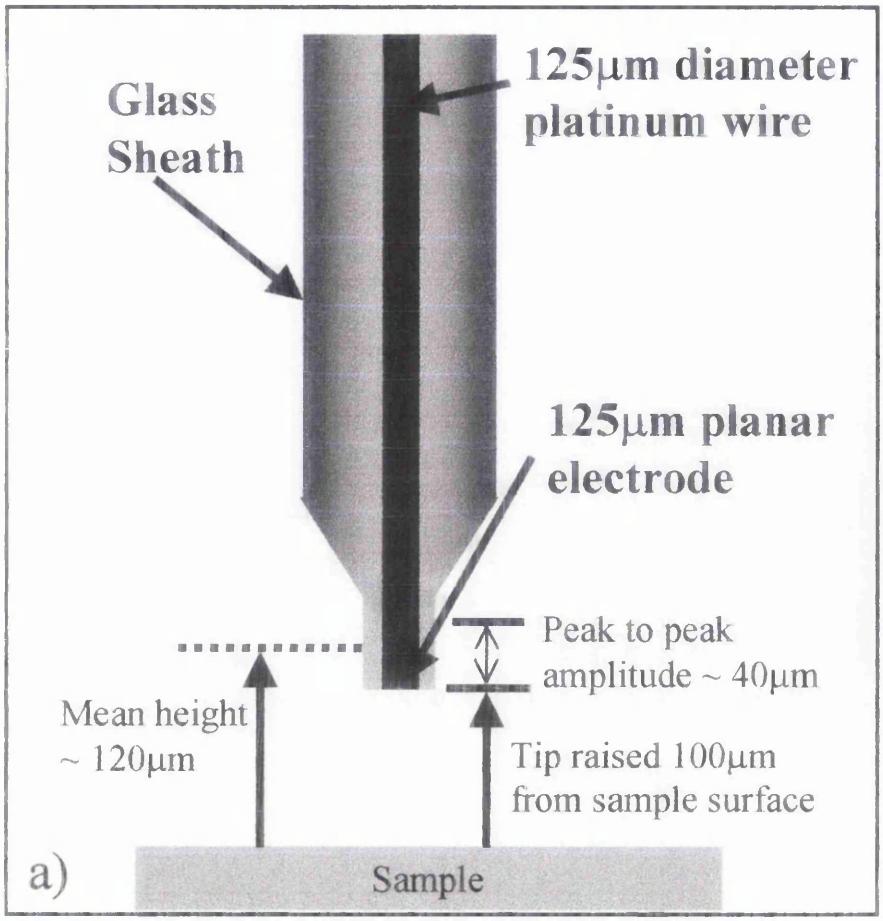

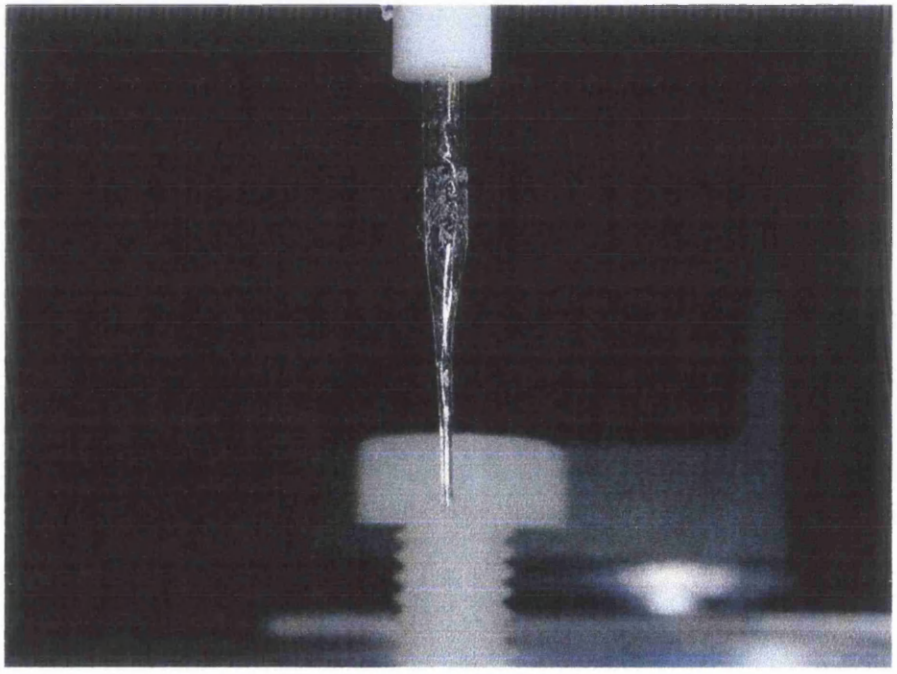

b)

Figure 2.5: a) Schematic diagram of SVET tip, b) optical picture of tip.

A theoretical value of the calibration factor G_{ther} can be obtained by measuring Δz in air and taking a value for κ from literature. The mechanical peak to peak amplitude of vibration Δz was measured experimentally using a travelling microscope and stroboscopic illumination. The vibrator drive frequency was 140Hz and the drive voltage amplitude 0.7 V rms, as used throughout in SVET corrosion experiments. The stroboscope was set to flash at 140 ± 1 Hz, freezing the tip motion and allowing the limits of tip vibration to be located using the travelling microscope. The value of Δz thus obtained was 35μm ± 5μm using κ = conductivity of 3.5%w/w NaCl[5] = 5.08 Ω^{-1} m^{-1}. The theoretical value of G (G_{ther}) could then be calculated as, G_{ther} = 5.08 / $35x10^{-6}$ = $1.45x10^{5} \pm 0.2x10^{5}$ $Am^{-2}V^{-1}$.

However, in practice Δz is not easily determined in solution, and the influence of solution viscosity on Δz is not known. Furthermore, the efficiency with which ΔE is detected by the SVET probe / lock-in amplifier combination is also not known. For these reasons the relationship between ΔE_z and jz is best determined empirically by calibration. Three separate approaches were made to calibrating the SVET signal in terms of current density, and the results compared. All calibrations involved passing a known current through a geometrically well defined calibration cell containing 3.5% w/w aqueous NaCl electrolyte.

Calibration under uniform current density conditions:

This approach has the advantage of not requiring precise tip location relative to the calibration source. However, it does not take into account the screening (electrolyte displacement) effects and non-linearity effects which may occur when the SVET probe is vibrated close to a point source-like feature such as a corrosion pit. A calibration cell was constructed which consists of a nylon cylinder (diameter ~ 60mm)

hollowed out to a depth of ~ 80mm, and has a glass tube (internal diameter ~ 6mm) protruding from one side (figure 2.6) with a 90° bend. The length of the glass tube was sufficient so that the current density throughout the cross sectional area was uniform. The anode and cathode were connected to a galvanostat, and the set-up was such that all current must pass through the glass tube, as the anode was positioned in the nylon cylinder and the cathode in the bulk electrolyte. Experiments were first carried out to see how current density varies with position in the glass tube.

Experiment A: This experiment was carried out to see how current varies with position across the diameter of the tube at varying heights respective to the glass tube edge. The left hand edge of the tube was taken to be $x = 0$ mm, and the probe tip was moved in 0.2mm steps toward the right hand edge. All measurements were taken for i = 100μA, and readings of the potential were recorded from the lock-in amplifier. Measurements were taken for z (height) = +0.5, 0, -0.5, -1 and –1.5mm, taking $z = 0$ when the end of the SVET tip is level with the top edge of the glass tube (see figure 2.7). A graph of results can be seen in figure 2.8.

Experiment B: This experiment was carried out to see the depth at which the current becomes uniform within the tube. The probe tip was positioned directly over the centre of the glass tube, 1mm above the edge. The galvanostat was set to 100μA, and the tip was lowered in 0.2mm steps into the tube (figure 2.9). A reading of the potential was taken for each height and a graph of the results can be seen in figure 2.10.

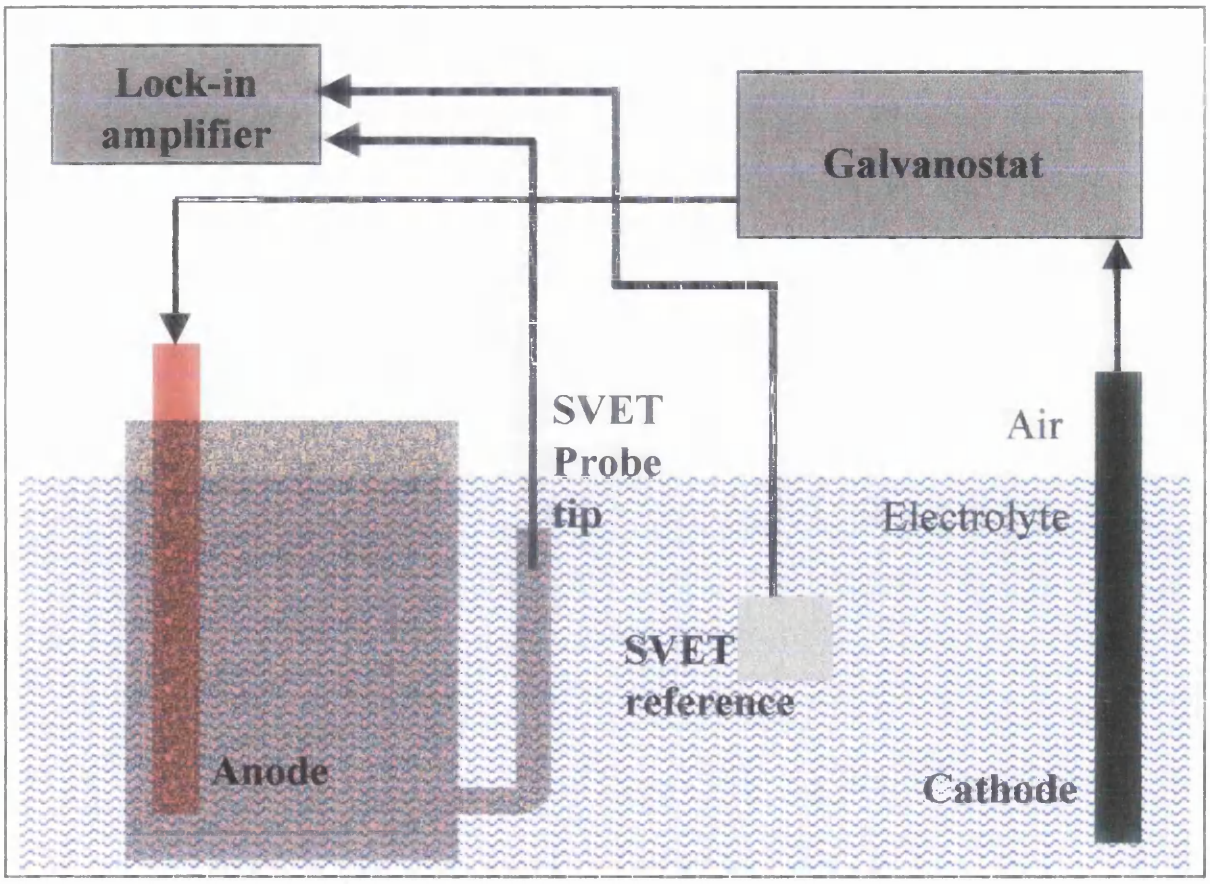

Figure 2.6: Schematic diagram of apparatus for calibration using current density cell.

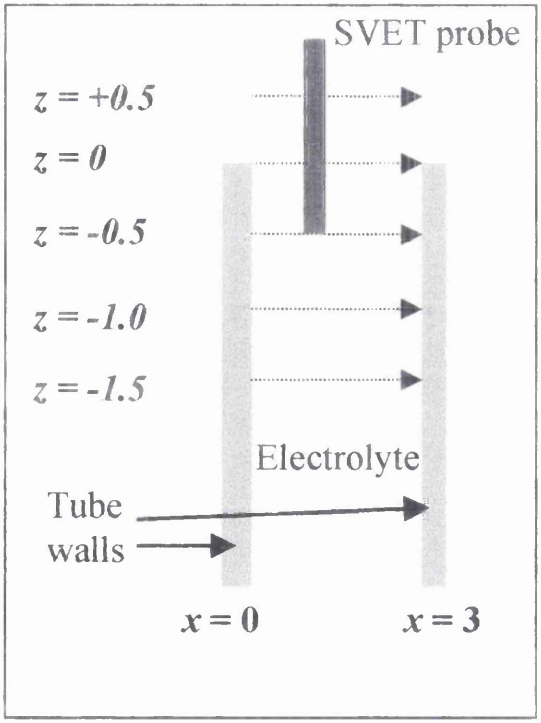

Figure 2.7: Schematic diagram of experimental procedure to see how lock-in potential varies with horizontal tip position within calibration tube.

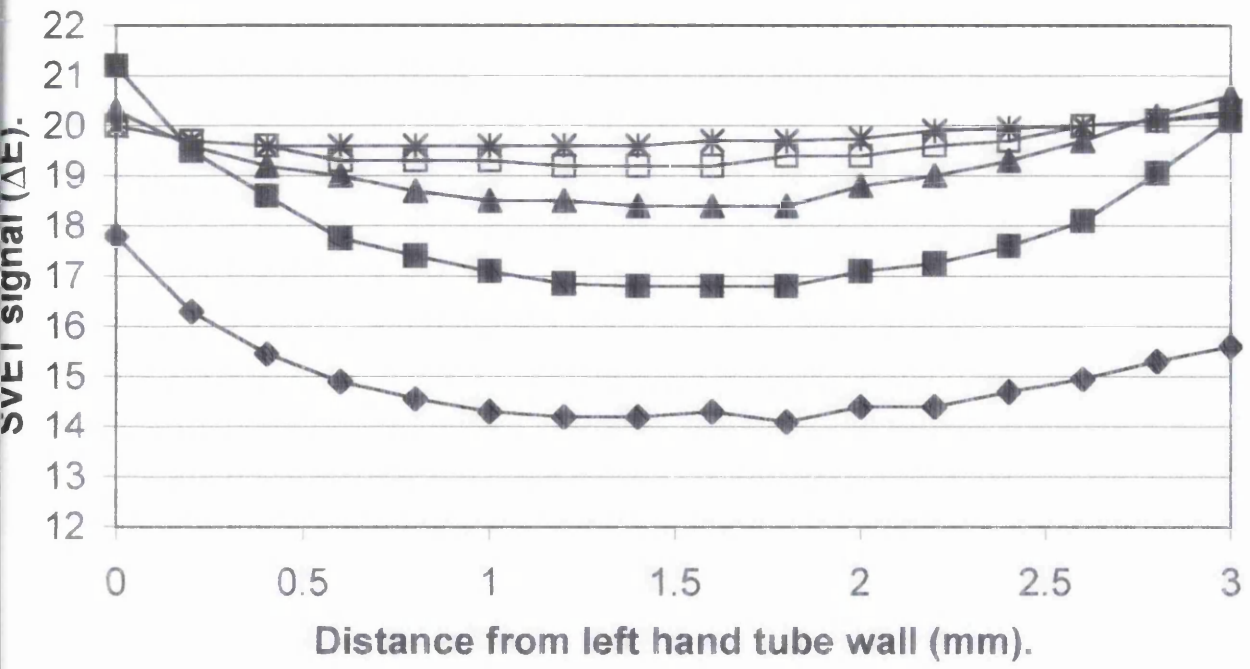

Figure 2.8: Plot showing how SVET signal (ΔE) varies across glass tube, distance expressed relative to left hand tube wall. Probe position at various distances from tube opening, ◆ +0.5mm, ■ 0mm, ▲ -0.5mm, □ -1mm, ✳ -1.5mm.

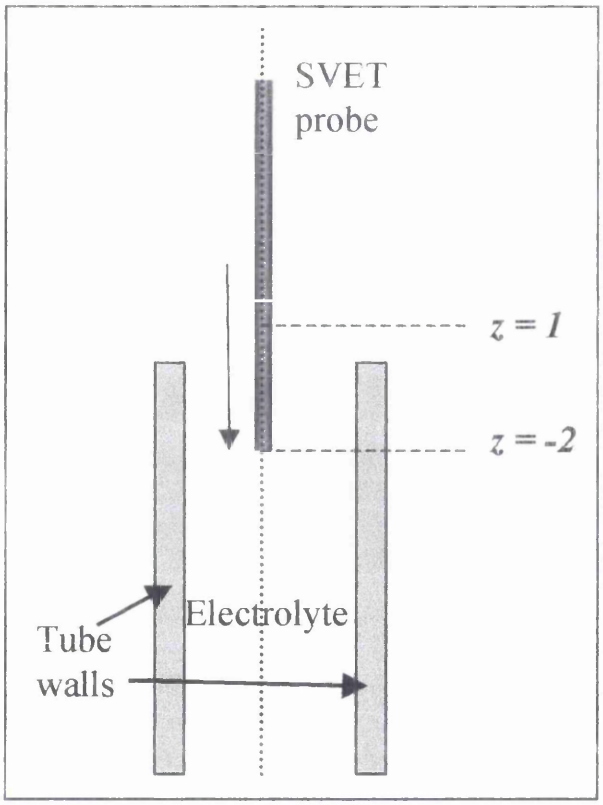

Figure 2.9: Schematic diagram of experimental procedure to see how lock-in potential varies with vertical tip position.

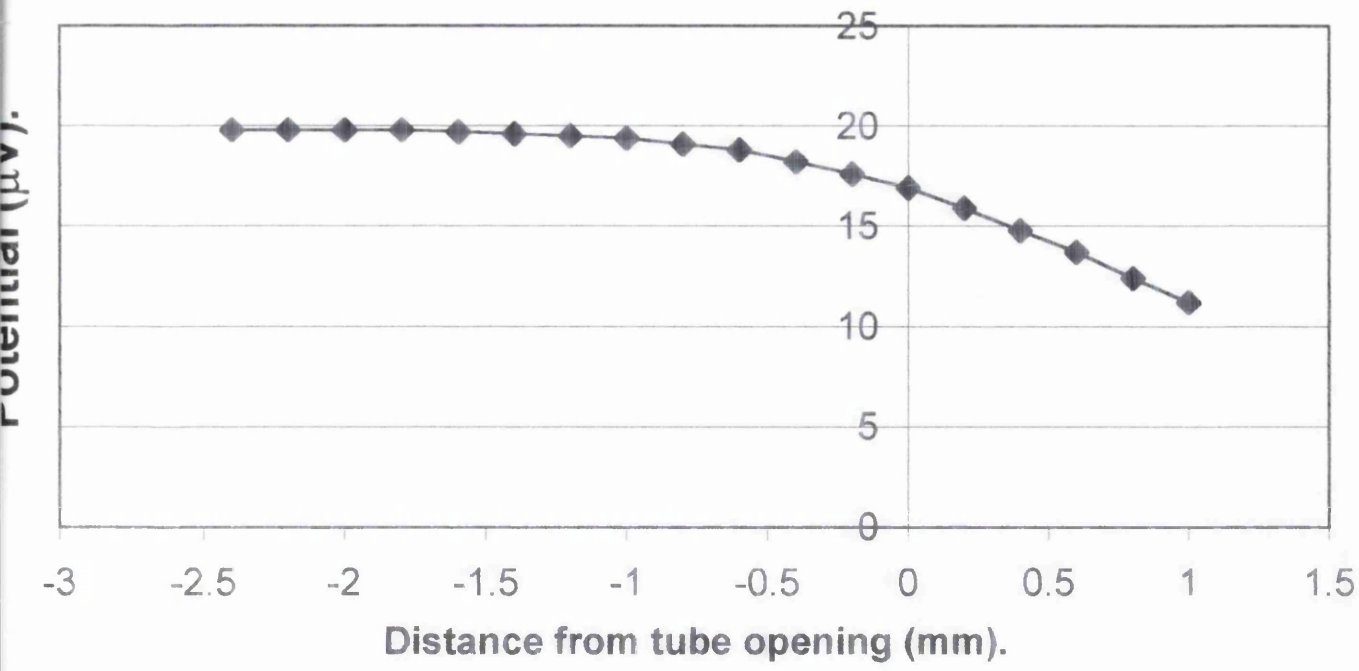

Figure 2.10: Plot showing how lock-in potential varies with distance from tube opening.

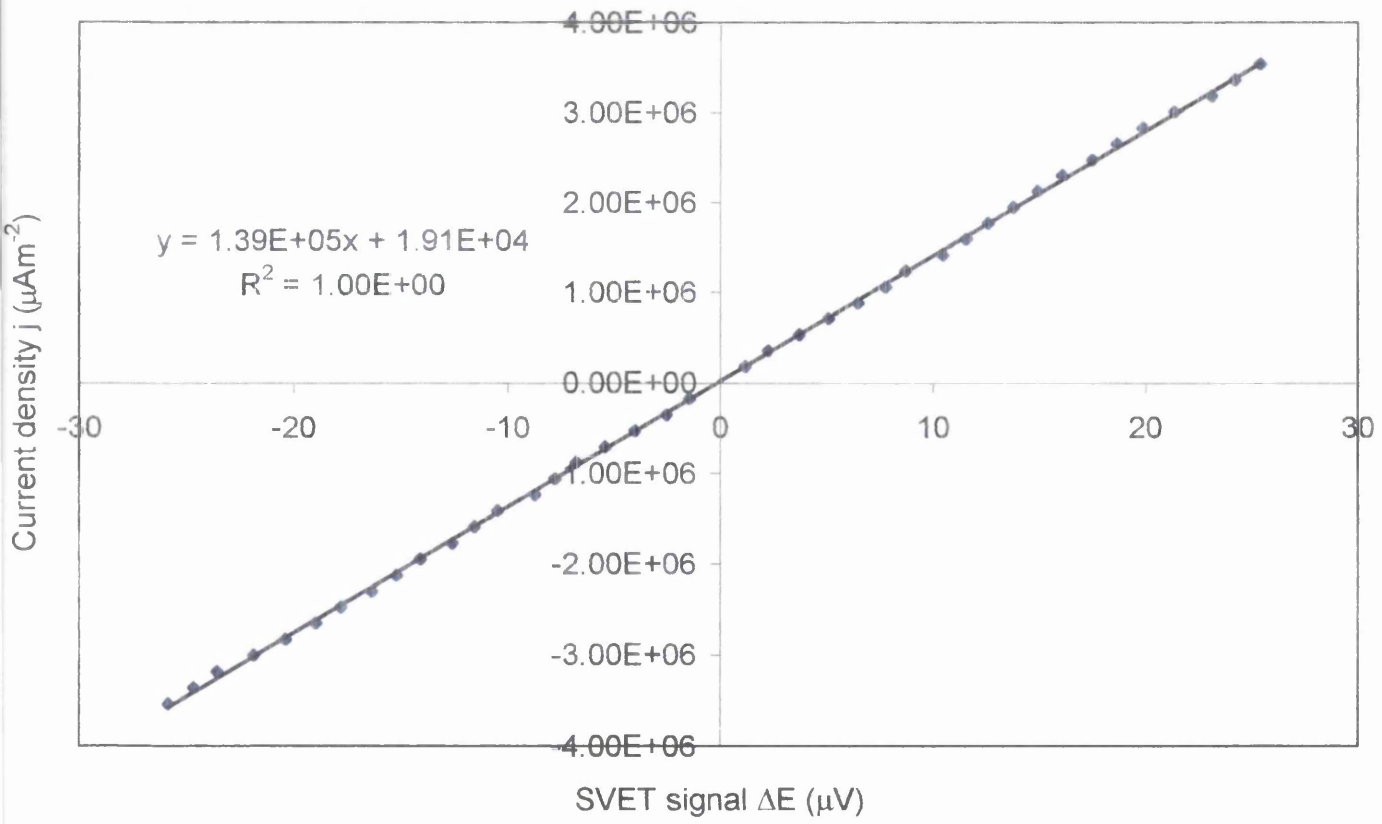

Figure 2.11: SVET calibration plot obtained using uniform current density cell, probe tip positioned in centre of tube, and 3 mm below tube opening.

Calibration: To calibrate using this method the SVET probe was positioned in the centre of the glass tube, with the tip ~ 3mm below the edge of the tube, as the results to the experiments explained previously show that the current density is most constant in this position. ΔE was measured for jz varied systematically between –3.5 and +3.5 A m^{-2}. A plot of jz vs. ΔE can be seen in figure 2.11 and gave a straight line (correlation coeff. 0.9999) with slope (G_{tube}) = 1.39 ± 0.1 x 10^5 $Am^{-2}V^{-1}$. This is in reasonable agreement with the G_{ther} value of 1.45 ± 0.2 x 10^5 $Am^{-2}V^{-1}$ calculated from equation 2.10 using $\kappa = 5.08\ \Omega^{-1}cm^{-1}$ (for 3.5% aqueous NaCl at 25^{0}C)[5] and Δz = 35 ± 5 μm, as measured stroboscopically in air.

Point current source stationary in space calibration:

As stated previously, the tubular calibration cell cannot take into account the displacement of solution, and consequent influence on current flux density,[6] produced when the SVET probe tip approaches what is essentially a point current source such as an active corrosion pit. In order to determine G under conditions more relevant to the quantification of pitting corrosion, the SVET probe tip was positioned over the "point source" calibration electrode. The "point source" comprised of a 25μm Pt microdisc working electrode set in a horizontal insulating plane (Perspex block) and a remote 1cm^2 Pt counter electrode, a schematic diagram of which can be seen in figure 2.12. The SVET probe was positioned at heights (h) of 60, 100 and 120μm over the central microdisc electrode. The probe height was determined by lowering the probe tip in 10μm increments until it audibly buzzes. At this point the tip is in contact with the surface and the tip amplitude is at its most negative. The tip is then raised a known amount (100μm for all SVET experiments). Thus the height of the tip above

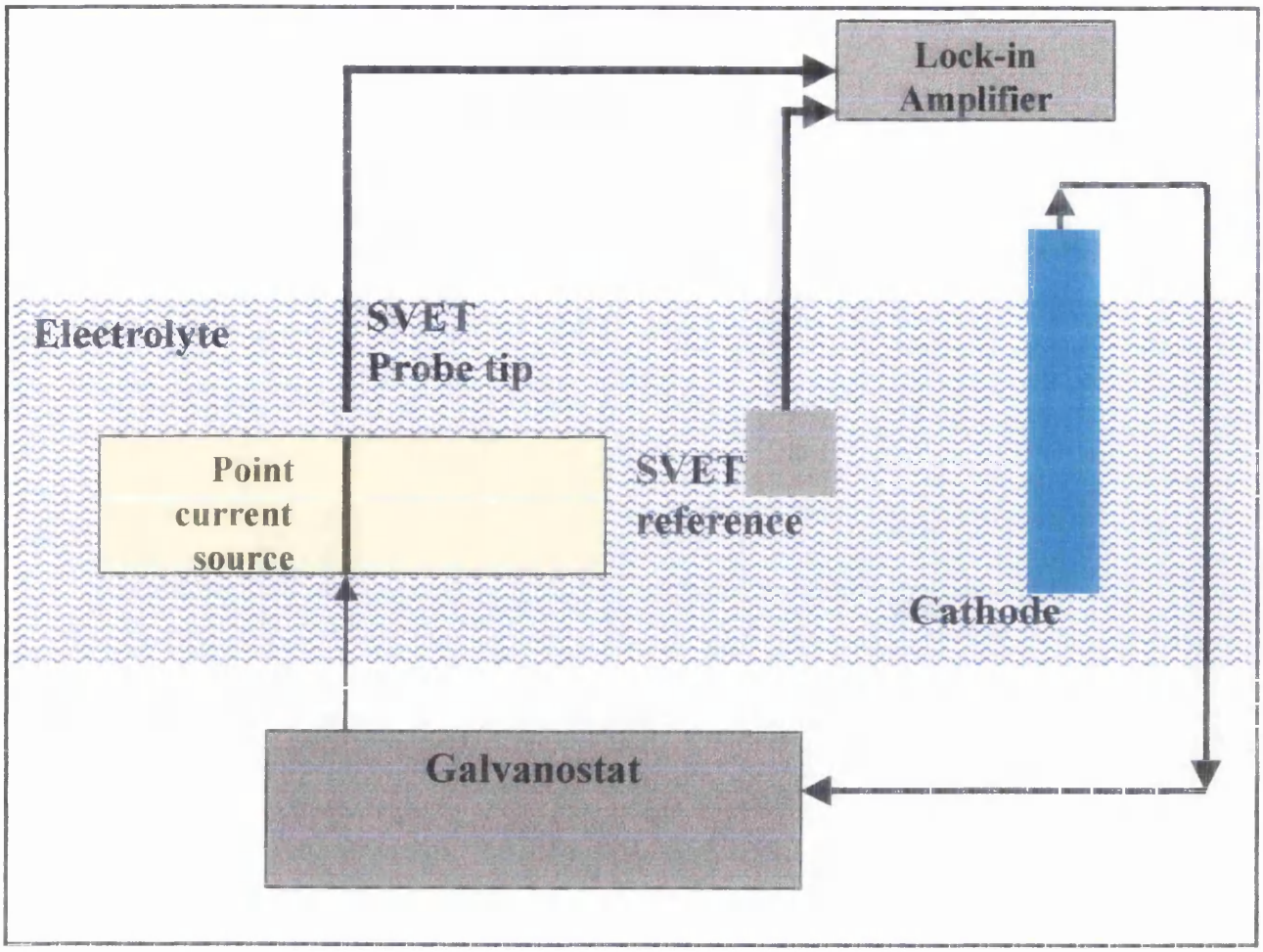

Figure 2.12: Schematic diagram of point source calibration equipment.

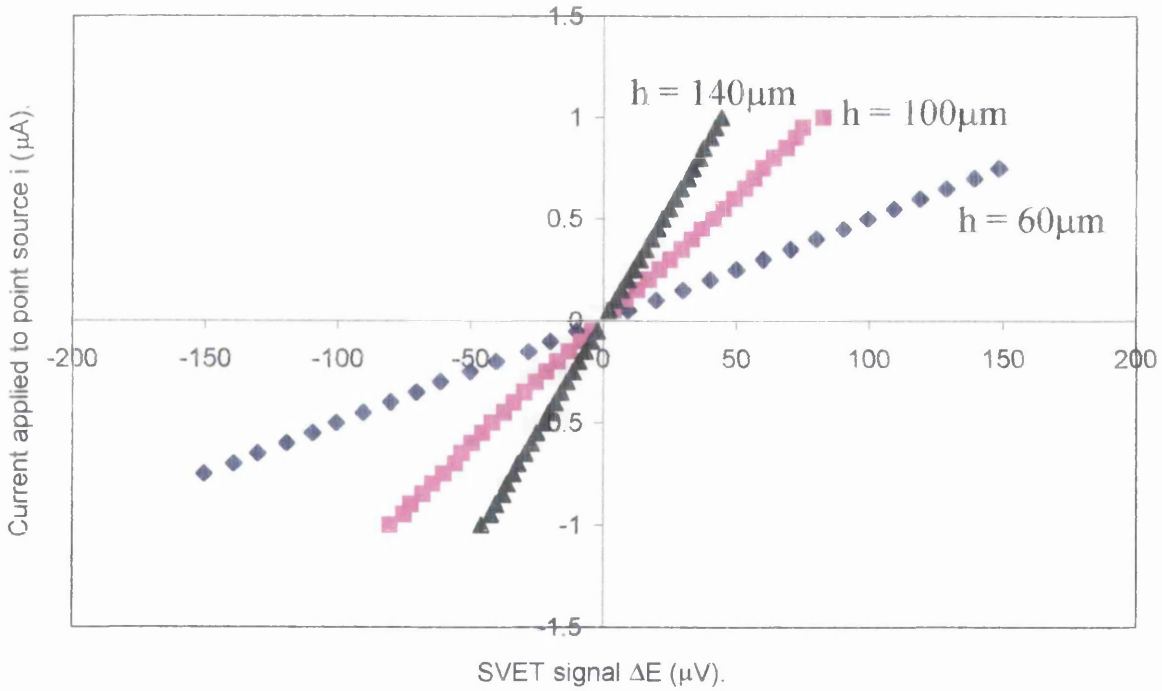

Figure 2.13: Plot showing how SVET signal varies with applied current for point current source cell stationary in space, at three different probe heights above the point source.

the surface is 100μm + the amplitude of vibration 20μm, which is a mean value ~120μm (see figure 2.5a). The value of i was varied systematically between -1μm and 1μm. A graph showing how the SVET signal varies with applied current for each probe height can be seen in figure 2.13. A plot of j ($= i/2\pi h^2$) vs. ΔE can be seen in figure 2.14 which gives a straight line (correlation coeff. 0.998) with slope (G_{point}) = $1.31 \pm 0.1 \times 10^5$ $Am^{-2}V^{-1}$. Again this is in reasonable agreement with the G_{ther} value of $1.45 \pm 0.2 \times 10^5$ $Am^{-2}V^{-1}$ calculated from equation 2.10. However, under experimental conditions the SVET probe is scanned over the surface hence the SVET was calibrated in a third and final way.

Point current source integration calibration:

In some of the experiments the total anodic current emerging from a population of corrosion pits is estimated by numerical integration of jz values over the scanned area. In order to determine G under conditions more relevant to the numerical integration procedure the SVET probe tip was scanned over the "point source" at a constant height of 100μm over a 2 x 2mm area above the central microdisc electrode, in 0.1 steps. An example of the SVET signal (ΔE) distribution obtained can be seen in figure 2.15. Given that the efficiency with which the point source current i is detected tends to unity as the area over which jz values are integrated tend to infinity, equations 2.1 and 2.6 may be combined to give

$$I = G \int_{-\infty}^{\infty} \int_{-\infty}^{\infty} \Delta E_{(x,y)} \, dx \, dy \qquad [2.11]$$

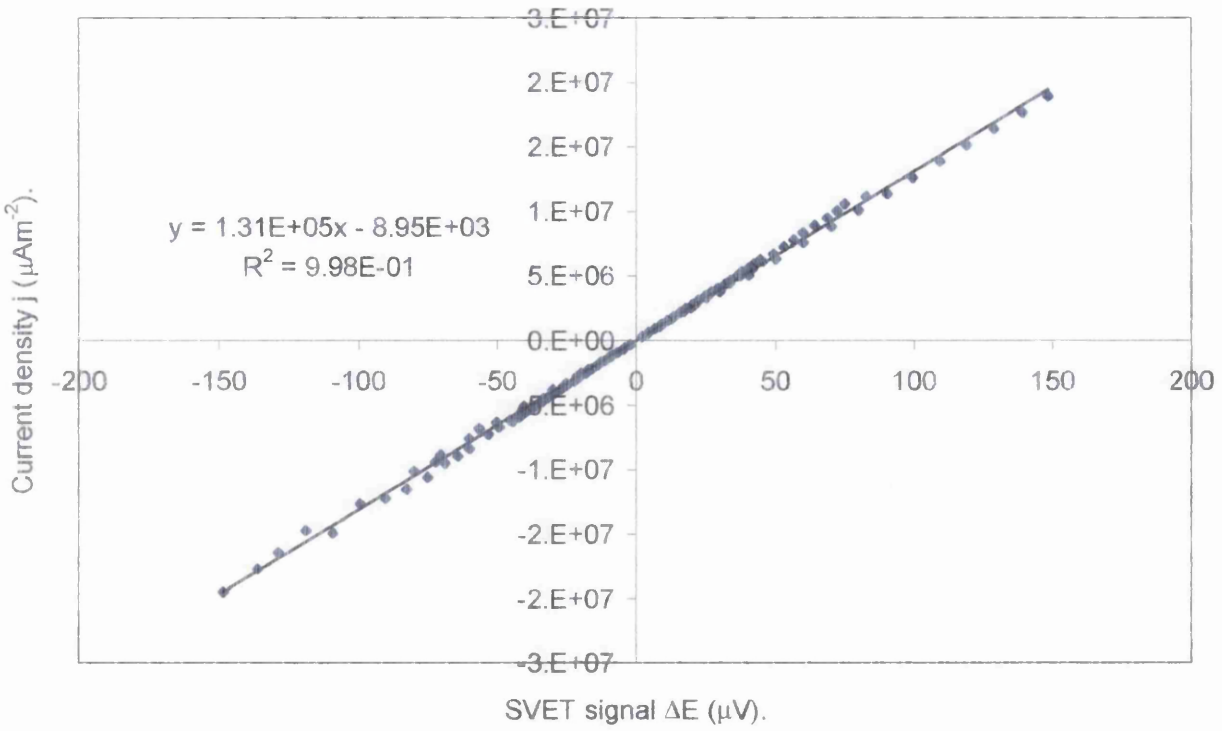

Figure 2.14: SVET calibration plot obtained using point current source cell stationary in space.

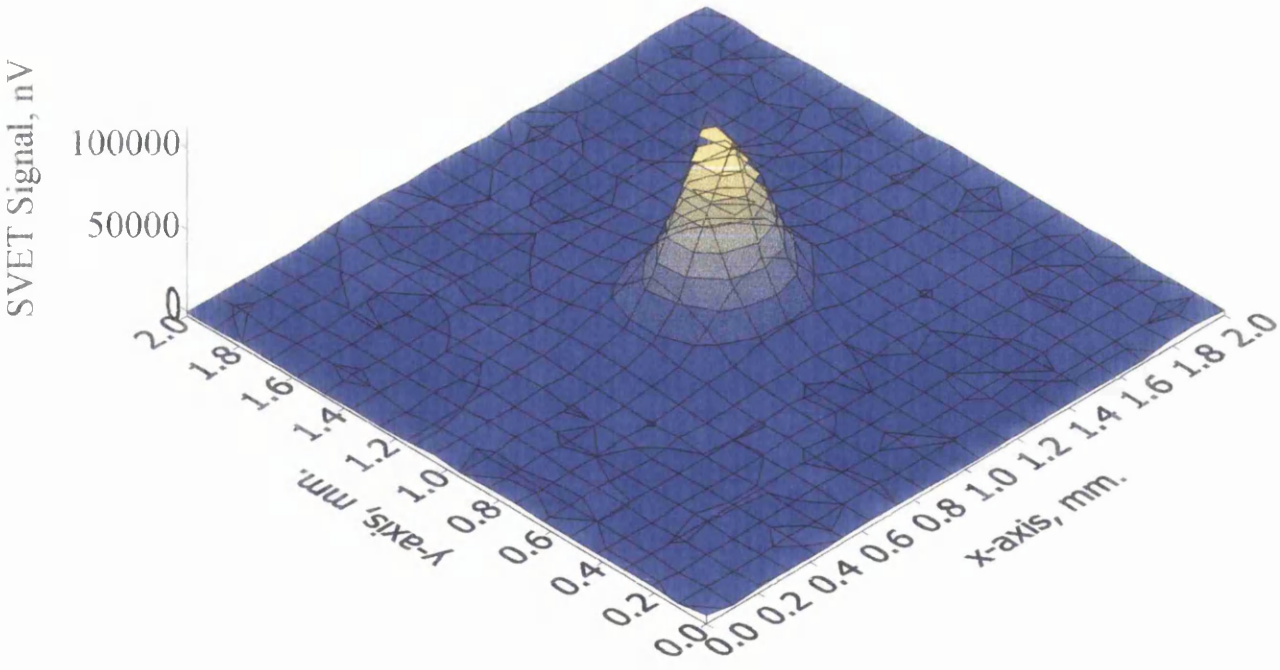

Figure 2.15: Example of a SVET surface plot used in integration calibration.

Thus, the value of G may be obtained by comparison of i with the area integral of the SVET signal. The value of i was varied systematically between 1μA and -1μA. A plot of i *vs.* the integral of $\Delta E_{(x,y)}$ over the scan area obtained numerically using the trapezium method can be seen in figure 2.16 and gave a straight line (correlation coeff. 1.00) with slope (G_{int}) = 1.30 ± 0.2 x 10^5 $Am^{-2}V^{-1}$. Given the 20:1 ratio of x and y integration intervals to SVET probe height (z) used in the integrated point source calibration experiment, figure 2.1 suggests that current detection efficiency should be 90%. However, the value of G obtained is actually 8% lower than that obtained using the tubular calibration cell or calculated using equation 2.10, *i.e.* larger values of SVET ac voltage signal (ΔEz) are being produced than are predicted for a given value of i. This finding is consistent with the SVET probe tip displacing solution proximal to the "point source" electrode when the probe and point source are physically close together. Thus, the concentration of ionic current in the remaining solution results in higher local current flux densities and higher potential gradients than those predicted by equation 2.5.

The integration calibration method (G = 1.30 ± 0.2 x 10^5 $Am^{-2}V^{-1}$) was used to convert SVET potential into current density before any quantification of the results was carried out, for all SVET experiments. This method was deemed to be the most appropriate as it was obtained using the point current source, thus taking into account the geometry of the problem, whilst being independent of the scan height. As opposed to the point source stationary in space calibration, which is largely dependant upon the height of the probe tip which could produce large errors in the results.

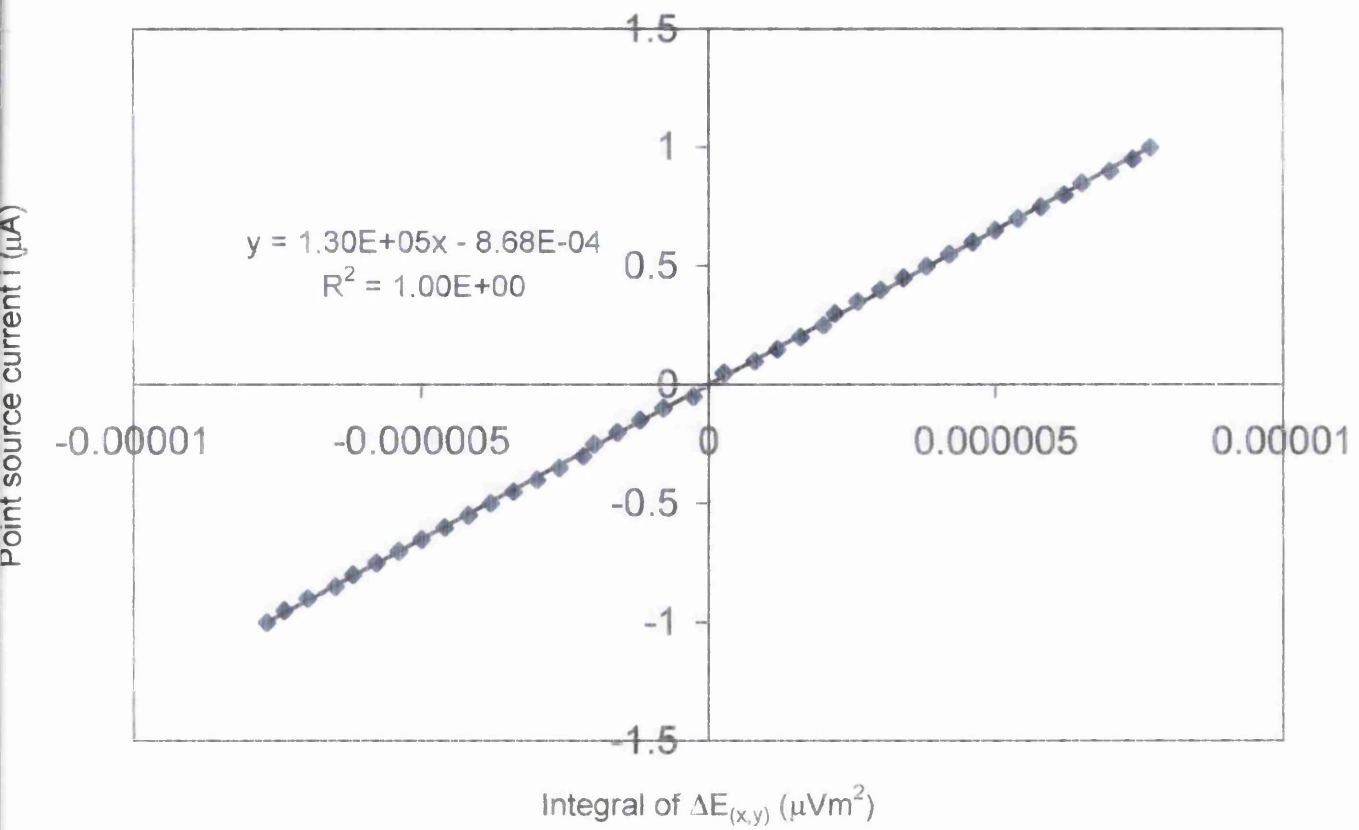

Figure 2.16: SVET calibration plot obtained using integration of point current source scan.

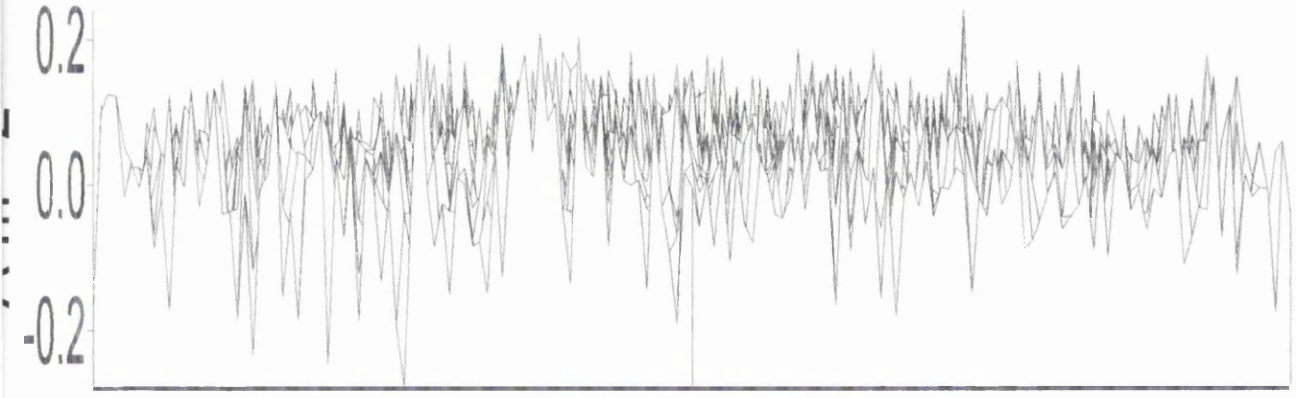

Figure 2.17: SVET surface plot of data recorded whilst SVET was scanning in 3.5% w/w NaCl over insulating plane turned for side view.

2.1.4: SVET experimental noise.

Whilst using the SVET experimentally there are two types of noise which can produce error in the results obtained, i) instrumental noise and, ii) environmental noise. Instrumental noise is determined by the noise floor of the lock-in amplifier, and the phase noise introduced by the vibration amplifier. Environmental noise is induced in the electrolyte and/or probe by the electrical nature of the environmental surroundings. This could be influenced by factors such as, a) mains noise, b) noise generated by other equipment and c) radio frequency noise in the atmosphere. The proportion of instrumental noise was deemed to be insignificant relative to environmental noise. This was determined by shorting the lock-in input, the instrumental noise observed was effectively zero compared to experimental signal levels recorded. Hence it was determined that the experimental noise observed was produced by the environment. These factors where minimised using screening techniques, as described in section 2.1.2. However, the level of background noise was determined by scanning the SVET probe over an insulating plane, and was observed to have an amplitude corresponding to a calibrated normal current density fluctuation of $\pm$ 0.2 Am^{-2} peak to peak (as can be seen in figure 2.17).

2.1.5: SVET experimental set-up.

Samples were prepared as described in each section. After preparation the samples were securely fastened to the levelling table in the tank, as can be seen in figure 2.3, and the table was initially levelled using a small spirit level, by adjusting the three levelling screws until the air bubble was in the centre of the level. The tank was then filled with the electrolyte solution up to the level of the base of the sample, and left

for 20 minutes. This was to allow any expansion in the materials used to prepare the samples before the surface was accurately levelled using the buzzing technique described in section 2.1.3 for determining the height of the tip. Once the sample has been levelled to within 10μm the tip was raised 100μm from the sample surface, resulting in a mean scan height of ~ 120μm. The step size used in height measurement gives an error of ± 10μm in the subsequent scan height. Probe amplitude ~ 20μm measured as described in section 2.1.3. SVET scan parameters were set via the micro computer, and then the tank was filled with the electrolyte before the experiment was started. The electrolyte used was 3.5% w/w aqueous NaCl that was unstirred and open to the air for all experiments, any additions to the solution are stated in each section.

2.2: Scanning Kelvin Probe (SKP).

2.2.1: Apparatus.

The Scanning Kelvin Probe apparatus is shown schematically in figure 2.18a[7], and an optical picture can be seen in figure 2.18b. The vibrating reference probe assembly was mounted in a fixed position above the moving test sample. The reference probe itself consisted of a 125μm diameter gold wire, which was vibrated along the vertical axis using a moving coil electromechanical actuator (8Ω 1W loudspeaker). Reference probe vibration amplitudes were checked using stroboscopic observation in conjunction with a travelling microscope, as described for the SVET (section 2.1.3). The experimental set-up was such that the tip of the vibrating reference probe was held at earth potential and positioned inside a stainless steel environment chamber, which was also at earth potential. The electromechanical actuator and vibrator drive

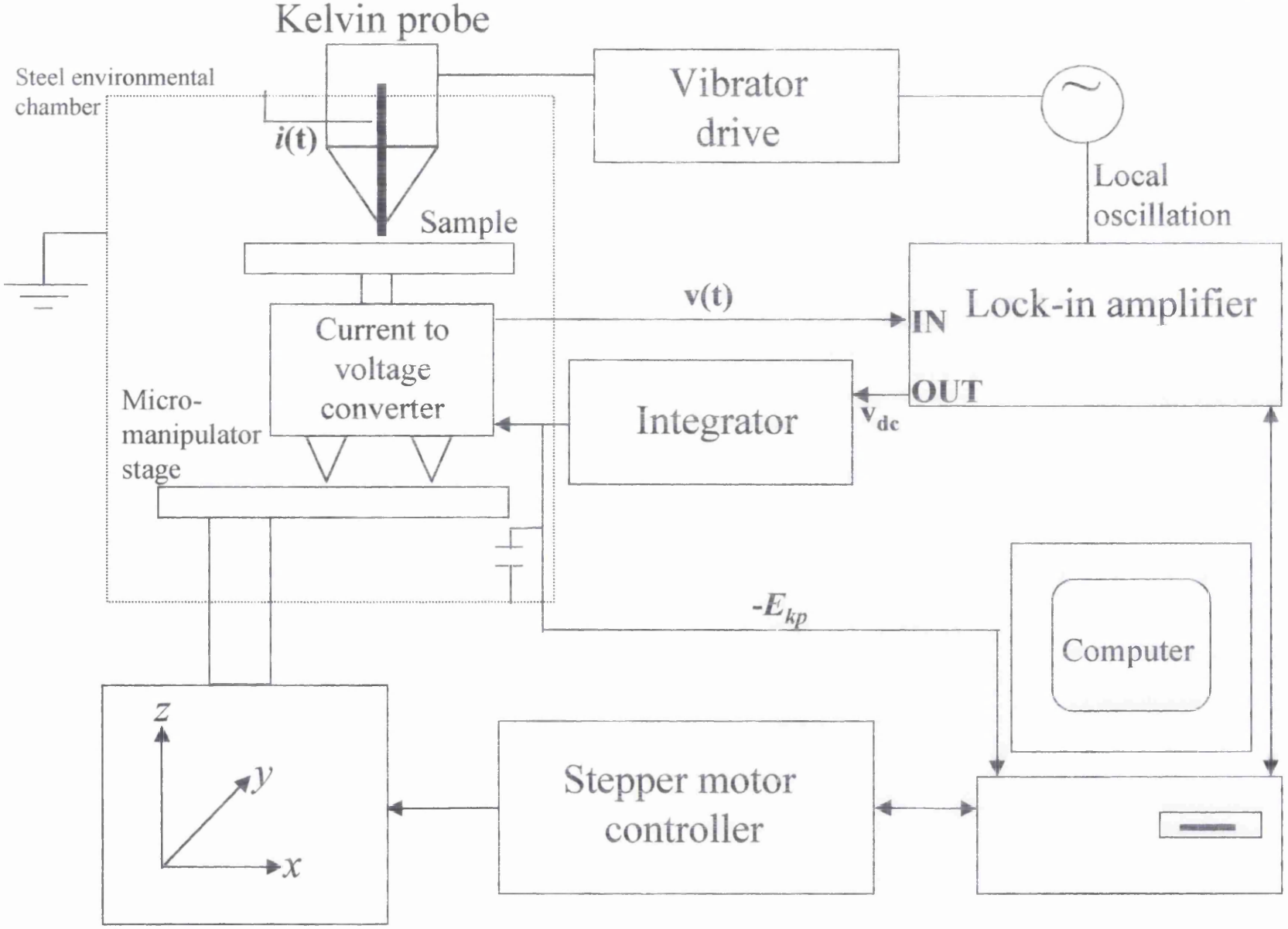

Figure 2.18a: Schematic diagram of major components of the Scanning Kelvin Probe (SKP) apparatus.

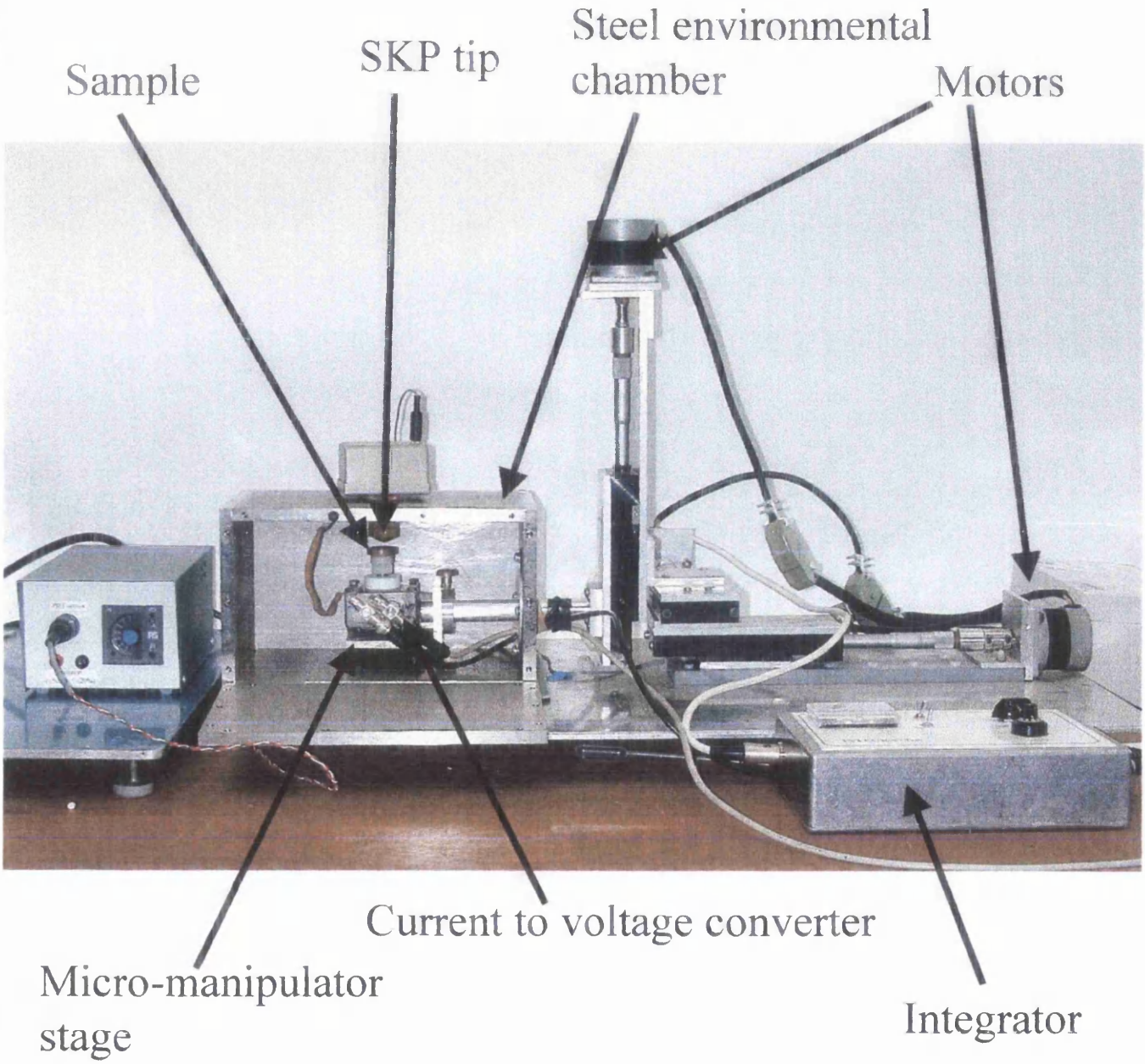

Figure 2.18b: Optical picture of Scanning Kelvin Probe (SKP) apparatus.

electronics were positioned outside the environmental chamber in order to ensure effective electrostatic and magnetic shielding of both the reference probe and sample. Vibration was conducted to the probe tip via a 50mm long glass push rod.

The positioning and scanning of the test sample was carried out using a micro-manipulation stage, consisting of three orthogonally arranged (*x, y, z*), stepper motor driven, linear bearings (Time and Precision Ltd). To perform each measurement the ac current generated in the circuit connecting the sample and vibrating probe was amplified and converted into an ac voltage signal, using a dc biased trans-impedance amplifier circuit a diagram of which can be seen in figure 2.19. The ac voltage signal was detected using a lock-in amplifier (Perkin Elmer model 7260). The dc output of the lock-in amplifier was transmitted to a feedback system based on an integrator circuit which controlled the dc bias applied to the sample via the current to voltage converter so as to automatically null the ac current. The magnitude of the dc bias (equivalent to $-E_{kp}$ as defined in section 1.2.2) applied via the integrator, was digitised and logged. Probe scanning and data logging were all carried out under micro-computer control (IBM compatible supplied by Mertec Ltd).

2.2.2: SKP calibration.

Prior to use, the SKP was calibrated in terms of electrode potential using an established procedure[8]. This involved measuring E_{corr} (*vs.* SHE) and E_{kp} simultaneously for a series of couples (Ag/Ag^{+}, Cu/Cu^{2+}, Fe/Fe^{2+} and Zn/Zn^{2+}) using calibration electrolytes comprising of a 0.5 mol dm^{-3} solution of the relevant metal chloride (nitrate in the case of Ag) salt. The influence of a PVB coating on calibration was taken into account by placing a free standing PVB film in contact with

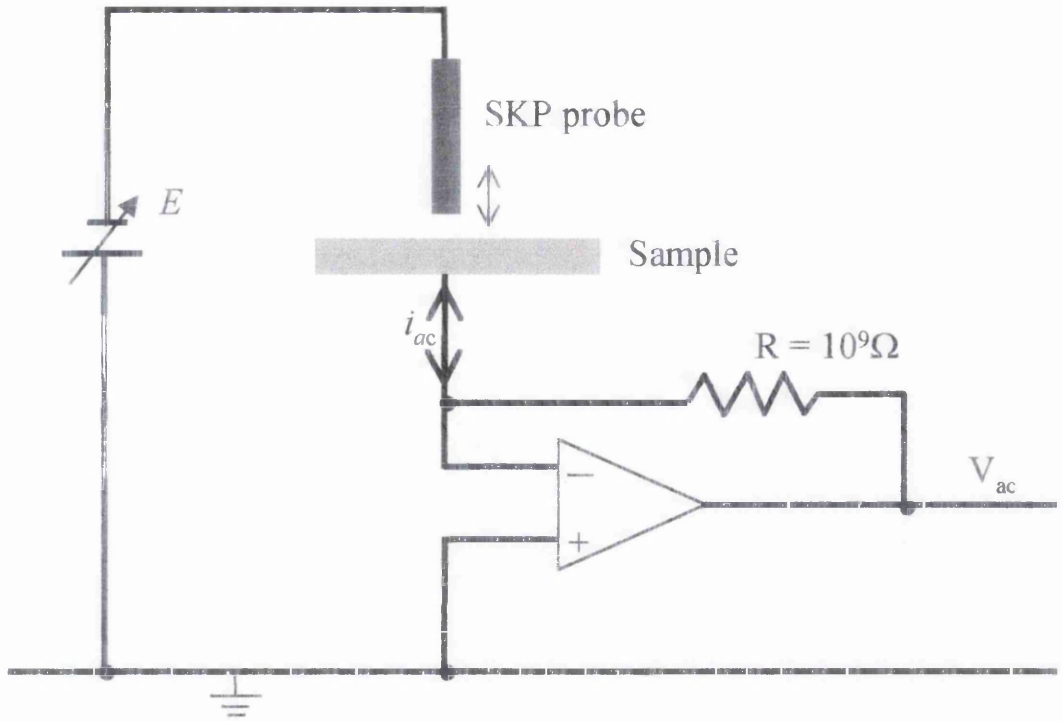

Figure 2.19: Circuit diagram of current voltage converter used in SKP equipment, as seen in figure 2.18, where E = experimentally applied bias potential, i_{ac} = current flow in external circuit due to Volta potential difference and $V_{ac} = R.i_{ac}$.

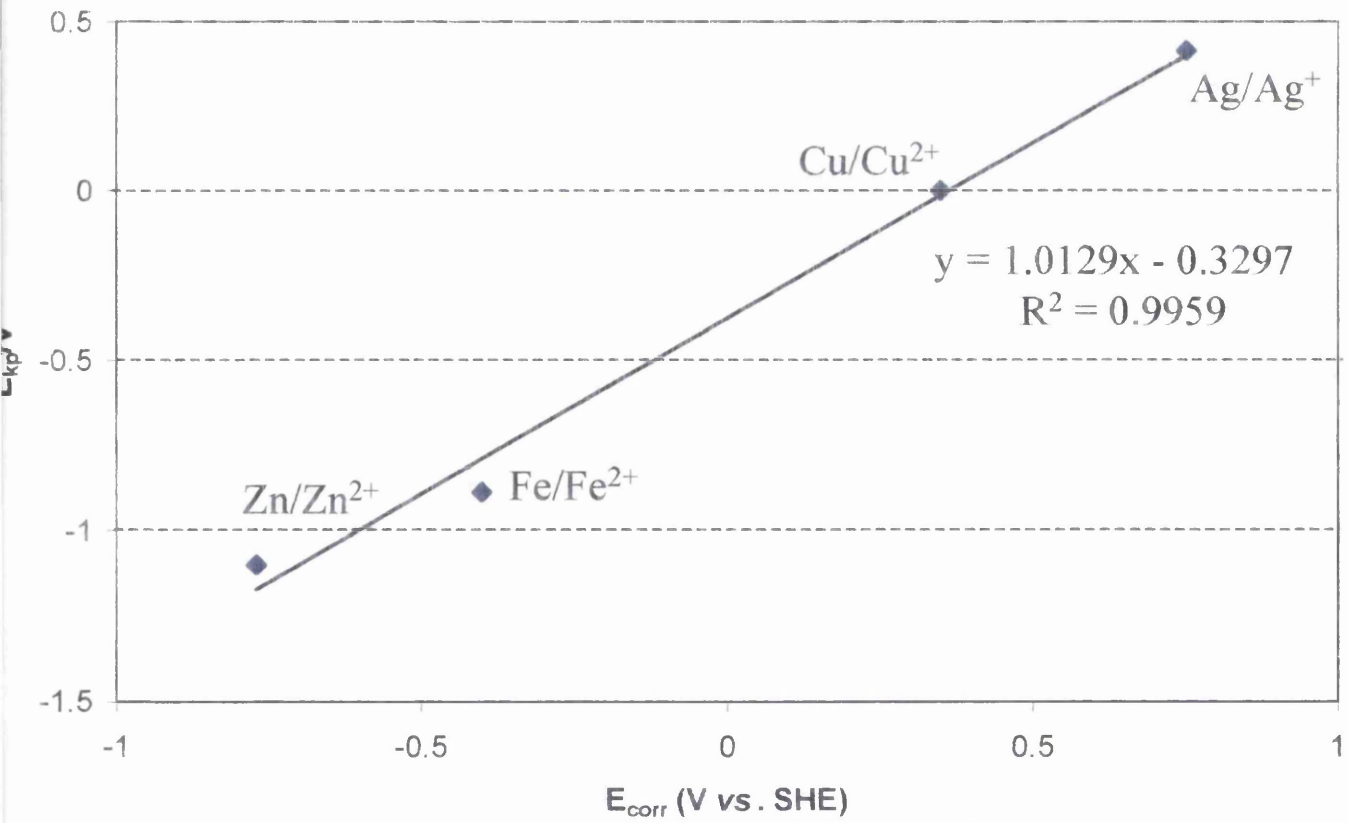

Figure 2.20: Calibration plot of E_{kp} as a function of E_{corr} *vs.* SHE for Zn/Zn^{2+}, Fe/Fe^{2+}, Cu/Cu^{2+} and Ag/Ag^+ couples covered with free standing PVB films, taken at 25^0C.

the meniscus of the calibration electrolyte, allowing the electrolyte, PVB film and SKP chamber to become equilibrated, and then measuring E_{kp} at PVB / air interface.

The calibration plot obtained can be seen in figure 2.20, which shows E_{kp} *vs.* E_{corr} for the four couples covered with a 30μm PVB film. The line shown in figure 2.20 has a slope of 1 within experimental error and a *x*-intercept value of 330mV. Calibration was carried out before each experiment, and the calibration constant was determined to be 330 ± 50mV. This constant obtained may be used in conjunction with equation 1.18 and the E_{kp} values obtained in the course of a SKP scan to calculate the instantaneous spatial distribution of E_{corr} values existing at the sample surface.

2.2.3: SKP experimental set-up.

Samples were prepared as described in section 7.2.1. They were then securely fastened to the movable platform in the thermostatically controlled (20°C) environmental chamber (as can be seen in figure 2.18b). The stainless steel environment chamber of the SKP, maintained at a constant relative humidity of 93% by equilibration of the experimental atmosphere (air) with saturated $Na_2SO_4.10H_2O$ (aq). The scanning reference probe consisted of a 125 μm diameter gold wire vibrated along its long axis and normal to the sample surface with amplitude 40μm and frequency 280Hz. Repetitive scans were carried out every 3 hours on a 1 cm^2 area of the coated sample encompassing the scribe, using a data point density of 10 points per mm and a mean probe to sample height of 100 microns.

2.3: High Resolution Microscopy.

Two types of Secondary Electron Microscopes were used to take high resolution pictures of aluminium alloy surfaces. The Philips XL30 CP (a picture of the machine can be seen in figure 2.21) with tungsten element was primarily used to take high resolution pictures of the sample surface. It was also used to record back-scatter images of the surface so as to obtain the greatest colour contrast between the aluminium matrix (soft and so dark in back-scatter mode) and the precipitate particles (harder and so light in back-scatter mode). These high contrast back-scatter images were used to find the percentage area of precipitates on the sample surface. The JEOL 35C (a picture can be seen in figure 2.22) was used to determine the types of precipitate observed on the surface, using an Oxford Link Isis EDX system attached. The basic principles used in these microscope systems can be found elsewhere[9,10,11,12].

2.4: Optical Scanning System (OSS).

The BAE System OSS combines a Mitutoyo optical microscope with a Wentworth Laboratory autostepping stage mounted on an anti-vibration table in a system originally designed to inspect silicon wafers (a picture of the equipment can be seen in figure 2.23). A PC controlled, motorised stage, moves the sample under the microscope and allows precise adjustments of sample position. BAE in-house software running on the PC is used to automate the process of capturing images using a digital camera (JVC KY-F55B). The corroding sample is scanned under the optical microscope and individual images are collected and stored on the PC. The images have 5% overlap and are montaged using additional BAE in-house written software to produce a high resolution map of the surface. Approximately 400 images were

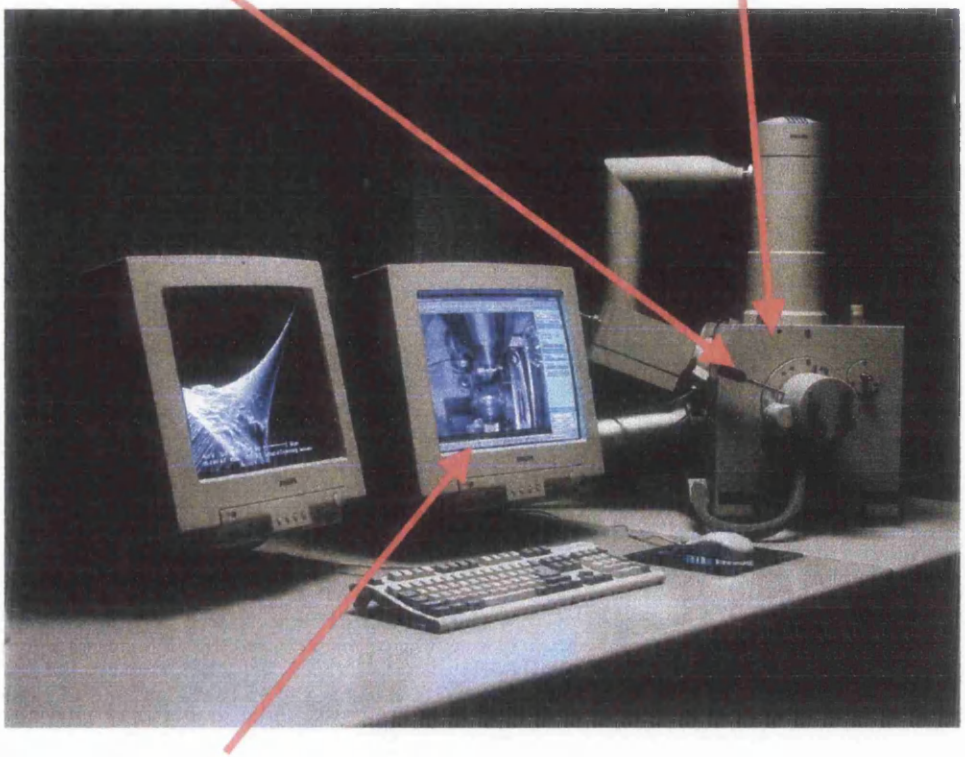

Figure 2.21: The Philips XL30 CP electron microscope used to obtain SEM and back scatter images.

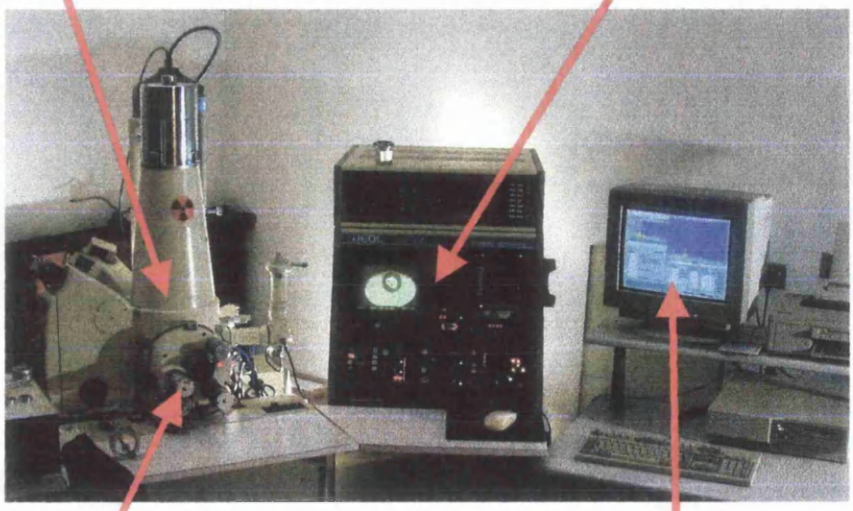

Figure 2.22: The JEOL 35C electron microscope used with the Oxford Link Isis EDX system attached.

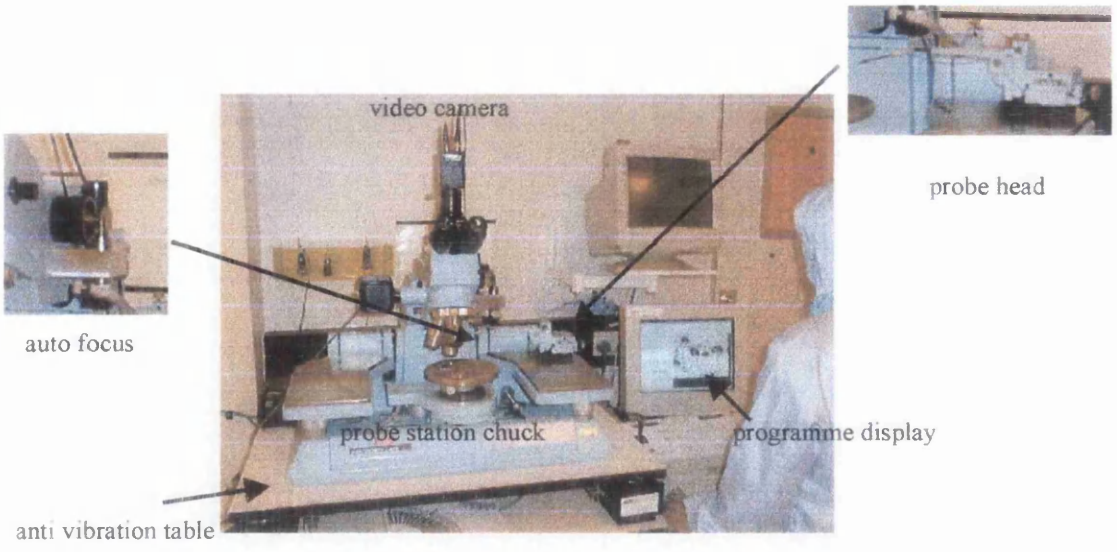

Figure 2.23: The Wentworth clean room microscope used for high resolution OSS optical mapping.

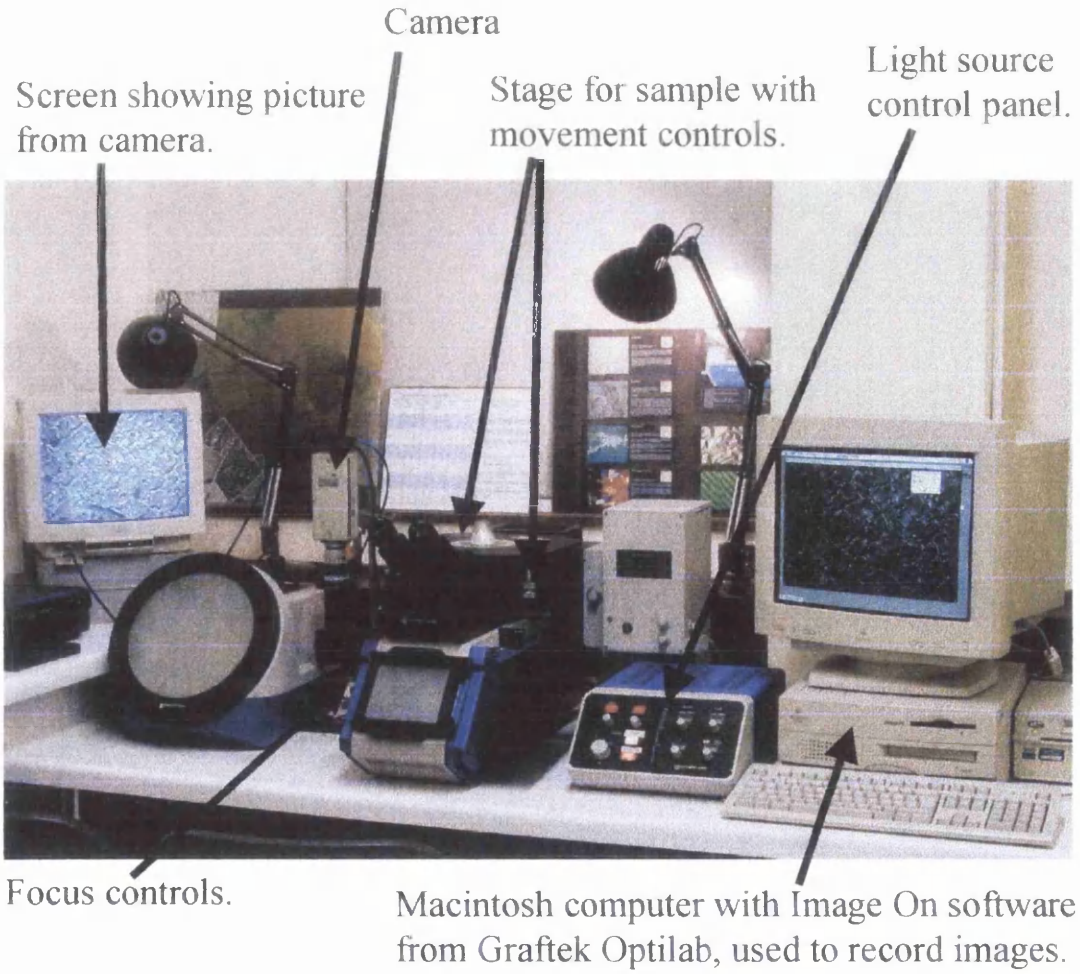

Figure 2.24: The Reichert-Jung MeF3 Optical Imaging used for high resolution optical pictures.

montaged for the SVET work which mapped an area of 5x5mm to a resolution better than 3μm.

2.5: Reichert-Jung MeF3 Optical Imaging.

To photograph the exposed sample surface after corrosion experiments a Reichert-Jung MeF3 inverted light microscope was used (a picture of the equipment can be seen in figure 2.24). Attached to the microscope was a camera with a frame grabber, which was then connected to a Macintosh computer. The software used was 'Image On' software from Graftek Optilab. The corroded surface was placed face down on a flat *x-y* movable platform above the objective lens. The platform was moved so that the surface was visible on the computer screen. The contrast was optimised using the microscopes contrast control panel and the surface was bought into focus using the manual coarse and fine focus controls. Once the required image was visible on the computer screen and was in focus, the image was captured and saved to file. To obtain pictures of the whole corroded surface the magnification was set to its lowest setting (x20), when pictures of pits were required magnification was increased accordingly.

2.6: Other Methods of Optical Imaging.

The two methods described in section 2.4 and 2.5 were used to obtain optical micrographs of small sections of the sample, as they are capable of producing high magnification images. Before other techniques of low magnification imaging became available, the inverted light microscope was used to produce montage pictures of the whole surface (see figures 3.20 and 6.3). To obtain good quality images of the whole surface two methods were used. i) Scanning the surface at high resolution using a

Hewlett Packard ScanJet 5200C scanner connected to an IBM compatible computer.

ii) Image photography using a Nikon Coolpix 950 digital camera, which was used to obtain angled pictures which emphasise surface colour and texture.

2.7: Materials.

Aluminium alloy 2024, (composition shown in table 2.2) was obtained from BAE Systems, Sowerby research centre in two forms. AA 2024-T3 samples in the form of thin plates with a thickness of 2mm and varying lengths and breaths, and AA 2024-T351 samples in the form of 26mm cubes. The AA2024-T351 cube samples were cut from a hot-rolled billet of AA2024-T351 which was an intermediate stage in manufacture of the lower skin of an Airbus wing. The cubes were cut such as the 'top', 'side' and 'end' of the cube were defined in relation to the rolling direction of the original billet as shown in figure 4.1. The alloy T number indicates how the alloy was heat treated and worked. T3 specifies that the alloy has been solution heat treated, cold worked and naturally aged to a substantially stable condition[13,14], as discussed in section 1.1.1. Whereas T351 indicates that as well as being solution heat treated, cold worked and naturally aged to a substantially stable condition as for T3, the alloy has also been stretched[13,14].

Element.	**% Alloy.**
Silicon	0.5
Iron	0.5
Copper	3.8 – 4.9
Manganese	0.3 – 0.9
Magnesium	1.2 – 1.8
Chromium	0.1
Zinc	0.25

Table 2.2: Table showing composition of experimental alloy 2024-T3[13,14].

Platinum and gold wire used in the SVET and SKP tips respectively were obtained from Goodfellow. Platinum wire stated as 99.9% pure, gold wire stated as 99.99% pure.

2.8: Computer software.

2.8.1: Presentation of data.

On completion of each SVET and SKP scan, a matrix of data points was stored on the micro-computer. This data was manipulated in various ways using a cartography package called Surfer 6 supplied by Golden Software. This package was used to present the data in one of three ways using the surface, contour and image functions in the map menu. The surface and contour functions were mostly used to present the SVET data, whereas the image function was used for the SKP data. The surface plots were best used to show peak values in the data, whereas the contour and image plots where used to show information on current or potential distributions.

2.8.2: Finding x-y co-ordinates of detected features.

Once a contour or image of data has been plotted using Surfer 6, it is possible to digitise the map using the "Digitise" function in the map menu. This function allows the user to determine the *x* and *y* co-ordinates of any point on the map, by clicking on the map using the mouse cursor. When a point has been clicked on, a red cross is left in that position, and the *x* and *y* co-ordinates of that point are recorded in a digit.dat box on the screen. This function was used to determine the position of pits detected by the SVET, and also determine the progression of filiform filaments detected by the SKP.

2.8.3: Determining peak current density values at SVET detected pit sites.

Once the positions of the pits detected by the SVET were determined for a given experiment, it was possible to determine their peak current density value for each scan using the Surfer software. That is to say the current density immediately above the pit opening. The *x* co-ordinates of the pit sites were recorded in the first column of a dat file, the *y* co-ordinates of the pit sites were recorded in the second column, and the third column of the dat file was filed with zeros. Then using the residual function in the grid menu the difference between the level set in the third column (zero) and the actual recorded value at that point for each scan was recorded in the next available column.

2.8.4: Determining areas and sums of total anodic or cathodic activity.

The Surfer software was also used to determine the total anodic or cathodic activity for the recorded data. It has been shown that corrosion current may be quantified by integrating SVET normal current density data over the area scanned (as seen in section 2.1.1). Integrations were performed using the "Volume" function in the surface grid menu, which shows the positive volume above a known level (see threshold levels in section 3.3.3) as the cut value, which is equal to the sum of the anodic activity recorded by the SVET. For the SKP data the area of anodic and cathodic activity is the value required to make the technique quantitative. This was determined using the same function as for determining volume in Surfer 6, however it was the positive and negative planar areas required from the same data readout.

2.9: Reference:

[1] D. R. Arnott, B. R. W. Hinton and N. E. Ryan, *Mater. Performance*, **26**, 211 (1987).
[2] B. R. W. Hinton and L. Wilson, *Corros. Sci.*, **29**, 967 (1989).
[3] S. O'Driscoll, H. N. McMurray and P. C. Morgan, *"Corrosion and Corrosion Protection", Proceedings of the International Symposium*, P.V. 2001-22, (Ed. J. D. Sinclair, R. P. Frankenthal, E. Kalman and W. Plieth) The Electrochemical Society, N.J, 452 (2001).
[4] Positioning Systems, *Catalogue GBP 09 – 6*, Time and Precision Industries Ltd.
[5] CRC Handbook, 62nd Edition, (Ed. R. C. Weast) CRC Press, Florida USA, D233 (1981).
[6] H. J. Eyring in *Physical Chemistry*, Vol 9A, Academic Press 1970, p 359.
[7] G. Williams, H. N. McMurray and D. A. Worsley, *Forensic Science*, **46**, 1085 (2001).
[8] A. Leng, H. Streckel and M. Stratmann, *Corrosion Science*, **41**, 547 (1999).
[9] H. N. Southworth. *"Introduction to Modern Microscopy"*, (Ed. Prof Sir N. Mott and G. R. Noakes) Wykeham Publications Ltd, (1975).
[10] P. J. Goodhew, F. J. Humphreys and R. Beanland, *Electron Microscopy and analysis.* Taylor and Francis, (2000).
[11] J. W. S. Hearle, J. T. Sparrow and P. M. Cross. *The use of the Scanning Electron Microscope.* Pergamon Press, (1972).
[12] J. W. Edington, *Electron Diffraction in the Electron Microscope.* MacMillan, (1975).
[13] A. Perrone and O. Lotti, *"Present Status Standardisation of High – Strength Aluminium Alloys for Aerospace Applications"*, *Aluminium Alloys in the Aircraft Industry – Symposium*, Technicopy Ltd, 21 (1976).
[14] C. L. Burton, L. W. Mayer and E. H. Spuhler, *"Aircraft and Aerospace Applications", Aluminium Design and Application*, (Ed. K. R. Van Horn) American Society for Metals, **2**, 415 (1967).

Chapter 3.

Chapter 3: Quantification of surface pitting corrosion of polished AA2024-T3 using the Scanning Vibrating Electrode Technique (SVET).

3.1: Introduction.

Aluminium alloys are widely used within the aerospace industry, due to their high strength to weight ratio. The AA2024-T3 alloy investigated here, is used in the aircraft industry for many applications including fuselage and door skin, dorsal fin and trailing edge panels[1]. However, it has been found to be particularly prone to localised corrosion, such as pitting and exfoliation[1,2,3]. Pitting is a form of highly localised corrosive attack which can result in premature breakdown of structural parts[3], or even be a precursor to more complex damage such as corrosion fatigue crack initiation and growth[4]. Consequently there is a great demand for knowledge regarding initiation and propagation of pitting corrosion on aluminium alloys. In the work to be described here, the aim has been to develop the Scanning Vibrating Electrode Technique (SVET), as a fully quantitative means of investigating the localised corrosion characteristics of AA2024-T3. The number density, location, lifetime and size evolution of surface pits on AA2024-T3 was determined from SVET data. A comparison of these SVET results was also made with high resolution optical images and SEM pictures.

3.2: Experimental.

3.2.1: Materials.

AA2024-T3 samples, as described in section 2.7, were prepared following the sequence in figure 3.1. Coupons of 3 cm by 3 cm (typically) were ground using increasingly fine grades of silica paper (400, 800, 1200 and 1600) to remove any surface scratches. The surface was then polished to a mirror finish, first using 6μm diamond paste on a rotating polishing disk, and finished with 1μm diamond paste on a rotating polishing disk. The sample surface was cleaned using a non-ionic surfactant between each stage of polishing. Following polishing the sample was immersed in Methyl Ethyl Ketone (MEK) for 10 mins to remove surface grease. After polishing, two scratches (~2 cm in length) were scribed at right angles using a diamond cutter (as shown in figure 3.1d). This was done so that the point of intersection between the two scratches could be used as a reference point for high resolution optical scanning, and SVET scans. The sample area for SVET investigation (≈ 10mm x 10mm) was isolated from the rest of the sample using PTFE insulation tape obtained from 3M Ltd. The only part of the sample left un-coated was the area to be scanned as shown in figure 3.1e.

On completion of the SVET experiment the samples were removed from the electrolyte and immersed in an inhibited phosphoric acid solution comprising of 3.5% v/v phosphoric acid (d 1.75) and 2.0% w/v Chromic acid at 80^0C for 10 minutes. This was used to remove any corrosion product deposited on the surface during the experiment, so that optical and SEM images could be taken.

All other materials were purchased from Aldrich in their highest purity and all solutions were prepared in distilled water.

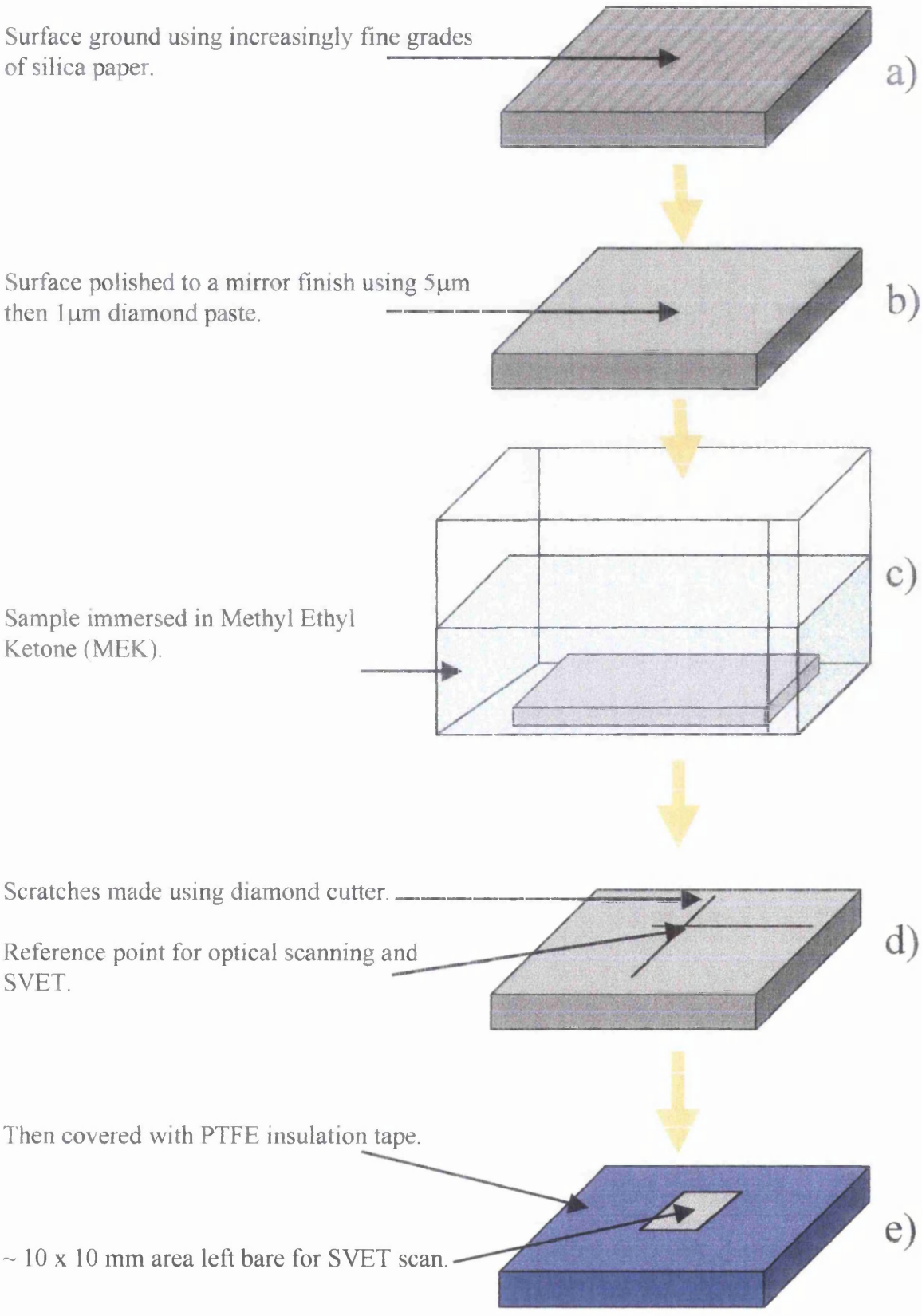

Figure 3.1: Schematic diagram showing preparation of AA2024-T3 sample surface prior to SVET corrosion experiments.

3.2.2: Methods.

SVET:

The SVET operates by measurement of the electrical potential gradient in solution, at known points above a corroding metal surface using a movable microtip electrode, as described in chapter 2. The apparatus used was as described in section 2.1.2, and set-up as described in section 2.1.4. The probe typically made 50 measurements per centimetre, generating a regular matrix of 2500 data points for the 10 x 10 mm area of the sample with a total scan time of 20 minutes. Each individual SVET data point was acquired with the probe stationary and was an average of ten successive signal measurements. The samples were scanned using SVET immediately on immersion and at hourly intervals thereafter for varying periods of time.

Optical microscopy:

On completion of the SVET experiment, optical pictures were taken of the sample surface by one of three methods. i) The first method was the in-situ (OSS) optical mapping as described in section 2.4. Whilst still immersed in the electrolyte a high resolution colour picture of part (5 x 5 mm) of the sample surface was produced. ii) The second method used the inverted light microscope with camera attached as described in section 2.5. iii) The third method used the scanner as described in section 2.6. For both of these methods the sample was rinsed in distilled water to stop corrosion, then air dried before the optical pictures were taken. These methods were also used to take pictures after the surface was cleaned by immersing the sample in the inhibited phosphoric acid solution for 10 min at 85^0C.

Electron microscopy:

After the samples were cleaned they were cut down to 0.5 x 0.5 cm coupons, so that when they were in position in the SEM (see section 2.3), the sample could be rotated to allow the angle of incidence to be changed. This was done so that the pit could be seen from as many angles as possible, and pit geometry could be better determined.

3.3: Results and Discussion.

3.3.1: Presentation of SVET data.

On completion of each scan, a matrix of 2500 data points was stored on the micro-computer. The SVET potential data was converted into normal current density in the plane of scan, $jz_{(x,y)}$ using the point source integration calibration constant described in section 2.1.3. Information from this $jz_{(x,y)}$ matrix was presented in various ways using the Surfer 6 cartography package as described in section 2.8. The two methods used in this work were surface plots, and false colour maps as described in section 2.8.1. Figure 3.2 shows the same SVET data represented in two ways, a) Surface plot, b) False colour map. The surface plot shown in figure 3.2a was built up of a series of 50 line scans along the x-axis, with successive line scans being systematically displaced along the y-axis. Each line scan comprised of 50 data points and took approximately 20 seconds to complete. Scans commenced at the point denoted as the origin of the corresponding surface plot. The z-axis corresponds to the calibrated SVET signal, so peaks on the z-axis correspond to large positive normal current density ($jz_{(x,y)}$) values. Whereas, the x and y axes correspond to the spatial position of the SVET probe whilst measuring the signal. In figure 3.2b points of the same normal current density were joined by contours spaced by a given interval, and the level is depicted by a colour gradient from (in this case) blue to yellow. Again the x and y axes correspond to the

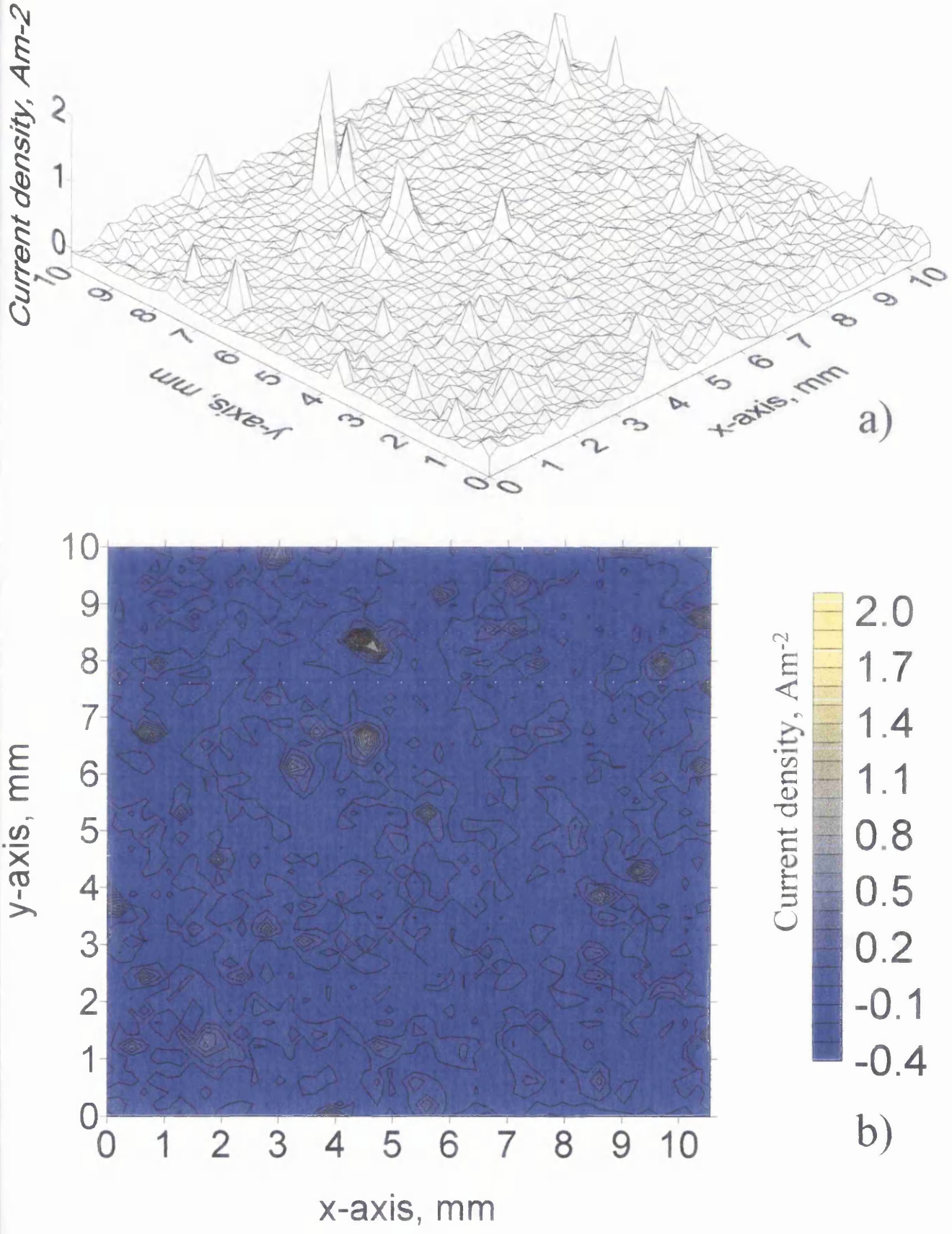

Figure 3.2: Calibrated SVET data represented in two ways a) Surface plot, b) False colour map.

spatial position of the probe. Both methods have their advantages, and each was used during the evaluation of the experimental data. Contour plots can easily be compared with photographs and images of the sample surface, whereas surface plots are of advantage in making the accurate measurement of peak current density.

Normal current density, $jz_{(x,y)}$, distributions were determined as a function of time above the surface of AA2024-T3 freely corroding in 3.5% w/w aqueous NaCl. Figure 3.3 shows current density surface plots obtained immediately following immersion and at hourly intervals thereafter for a 17 hour experiment. As can be seen in figure 3.3 pitting corrosion of the surface commences immediately after immersion in the electrolyte. Active pits are visible as discrete peaks of positive jz. Following initiation, individual pits propagate for varying periods of time before passivating. Thus it may be seen from figure 3.3 that some pits remain active over a 1 hour period or longer (lettered a-f in figure 3.3) whereas many more do not. In principle, SVET data of the sort shown in figure 3.3 should allow the time-dependence of individual pitting events to be observed over two different time-scales. The first of these is the time between successive line scans, here 30 seconds. The second is the time between area scans, here 1 hour. Using the point density shown in figure 3.3 the current from an individual pit is typically detected in 4-5 successive line-scans. This implies a pit lifetime of > 2-2.5 minutes, which is consistent with stable pitting. However, if a pit is detected in only one line scan, and not in its neighbours, then it may be concluded that the lifetime of that particular pitting event is <30 seconds, which is consistent with metastable pitting. However, at any instant the SVET probe sees only a very small fraction of the sample surface and this, together with the relatively slow rate of scan, implies that SVET will detect only a very small fraction of the total number of metastable pitting events. Typically, each SVET area scan contains only one or two

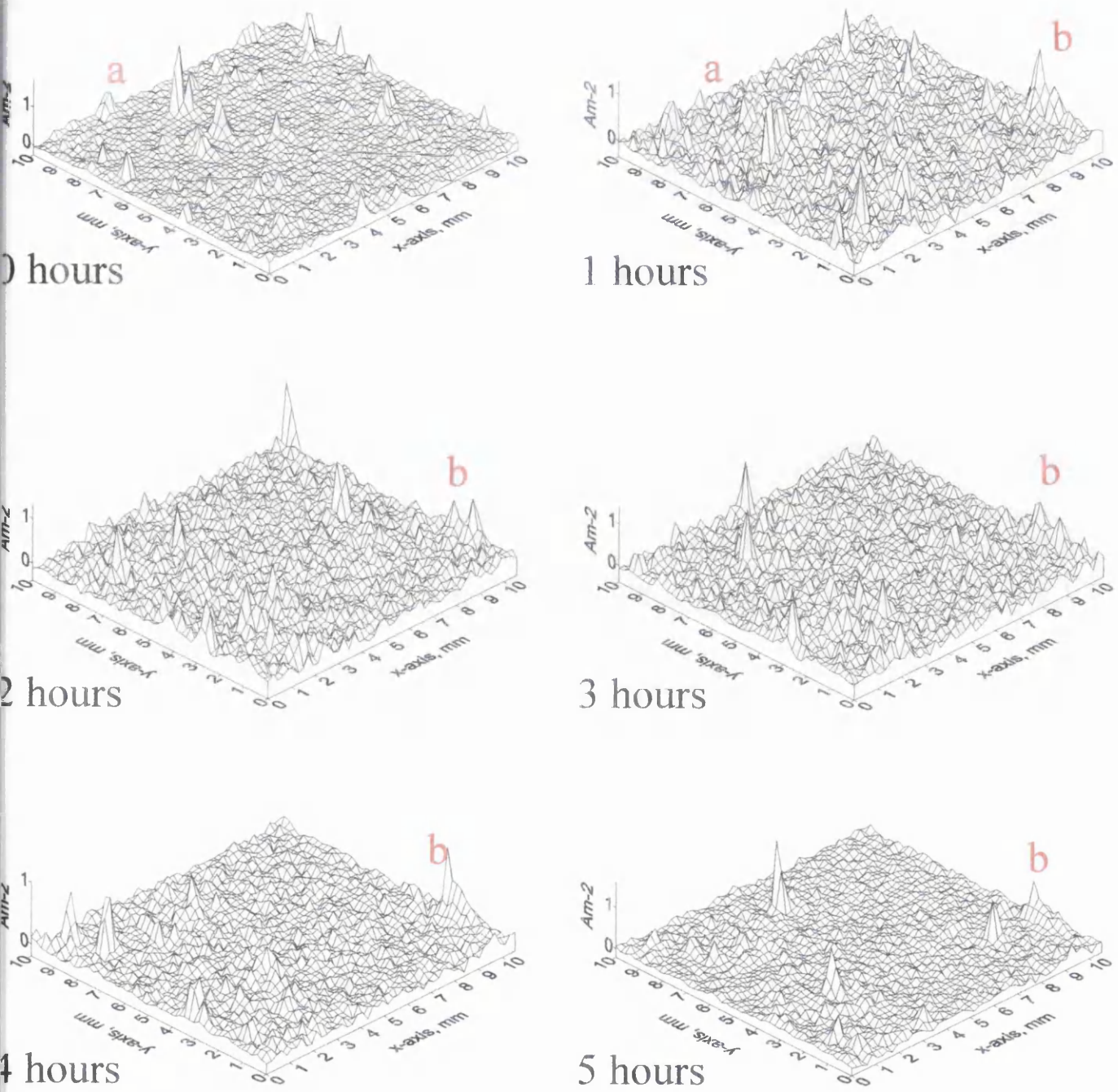

Figure 3.3: Surface plots of SVET scans for polished AA2024-T3 freely corroding in 3.5% w/w NaCl, after X hours immersion.

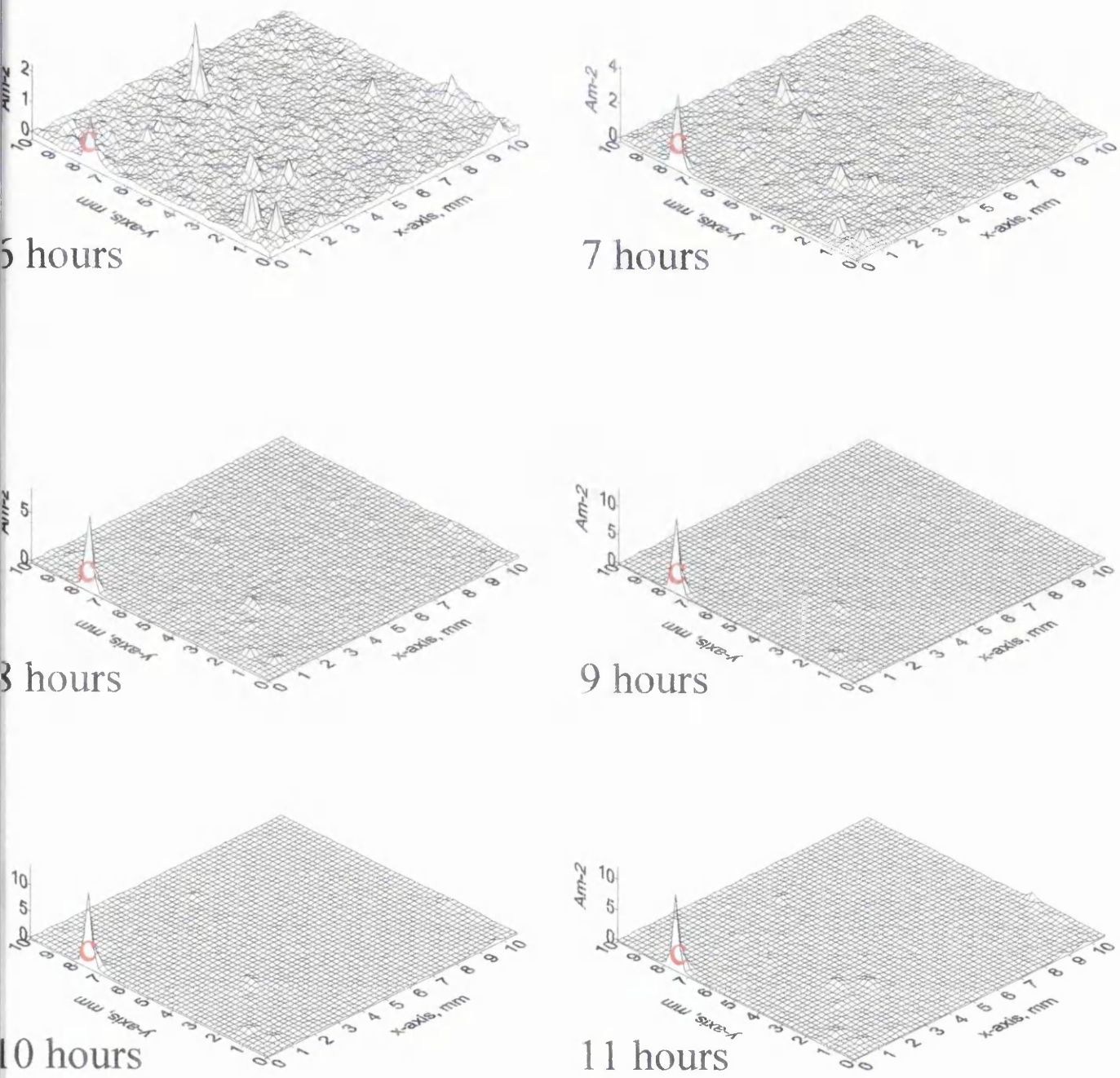

Figure 3.3: Surface plots of SVET scans for polished AA2024-T3 freely corroding in 3.5% w/w NaCl, after X hours immersion.

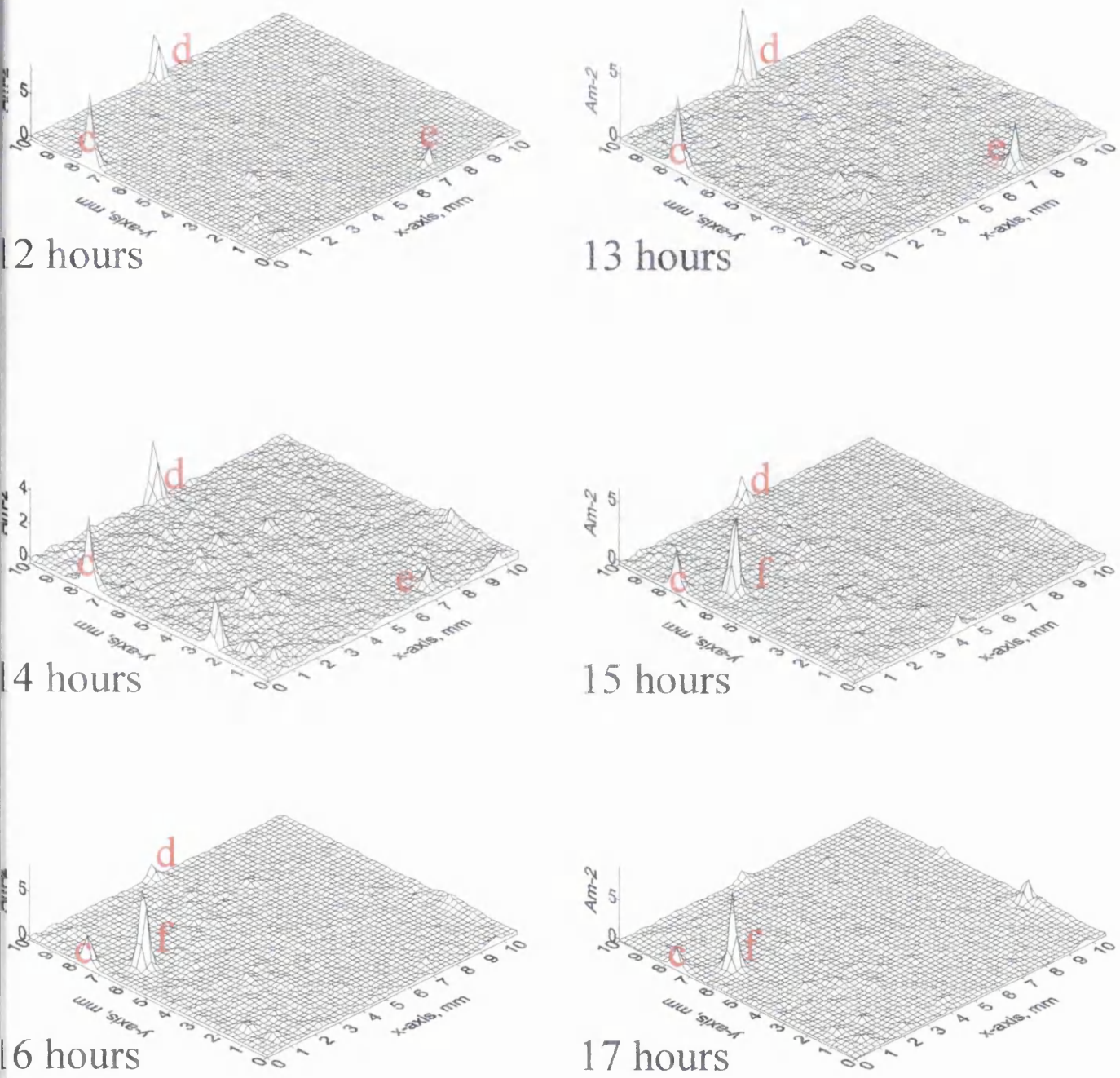

Figure 3.3: Surface plots of SVET scans for polished AA2024-T3 freely corroding in 3.5% w/w NaCl, after X hours immersion.

$jz_{(x,y)}$ features which could be interpreted as metastable pitting, *i.e.* features with lifetime <30 sec. Figure 3.4 shows a surface plot where only the data points of the same y value are joined. This makes it easier to see peaks which only last one line of scanning, implying metastable pitting. Furthermore, the peak $jz_{(x,y)}$ values associated with these metastable pitting events are typically more than an order of magnitude lower that that associated with stable pits. Consequently, we may assume that the $jz_{(x,y)}$ distributions seen in figure 3.3 derive substantially from stable pitting events.

Initially the surface is covered in a large number of very low intensity pits (peak values <2 Am^{-2}) most of which seem to last less then one hour. However, after 6 hours immersion a small number (between 1 and 6) of high intensity pits were detected (peak values between 2 and 15 Am^{-2}), whilst the majority still have a peak value <2 Am^{-2}. Most of the high intensity pits remain active for many hours, some examples are marked c to f in figure 3.3. From figure 3.3 it can also be seen that whilst the anodic (positive) activity is very localised, the cathodic (negative) activity is generalised, and in fact seems cover the whole of the remaining sample area.

The peaks in the current density are very narrow, this makes them very hard to depict well using contour maps (figure 3.2) as the lines of equal $jz_{(x,y)}$ are very close together. It is possible to spread out the contours, however this greatly reduces the detail of the maps. Another method is to restrict the scale so that its maximum level is low (~1 Am^{-2}) whilst keeping the gap between contours small (~0.1 Am^{-2}). The result can be seen in figure 3.5, which shows some of the same scans as figure 3.3. It can be seen that the lower level activity is now visible on these maps, however the actual intensity of the more active pits is not visible. In the same way the z-axis on the surface plots can be 'blown up' so that the lower level activity is exposed, as can be seen in figure 3.6. However this results in very large, often unmanageable, pictures.

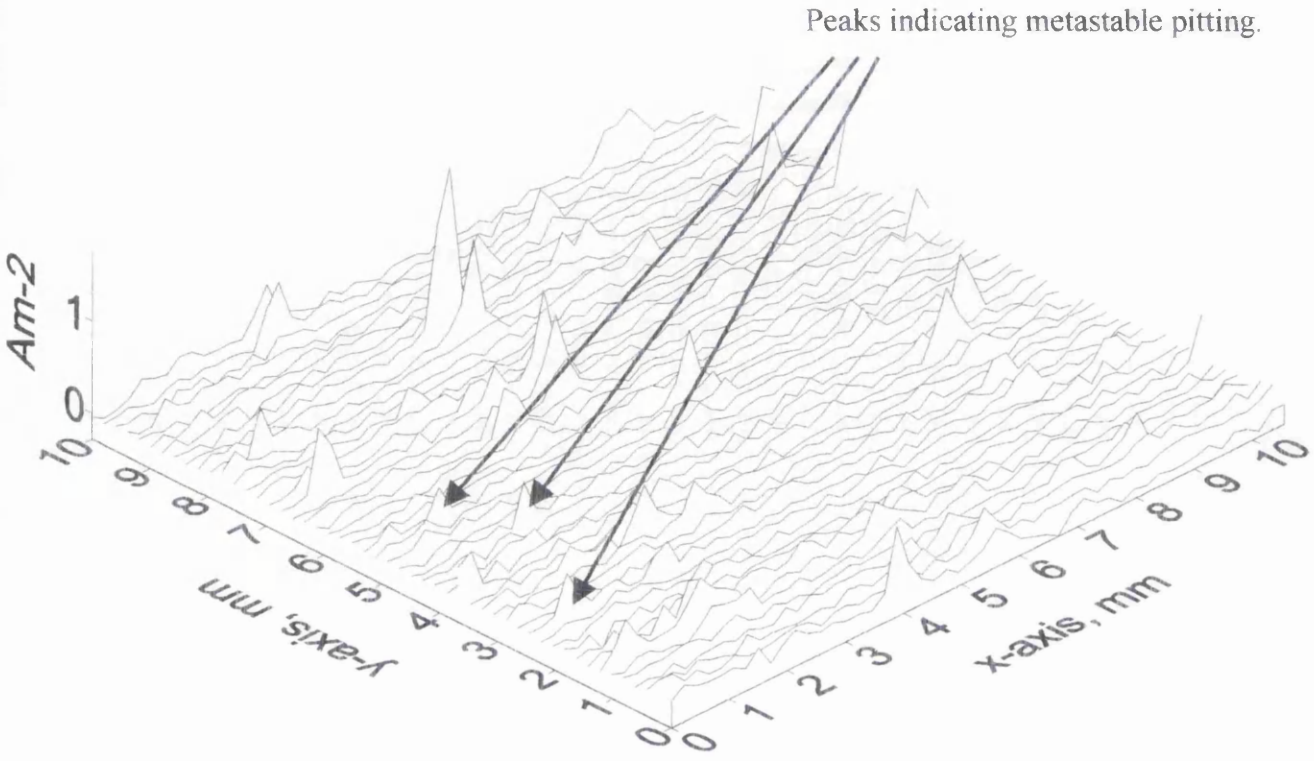

Figure 3.4: Surface plot of SVET scans for polished AA2024-T3 freely corroding in 3.5% w/w NaCl immediately after immersion.

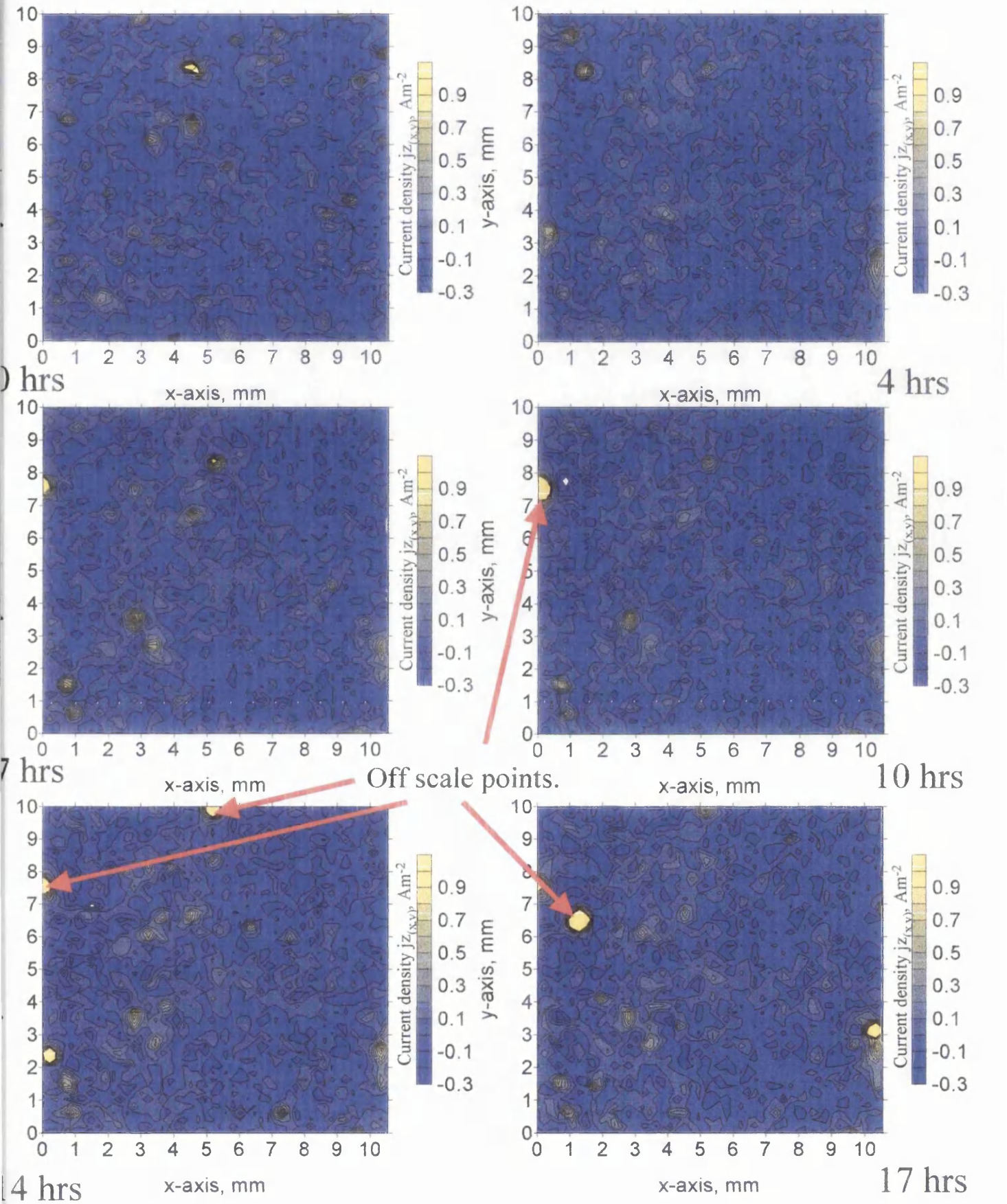

Figure 3.5: False colour maps of SVET scans for polished AA2024-T3 freely corroding in 3.5% w/w NaCl, after X hours immersion, current density scale set to 1 Am^{-2} maximum.

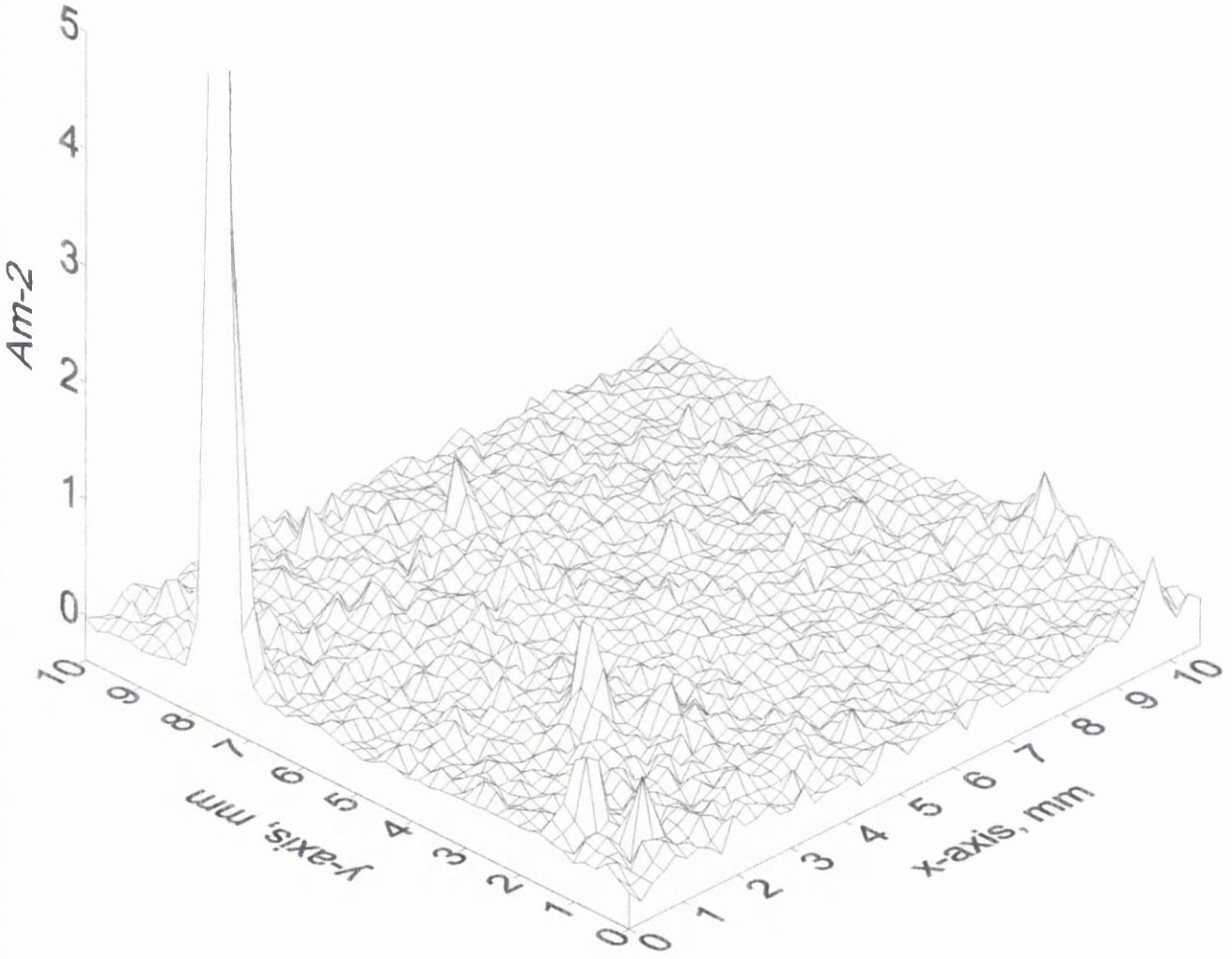

Figure 3.6: 'Blown up' Surface plot of SVET scan for polished AA2024-T3 freely corroding in 3.5% w/w NaCl, after 10 hours immersion.

These are examples of how manipulating the data in various ways can yield different information.

3.3.2: Optical images.

A high resolution in-situ optical picture was taken of part of the sample surface on completion of the SVET experiment, as described in section 3.2.2. Figure 3.7a shows the high resolution optical image for the same sample as used in figure 3.3. Figure 3.7b is a schematic diagram showing how the position of the optical picture relates to the SVET scans. As can be seen in figure 3.7 the majority of the sample surface has become 'copper' in colour, however there are small areas (diameters ranging from ~10μm to 1mm) of very dark deposit (examples marked a to c on figure 3.7a), some of which have a very light coloured halo (examples marked d to f on figure 3.7a).

Figure 3.8 shows the high resolution micrograph overlaid with contours of SVET data for 0, 4, 7, 10, 14 and 17 hours. It can be seen that areas of high activity recorded by the SVET correspond very closely to the dark disk like features on the surface after 17 hours. This would suggest that these dark disk like features are sites of anodic pitting.

3.3.3: Quantification of SVET data.

If a collection of point current sources of the same sign, i_1, i_2 ....i_n, are set at different points on an insulating x,y plane, with the current drain at infinity, then the total current (i) will be given by $i = i_1 + i_2 .... + i_n$. Furthermore, the normal current density contributions from each point source will be additive, such that total normal current density at any point $jz_{(x,y)} = jz_{(z,y)1} + jz_{(z,y)2} .... + jz_{(z,y)n}$. Under these circumstances, the

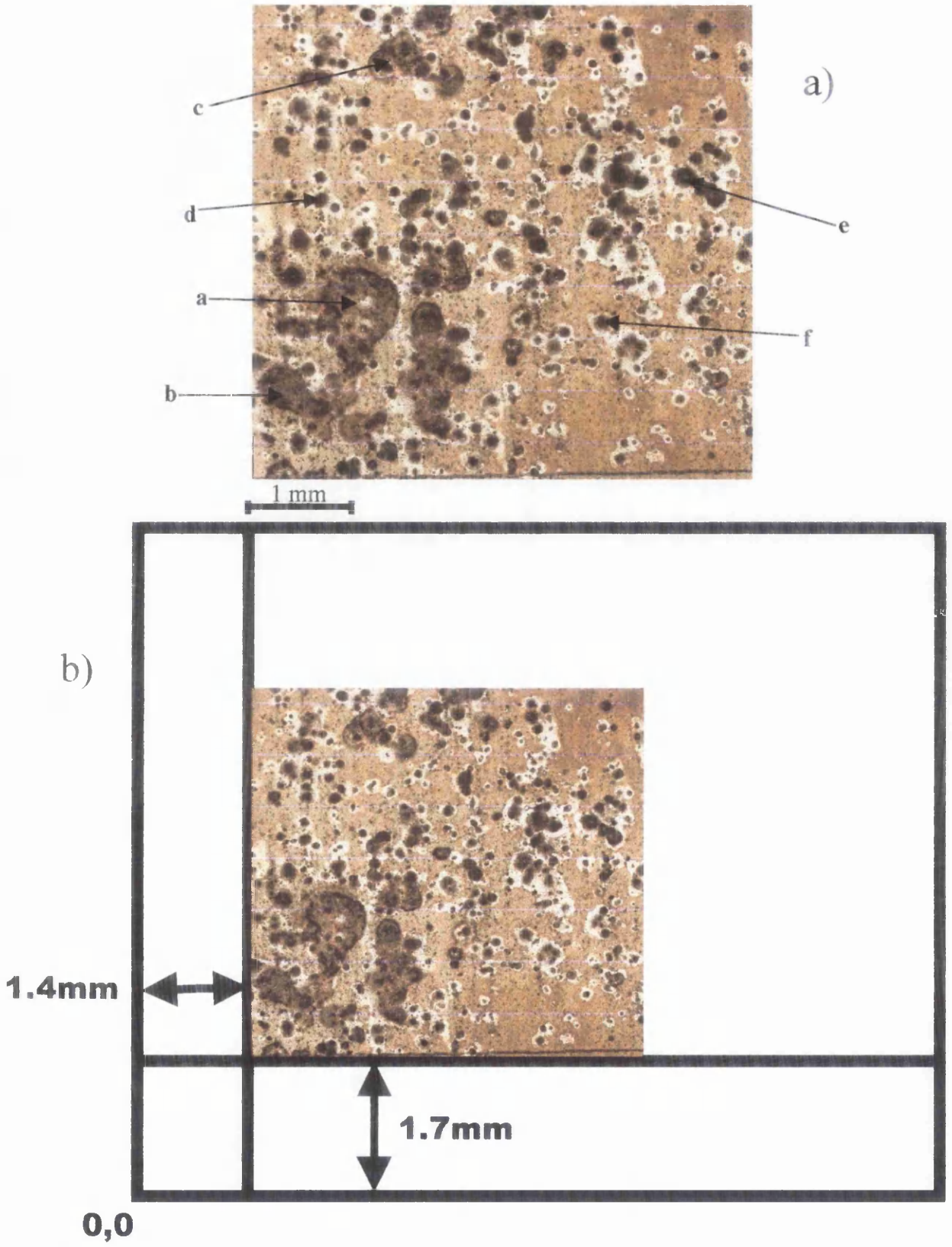

Figure 3.7: a) In-situ high resolution optical picture of corroded surface after 17 hours immersion in 3.5% w/w NaCl, picture corresponds to SVET data in figure 3.3. b) Diagram showing position of optical image relative to SVET scans.

Figure 3.8: SVET data contour lines after X hours, set over in-situ image of surface after 17 hours immersion in 3.5% w/w NaCl.

SVET ac voltage signal ΔE will be related to $jz_{(x,y)}$ by equation 2.11 and (i) may be obtained using the numerical area integral of $jz_{(x,y)}$. As show in section 2.1.1 for a single point current source, i will be accurately estimated provided the x and y integration intervals are large by comparison to probe height h and all the point sources lie well within the limits of the x and y intervals. Current contributions from point sources lying a distance less than $10h$ from the limits of the x or y intervals will be significantly underestimated.

The above scenario may be approximated by a metal surface, polarised via an external circuit, which undergoes pitting such that the pitting current is equal to current flowing in the external circuit, the remainder of the surface being electrochemically inactive. However, it is less clear how closely the above scenario approximates to a metal surface, which undergoes pitting under free corrosion conditions. Under these circumstances the anodic pits may certainly resemble point current sources but the cathode (current drain) will now be the surrounding metal surface. Consequently, equation 2.6 may underestimate jz as some lines of current flux may loop between anodic and cathodic sites without cutting the plane of scan.

The total anodic current (i_a) present in each of the $j_{(x,y)}$ distribution maps exemplified in figure 3.3 was determined using equation 3.1 with a threshold (Th) current density value of 0.2 Am^{-2}.

$$i_a = A.J_{corr} = \int_{x=0}^{x=X} \int_{y=0}^{y=Y} (jz_{(x,y)} > Th)\, dx\, dy \qquad [3.1]$$

Where A is the sample area, X and Y are the length and width of the SVET scan and Th is a threshold current density above which integration is performed.

The use of a non-zero threshold was made necessary by practical considerations such as the finite level of random electrical noise superimposed on the SVET signal (typically 1.6 μV peak-to-peak, corresponding to ± 0.2 Am^{-2}) and finite base-line stability over the experimental period (see section 2.1.4). Figure 3.9a shows a surface plot of SVET data recorded whilst the probe was scanned in the experimental electrolyte over an insulating plane. This was done to determine the level of background noise detected by the SVET probe in each experiment. As can be seen in figure 3.9a apparent background $j_{(x,y)}$ values oscillate around zero with a peak to peak amplitude of ~ ± 0.2 Am^{-2}. Although this noise level is negligible, compared to the signal picked up over a sample freely corroding in electrolyte, it is not negligible when inhibiting is significant. Noise may therefore result in relatively large errors in i_a values obtained using equation 3.1 with $Th = 0$, where surface pitting corrosion has been inhibited (see chapter 6). Figure 3.9b shows the same scan as figure 3.9a but the surface plot has been rotated to show the side view. The horizontal coloured lines show different values of threshold, used to determine the sensitivity of J_{corr} with respect to threshold value. Figure 3.10 shows how J_{corr} varies with threshold value for five SVET scans. For $Th \leq 0$ Am^{-2} the value obtained for J_{corr} is strongly dependant on Th. However, for $Th > \sim 0.05$ Am^{-2} J_{corr} changes much more slowly with Th because now only pitting currents above background noise are being included in the current integral. Never the less J_{corr} is seen to decrease slowly with Th even for $Th > 0$, for these reasons a compromise value of $Th = 0.2$ Am^{-2} was adopted as giving good noise immunity whilst not excessively underestimating J_{corr}.

In this manner one value of J_{corr} was obtained from each hourly SVET scan, by using the grid, volume function in Surfer 6 as described in section 2.8.4. The

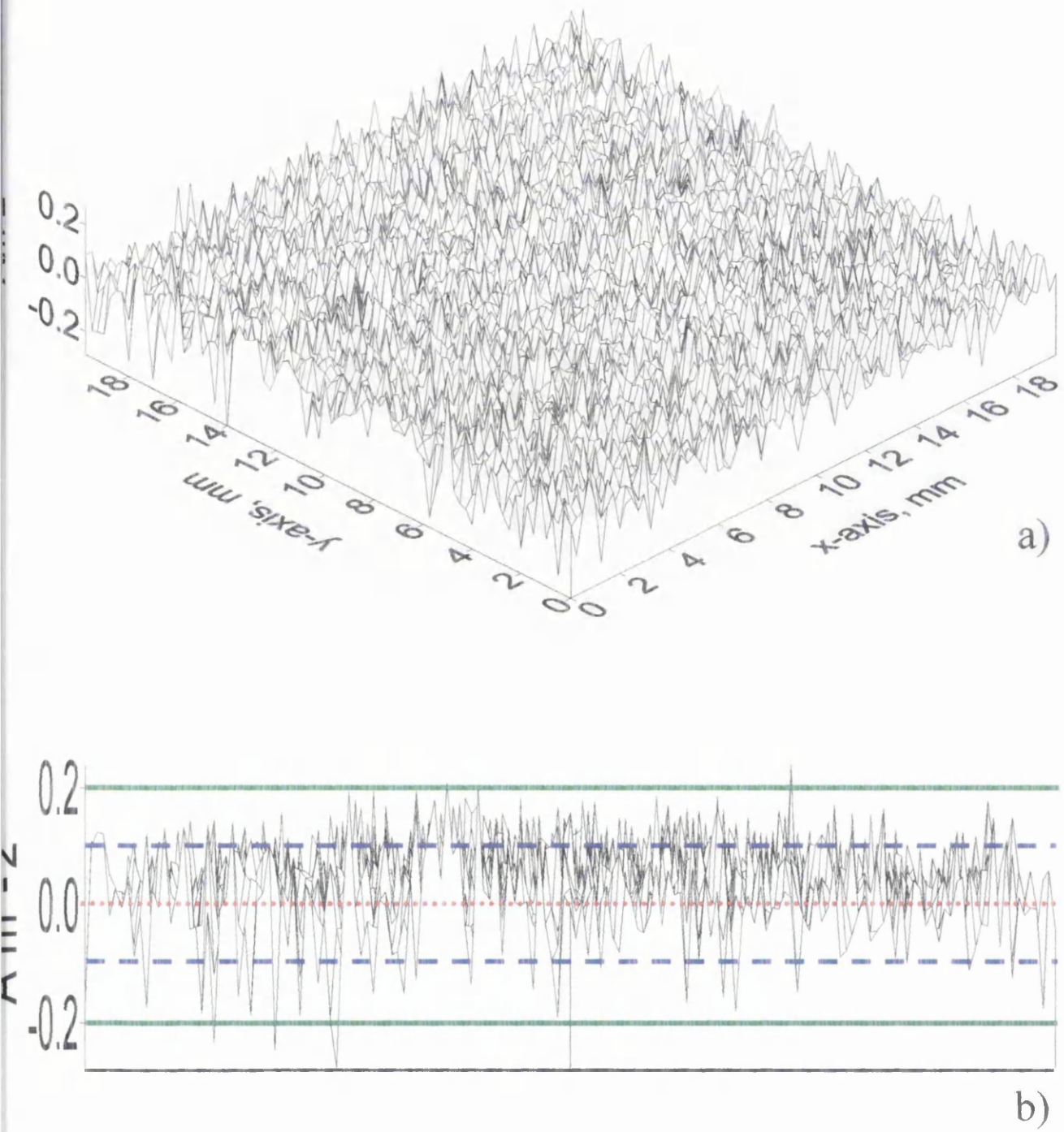

Figure 3.9: a) SVET surface plot of data recorded whilst SVET was scanning in 3.5% w/w NaCl over insulating plane. b) Surface plot a) turned for side view, coloured lines show threshold levels (Th) of 0.2 Am^{-2} (green), 0.1 Am^{-2} (blue) and zero (red).

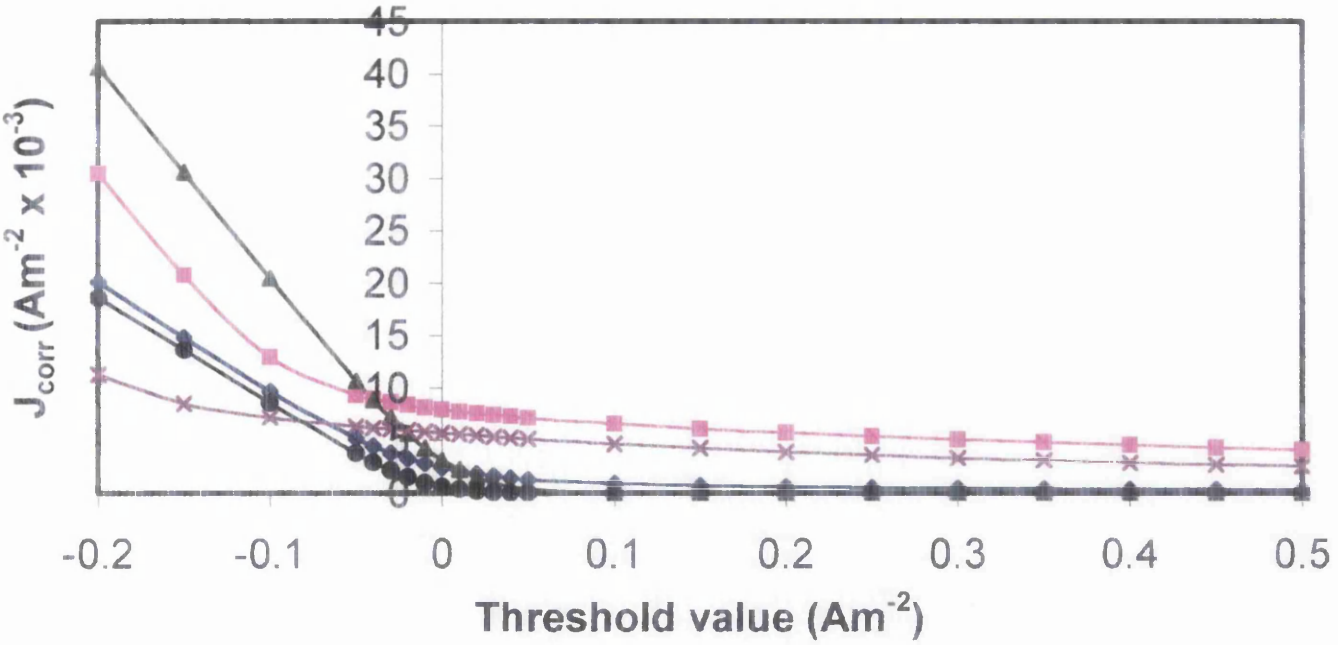

Figure 3.10: Plot showing how J_{corr} varies for different values of threshold for four arbitrary SVET scans in 3.5% w/w aqueous NaCl. (Black line with circle symbols shows values for background noise scan shown in figure 3.9).

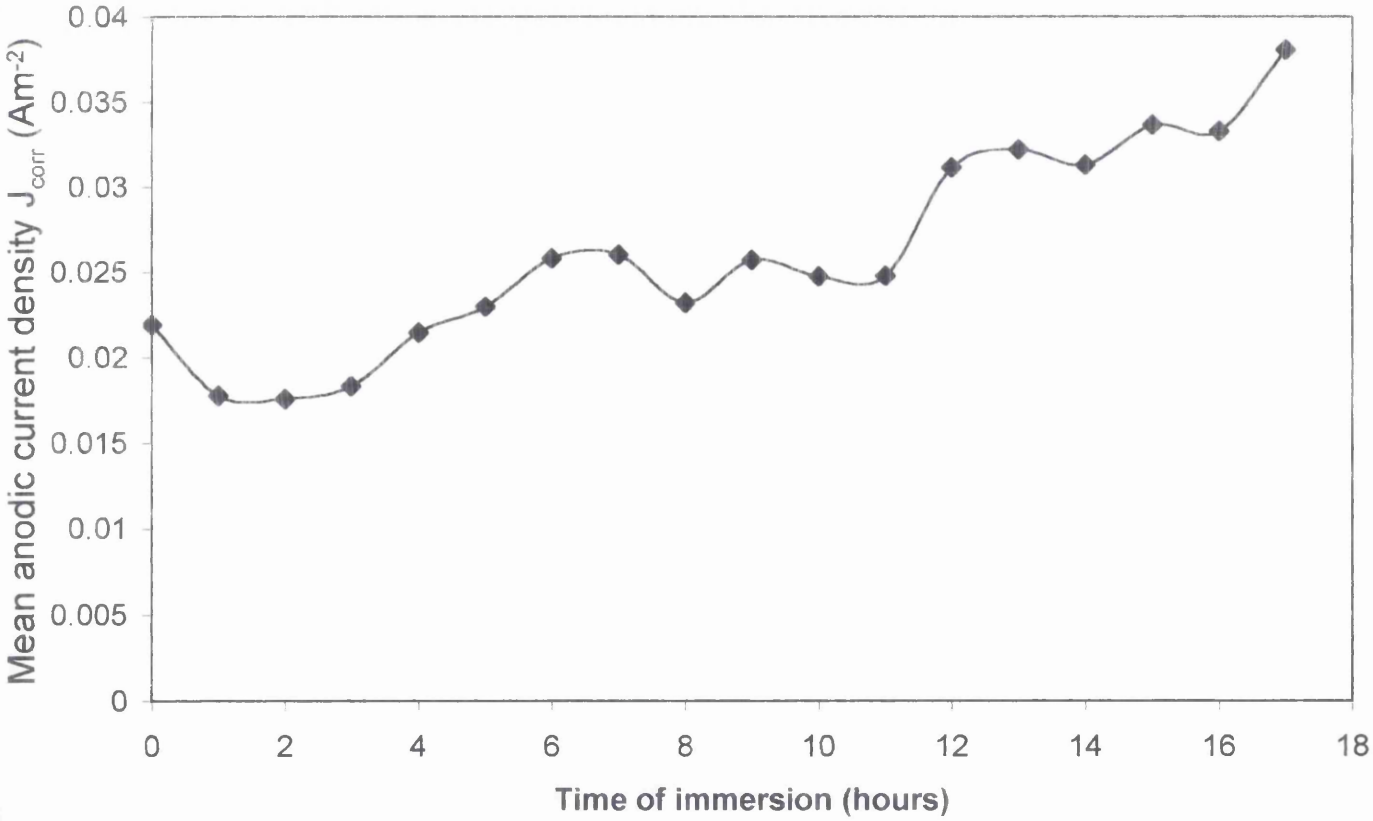

Figure 3.11: Plot showing how J_{corr} varies with time of immersion for polished AA2024-T3 in 3.5% w/w aqueous NaCl at 25°C.

variation of J_{corr} with time can be seen in figure 3.11, initially $J_{corr} = 0.02$ Am^{-2} rising slowly to ~ 0.04 Am^{-2} over the 17 hour experimental period.

The total quantity of charge emitted from corrosion pits over the 17 hour experimental period was calculated from J(t) using

$$Q = \frac{3F \, x \, teal}{27} = \int_{t=0}^{t=tm} J(t) \, .dt \qquad [3.2]$$

Where Q is the charge in Cm^{-2}, tm is the immersion period (in seconds), F is the Faraday constant and *teal* is the total equivalent aluminium (atm. wt 27g) loss in gm^{-2}. The integration of J(t) values was performed numerically using Eulers method. The value of Q obtained from the 17 hour immersion experiment, was 1692 Cm^{-2}, which corresponds to a *teal* value of 0.158 g m^{-2}.

3.3.4: Number density of active pits detected by SVET.

To determine the number density of pits detected by the SVET for each scan it is necessary to first define what is to be considered a pit. Figure 3.3 shows surface plots of SVET data, it can be seen that the surface is covered with peaks which correspond to large positive $j_{(x,y)}$. Figure 3.8 shows contour plots of $j_{(x,y)}$ data overlaid on an optical micrograph of the surface, after completion of the SVET experiment. This shows that the large positive peaks in $j_{(x,y)}$ detected by the SVET correspond with areas of pitting on the surface. From this it was determined that large anodic peaks in $j_{(x,y)}$ correspond to anodic pitting activity on the surface. However, in section 3.3.3 it was explained how low level noise on the SVET signal makes it necessary to use a threshold (*Th*) on the SVET data to determine anodic current density. A similar approach was also used to determine pit number density, figure 3.12 shows a side

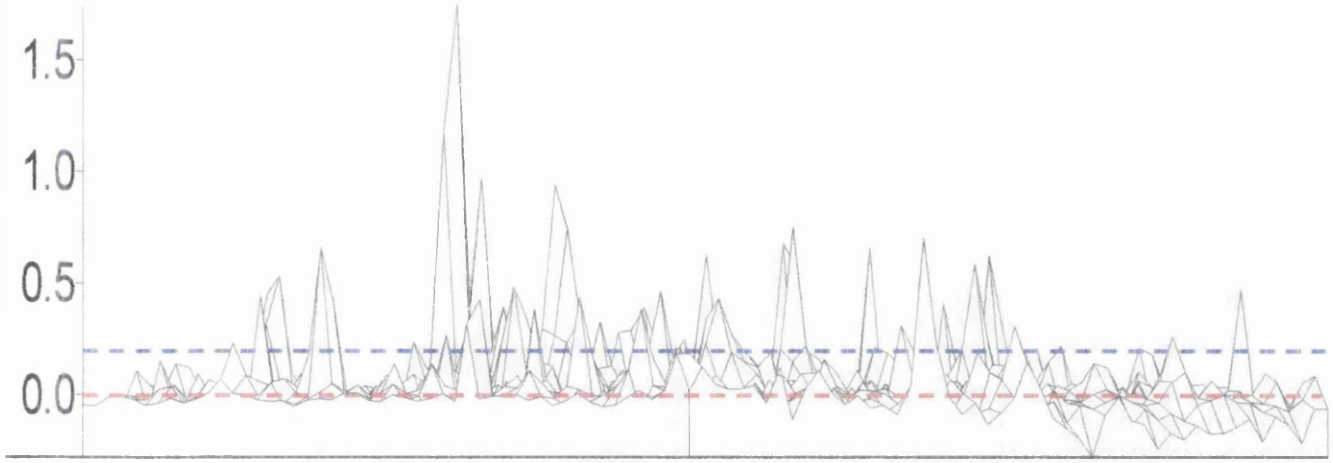

Figure 3.12: SVET surface plot SVET data recorded whilst scanning over polished AA2024-T3 in 3.5% w/w NaCl turned for side view, Red line shows threshold level of 0 Am^{-2}, Blue line shows threshold level of 0.2 Am^{-2}.

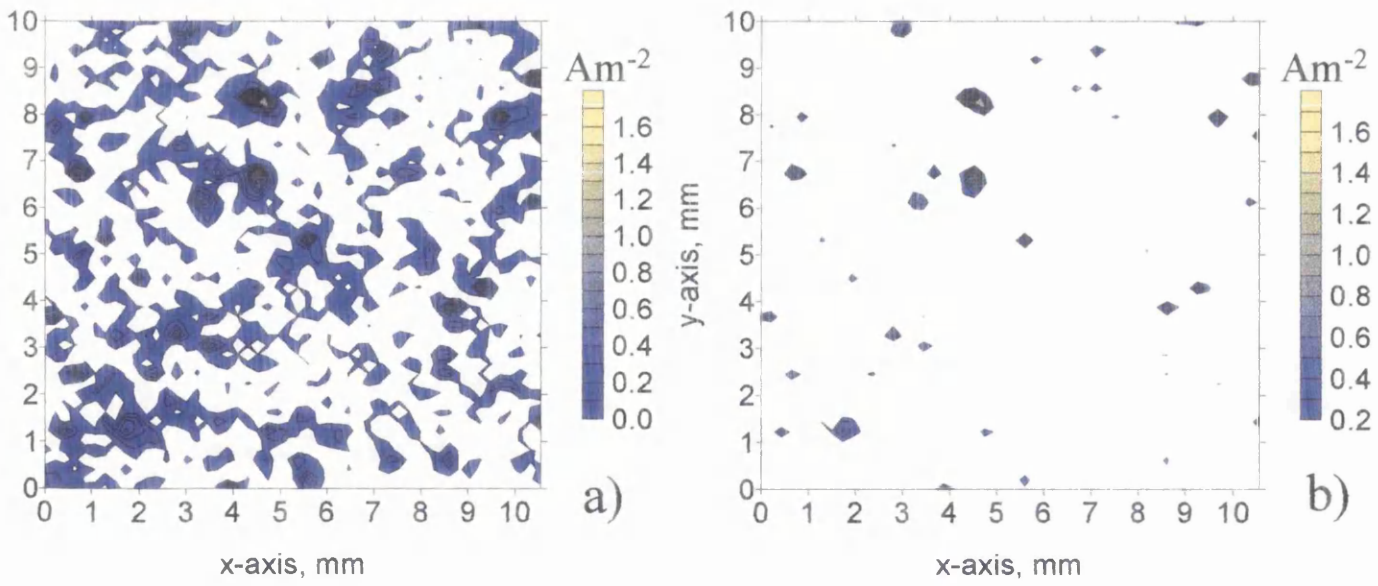

Figure 3.13: SVET contour plots of the same data as figure 3.12, Figure 3.13a shows threshold level of 0 Am^{-2}, Figure 3.13b shows threshold level of 0.2 Am^{-2}.

view of a SVET surface plots taken straight after immersion in the electrolyte. It shows that at Th = 0 Am^{-2} there are many $j_{(x,y)}$ peaks which could be taken as pits, however figure 3.13a, showing the same information but presented using a contour plot, indicates that not all the $j_{(x,y)}$ peaks at this level are pit-like in shape. The blue line in figure 3.12 shows the threshold level at Th = 0.2 Am^{-2}. It can be seen that at this level any peaks cutting the threshold are made up of many points, indicating pitting activity not noise. Figure 3.13b reinforces this, as all activity over 0.2 Am^{-2} greatly resembles activity seen using a point current source (see section 2.1.3). For these reasons a pit was defined as any discrete feature associated with $j_{(x,y)}$ values > Th = 0.2 Am^{-2}. Obviously this is an arbitrary definition and only has meaning for the work currently under discussion.

To determine pit density of each scan the SVET data was presented as in figure 3.13b. The number of pits was counted with the aid of the Map, Digitise function in Surfer 6 software as described in section 2.8.2. This function digitises the contour map so that when a point is 'clicked' on with the mouse, it leaves a red cross in that position, and records its x-y co-ordinates (see figure 3.14). Using this the number density of pits detected by the SVET for each hourly scan was determined, a plot of which can be seen in figure 3.15. Figure 3.15 shows that pit density detected by the SVET during the experimental period does not change greatly with time, at t=0, pit density = 600000 pits m^{-2}, and for the remaining experimental period pit density remains within 750000 and 450000 pits m^{-2}.

3.3.5: Calculating pit dimensions from SVET data.

As described in section 3.3.4, a pits x,y co-ordinates were determined using the Map, Digitise function in Surfer 6. From a pits x,y co-ordinates the current density $j_{(x,y)}$ at

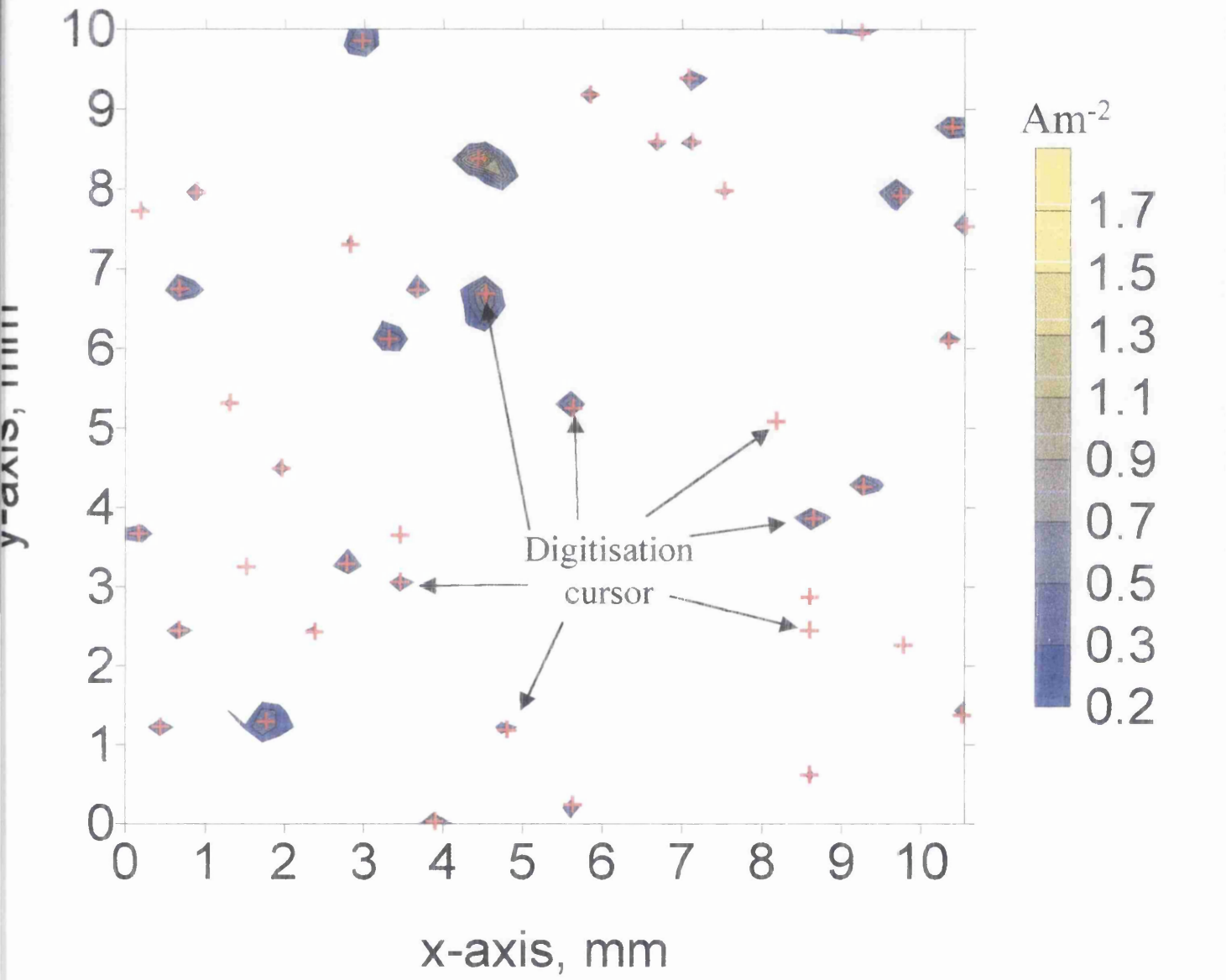

Figure 3.14: SVET contour plots of the same data as figure 3.12, showing map-digitise function in Surfer 6 software. Red crosses show position of cursor when x,y co-ordinate was recorded for pit.

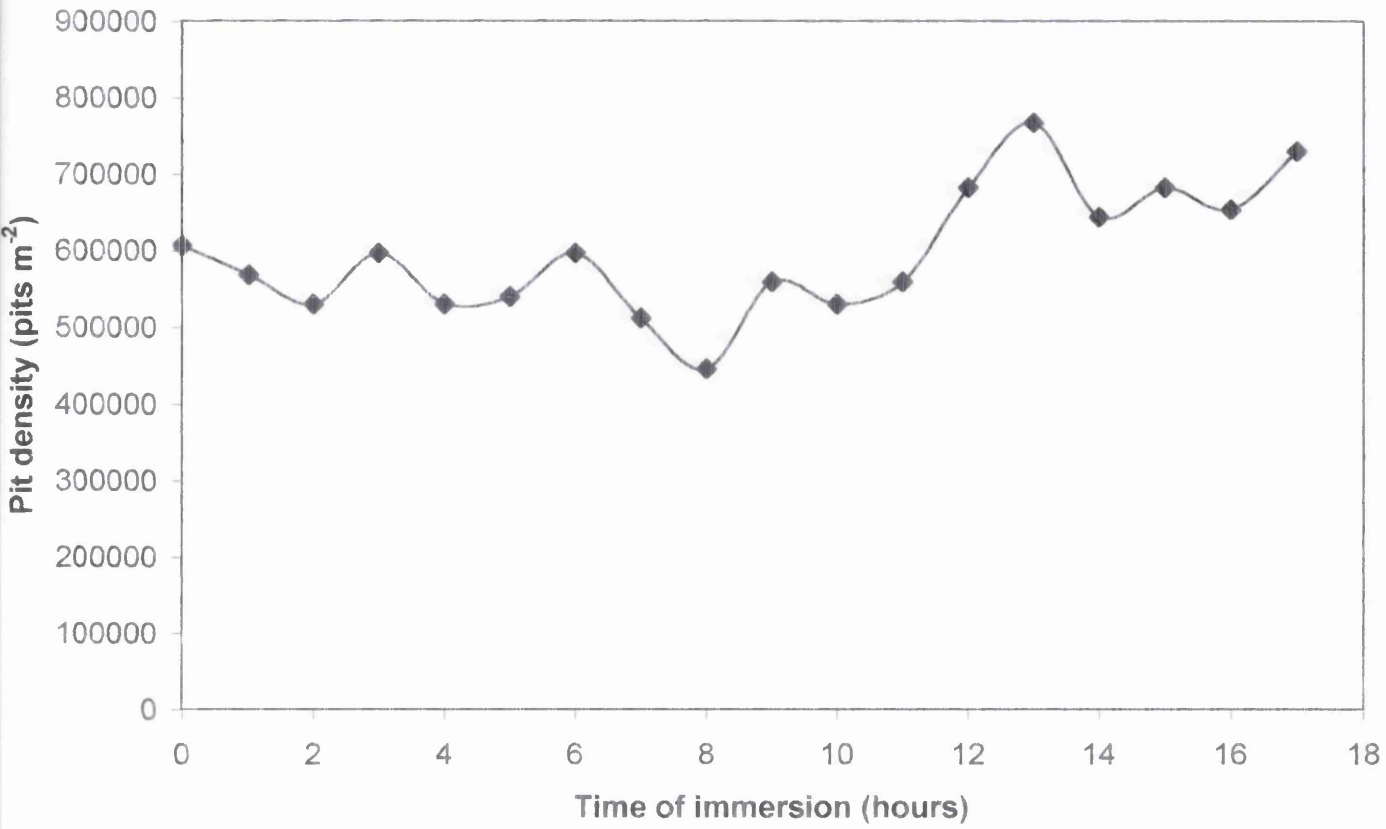

Figure 3.15: Plot showing how active pit number density varies with time of immersion for polished AA2024-T3 in 3.5% w/w aqueous NaCl at 25°C.

that point was determined using the Grid, Residual function in Surfer 6 as described in section 2.8.3. From this peak value of $j_{(x,y)}$ the anodic current was determined using equation 2.11 when $r = 0$ and $z = h$, i.e. $i = j_{(x,y)}.2.\pi h^2$. Assuming i to be constant for the hour between SVET scans, and all metal loss to be aluminium. The mass of aluminium lost (*teal*) from that site for that hour can be determined using

$$teal = \frac{27\ it}{3\ F} \qquad [3.3]$$

where t is time between SVET scans.

Using this it is possible to determine the diameter of the pit using equation 3.4, if it is also assumed that the pit is hemispherical in nature.

$$d = 2\left(\frac{3}{2\pi\rho}\sum_{t=0}^{t=tm} teal\right)^{1/3} \qquad [3.4]$$

Where d is pit diameter and ρ is the density of aluminium = 2.0702 gcm^{-3}.

From figure 3.15 it can be seen that there may be over one hundred pits active during any scan. This large number makes it difficult to present pit diameter for each pit individually.

To illustrate how pit diameters change with immersion time, histograms of the number of pits with each pit diameter were produced for each scan, however before pit diameter could be measured, the x,y co-ordinates for each pit was determined. As can be seen in figure 3.3 some pits stay active over many hours of immersion, whereas others are only active for one SVET scan. To produce the histograms a file containing x,y co-ordinates for all pits becoming active during the SVET experiment must be produced. In so doing it is important that each pit is counted only once. This requirement was achieved in the following way. Firstly a false colour map was produced and the x,y co-ordinates for each pit were recorded in the same way as

described in section 3.3.4 (see figure 3.14). Secondly a false colour plot for the subsequent SVET scan was produced, however the contours were made a different colour (to be distinct from the first plot) and they were not filled in. The second plot was overlaid on the first (so the first plot could be seen through the second). Then any pits not recorded from the first scan were recorded from the second, as can be seen in figure 3.16. This procedure was repeated for each SVET scan for the experimental period. The theoretical diameter of each pit after each scan was determined as described previously using equation 3.4. Following this procedure pit diameter histograms were produced for each hour of immersion, examples of which can be seen in figure 3.17 for hours 0, 4, 7, 10, 14 and 17. For this sample over 400 pits were recorded throughout the experimental period, and as can be seen from figure 3.17, diameters after 17 hours immersion the 3.5% NaCl vary from between 25 and 155μm. Figure 3.17 also shows how the distribution in pit diameters broadens with longer immersion time (from 50μm at t=0 to 130μm at t=17hr), and the mode value increases with immersion time (from 20μm at t=0 to 40μm at t=17hr).

3.3.6: Comparing SVET pit diameter with Optical pit diameter.

Figure 3.8 shows SVET contour plots overlaid on an in-situ high resolution optical micrograph. It shows that the contour plots correspond very closely with the dark areas on the surface, hence it is possible to associate a SVET diameter calculated from equation 3.4 (see section 3.3.5) with an optical diameter measured from the optical micrograph. The optical diameter was taken to be the maximum distance from one edge of the dark disk to the opposite edge. Figure 3.18 shows the optical micrograph with 11 'pits' circled, these were chosen as their co-ordinates correspond very closely with 'pit' co-ordinates on SVET surface plots. Figure 3.19 shows four of the selected

SVET false colour plot for t=0, when threshold = 0.2 Am^{-2}. Red crosses show examples of points taken as x,y co-ordinates for pits. This was completed for all pits as shown in figure 3.14.

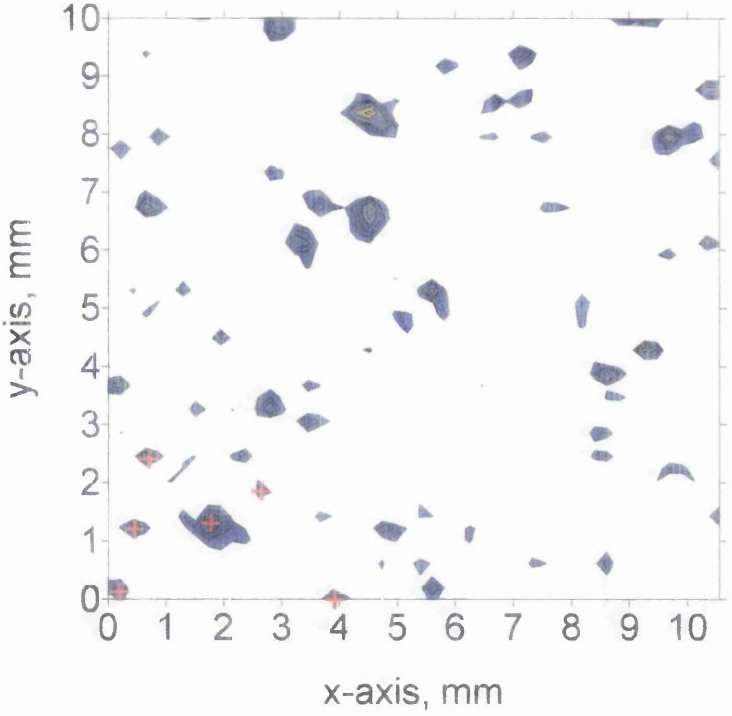

SVET false colour plot for t=0 overlaid with contour plot for t=1 hr, where green contours = 0.2 Am^{-2} any higher activity is represented by red contours. Areas surrounded by purple triangles show conserved pits, therefore there co-ordinates have already been recorded.

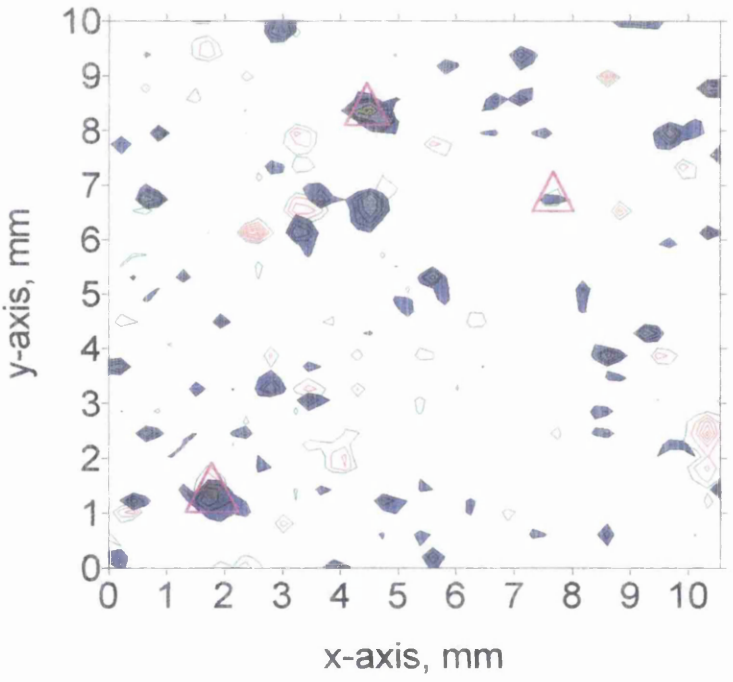

Figure 3.16: Plots showing how x,y co-ordinates of all pits active during experimental period were determined

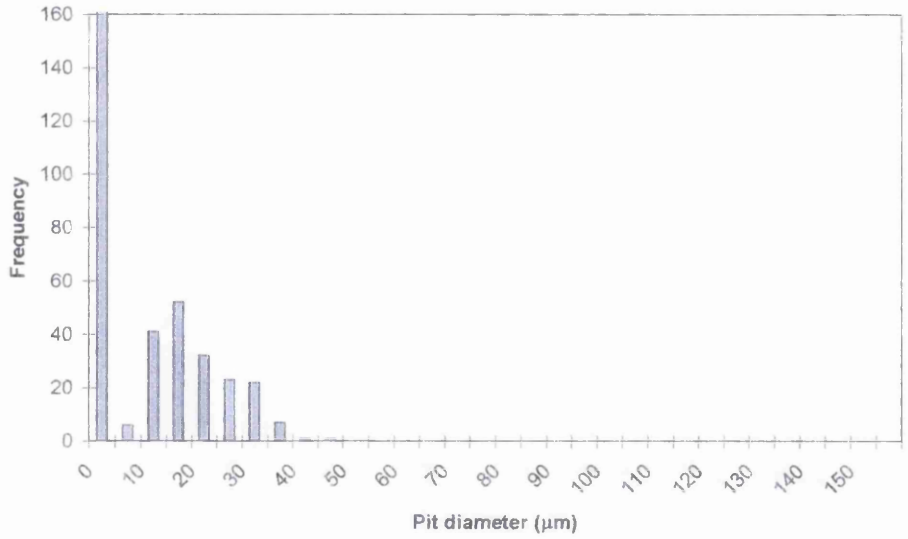

0 hr

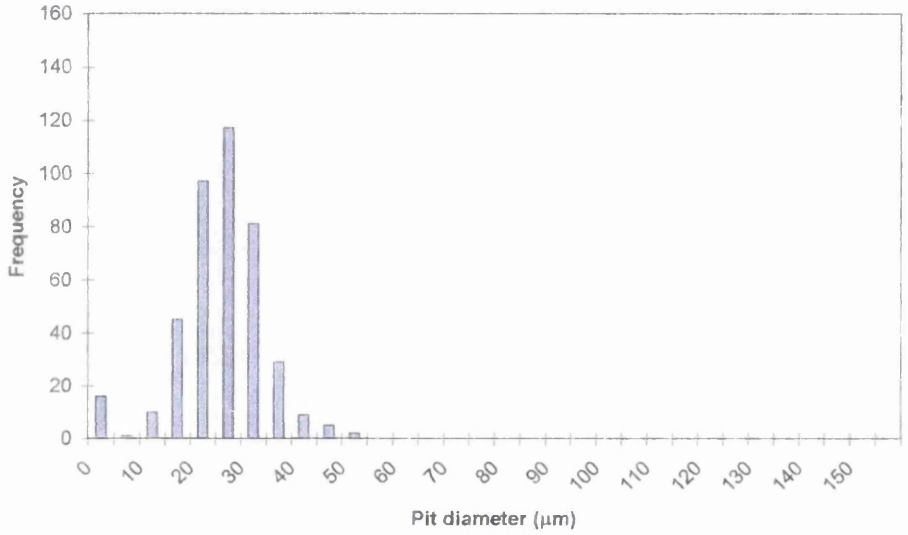

4 hr

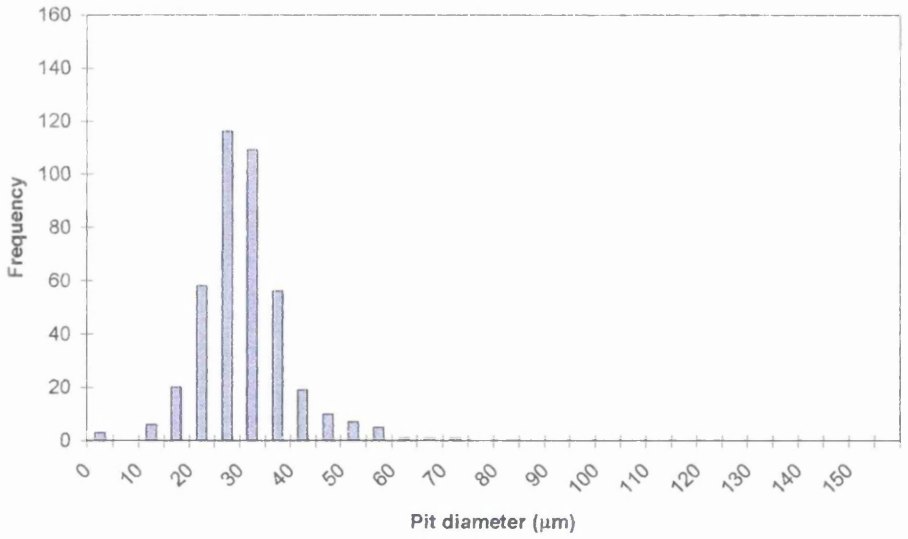

7 hr

Figure 3.17: Histograms of numbers of pits with each diameter determined using equation 3.4 after 0, 4, 7, 10, 14 and 17 hours immersion in 3.5% NaCl.

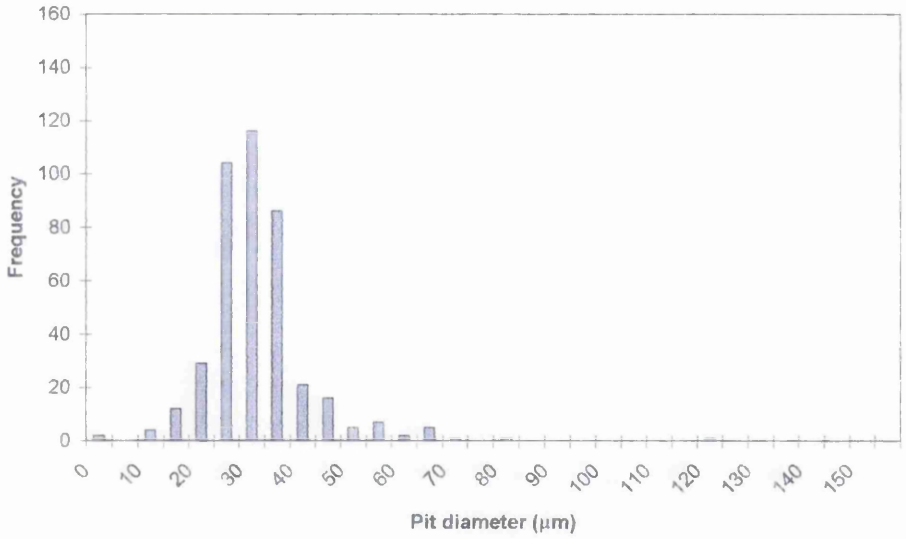

10 hr

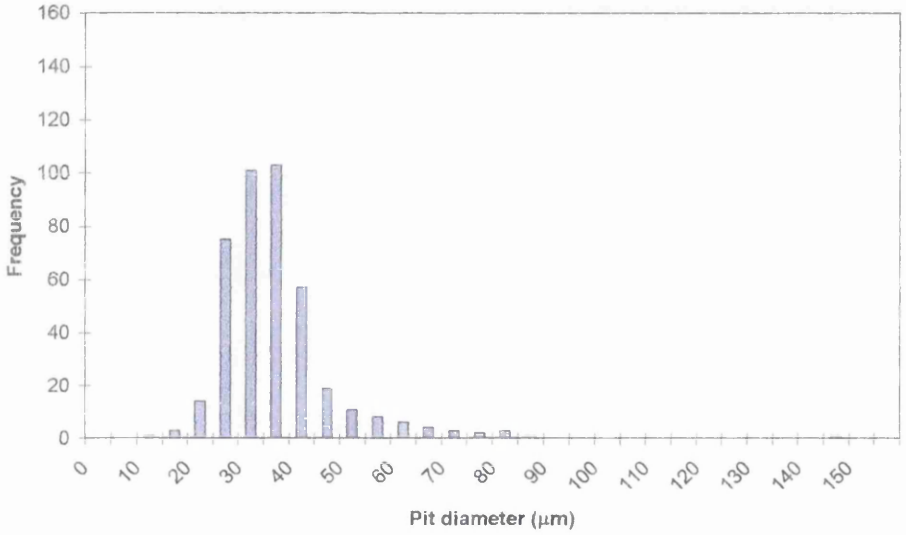

14 hr

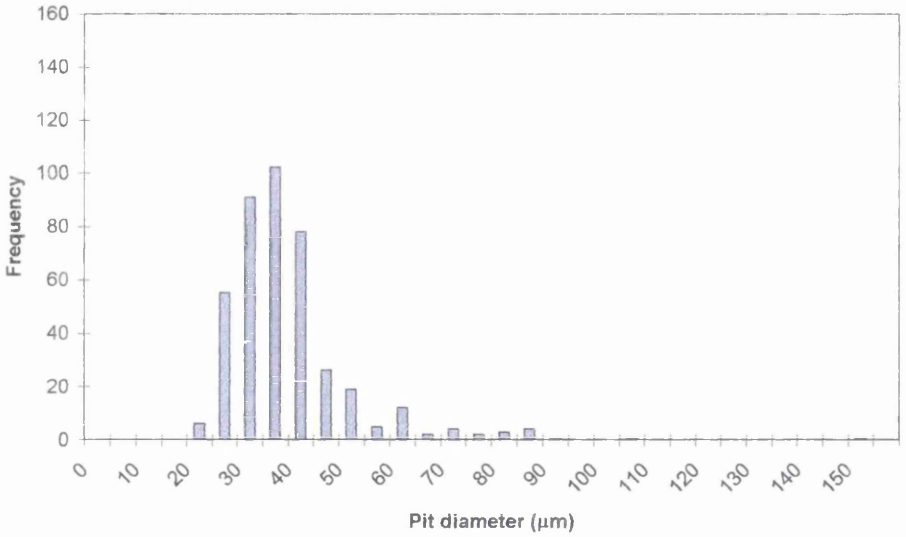

17 hr

Figure 3.17: Histograms of numbers of pits with each diameter determined using equation 3.4 after 0, 4, 7, 10, 14 and 17 hours immersion in 3.5% NaCl.

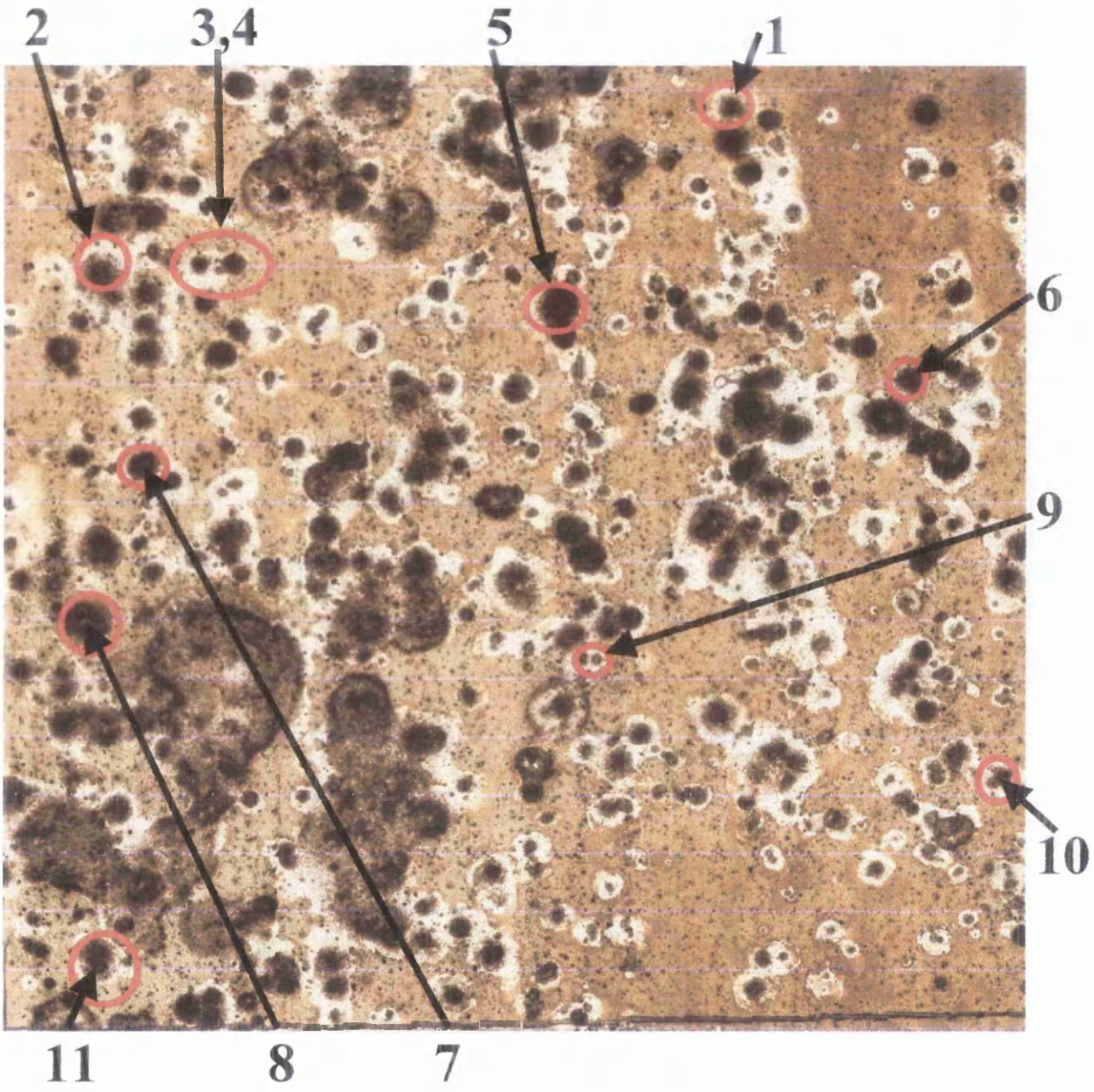

Figure 3.18: In-situ optical image of AA2024-T3 surface after 17 hours immersion in 3.5% NaCl at 25^{0}C, showing position of pits used to compare SVET diameters with optical diameters.

pits at high magnification. Figure 3.20 shows a plot comparing the pit diameters determined by the optical micrograph (blue) with the diameter determined experimentally using equation 3.4 (red) for the same 'pits'. It shows that the diameters determined from the optical micrograph are considerably larger then those determined using equation 3.4, the optical diameter is larger by a factor of between 1.3 to 7.3. This difference in determined diameter could be due to a number of factors including, i) error in determining pit diameter from the optical picture, ii) the pits not being hemispherical in nature producing an error in calculated d values and, iii) the SVET not detecting all the anodic current emerging from the pit.

On closer investigation it was concluded that the largest errors probably occur through misinterpretation of the optical picture, as the large dark disk like features visible in figures 3.18 and 3.19 are not actually the pit opening but a deposit of corrosion product at the pit mouth. Hence, to determine how well the SVET measures anodic activity the size and shape of resulting pits must be more accurately determined. To discover the real shape and size of the pit openings it is first necessary to remove any deposit of corrosion product. Consequently, after the SVET corrosion experiment was completed, the sample was rinsed in distilled water to stop corrosion activity, then optical images were taken of the surface using the inverted light source microscope as described in section 3.2.2 (see figure 3.21), and two of the disk like features at higher magnification (figure 3.23a). To remove the corrosion deposit the sample was cleaned as described in section 3.2.2. Then further optical images were taken of the surface (figure 3.22) of same small areas as examined before cleaning (figure 3.23b). It can be seen from figure 3.23 that after immersion in the cleaning solution the dark disk-like features are removed to show the opening of the pits. Figure 3.23b shows that the actual pit openings are much

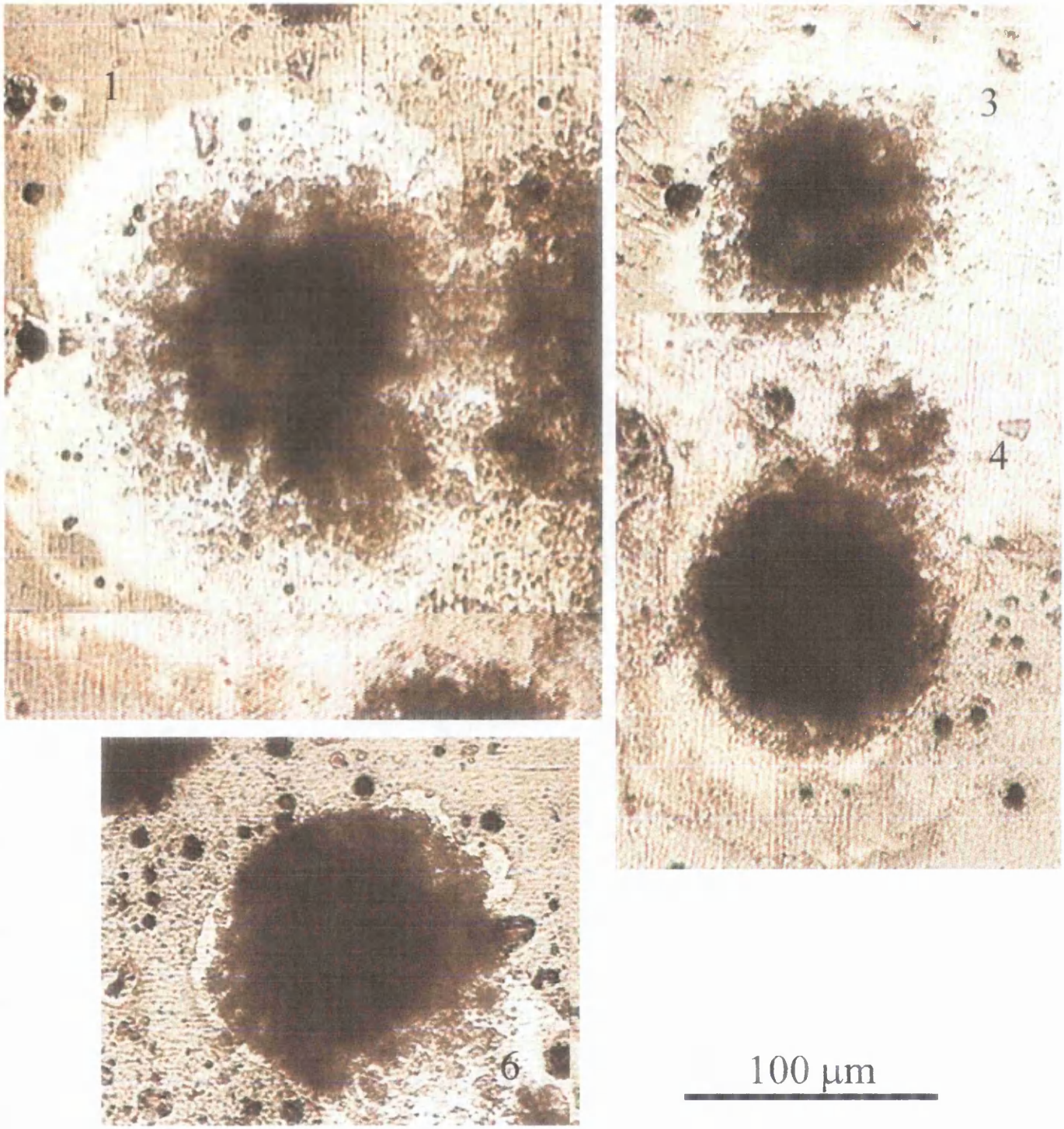

Figure 3.19: In-situ optical images showing examples of pits at high magnification, numbered as in figure 3.18.

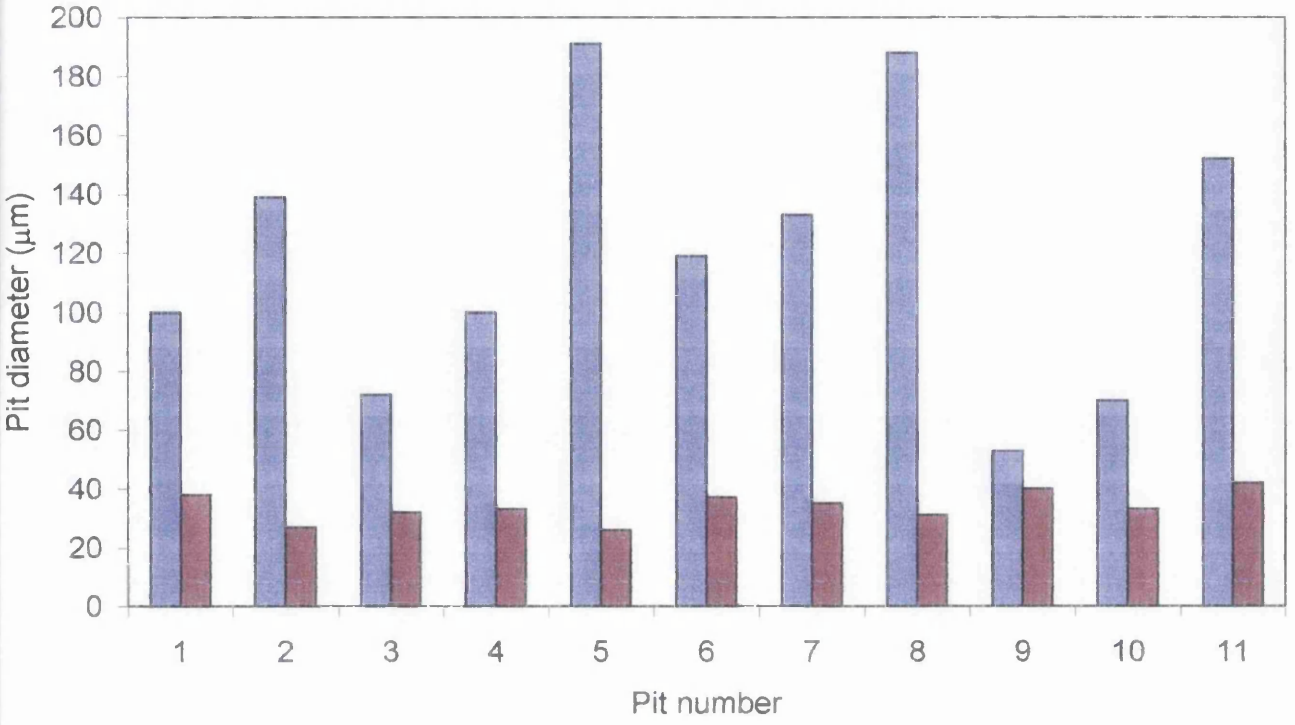

Figure 3.20: Plot showing diameters of 'pits' determined by optical image (blue), and SVET measurements using equation 3.4 (red). Numbered as shown in figure 3.18.

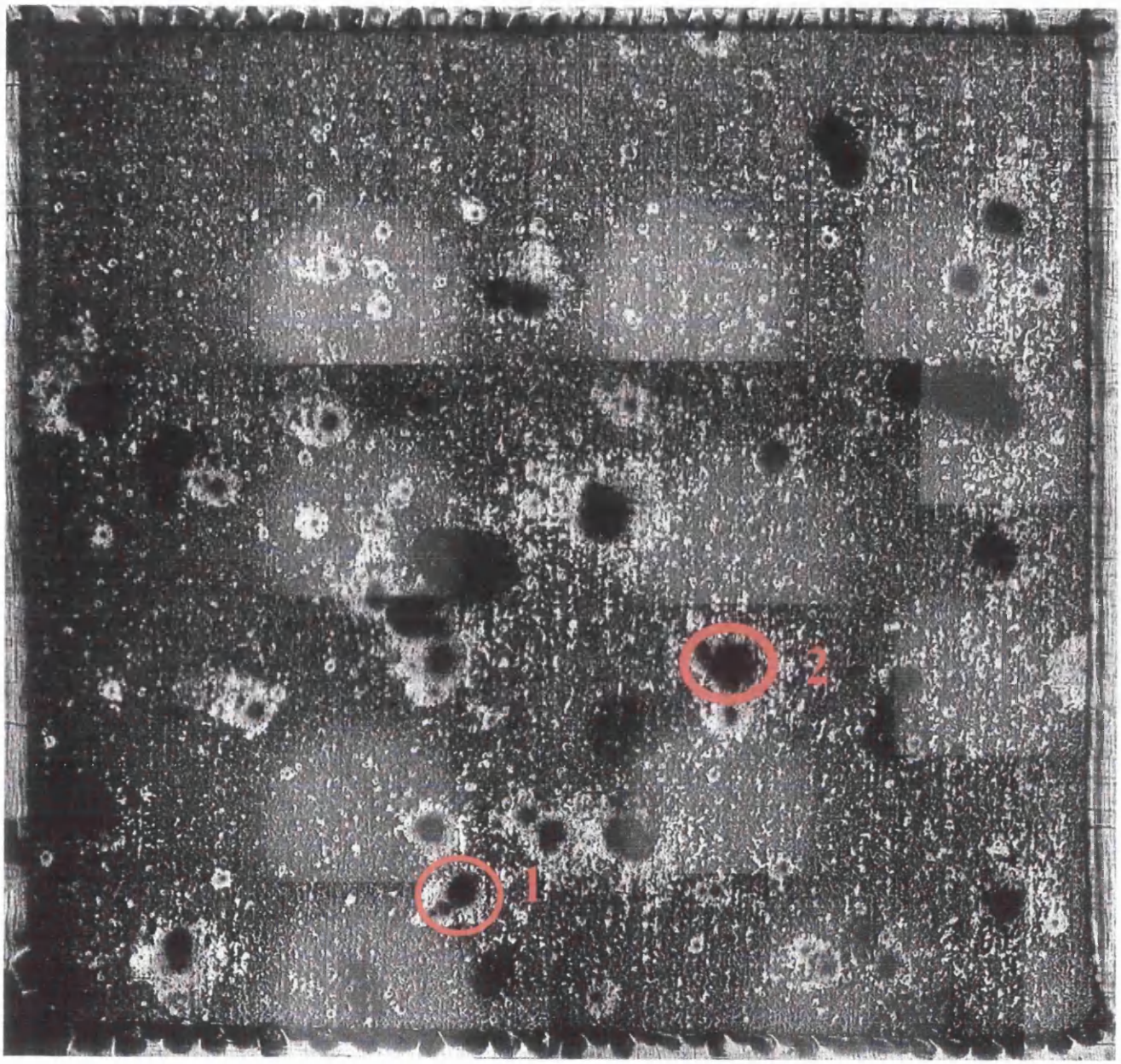

Figure 3.21: Inverted light source optical image of polished AA2024-T3 after 24 hours immersion in 3.5% NaCl.

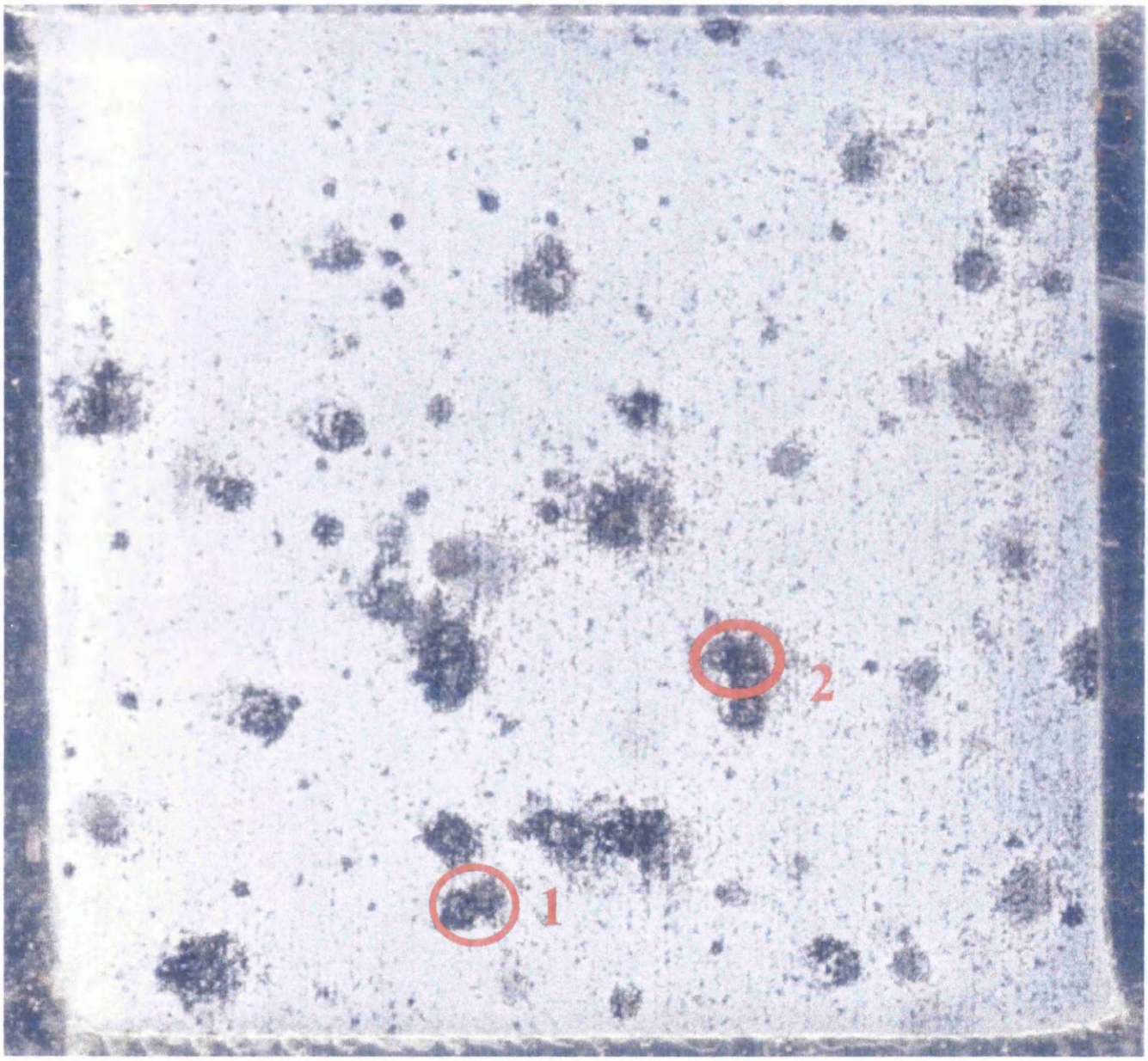

Figure 3.22: Scanned optical image of polished AA2024-T3 after 24 hours immersion in 3.5% NaCl, and then immersed in 3.5% v/v phosphoric acid (d 1.75) and 2.0% w/v Chromic acid for 10 min at 85^{0}C.

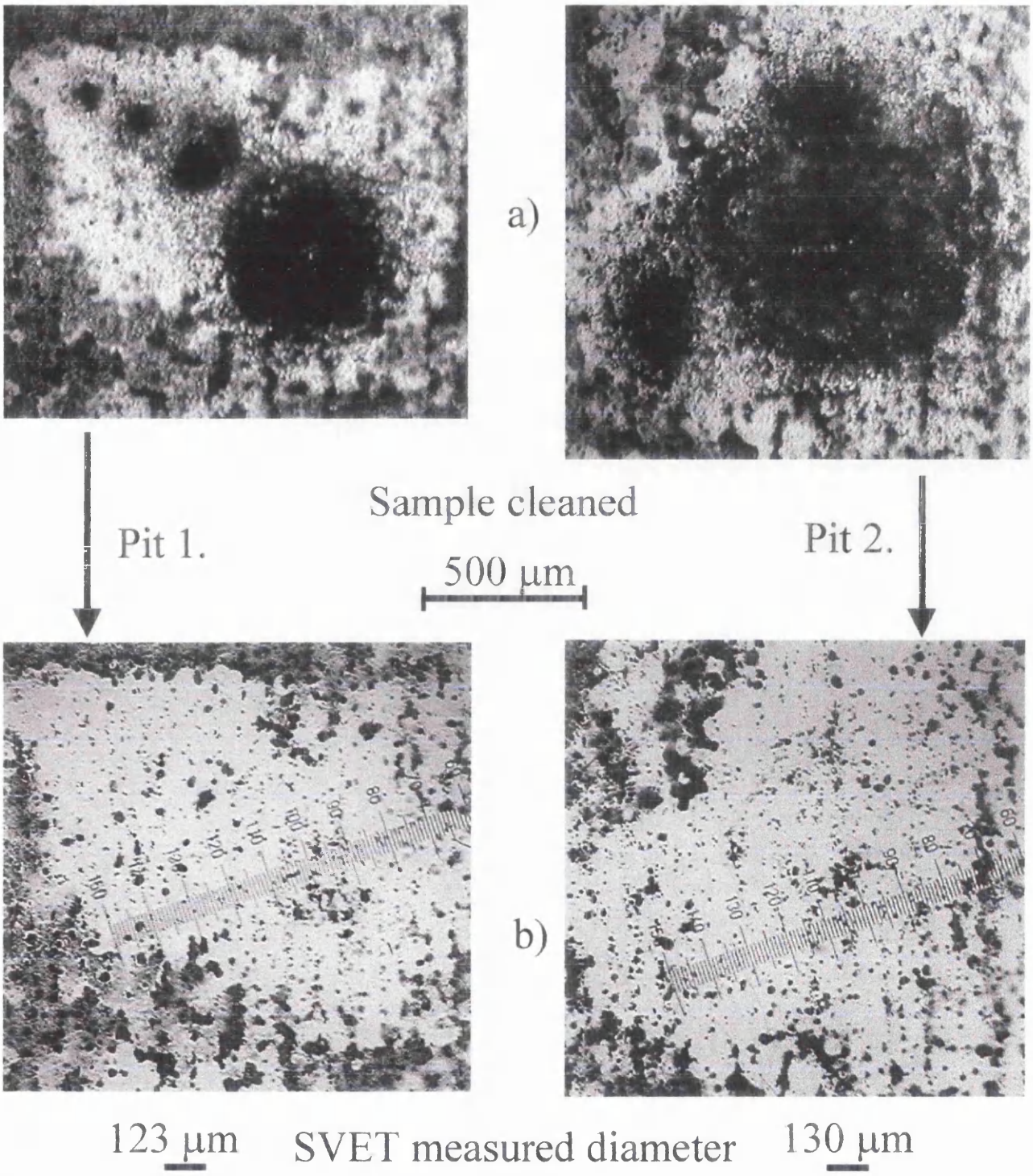

Figure 3.23: Inverted light source optical image of polished AA2024-T3 after a) 24 hours immersion in 3.5% NaCl, and b) after immersion in 3.5% v/v phosphoric acid (d 1.75) and 2.0% w/v Chromic acid for 10 min at 85^{0}C. For two small areas Pit 1 and Pit 2. Also shown is SVET diameter calculated from equation 3.4. Numbered as shown in figures 3.20-21.

smaller then the dark disks covering them after corrosion, also the pit openings are not one large opening but lots of small ones very close together. This finding poses the further question: whether these features consist of one large pit with lots of openings (lacy cap), or lots of small pits so close together the SVET can not spatially resolve them as shown schematically in figure 3.24.

To conclusively determine the nature of the pits it would be necessary to slice through the sample so as to cut the pit in half whilst not distorting the substrate material. Such an undertaking is non trivial and the equipment required to do this reliably was not available. However, figure 3.25 shows some high magnification SEM pictures taken in the same areas as pit 1 and 2 in figure 3.23. The angle of incidence was increased so that the edges of the pits could be seen. If no subsurface interconnection was visible between each of the small surface openings then a group of small pits would be the most likely hypothesis. However, if the small openings appear to open into a single cavity then the pit would seem to resemble the lacy cap. Figure 3.25b shows the same opening as figure 3.25a but the angle of incidence has been increased to 61^0. Figures 3.25b-d suggest that although individual surface openings are not isolated, as in figure 3.24b, they also do not connect with a single, geometrically simple, subsurface cavity, as in figure 3.24a. Rather, individual surface openings seem to be interconnected via a maze or gallery produced by subsurface metal excavation, as shown in figure 3.24c. Furthermore, the walls of the interconnecting galleries are not smooth but very rough, showing evidence of preferential phase dissolution or crystallographic etching. What is certain from the SEM pictures is that the pits produced by immersing AA2024-T3 in 3.5% w/w NaCl for over 10 hours are not hemispherical in nature.

a) Lacy cap.

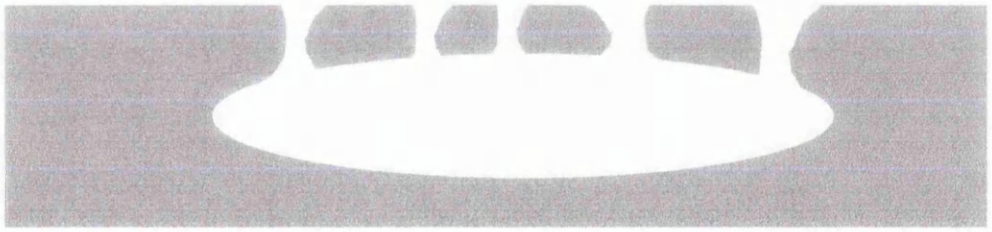

b) Group of small pits.

c) Galleried pit.

Figure 3.24: Diagrams showing possible shapes of pits produced by immersing AA2024-T3 in 3.5% w/w NaCl for over 10 hours, a) One 'large' pit with many small openings (lacy cap), b) group of small pits very close together, c) group of small pits connected via galleries.

a) 0 degree incidence.

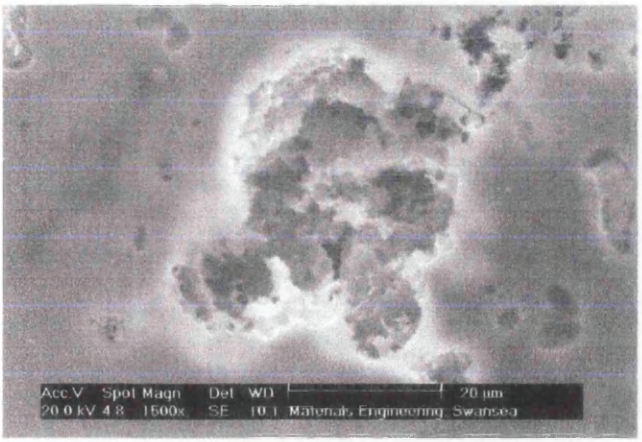

b) 61 degree incidence.

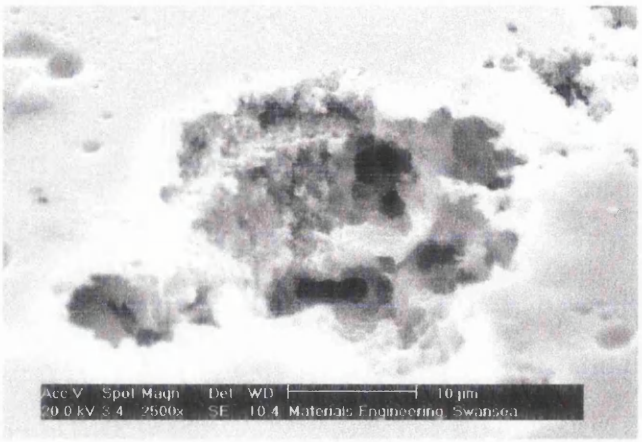

c) 45 degree incidence.

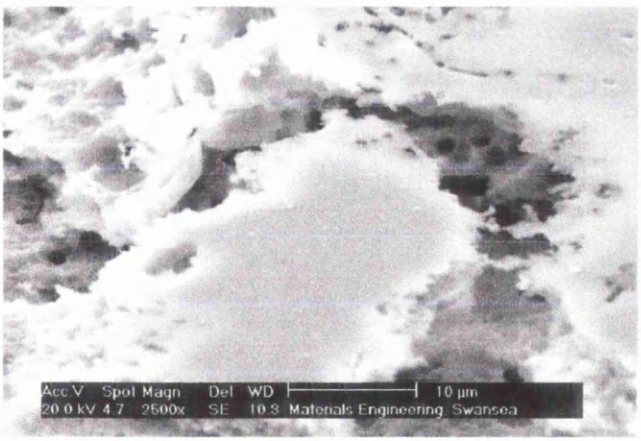

d) 71 degree incidence

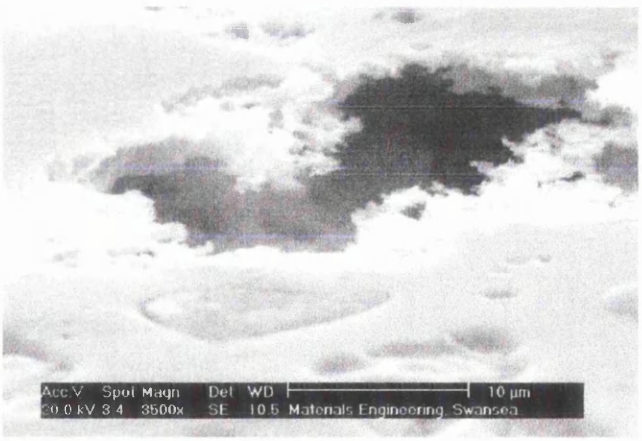

Figure 3.25: High magnification SEM images of Pits 1 and 2 at various angles of incidence.

3.4: Conclusions.

It has been shown that current density data obtained using SVET corresponds closely to optical images of the corroded surface, in terms of number and location of anodic pits. Anodic activity in the SVET data coincide with areas of metal loss and corrosion product deposition on the surface after corrosion. By using a 'thresholded' numerical integral of the SVET current density data, a series of instantaneous values for the area averaged anodic current density were obtained, which may be used to quantify the rate of pitting corrosion of AA2024-T3 in 3.5% w/w NaCl in terms of average metal loss over the exposed area.

The characteristics of pit population were also determined, firstly by determining how pit density varies over experimental period, then by determining how theoretical pit diameter varies with time of immersion (calculated from localised metal loss). High resolution images of a cleaned post corrosion surface were used to determine the accuracy of pit diameters calculated using SVET data. By so doing it has been determined that surface pitting corrosion of AA2024-T3 in 3.5% w/w NaCl is not hemispherical in nature, and in fact more resembles a network of tunnels.

3.5: Reference:

[1] V. Guillaumin and G. Mankowski, *Corrosion Science*, **41**, 421 (1999).
[2] M. C. Reboul, T. J. Warner, H. Mayet and B. Baroux, *Materials Science Forum*, **217**, 1553 (1996).
[3] P. Campestrini, E. P. M. van Westing, H. W. van Rooijen and J. H. W. de Wit. *Corrosion Science*, **42**, 1853 (2000).
[4] N. R. Cawley and D. G. Harlow, *Journal of Materials Science*, **31**, 5127 (1996).

Chapter 4.

Chapter 4: Investigation into how precipitate distribution affects pitting corrosion of AA2024-T351 using (SVET).

4.1: Introduction.

It is thought that large intermetallic particles precipitated within the aluminium matrix may accelerate pitting corrosion of AA2024[1]. The shape, size and chemical composition of these precipitates are determined by the heat treatment and forming carried out on the alloy[2]. There are two principle types of precipitates that occur in AA2024. The first of these comprise of Al-Cu-Mg particles, which tend to be anodic relative to the matrix. The second comprise of Al-Cu-Mn-Fe-Si particles, which tend to act as cathodic sites relative to the aluminium matrix[3]. Aluminium alloys containing larger amounts of copper have been found to be more susceptible to pitting corrosion than others[4]. It is widely thought that the Al_2CuMg (S phase) intermetallic particles are responsible for the majority of pitting corrosion in AA2024[5,6]. However, the exact mechanisms underlying this phenomenon are not yet understood, and are still the subject of research. Here it has been our aim to determine the number density and distribution of precipitate particles on the surface using SEM back-scatter imaging. How this number density and distribution affects the pitting corrosion characteristics of AA2024-T351 was investigated using a quantitative SVET as described in chapter 3. A comparison was also made of the corrosion characteristics of AA2024-T351 and AA2024-T3.

4.2: Experimental.

4.2.1: Materials.

Two cube samples of AA2024-T351 as described in section 2.7 were used. One was kept in the form of a cube, so that the side and end could be scanned using the SVET. The other was cut into seven slices from top to bottom, so that SVET scans could be carried out for different depths through the cube. A schematic diagram can be seen in figure 4.1. The top surface, end and side of the AA2024-T3 sample was scanned for comparison. All samples were prepared following the sequence in figure 4.2. The surface to be corroded was ground using increasingly fine grades of silica paper (400, 800, 1200 and 1600) to remove any surface scratches. The surface was then polished to a mirror finish, first using 6μm diamond paste on a rotating polishing disk, and finished with 1μm diamond paste on a rotating polishing disk. The sample surface was cleaned using a non-ionic surfactant between each stage of polishing. Following polishing the sample was immersed in Methyl Ethyl Ketone (MEK) for 10 mins to remove surface grease. The sample area for SVET investigation (see section 4.2.2 for the area for each type of surface) was isolated from the rest of the sample using PTFE insulation tape obtained from 3M Ltd. The only part of the sample left un-coated was the area to be scanned, as shown in figure 4.2d.

All other materials were purchased from Aldrich in their highest purity and all solutions were prepared in distilled water.

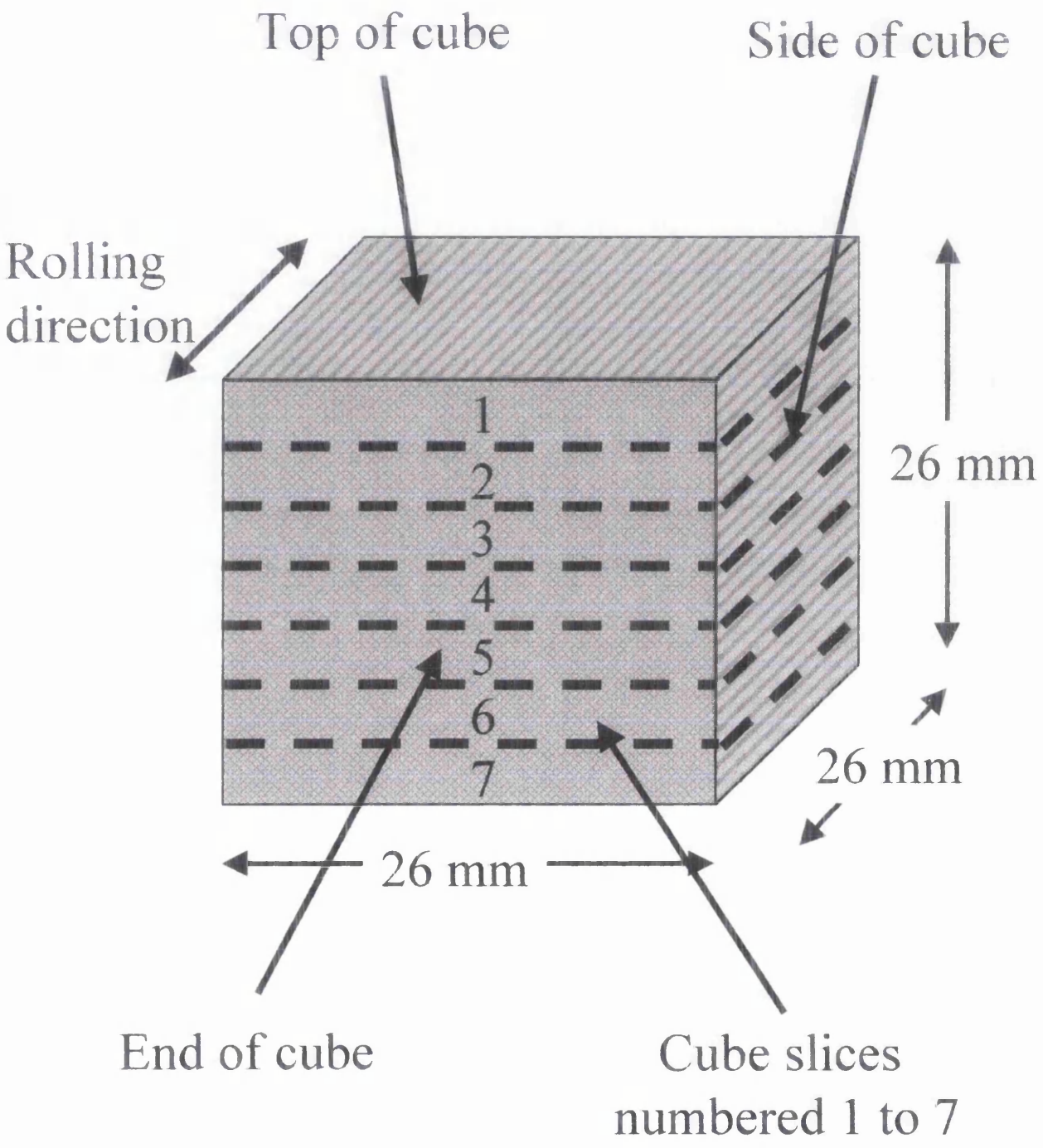

Figure 4.1: Schematic diagram showing AA2024-T351 cube sample with different surfaces and cube slices labeled.

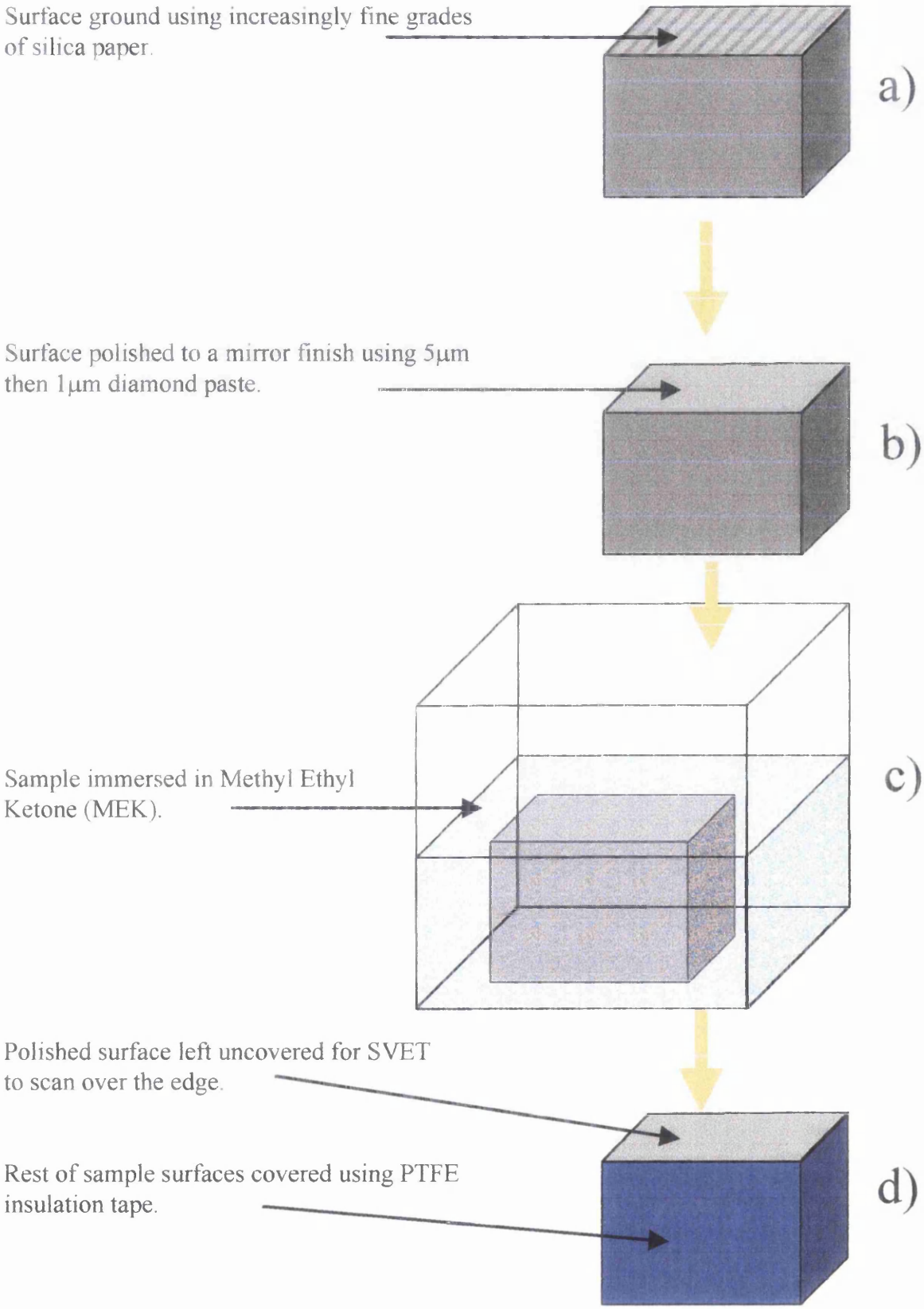

Figure 4.2: Schematic diagram showing preparation of AA2024-T351, and AA2024-T3 sample surface prior to SVET corrosion experiments.

4.2.2: Methods.

SVET:

The methods used for this study were as described in section 3.2.2 with the following adjustments.

The scan area for the side and end of the 2024-T351 cube scans was typically 25 mm x 25 mm, the data matrix generated was 100 x 100 points and total scan time was 80 minutes. The samples were scanned using SVET immediately on immersion and at 80 minute intervals thereafter for a period of 24 hours.

For the top of 2024-T351 cube slices and 2024-T3 top surface (see section 2.7) experiments the scan area was typically 20 mm x 20 mm, the matrix generated was 80 x 80 points and total scan time was 40 minutes. The 2024-T3 thin plate samples end and side (as shown in figure 4.3) experiments scan area was typically 3 mm x 30 mm, the matrix generated was ~ 15 x 140 points and total scan time was 15 minutes. The samples were scanned using SVET immediately on immersion and at hourly intervals thereafter for a period of 24 hours.

Each SVET measurement was made with the probe stationary, and was an average of ten measurements.

Optical microscopy:

On completion of the SVET experiment the sample was rinsed in distilled water to stop corrosion, then air dried before the optical pictures were taken. Optical pictures were taken using the scanner, and angled digital photographs as described in section 2.6.

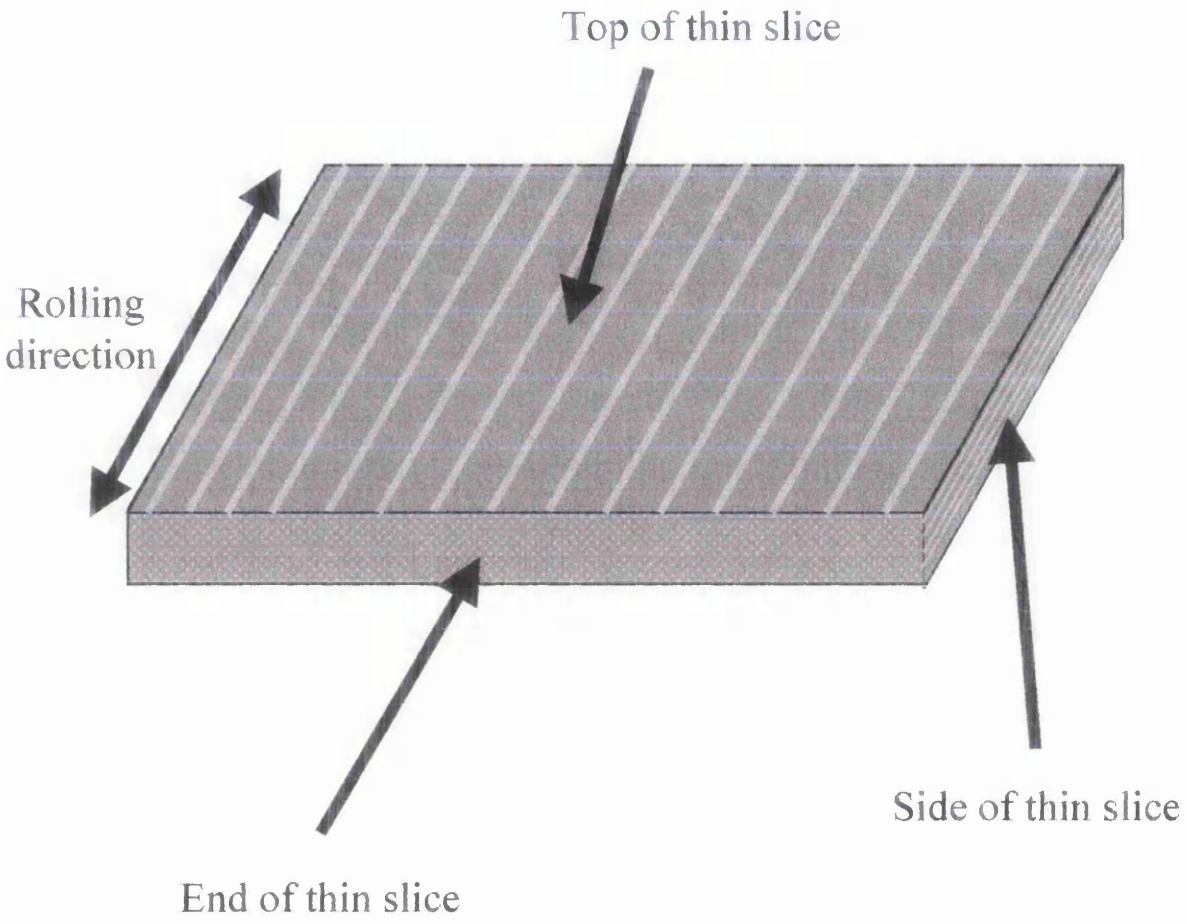

Figure 4.3: Schematic diagram showing AA2024-T3 thin slice sample with different surfaces labeled.

Electron microscopy:

After the side of the AA2024-T351 cube sample was polished to 1μm it was placed in the SEM described in section 2.3. The aim was to determine the distribution of precipitate particles from the top to the bottom of the cube sample side. This was done using the back-scatter mode at the highest possible contrast, as described in section 2.3, so the precipitates show up as white on a black background. Firstly, the sample was lined up so that the top edge of the cube could be seen, then six micrographs were recorded along the edge between X = 0 mm and X = 1 mm. A schematic diagram can be seen in figure 4.4. Then six micrographs were recorded between X = 1 mm and X = 2 mm. This was repeated until the centre of the cube was reached (it had previously been determined using a travelling optical microscope that the precipitate particle distribution was approximately symmetrical round the top-bottom mid line). Once the back-scatter images were recorded it was necessary to determine the area of precipitates on the micrographs. This was carried out using the Graftek, Optilab Pro image analysis package. A contrast threshold was set so that the white precipitates were distinguished from the black matrix. Then, using the 'particle count' function, the fractional area of precipitates was recorded for each micrograph, and the average of six micrographs was determined for each X co-ordinate.

To discriminate between Al-Cu-Mg and Al-Cu-Mn-Fe-Si particles the polished surface was then characterised using a combination of EDX described in section 2.3, and high resolution SEM. The Oxford Link Isis, spot chemical analysis was used to chemically identify individual particles visible in the micrographs. To determine the fractional area ratio of the two precipitate types, the micrographs were printed onto thick paper then each particle image was cut out using scissors. All the

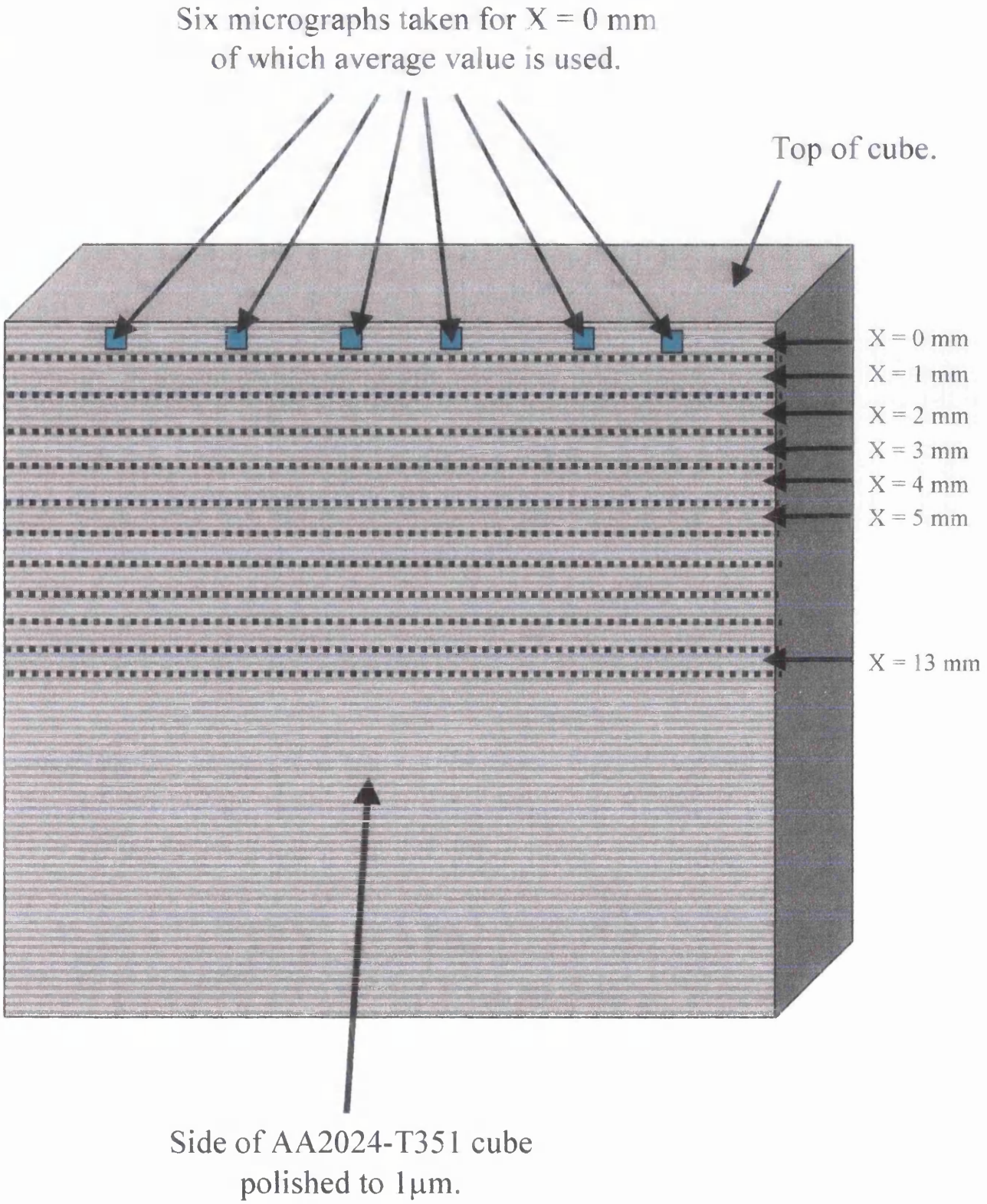

Figure 4.4: Schematic diagram showing methodology in determining distribution of precipitates on the side and end surface of AA2024-T351.

Al-Cu-Mg particles and Al-Cu-Mn-Fe-Si particle images were weighed on an analytical balance and the ratio determined.

This process was then repeated for the cube end.

4.3: Results and Discussion.

4.3.1: Distribution of precipitates on AA2024-T351 cube surfaces.

As described in section 4.2.1 the AA2024-T351 sample was in the form of a 26mm x 26 mm x 26 mm cube. Figure 4.1 shows a schematic diagram of the cube, the 'top' surface of the cube would correspond to the surfaces used in previous experiments (see chapter 3) on the AA2024-T3 samples. On this surface the precipitates are evenly distributed. However, on the surfaces labelled 'side' and 'end' in figure 4.1 the precipitates are not evenly distributed but concentrated at the top and bottom of the cube. Figure 4.5 shows examples of the SEM back-scatter images recorded at a distance of 0, 7 and 13 mm from the top of the cube. Figure 4.6 shows how the fraction of sample surface (%) composed of intermetallic precipitates, as determined using SEM back-scatter, varies with distance from the top of the AA2024-T351 cube for the 'side' surface (blue diamond symbol) and the 'end' surface (red triangle symbol). The precipitate area values for the 'end' surface are much smaller than for the side surface. Figure 4.7 shows that this is because the precipitates are drawn out (stretched) along the side surface during rolling, so a larger area of the precipitate is visible from the side and top angles then from the end.

It is widely thought that the corrosion characteristics of AA2024 are mostly influenced by the Al-Cu-Mg particles rather then the Al-Cu-Mn-Fe-Si particles. For this reason it was necessary to determine the ratio of these particles, as described in section 4.2.2. Figure 4.8 illustrates example SEM pictures of the side surface. It

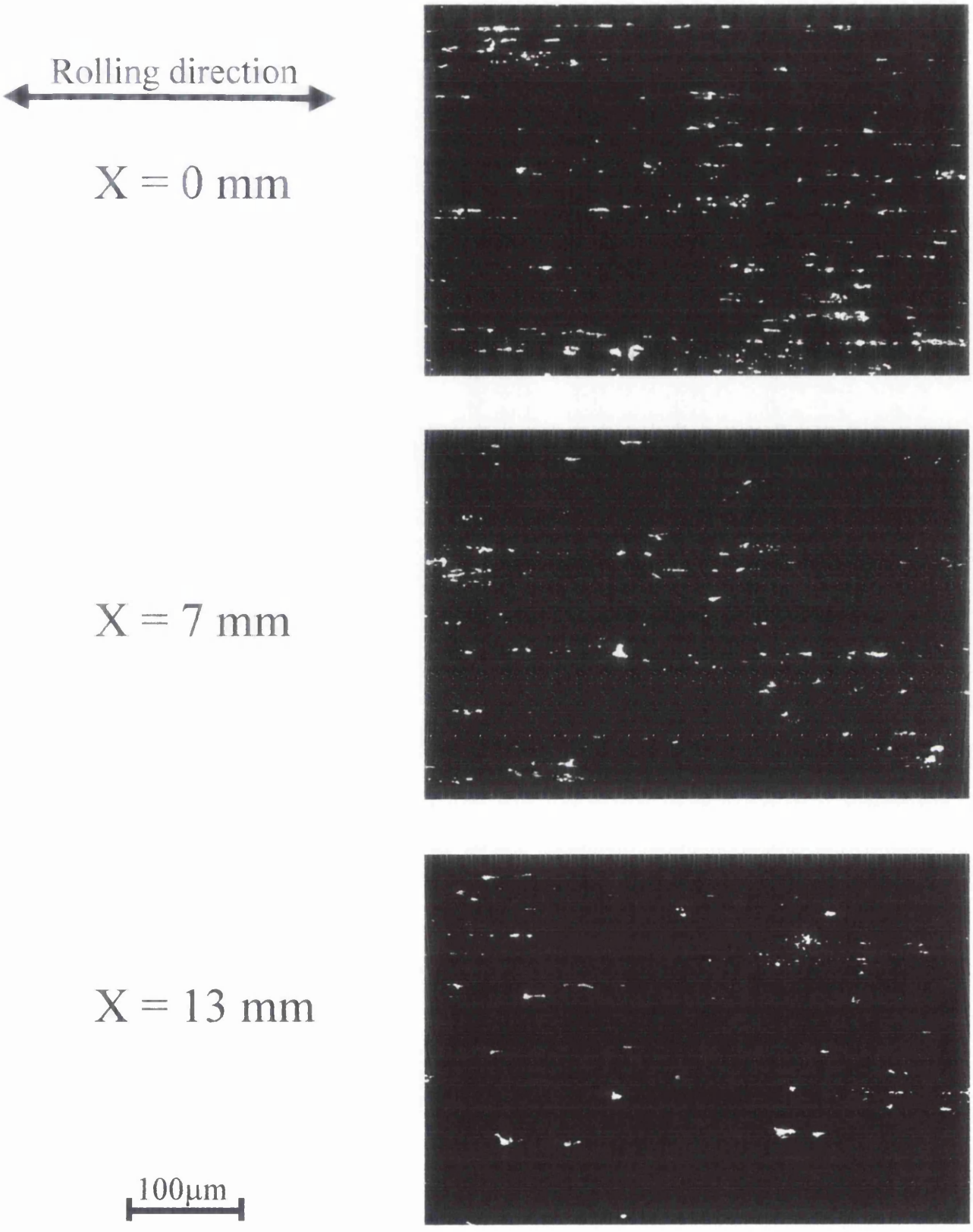

Figure 4.5: Examples of back-scatter micrographs from SEM for the side surface of AA2024-T351. The aluminium matrix appears black, and the transition metal containing intermetallics white.

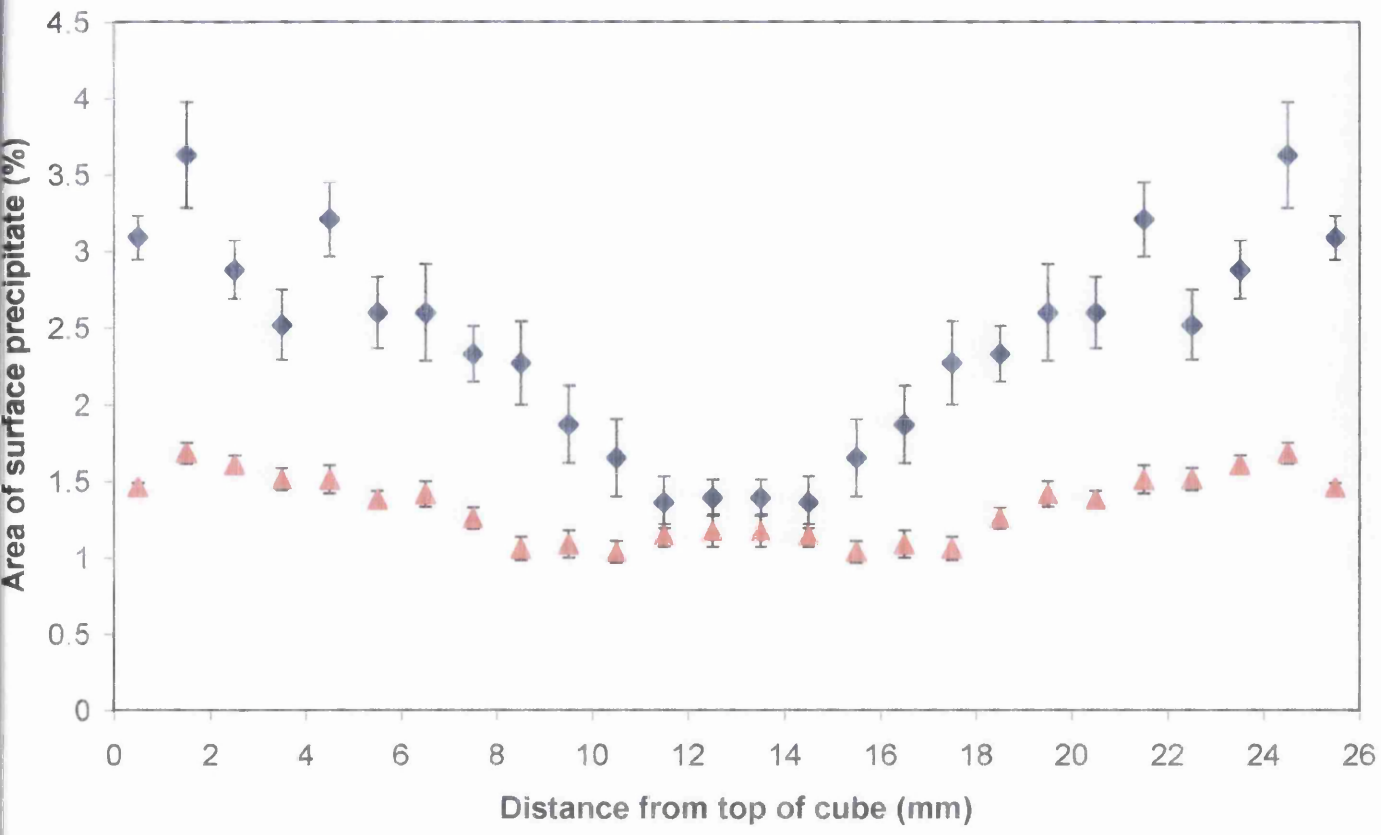

Figure 4.6: Graph showing how the percentage of the surface that is precipitates varies with distance from the top of the cube. ◆ = cube side, ▲ = cube end, error bars show ± standard deviation.

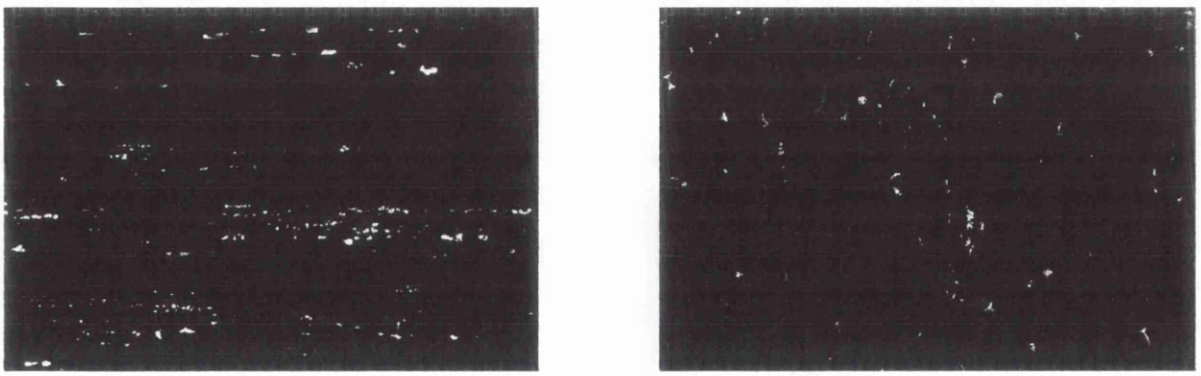

a) b)

Figure 4.7: Examples of back-scatter micrographs from SEM for the a) side surface and b) end surface of AA2024-T351 11 mm from top of cube.

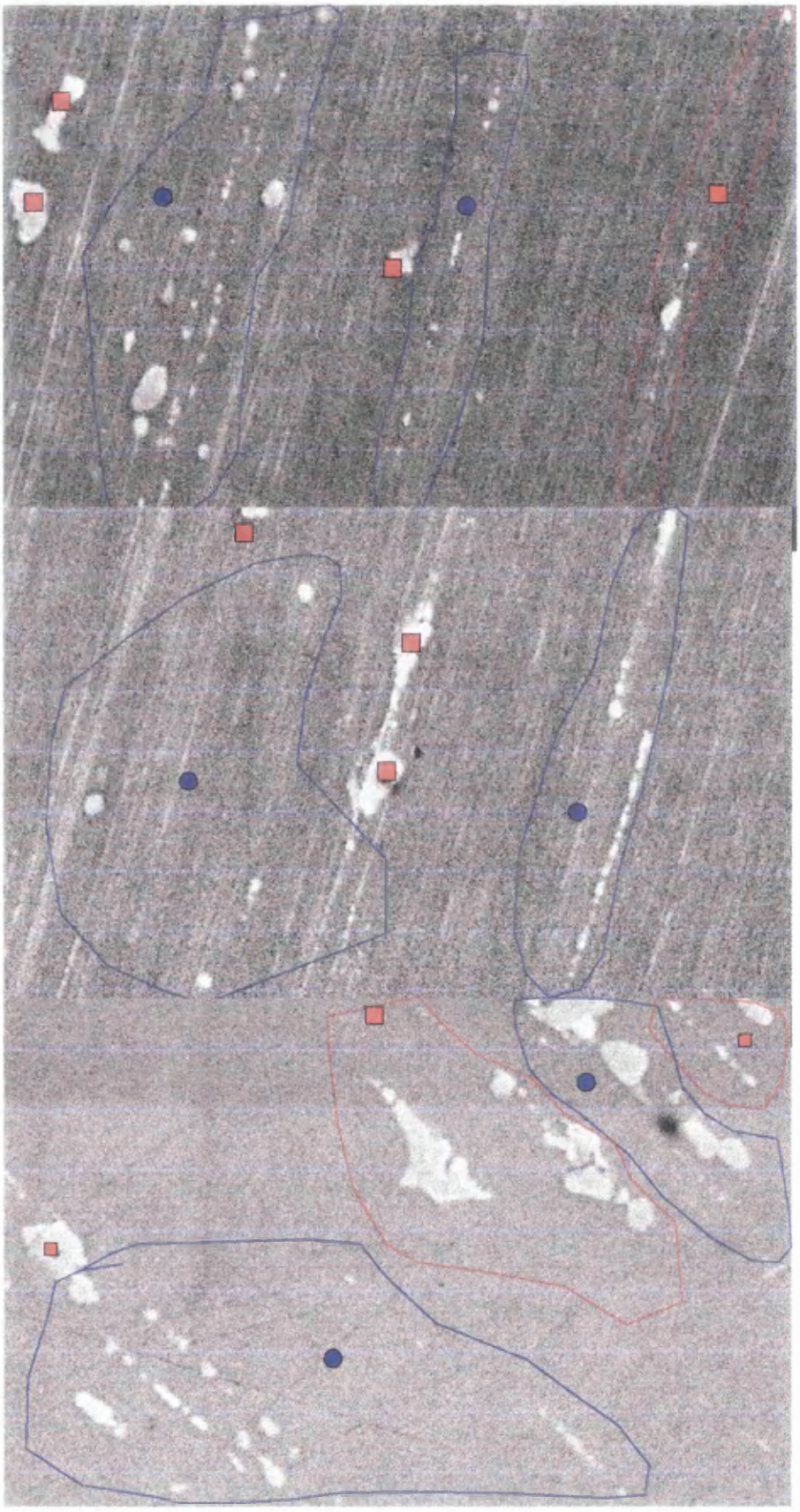

Figure 4.8: High resolution SEM pictures to determine the ratio of Al-Cu-Mg (● symbol) to Al-Cu-Mn-Fe-Si (■ symbol) precipitates on the side surface of AA2024-T351.

shows the two types of precipitates marked with red squares (Al-Cu-Mn-Fe-Si) or blue circles (Al-Cu-Mg). This was also carried out for the end surface of the cube. It was thus determined that approximately the same fractional surface area may be attributed to each type of precipitate on both the side and end surface.

4.3.2: Current distribution on corroding AA2024-T351 cube side and end.

To determine how particle distribution influences pitting corrosion of AA2024 it is necessary to investigate distribution of pitting corrosion on the surface. Figure 4.9 shows false colour maps of the SVET data, as described in section 3.3.1, obtained from an experiment of the cube side as described in section 4.2.2. This figure illustrates that most of the anodic current (yellow), and therefore pitting, is concentrated in the centre of the surface throughout the experiment. Figure 4.10 shows plots corresponding to the false colour maps in figure 4.9. Each point corresponds to the average current density value along the y-axis for each x co-ordinate. This demonstrates that the majority of pitting occurs in the centre of the surface, a position which coincides with the minimum density of intermetallic particle distribution shown in figure 4.6. Figure 4.11 is optical micrographs of the surface of the cube side after 24 hours immersion in 3.5% NaCl. Figure 4.11a shows that a contour plot generated from summated SVET data corresponds very closely with the pitted areas on the surface. Figure 4.11b shows the same surface however the micrograph was taken at a angle to the surface, this was so the colour of the surface was clearer. As can be seen the centre of the surface is covered with the dark disk like features described in section 4.3.6, and the rest of the surface is 'copper' in colour. However, unlike the surfaces in section 4.3.6 the two types of areas are

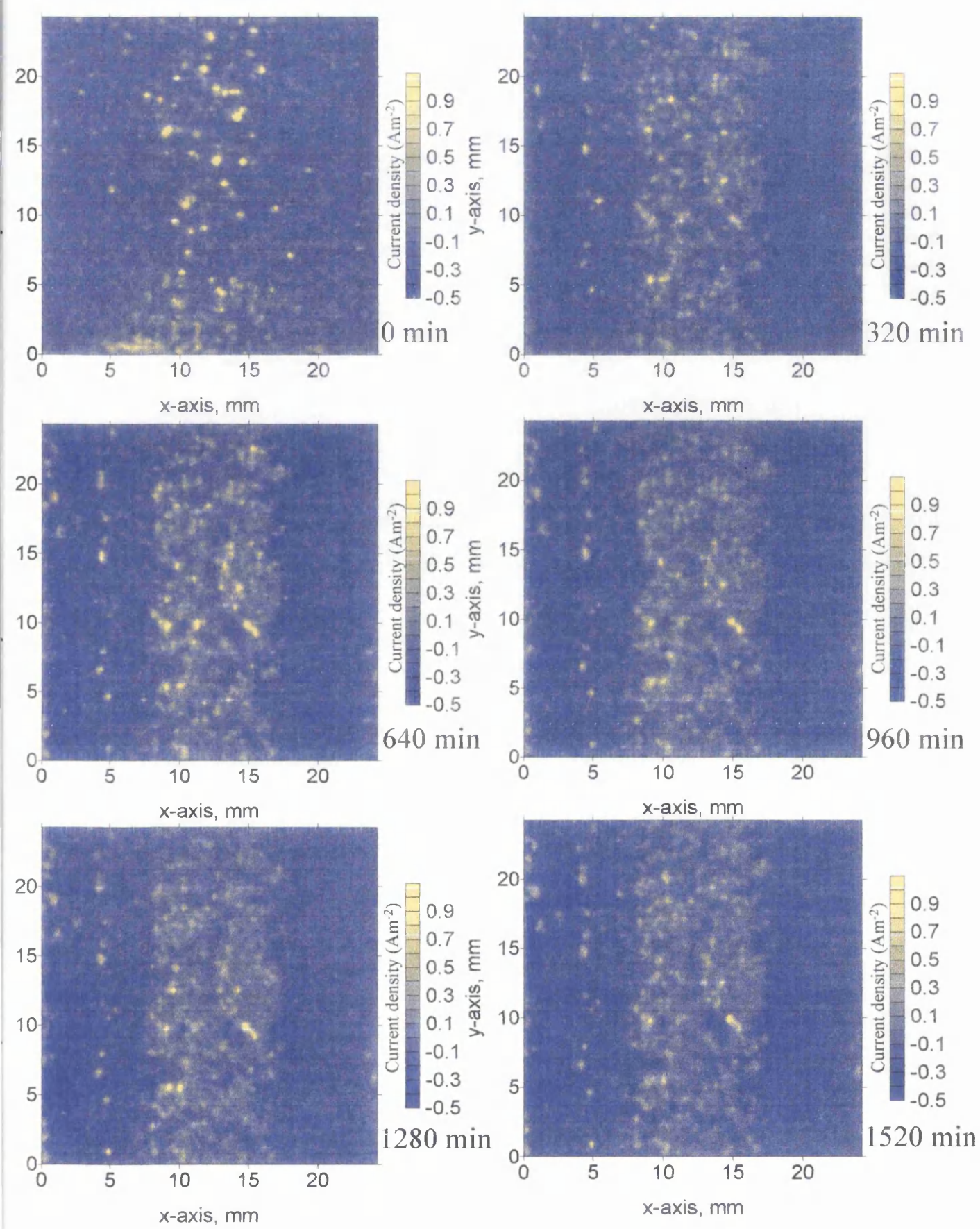

Figure 4.9: SVET contour plots for AA2024-T351 cube side, polished to 1μm then immersed in 3.5% w/w NaCl for 24 hours at 25^{0}C. The time indicated is time since sample immersion.

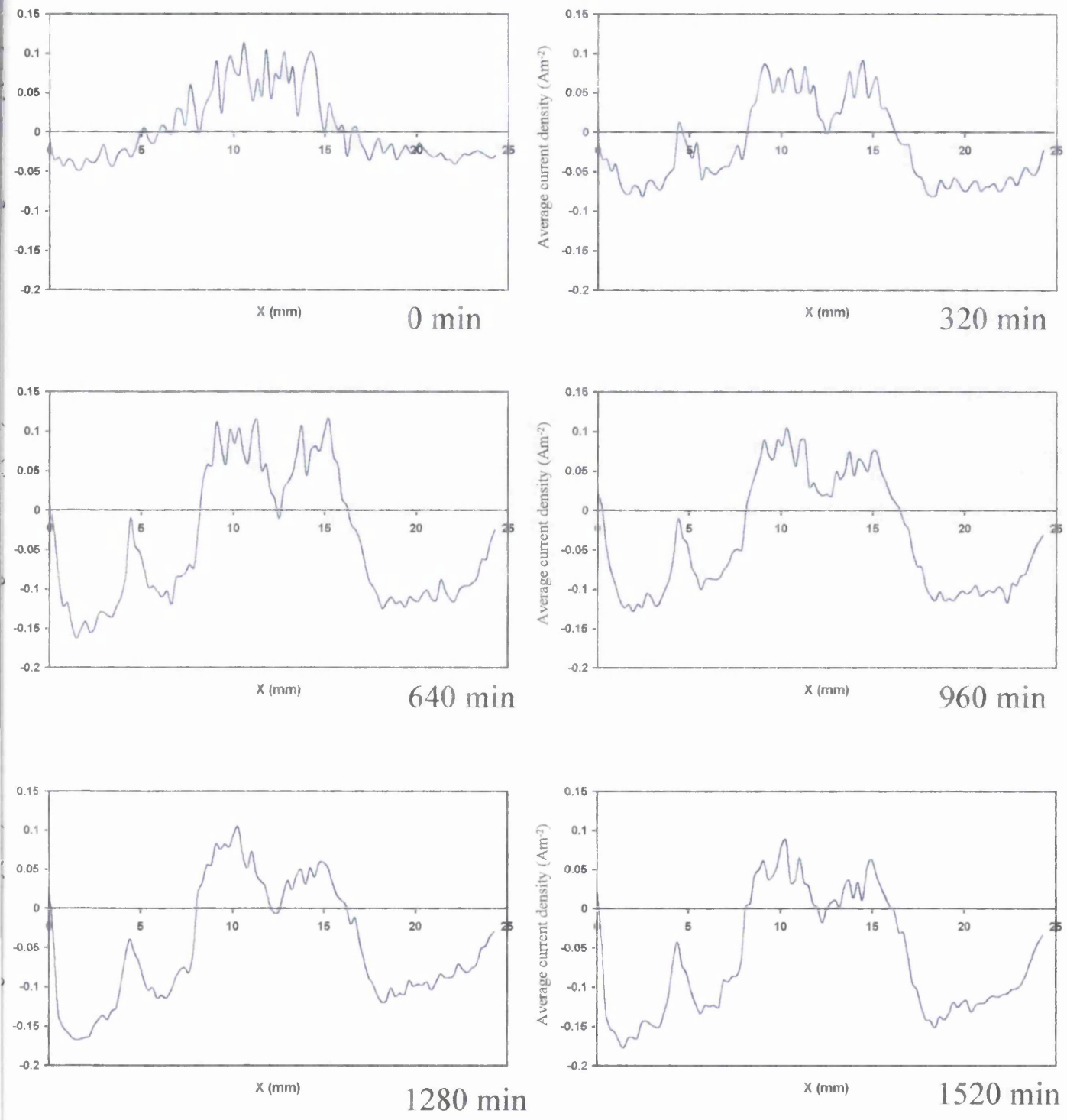

Figure 4.10: Graphs showing how average current density varies along *x*-axis of AA2024-T351 cube side, polished to 1μm then immersed in 3.5% w/w NaCl for 24 hours at 25^{0}C. The time indicated is time since sample immersion.

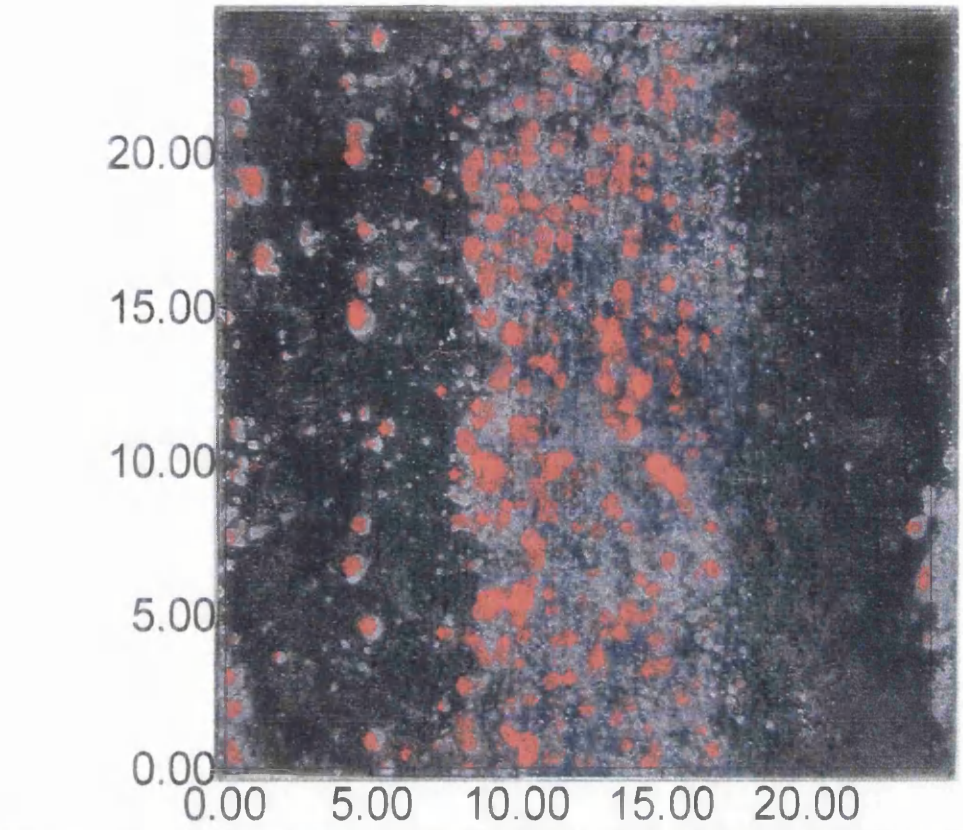

a)

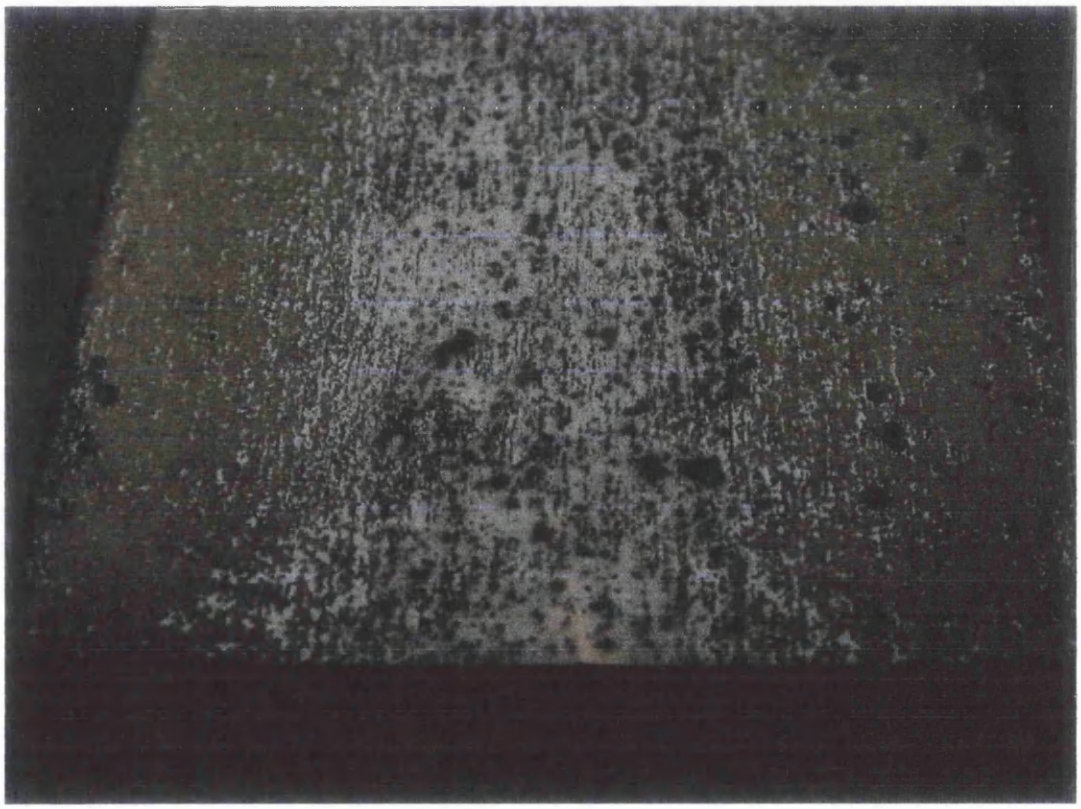

b)

Figure 4.11: Optical micrographs of cube side a) From above with summated SVET contour plots overlaid (red), b) Angled to show colouring. After 24 hours immersion in 3.5% w/w NaCl at 25^0C.

distinctly separate. The experiments carried out on the cube end yield very similar results to the cube side.

4.3.3: Distribution of corrosion on AA2024-T351 cube slices.

Section 4.3.2 describes how a non uniform particle distribution influences pitting corrosion on AA2024-T351. This section using the cube slices as described in section 4.2.1 determines how particle density influences pitting corrosion. SVET experiments were carried out as described in section 4.2.2 on each of the cube slices. Figure 4.12 shows example false colour plots of the SVET data obtained from slice 1. It demonstrates that pitting corrosion on the surface is much more uniform than for the cube side seen in figure 4.9, and greatly resembles the type of plot shown in section 3.3.1 for AA2024-T3. The same experiment was carried out on all seven cube slices, and the anodic current density was determined for each hour using equation 3.1 with a threshold of 0.2 Am^{-2}. Figure 4.13 shows how the current density varies with time of immersion for each cube slice. The slice distance from the top was estimated by measuring the thickness of each slice, and assuming the amount of metal removed between each slice in the cutting process was the same. Figure 4.14 shows how total aluminium loss varies with distance from the top of the cube. This was determined using equation 3.3 whilst making the same assumptions. It shows that there is a reduction in total metal loss towards the centre of the cube. From the top of the cube to the centre, the total metal loss has more then halved from ~ 0.07gm^{-2} to ~ 0.03gm^{-2}. From figure 4.15 which shows how total aluminium loss varies with area of surface precipitates, it can be seen that the reduction in pitting corrosion can be correlated with the reduction in precipitate surface area. It can also be seen that by reducing the

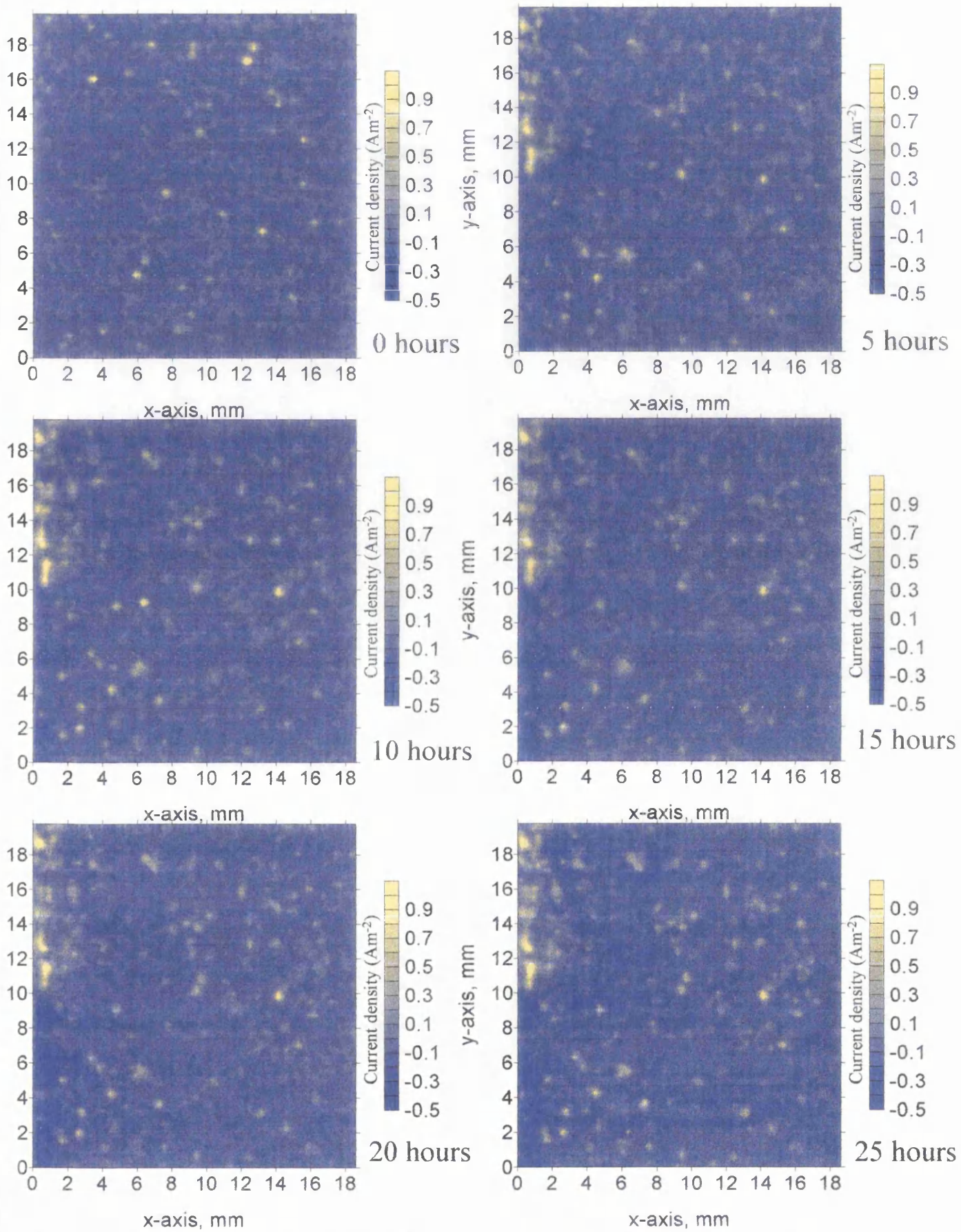

Figure 4.12: SVET contour plots for AA2024-T351 cube slice 1, polished to 1μm then immersed in 3.5% w/w NaCl for 24 hours at 25^{0}C.

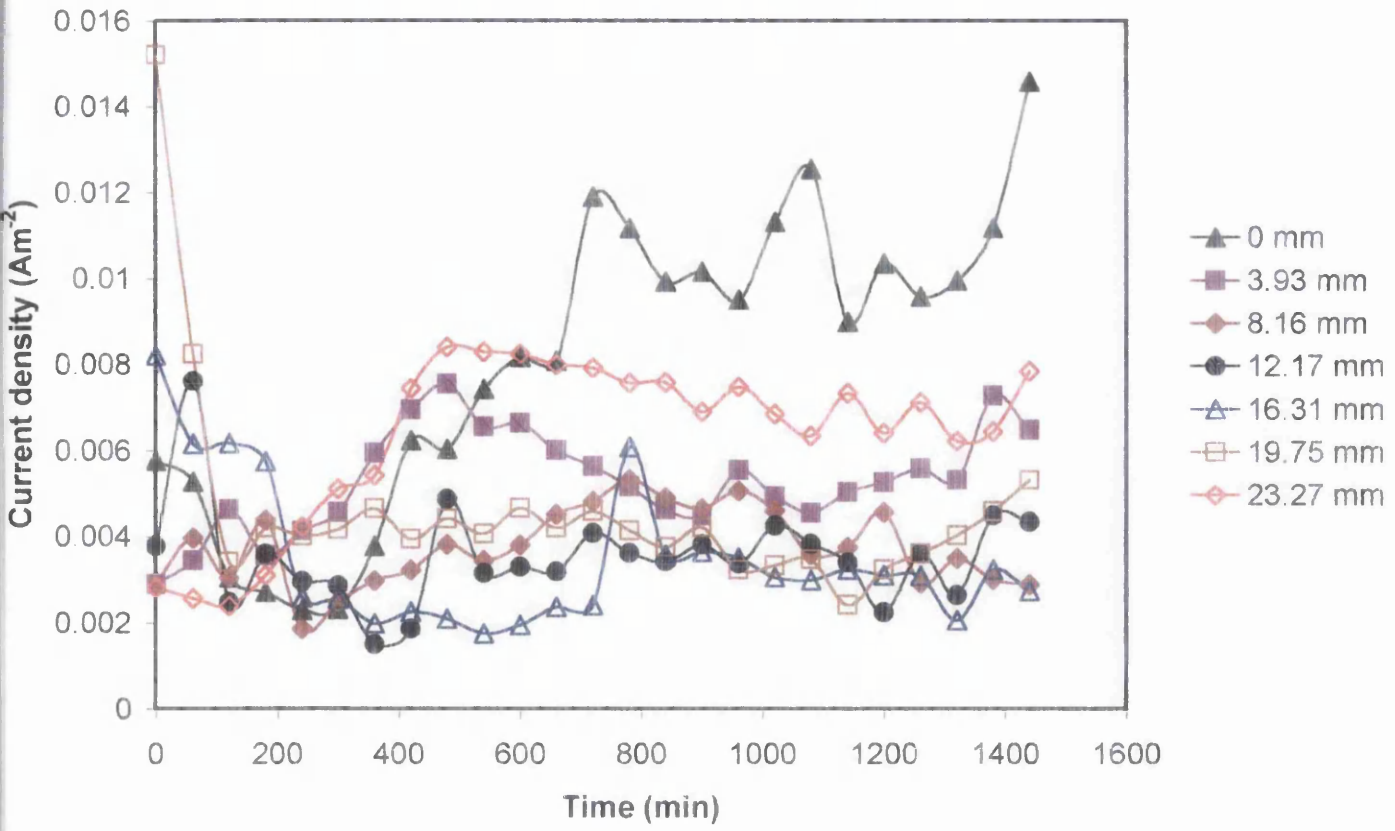

Figure 4.13: Plot showing how current density varies with time of immersion in 3.5% w/w NaCl at 25^{0}C. For varying depths from the top of the AA2024-T351 cube.

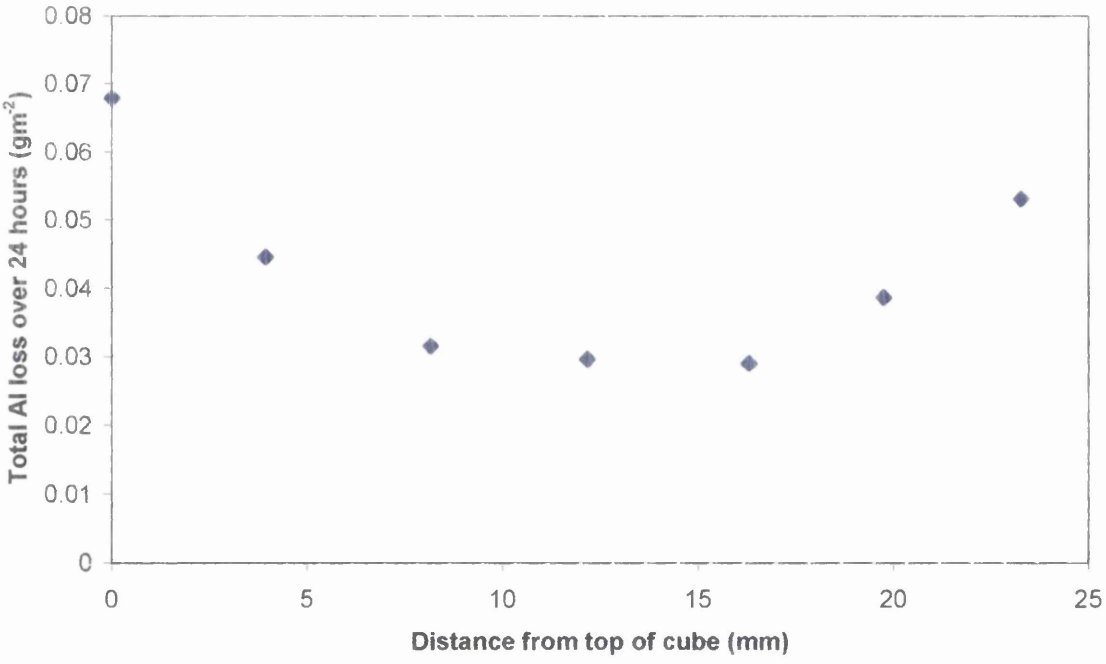

Figure 4.14: Plot showing how total aluminium loss varies with distance from top of AA2024-T351 cube after 24 hours immersion in 3.5% w/w NaCl at 25^{0}C.

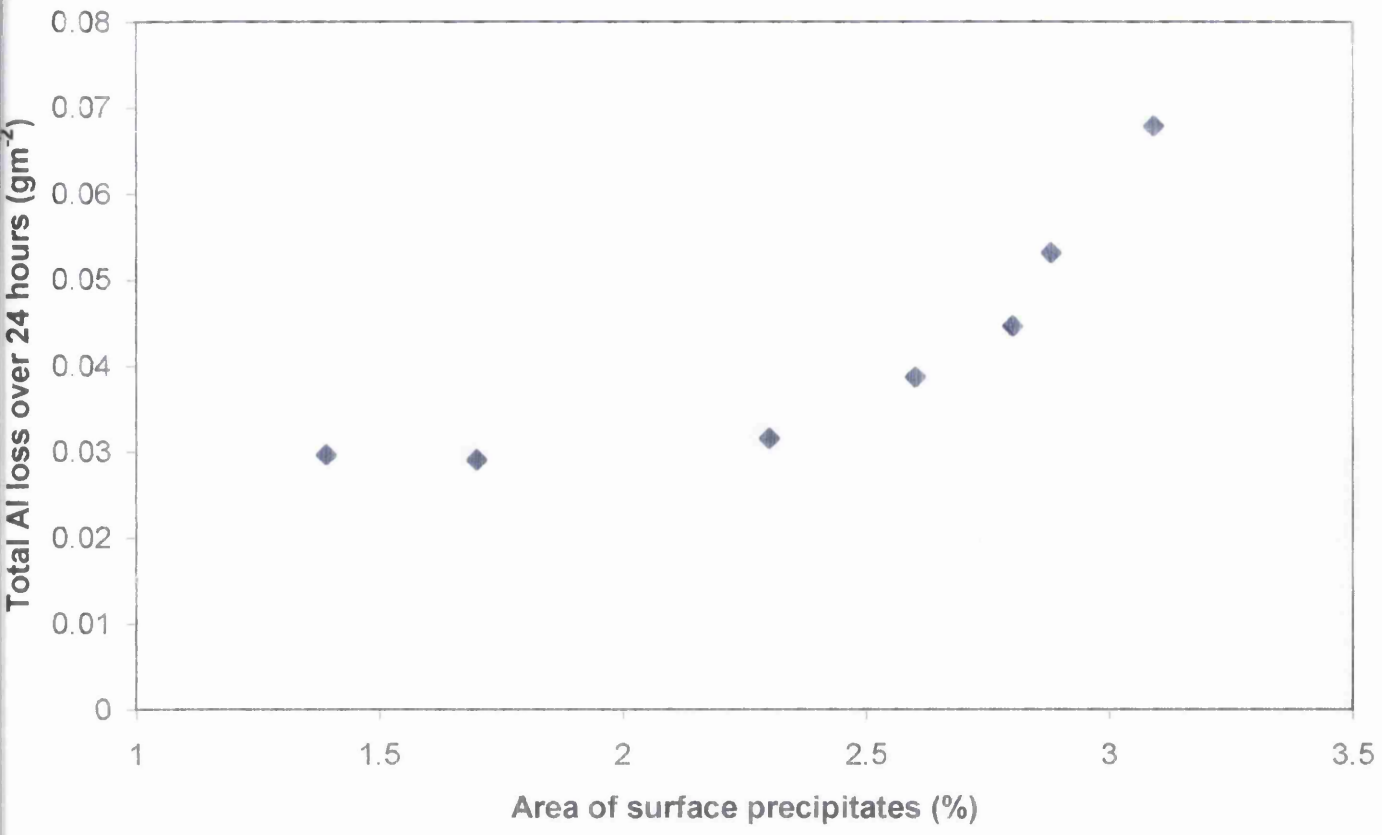

Figure 4.15: Plot showing how total aluminium loss varies with area of surface precipitates (%) for AA2024-T351 cube slices after 24 hours immersion in 3.5% w/w NaCl at 25^0C.

precipitate surface area by half (from ~ 3% to ~ 1.5%) the resulting pitting corrosion is reduced by half.

4.3.4: Comparing sample AA2024-T351 with AA2024-T3.

For comparison experiments were carried out on the end and side of the AA2024-T3 plate samples described in section 3.2.1. Figure 4.16 shows false colour plots from the SVET data obtained from the end of the plate. As can be seen the pitting corrosion seems to be a lot more random than in the case of the AA2024-T351 cube. This is supported by figure 4.17 showing graphs of the same kind as figure 4.10. It can be seen that there is no correlation between distance from the top of the sample and anodic activity. However, figure 4.18 shows how current density varies with time of immersion for all three surfaces (top, end and side) of both the AA2024-T351 cube and AA2024-T3 plate. As can be seen for both the plate and the cube the top surface is by far the most active, and the sides are slightly more active then the ends. It can also be seen that all three surfaces of the AA2024-T3 plate are much more active then the surfaces of the AA2024-T351 cube. Figure 4.19 shows the total aluminium loss for each of the six experiments in figure 4.18. From figure 4.19 it can be seen more clearly that all three sides of the thin slice sample were more active (losing ~ 3 times more aluminium) then the corresponding surface on the cube sample.

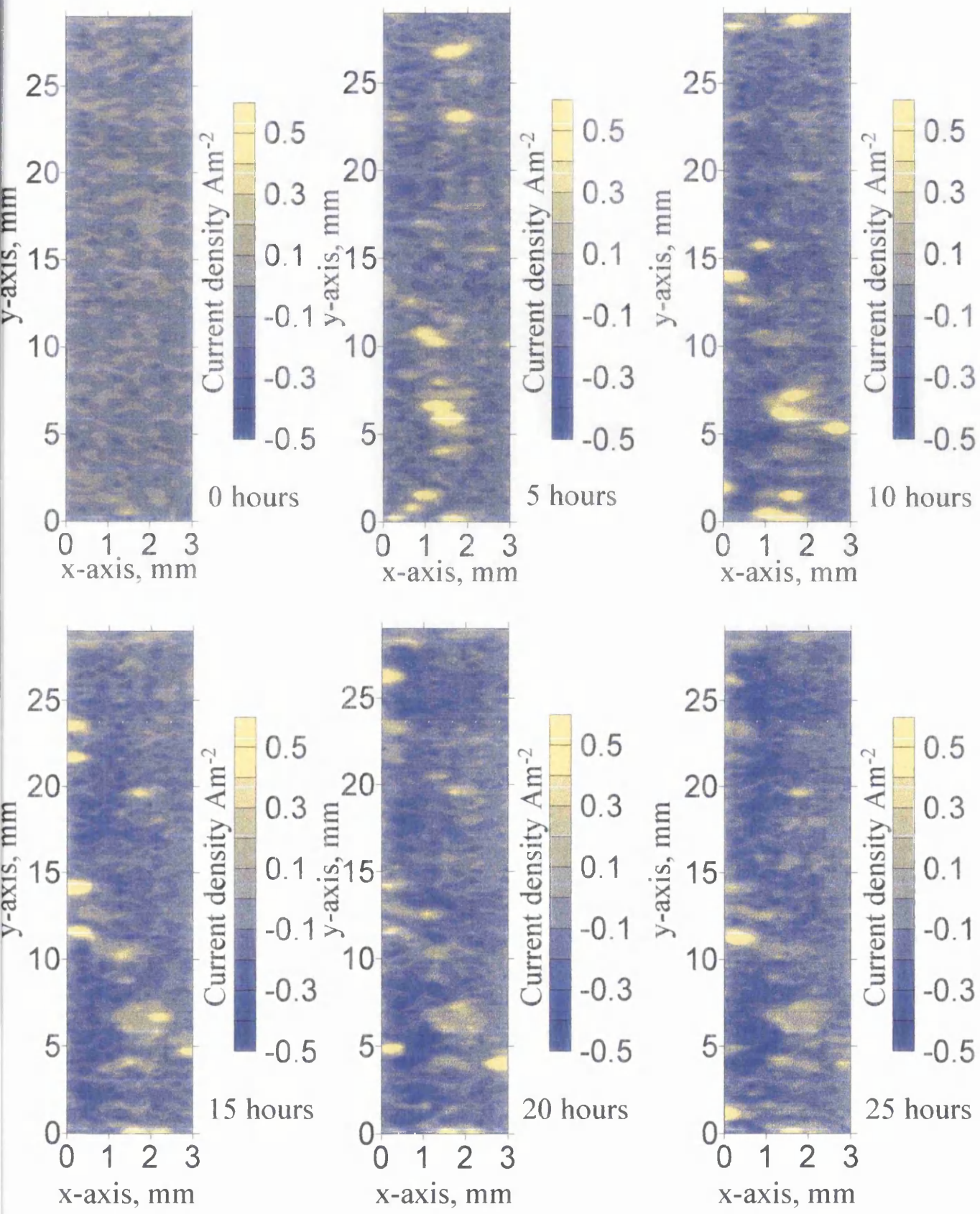

Figure 4.16: SVET contour plots for AA2024-T3 end, polished to 1μm then immersed in 3.5% w/w NaCl for 24 hours at 25^{0}C. The time indicated is the time since sample immersion.

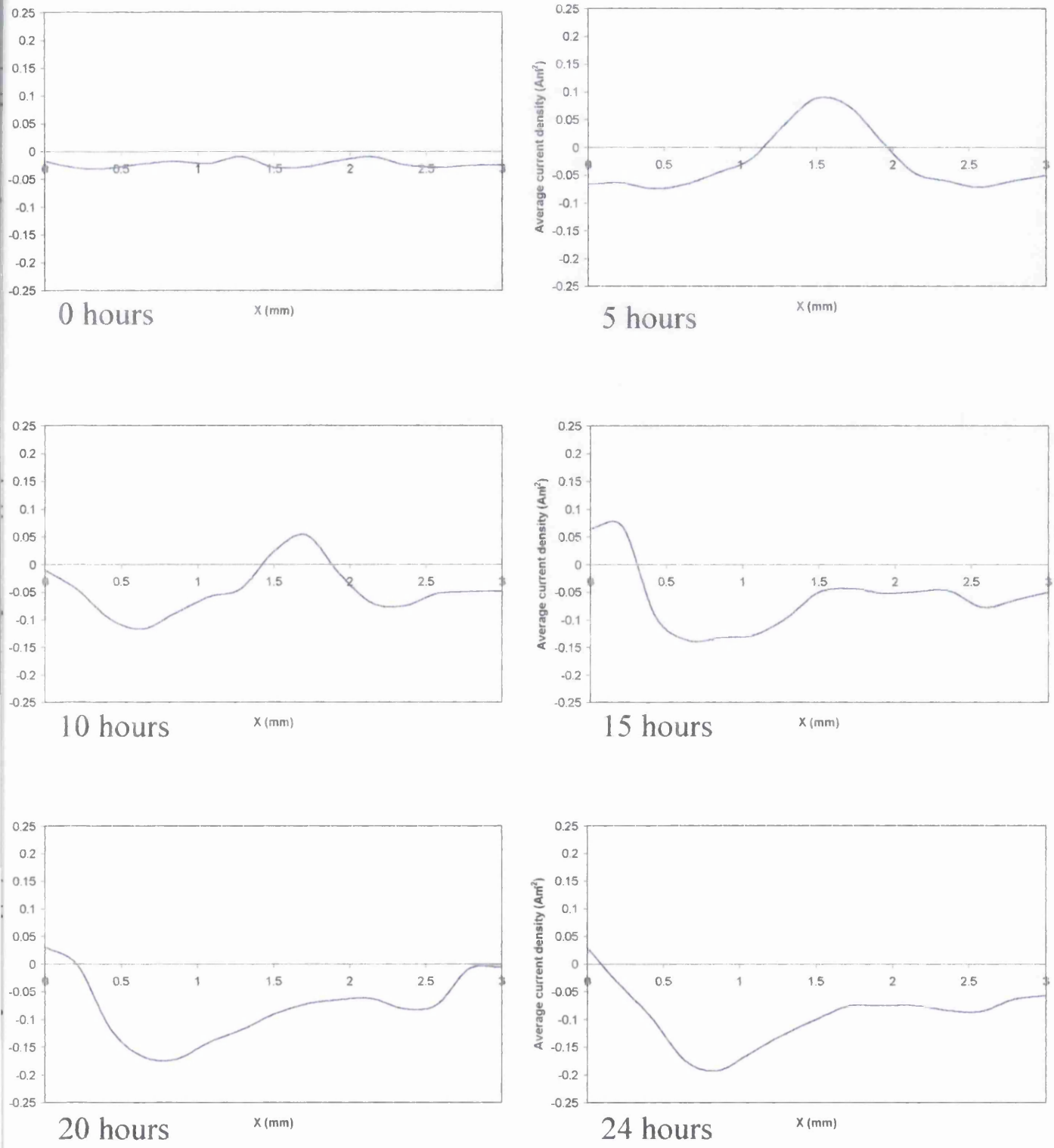

Figure 4.17: Graphs showing how average current density varies along x-axis of AA2024-T3 plate end, polished to 1μm then immersed in 3.5% w/w NaCl for 24 hours at 25^{0}C. The time indicated is the time since sample immersion.

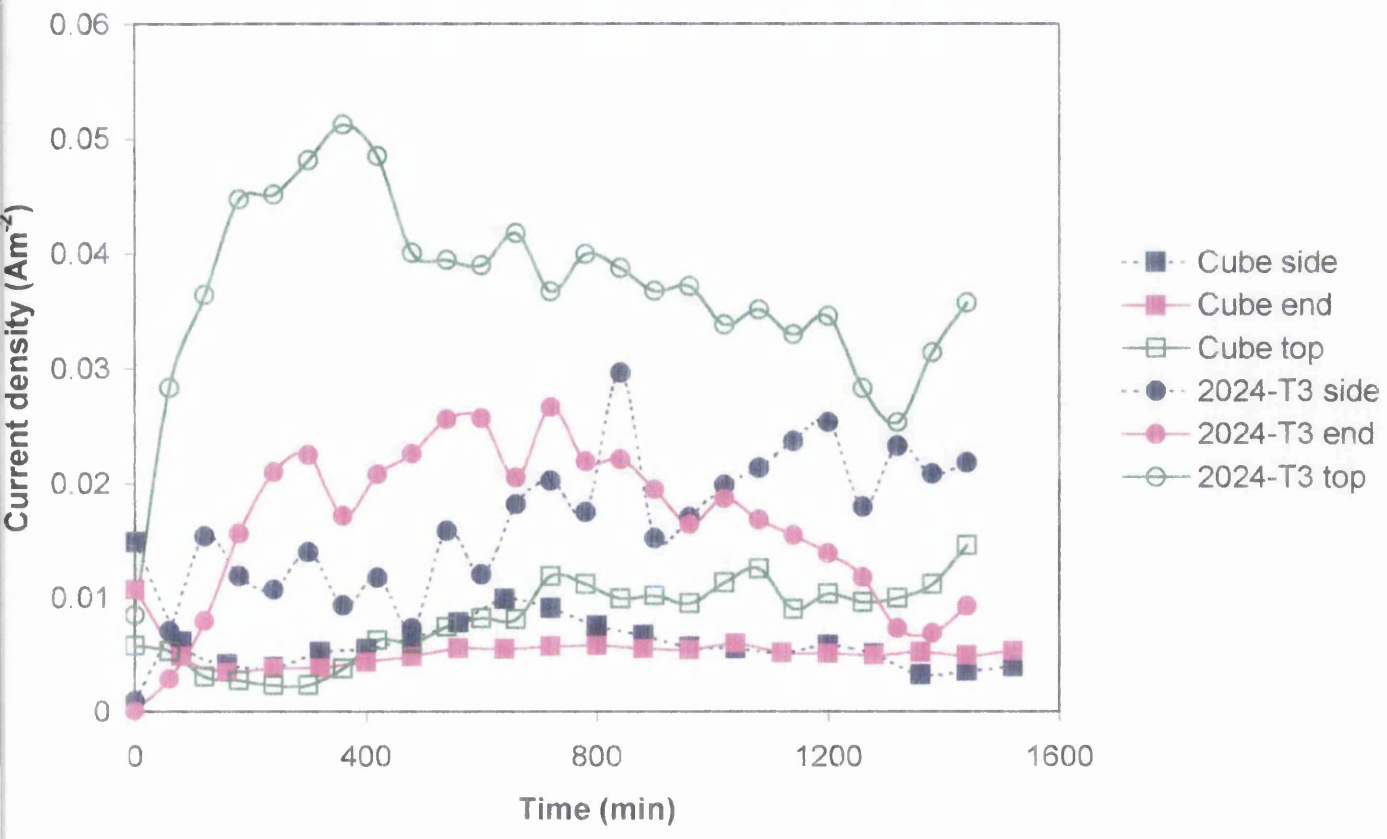

Figure 4.18: Plot showing how current density varies with time of immersion in 3.5% w/w NaCl at 25^{0}C. For all three sides of AA2024-T351 cube and AA2024-T3 plate.

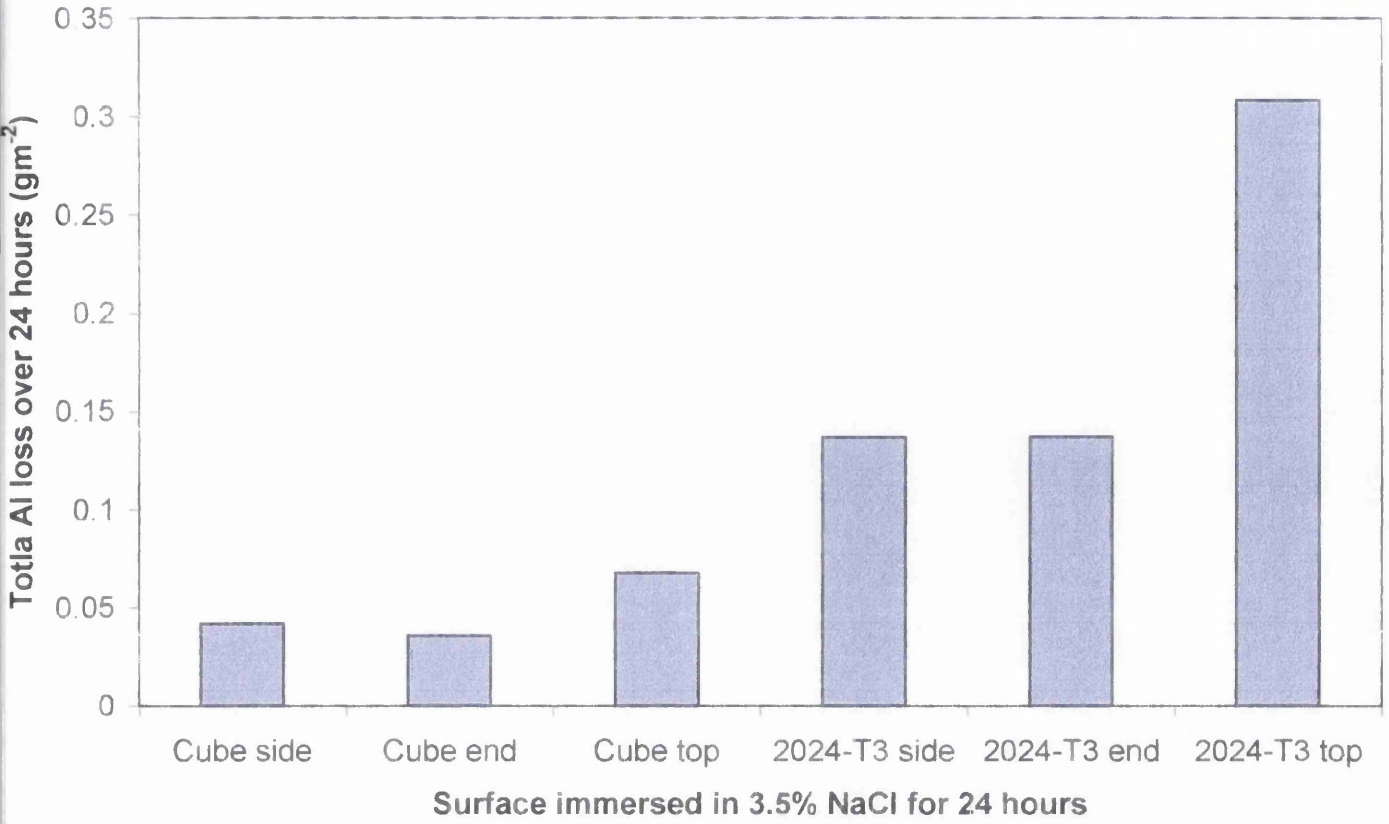

Figure 4.19: Plot showing the total aluminium loss after 24 hours immersion in 3.5% w/w NaCl at 25^0C. For all three sides of AA2024-T351 cube and AA2024-T3 plate.

4.4: Conclusions.

It has been shown that for cube sample AA2024-T3 the precipitate particles are concentrated along the top and bottom surfaces, so that in the centre of the cube there are far fewer particles then along the edge. It has also been shown that there is approximately the same surface area of Al-Cu-Mg particles to Al-Cu-Mn-Fe-Si particles on the surfaces of AA2024-T351. Using the SVET it has been determined that the majority of pitting corrosion on the side and end of the AA2024-T351 cube sample occurred towards the centre of the cube, i.e. where there were least precipitate particles. By slicing through the cube sample it was possible to obtain samples with different densities of particles. Using these samples it was determined that the higher the particle density, the more pitting corrosion was detected by the SVET. It was also determined that the AA2024-T351 cube sample is far less prone to pitting corrosion then the AA2024-T3 3 mm plate sample. We may therefore conclude that the precipitate particles act as effective cathodes. Thus when a non-uniform distribution of particles is present, cathodic activity is greatest in areas of lower particle concentration. Furthermore, when a uniform distribution of particles is present overall corrosion currents increase with particle concentration. It has not been possible to assign relative cathodic activities to the S phase and Fe-Mn particle populations. However, the known electro-catalytic proportions of Cu for cathodic O_2 reduction suggests that it is the S phase particles which are principally responsible for directing cathodic activity.

4.5: Reference:

[1] C. Blanc and G. Mankowski, *Materials Science Forum*, **289**, 499 (1998).
[2] P. Campestrini, E. P. M. van Westing, H. W. van Rooijen and J. H. W. de Wit, *Corrosion Science*, **42**, 1853 (2000).
[3] G. S. Chen, M. Gao and R. P. Wei, *Corrosion*, **52**, 8 (1996).
[4] C. Blanc, B. Lavelle and G. Mankowski, *Corrosion Science*, **39**, 495 (1997).
[5] V. Guillaumin and G. Mankowski, *Corrosion Science*, **41**, 421 (1999).
[6] C. Blanc and G. Mankowski, *Corrosion Science*, **40**, 411 (1998).

Chapter 5.

Chapter 5: Investigation into how selective dissolution of precipitate particles affects pitting corrosion of AA2024-T3 using (SVET).

5.1: Introduction.

As described in chapter 4, the intermetallic precipitate particles present on the surface of AA2024-T3 influences its corrosion characteristics[1,2,3,4]. The aim of the work to be described here, has been to determine the extent to which intermetallic precipitates present at the AA2024-T3 surface may be selectively removed using nitric acid/chloride mixtures. It has been a further aim to quantify the influence of precipitate removal on subsequent rates of pitting corrosion using SVET. The fractional area of alloy surface comprising of intermetallic particles was determined using SEM back-scatter as in chapter 4. The sample was then immersed in a nitric acid solution containing chloride ions for varying amounts of time to selectively remove intermetallic precipitates[5]. The pitting corrosion characteristics of the treated alloy surface were subsequently determined using a quantitative SVET as described in chapter 3.

5.2: Experimental.

5.2.1: Materials.

Aluminium alloy 2024-T3 as described in section 3.2.1, were obtained from BAE Systems, Sowerby research centre. All samples were prepared following the sequency in figure 3.1, as described in section 3.2.1. However, before the sample area was masked off using the PTFE tape the sample was immersed in a solution consisting of 50% w/v Nitric acid containing $3x10^{-2}$ M NaCl for varying periods of

time (0, 2, 5, 15, 30, 60 and 300 sec) to dissolve varying amounts of surface precipitates, and the sample was rinsed in distilled water immediately after to remove any remnants of the solution.

All other materials were purchased from Aldrich in their highest purity and all solutions were prepared in distilled water.

5.2.2: Methods.

Electron microscopy:

After the sample had been immersed in the nitric acid solution for a given length of time it was placed in the SEM described in section 2.3. The aim was to determine the percentage of precipitate particles left on the surface. This was done using the back-scatter mode at the highest possible contrast, so the precipitates show up as white on a black background. Eleven micrographs were recorded from random positions for each sample. Once the images were recorded it was necessary to determine the area of precipitates on the micrographs. This was achieved using the Graftek, Optilab Pro image analysis package. A threshold was set so that the white precipitates were distinguished from the black matrix. Then using the particle count function the percentage area of precipitates was recorded for each micrograph, and the average of eleven micrographs was determined for each sample.

SVET:

The methods used for this study are described in section 3.2.2 with these adjustments.

The scan area for all SVET experiments was typically 20 mm x 20 mm, so the matrix generated was 80 x 80 points and total scan time was 40 minutes. The samples

were scanned using SVET immediately on immersion and scanned at hourly intervals for a period of 24 hours. Each SVET measurement was made with the probe stationary and was an average of ten measurements.

Optical microscopy:

On completion of the SVET experiment the sample was rinsed in distilled water to stop corrosion, then air dried before the optical pictures were taken. Optical pictures were taken using the scanner as described in section 2.6.

5.3: Results and Discussion.

5.3.1: Investigation into how precipitate area varies with time of immersion in nitric acid/chloride solution.

Figure 5.1 shows example back-scatter images for a sample before being immersed in the nitric acid/chloride solution, and for samples immersed for 2, 5, 15, 30, 60, and 300 seconds. As can be seen there is a very high contrast between the aluminium matrix (black) and the precipitates present on the surface (white), with exception of the back-scatter images after the sample was immersed for 300 seconds. In this case it can be seen that the aluminium matrix appears mid-grey with small white areas (precipitate) and small black areas (determined to be holes from SEM images as can be seen in figure 5.1b). Table 5.1 shows the percentage of each image that is precipitate obtained using Graftek, Optilab Pro image analysis package. As can be seen in table 5.1 eleven images were produced for each experiment, and a mean value was obtained along with the standard deviation (σ) and the standard deviation on the mean (σ_m). i.e.

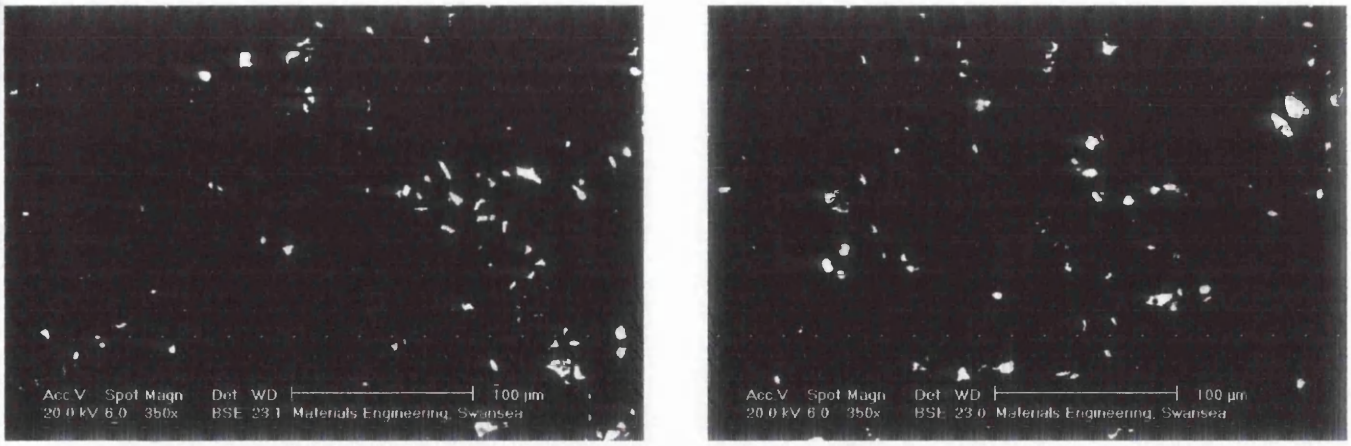

Immersion time = 0 sec.

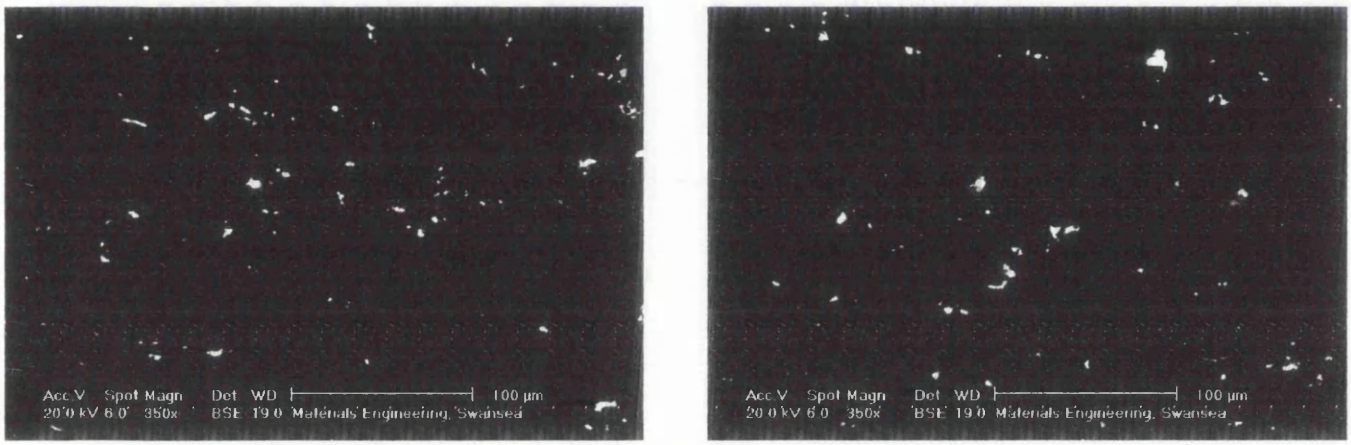

Immersion time = 2 sec.

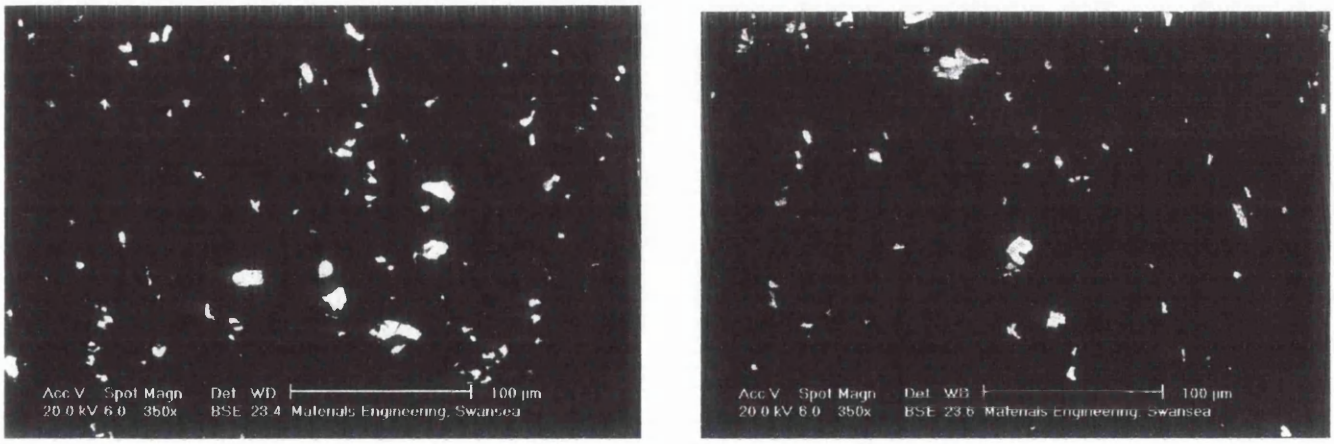

Immersion time = 5 sec.

Figure 5.1: Example SEM back-scatter images of AA2024-T3 surface after being immersed in 50% w/v nitric acid with 3 x10^{-2} M NaCl for various periods of time.

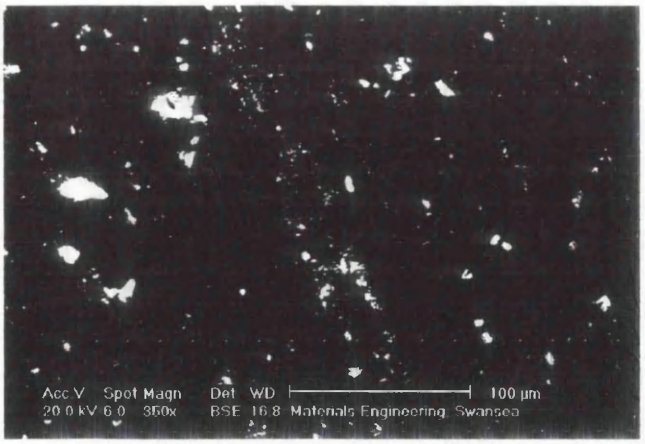

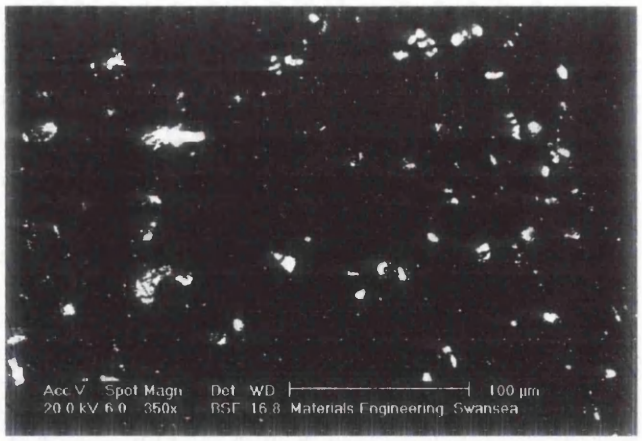

Immersion time = 15 sec.

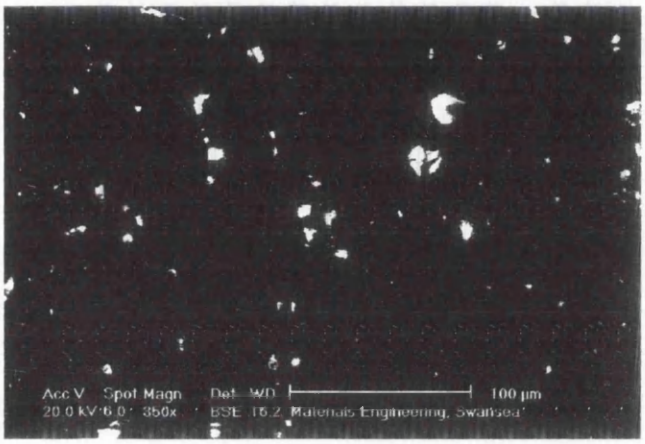

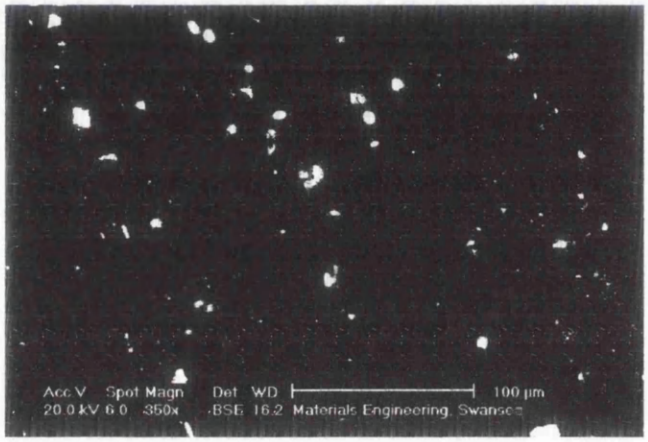

Immersion time = 30 sec.

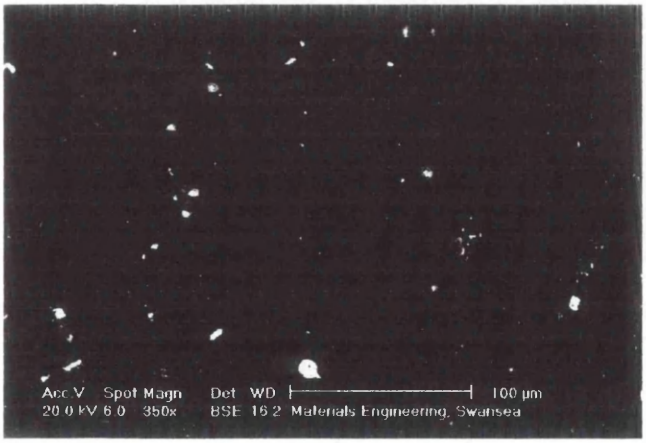

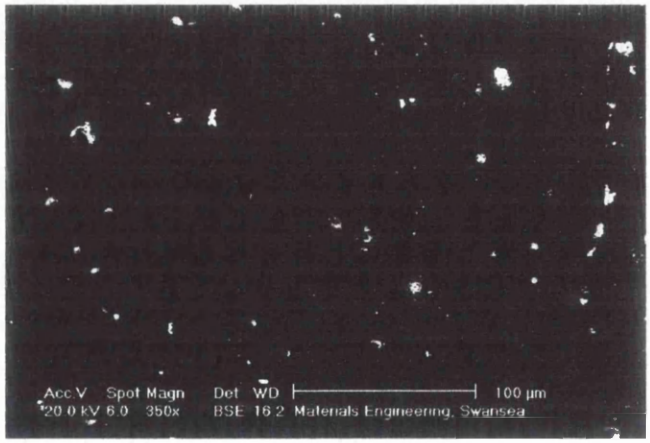

Immersion time = 60 sec.

Figure 5.1: Example SEM back-scatter images of AA2024-T3 surface after being immersed in 50% w/v nitric acid with 3 x10^{-2} M NaCl for various periods of time.

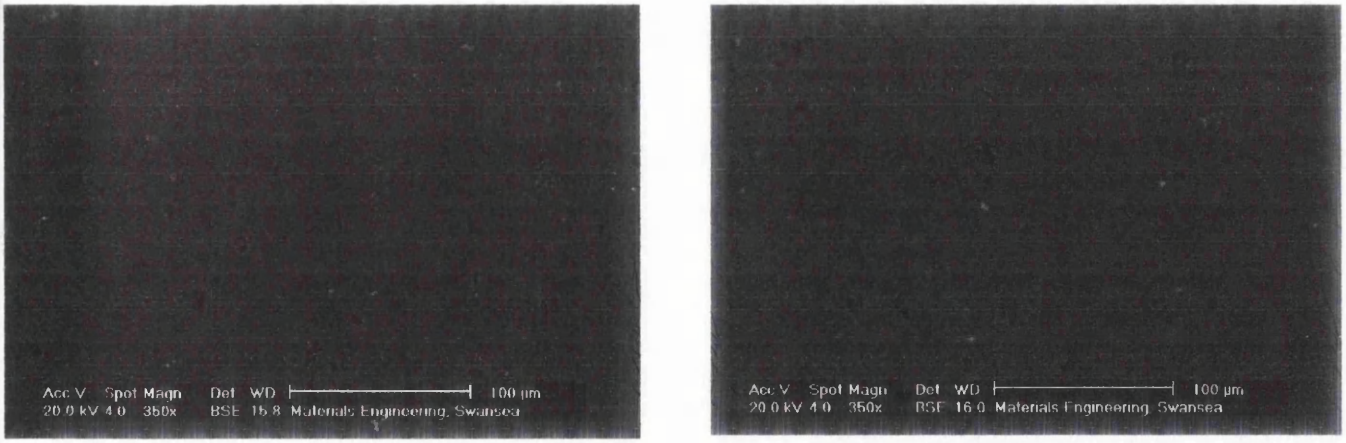

Immersion time = 300 sec.

Figure 5.1: Example SEM back-scatter images of AA2024-T3 surface after being immersed in 50% w/v nitric acid with 3 $x10^{-2}$ M NaCl for various periods of time.

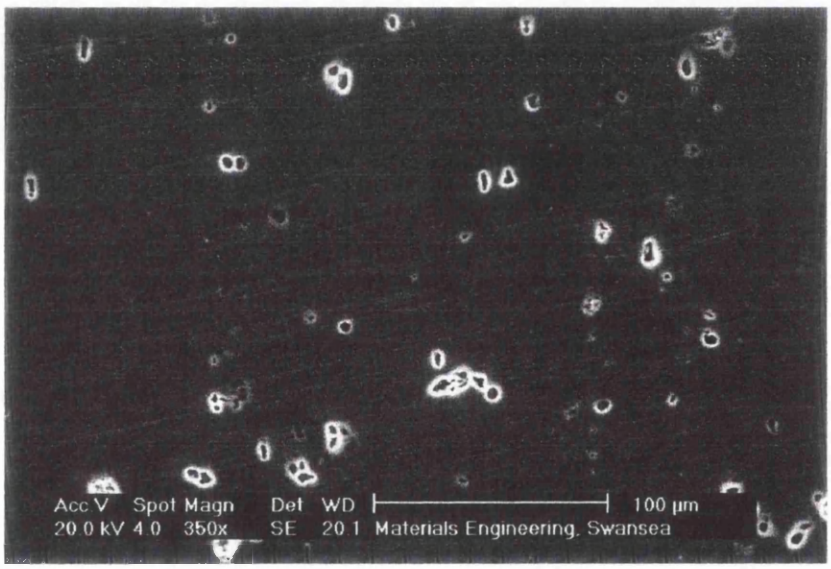

b)

Figure 5.1b: SEM micrograph of polished AA2024-T3 after being immersed in nitric acid/ chloride solution for 300 seconds.

$$\sigma_n = \frac{\sigma}{\sqrt{n}} \qquad [5.1]$$

where n is the population, in this case eleven. This determined the error due to the sample size. However, to determine the reproducibility it was necessary to repeat the experiments for the same immersion time. This was very labour intensive, so two measurements were chosen for repeating; the untreated case was measured three times, as this determined the reproducibility in the initial sample surface, also the 15 second immersion case was measured four times as a random treated surface.

Figure 5.2 shows a plot of the mean percentage of the surface which is precipitate for each immersion time in the nitric acid/chloride solution. The red solid line indicates the mean value for the untreated surfaces, with the dashed lines showing the corresponding values of $\pm\sigma_n$. The value for the 15 second immersion is the mean of the four experiments carried out, with the error bars indicating $\pm\sigma_n$. The values used for all other times were obtained from the single experiments shown in table 5.1, and the fractional error was assumed to be the same as the fractional error σ_f for the 15 sec experiments. i.e.

$$\sigma_f = \frac{\sigma_n}{mean} \qquad [5.2]$$

Which for the 15 sec immersion experiments = 0.32. Using this value and equation 5.2 σ_n was found for all other immersion times.

It may be seen from figure 5.2 that experimental error was relatively low on the untreated samples but was much higher on the 15 sec treated sample. The reason for this error is not clear. However, it does not appear to be a result of variation in precipitate area before immersion in the nitric acid/chloride solution, but due to

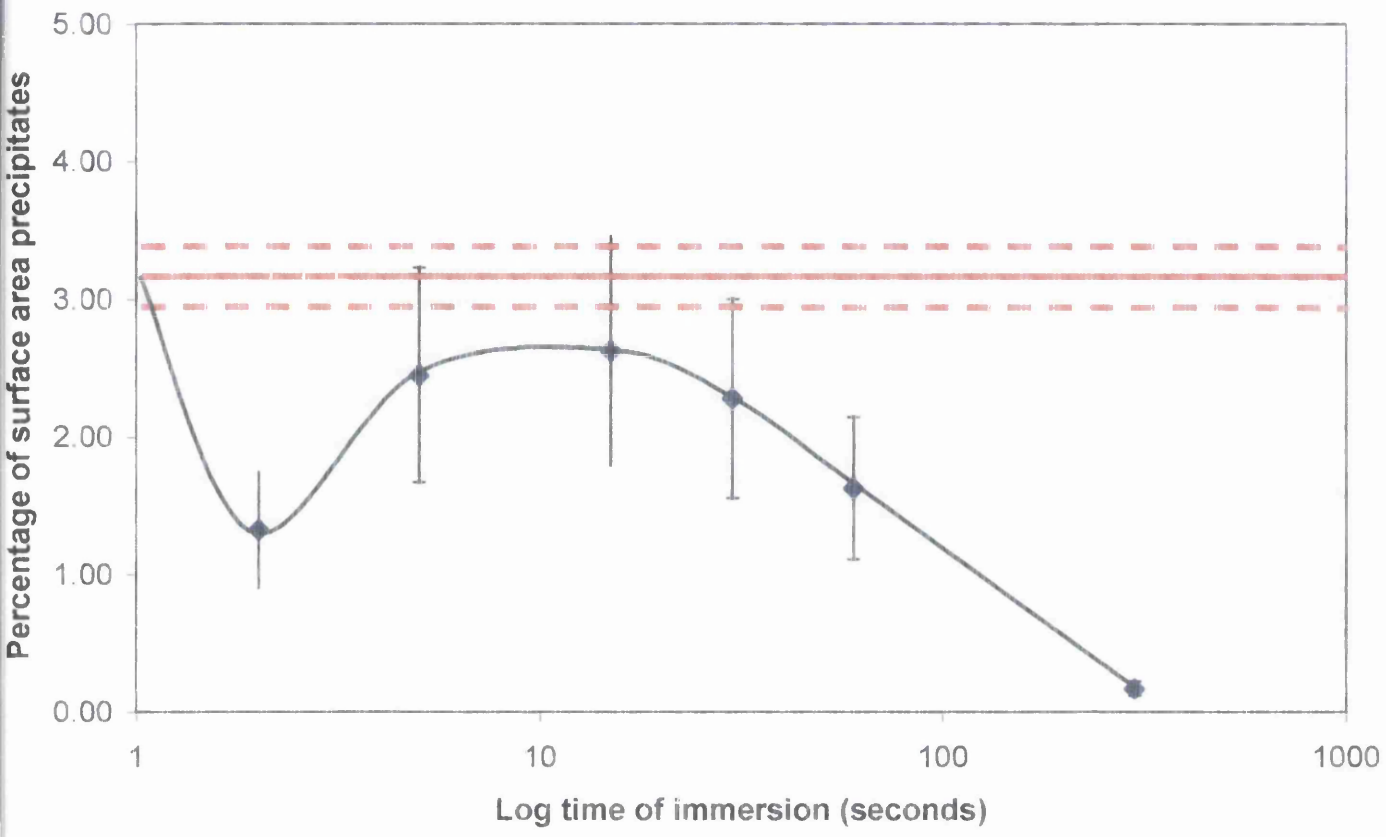

Figure 5.2: Plot showing how mean percentage of precipitate surface area varies with time of immersion in nitric acid/chloride solution. Solid red line shows mean percentage of precipitate for three untreated surface experiments, with dashed lines indicating ± standard deviation on the mean (σ_n). Standard deviation values for all other immersion times were calculated using the fractional error (σ_f) obtained from repeated 15 sec immersion experiments.

variation in the treatment. Possible sources of variation include experimental time, temperature and convection rates in the solution. Figure 5.2 shows that there is a general trend, such that, as time of immersion in the nitric acid solution is increased, the area of precipitates on the surface of the alloy is reduced. However, it can also be seen that for 2 seconds immersion there is a dip in particle area which rises again for 5 seconds immersion. This effect may be due to a large number of small precipitates (< 10μm) being initially present in the naturally occurring oxide layer (typically between 5 - 15 μm thick[6]), or a microstructure layer produced during the rolling or polishing processes, see figure 5.3a. These particles may be quickly removed by the nitric acid solution, but there may not be enough time to expose the particles beneath. At longer immersion times the particles initially present in the subsurface bulk alloy become exposed producing a transient increase in particle surface area. A schematic diagram illustrating this proposition can be seen in figure 5.3. This proposition may also help explain the large error in precipitate area between different samples after 15 seconds immersion in the solution. Small variations in immersion time may result in large variations in particle concentration if the removal of a thin, reactive, surface layer is involved

Before sample is immersed in the nitric acid solution the surface is covered in a thin (~ 5 to 15 μm) oxide film, or a damaged layer from rolling or polishing.

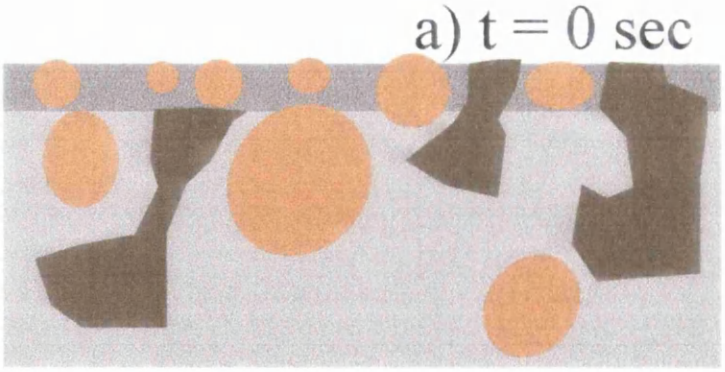

This thin film will be removed very quickly after immersion in the solution, and any particles held to the surface by the oxide film will 'fall out', thus reducing the surface area of precipitates.

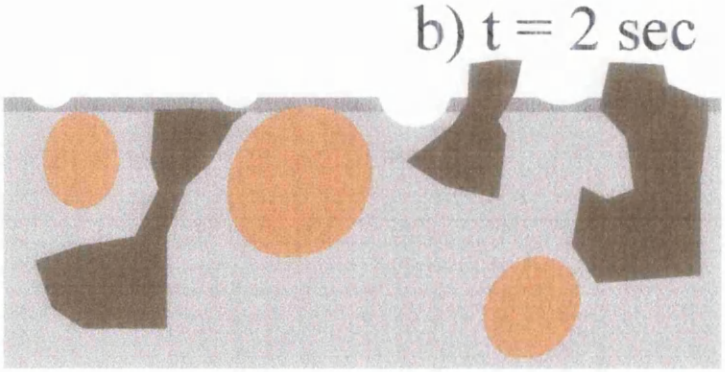

If the sample is left in the solution for longer periods of time (~ 5 sec) then the particles just under the oxide film are exposed to the surface, thus increasing the surface area.

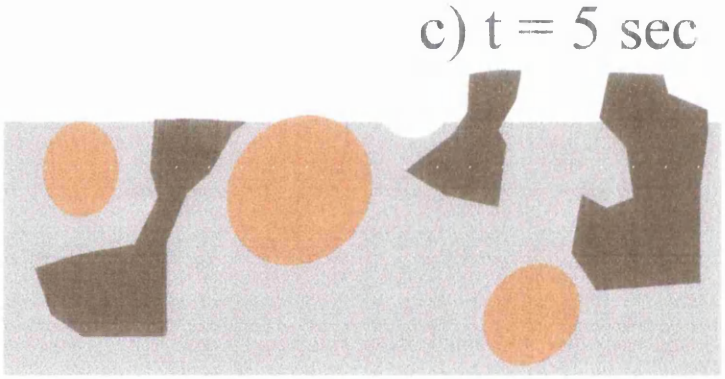

However, if the sample is left in for a very long time (>> 5 sec) then the particles start being dissolved out by the solution (which does not attack the matrix), thus reducing the surface area of particles. This would result in large holes being left on the surface.

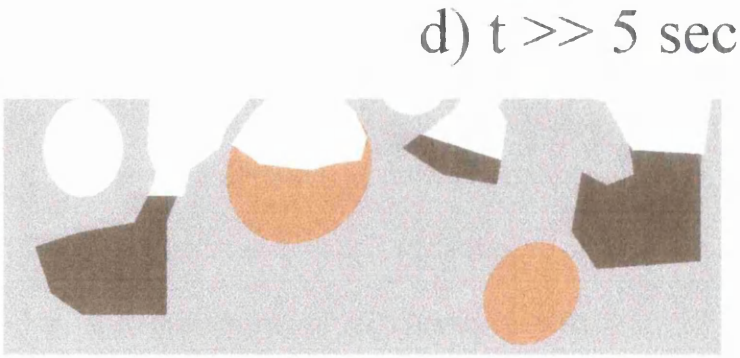

Figure 5.3: Schematic diagram showing possible reason for large reduction in precipitate surface area after only 2 seconds immersion in Nitric acid solution.

Table 5.1: Table showing percentage of AA2024-T3 surface area which consists of precipitate particles for three untreated samples, and after 2 sec, 5 sec, four x 15 sec, 30 sec, 60 sec, and 300 sec immersion in nitric acid/chloride solution. Eleven results were recorded for each sample so as to determine means and errors in the values obtained.

	Untreated			2 sec	5 sec	15 sec				30 sec	60 sec	300 sec
Image	1	2	3			1	2	3	4			
1	3.39	5.91	2.66	1.4	4.06	0.94	0.93	5.05	4.01	3.1	1.62	0.21
2	2.75	4.22	3.23	1.24	2.9	1.1	1.25	3.99	3.87	2.23	1.39	0.12
3	2.26	4.2	3.1	1.21	2.69	0.72	1.02	3	3.86	2	1.61	0.19
4	3.05	3.46	3.4	1.26	2.44	0.93	1.41	3.05	5.45	1.95	1.69	0.2
5	2.12	2.74	2.49	0.87	1.77	0.73	0.88	4.31	5.34	2.37	1.23	0.15
6	3.75	3.44	3.97	1.35	2.8	1.98	0.83	6.18	5.01	1.45	1.89	0.26
7	2.38	2.93	2.19	1.32	2.79	1.56	1.35	3.17	3.16	2.54	0.88	0.23
8	3.36	3.92	2.91	1.45	2.49	1.65	0.94	3.92	2.88	2.87	2.96	0.19
9	2.73	2.17	3.22	1.22	1.51	1.63	1.05	5.67	2.17	1.78	1.84	0.1
10	2.11	2.38	4.4	2.11	2.14	1.78	1.26	4.57	3.81	1.9	1.73	0.1
11	2.68	3.93	3.94	1.13	1.39	1.25	1	3.86	3.3	1.88	0.86	0.09
Mean	2.78	3.57	3.25	1.32	2.45	1.30	1.08	4.23	3.90	2.19	1.63	0.17
Standard deviation	0.55	1.05	0.66	0.30	0.75	0.44	0.20	1.06	1.03	0.49	0.58	0.06
Standard deviation on mean	0.10	0.19	0.12	0.06	0.14	0.08	0.04	0.19	0.19	0.09	0.10	0.01

5.3.2: Determining how corrosion characteristics change with time of immersion in nitric acid solution.

SVET experiments were carried out as described in section 5.2.2. Figure 5.4 shows a selection of false colour plots obtained from corroding polished AA2024-T3 in 3.5% w/w NaCl at 25^0C. As can be seen these plots are consistent with those obtained for the same sample under the same conditions in chapter 3. Figure 5.5 shows an optical micrograph of the surface after the SVET experiment was finished as described in section 5.2.2. As can be seen from the micrograph, areas of anodic activity correspond well with areas of pitting on the samples surface after the experiment was finished. Figure 5.6 shows a section of false colour plots obtained from a polished AA2024-T3 which has then been immersed in a nitric acid (see section 5.2.1) solution

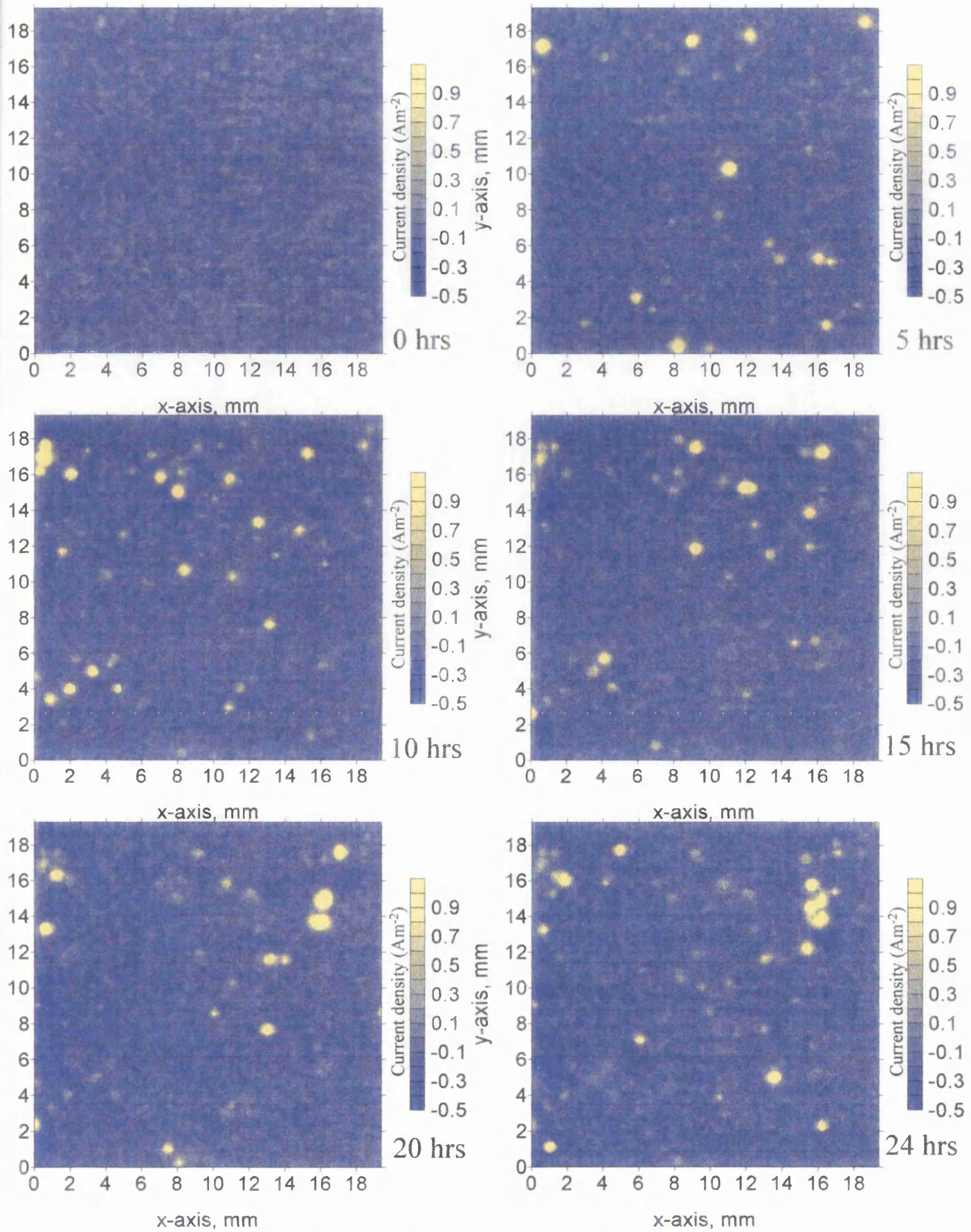

Figure 5.4: SVET contour plots for AA2024-T3 without being immersed in nitric acid solution, polished to 1μm then immersed in 3.5% w/w NaCl for 24 hours at 25^0C.

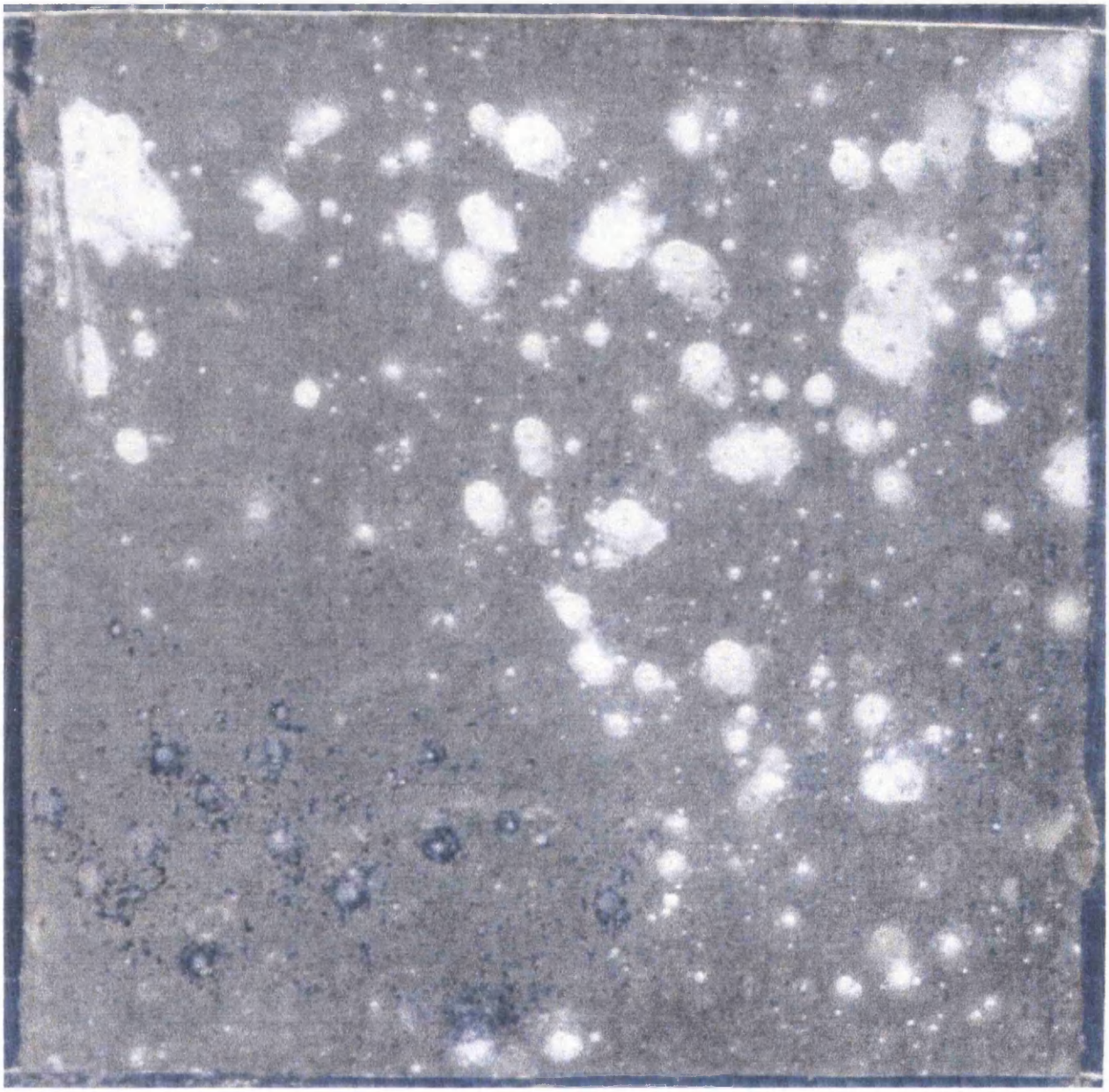

Figure 5.5: Optical micrograph for AA2024-T3 without being immersed in nitric acid solution, polished to 1μm then immersed in 3.5% w/w NaCl for 24 hours at 25^0C, corresponding to SVET plots seen in figure 5.4.

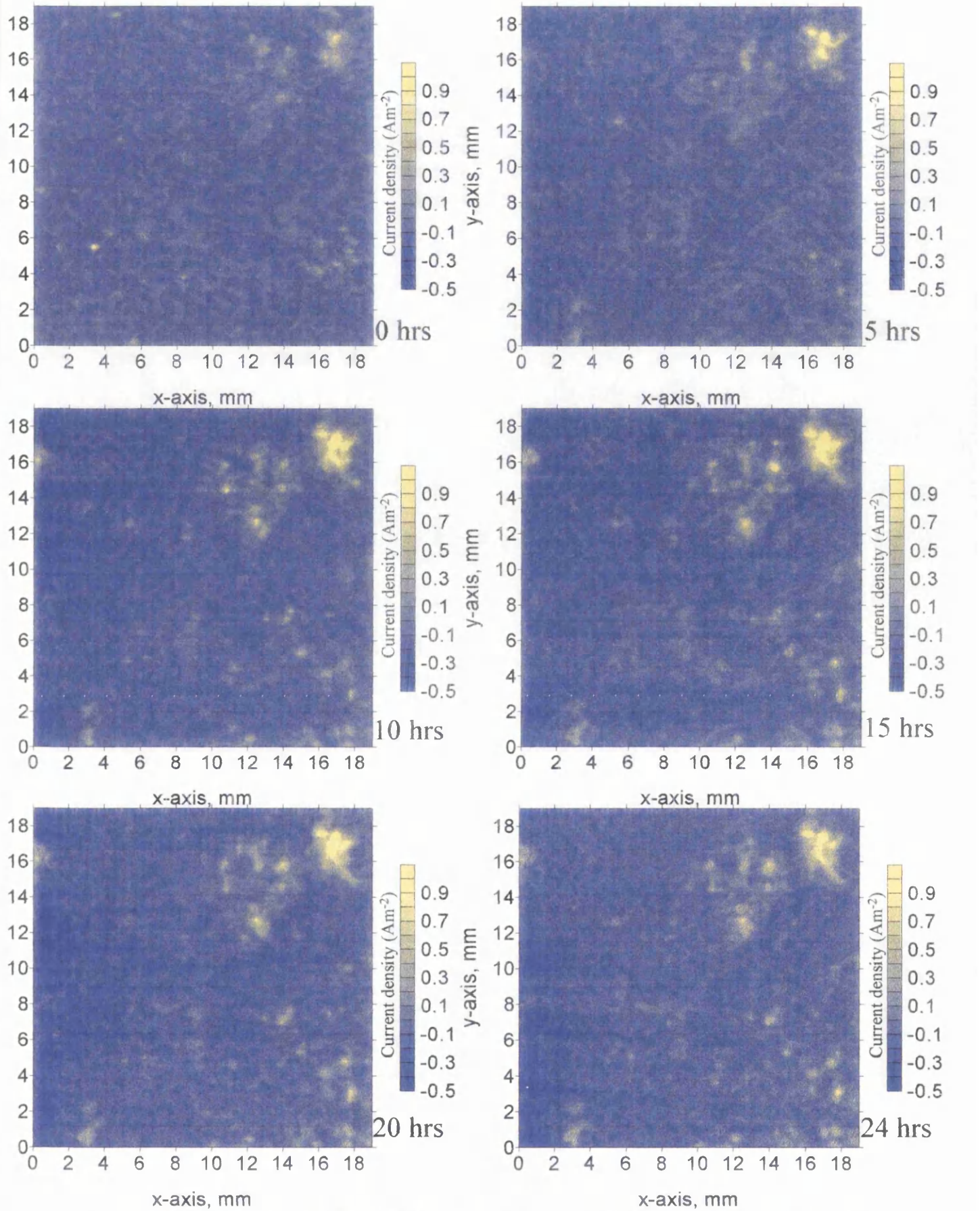

Figure 5.6: SVET contour plots for AA2024-T3 polished to 1μm then immersed in nitric acid solution for 2 seconds, then immersed in 3.5% w/w NaCl for 24 hours at 25^{0}C.

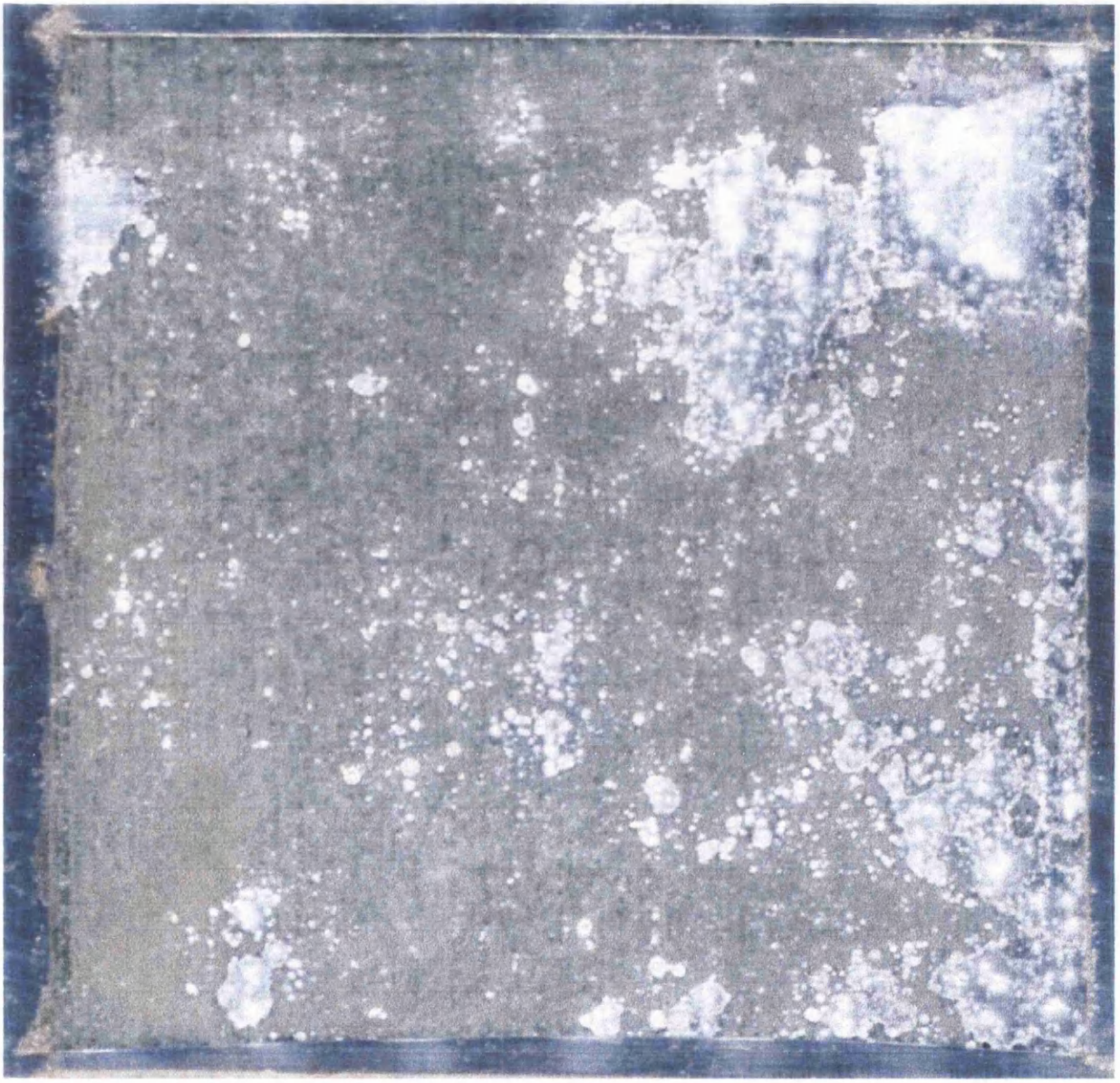

Figure 5.7: Optical micrograph of AA2024-T3 polished to 1μm then immersed in nitric acid solution for 2 seconds, then immersed in 3.5% w/w NaCl for 24 hours at 25^{0}C, corresponding to SVET plots seen in figure 5.6.

for 2 seconds, before being corroded in 3.5% w/w NaCl at 25^0C. Figure 5.7 shows an optical micrograph of the surface after the SVET experiment was finished, again it can be seen from the micrograph that areas of anodic activity correspond well with areas of pitting on the surface of the sample, after the experiment was finished. Comparing Figures 5.4 and 5.6 it can be seen that after 2 seconds immersion in the nitric acid solution pitting corrosion on the surface of polished AA2024-T3 seems to be greatly reduced. That is to say, pits appear to be fewer and of lower intensity when the sample was immersed in the solution for 2 seconds, before corrosion was initiated. Figure 5.8 shows a graph of how total aluminium lost over the 24 hour immersion in the electrolyte, obtained as described in section 3.3.3, varies with time of immersion in the nitric acid/chloride solution before corrosion was initiated. It shows that there is a minimum amount of metal loss after 2 seconds immersion in the nitric acid solution. This corresponds with a dip in the surface area of precipitates as seen in figure 5.2. However, from figure 5.2 it can be seen that for longer periods of immersion (> 60 seconds) in the nitric acid solution the percentage of the surface area that is precipitates is reduced again. This does not correspond to a reduction in total aluminium loss shown in figure 5.8; which shows that for very long periods of immersion in the nitric acid solution, the total aluminium loss over the 24 hour experimental period increases back to around the same level as for untreated samples, shown by the red line $\pm\sigma_n$ red dashed lines. This failure to reduce corrosion at high nitric acid immersion times may be due to the holes left in the surface after the precipitate particles have been dissolved acting to promote pit nucleation. These holes can be clearly seen in the SEM picture shown in figure 5.1b. Three SVET experiments were carried out for samples not treated in the nitric acid/chloride solution, and three were carried out for samples immersed for 15 seconds. The blue

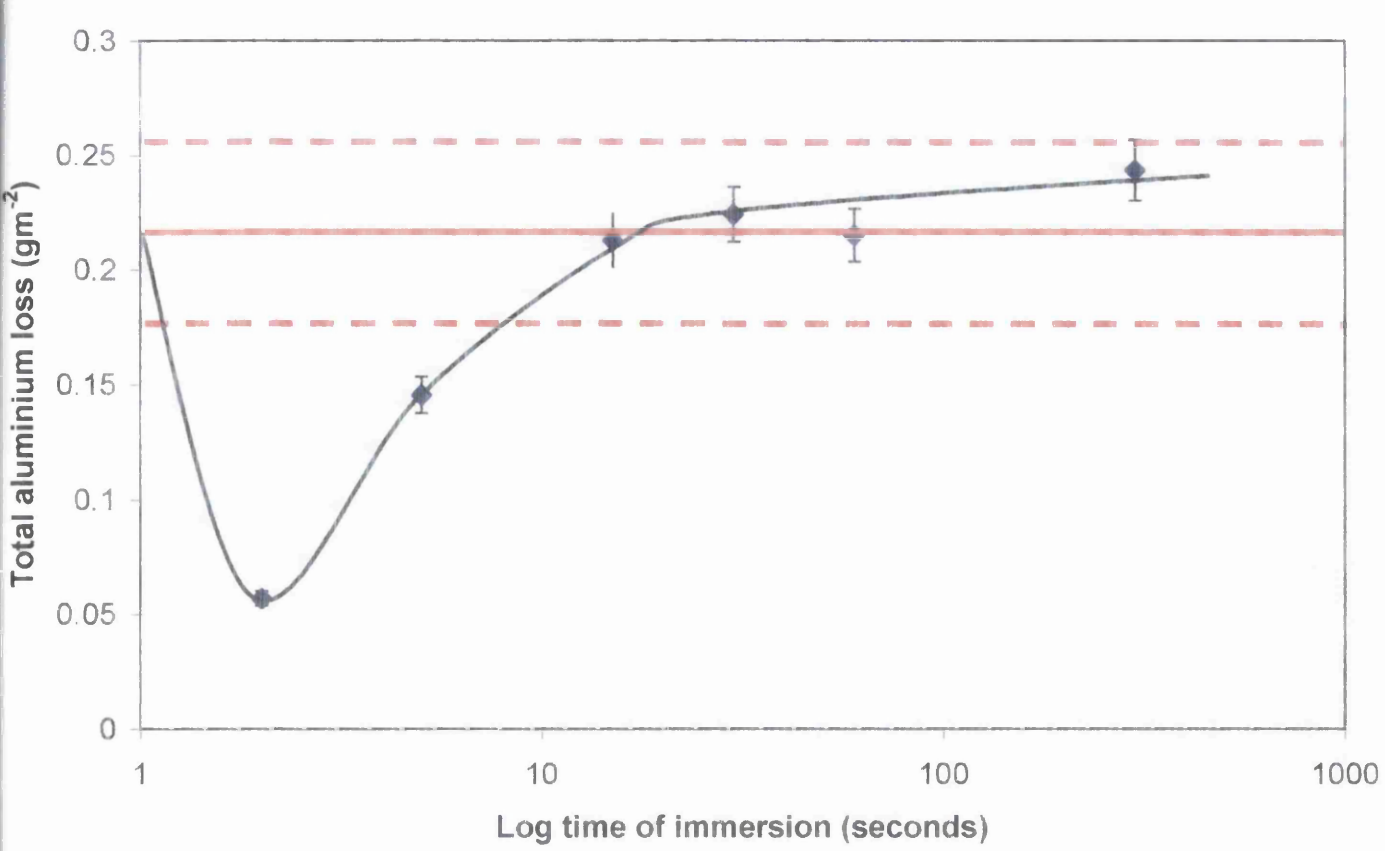

Figure 5.8: Plot showing how total aluminium loss varies with time of immersion in nitric acid solution. Solid red line shows mean value obtained for untreated samples with dashed lines indicating $\pm\sigma_n$. Errors in treated samples obtained from fractional error determined from three 15 second experiments.

diamond symbols show the mean of the three values with ± the standard deviation on the mean marked on the graph. Errors for the other immersion times were also determined using the fractional error from the 15 second experiments and equation 5.2. As can be seen the error in total aluminium loss for all times of immersion is not large, and the scatter for 15 seconds immersion is far less then that obtained in the measurement of percentage area of precipitate particles (see figure 5.2).

5.4: Conclusions.

It has been shown that the 50% w/v nitric acid, $3x10^{-2}$ M NaCl solution can dissolve out the precipitate particles present on the surface of AA2024-T3 without a large amount of damage being done to the matrix. Percentage surface area of precipitates was obtained for varying immersion times in the nitric acid solution, and it has been found that there was a dip in the amount of precipitates for 2 seconds immersion in the solution. However, generally, precipitate area decreases as immersion time increases. It has also been shown using SVET that the minimum amount of aluminium loss occurred after the sample was immersed in the nitric acid solution for only 2 seconds. Thus it would appear that reducing the concentration of particles at the alloy surface reduces corrosion current. This finding is entirely consistent with the cathodic activity of particles determined in the proceeding chapter. However, it would also seem that prolonged exposure to nitric acid/ chloride mixtures decreases corrosion resistance due to the creation of relatively large voids and defects in the alloy surface.

5.5: Reference:

[1] C. Blanc and G. Mankowski, *Materials Science Forum*, **289**, 499 (1998).
[2] P. Campestrini, E. P. M. van Westing, H. W. van Rooijen and J. H. W. de Wit, *Corrosion Science*, **42**, 1853 (2000).
[3] G. S. Chen, M. Gao and R. P. Wei, *Corrosion*, **52**, 8 (1996).
[4] C. Blanc, B. Lavelle and G. Mankowski, *Corrosion Science*, **39**, 495 (1997).
[5] A. Davenport, *Personal communication*, (2002).

[6] S. Wernick and R. Pinner, Surface Treatment of Aluminium, Robert Draper Ltd, **1**, 33 (1972).

Chapter 6.

Chapter 6: Study of surface pitting inhibition by Rare Earth Metal (REM) Salts using the Scanning Vibrating Electrode Technique (SVET).

6.1: Introduction.

Aluminium and its alloys are frequently protected from corrosion by the use of coatings incorporating corrosion inhibitor species. Chromate (Cr(VI)) compounds have been used extensively because of their efficiency and low cost[1,2]. However, it is now known that chromates are toxic[3] and highly carcinogenic[4], which has resulted in increasing pressure for the development of more environmentally acceptable alternatives[5,6]. Rare earth metal (REM) salts have received significant attention in this context by virtue of their non-toxicity and their ability to effectively stifle the cathodic reactions associated with metallic corrosion through the precipitation of thin, REM rich, (hydr)oxide films[7,8,9,10,11,12,13,14,15]. Previous studies of REM inhibition on aluminium have used classical measures of corrosion rate such as weight loss[16,17]. However, corrosion reactions are often highly localised, so that the influence of an inhibitor on the distribution of electrochemical activity may be as important (or more important) than its effect on the overall rate of metal dissolution. The aim of the work described here has been to develop the scanning vibrating electrode technique (SVET), as a fully quantitative means of investigating the influence of corrosion inhibitors on localised corrosion kinetics. It has been a further aim to use SVET to undertake a comparative study of chromate (CrO_4^{2-}) and the trivalent cations of cerium (Ce), yttrium (Y) and lanthanum (La) as inhibitors of pitting corrosion on AA2024-T3 aluminium alloy.

6.2: Experimental.

6.2.1: Materials.

Aluminium alloy 2024-T3 samples ≈ 2mm thick of varying dimensions were obtained from BAE Systems, Sowerby research centre. Composition of this alloy can be found in table 3.1. The sample alloy has a T number of 3, this indicates that the alloy has been solution heat treated, cold worked and naturally aged to a substantially stable condition[18,19]. Samples were cleaned using a slurry of 5μm alumina powder in aqueous non-ionic surfactant to remove the pre-formed oxide layer, followed by immersion in Methyl Ethyl Ketone (MEK) for 10 mins to remove surface grease. The sample area for SVET investigation (≈ 15mm x 15mm) was isolated from the rest of the sample using insulating lacquer (Lacomit) followed by PVC electrical insulation tape. NB The only part of the sample left un-coated was the area to be scanned (see figure 6.1).

All other materials were purchased from Aldrich in their highest purity and all solutions were prepared in distilled water.

6.2.2: Methods.

SVET:

The methods used for this study are described in section 3.2.2 with these adjustments. The scan area was typically 15 mm x 15 mm, so the matrix generated was 60 x 60 points and total scan time was 40 minutes. Each SVET measurement was made with the probe stationary and was an average of three measurements.

The inhibitors (cerium (III) chloride, lanthanum (III) chloride, yttrium (III) chloride and sodium chromate) were dissolved in the 3.5% w/w aqueous sodium

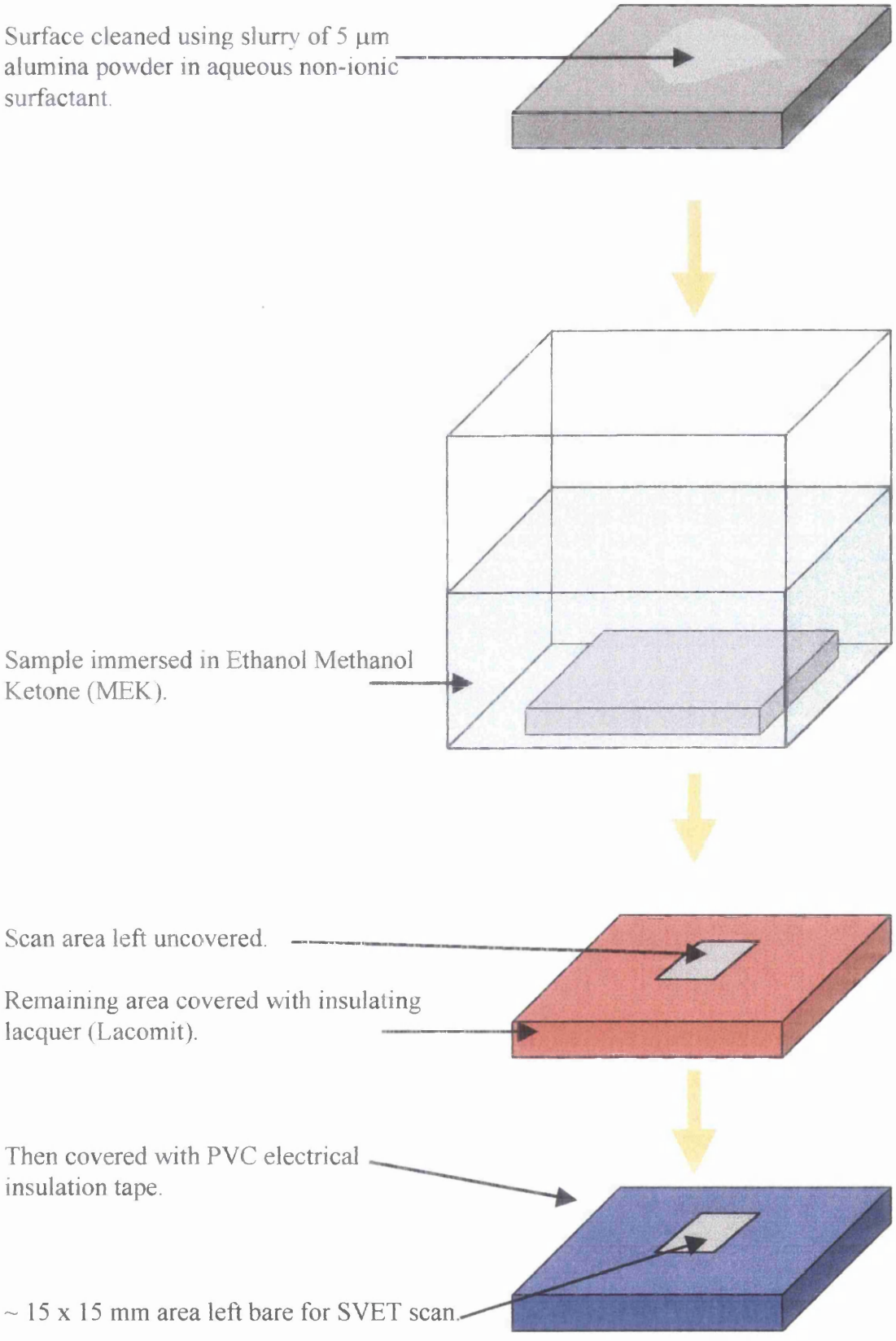

Figure 6.1: Schematic diagram showing preparation of AA2024-T3 sample surface prior to SVET corrosion experiments.

chloride bath electrolyte prior to sample immersion. Inhibitor concentrations were varied between 2.5 x 10^{-5} mol dm^{-3} and 2.5 x 10^{-3} mol dm^{-3} in five increments (on a logarithmic scale). Additional experiments where the highest and lowest concentrations of sodium chromate were added to the electrolyte five minutes before scan 5 started. The samples were scanned using SVET immediately on immersion and at hourly intervals thereafter for a period of 24 hours.

Optical microscopy:

On completion of the SVET experiment the sample was rinsed in distilled water to stop corrosion, then air dried before the optical pictures were taken. These were taken using the inverted light microscope with camera attached as described in section 2.5.

6.3: Results and discussion.

6.3.1: Uninhibited corrosion of AA2024-T3.

The SVET potential data was converted into normal current density in the plane of scan, $jz_{(x,y)}$ using the point source calibration constant described in section 2.1.3. Normal current density, $jz_{(x,y)}$, distributions were determined as a function of time above the surface of AA2024-T3 freely corroding in 3.5% w/w aqueous NaCl. Figure 6.2 shows representative $jz_{(x,y)}$ maps obtained immediately following electrolyte immersion and at 8 hour intervals thereafter, although SVET scans were actually carried out at 1 hour intervals. The surface plots shown in figure 6.2 are built up of a series of 60 line scans along the *x*-axis, with successive line scans being systematically displaced along the *y*-axis. Each line scan comprises data 60 points and

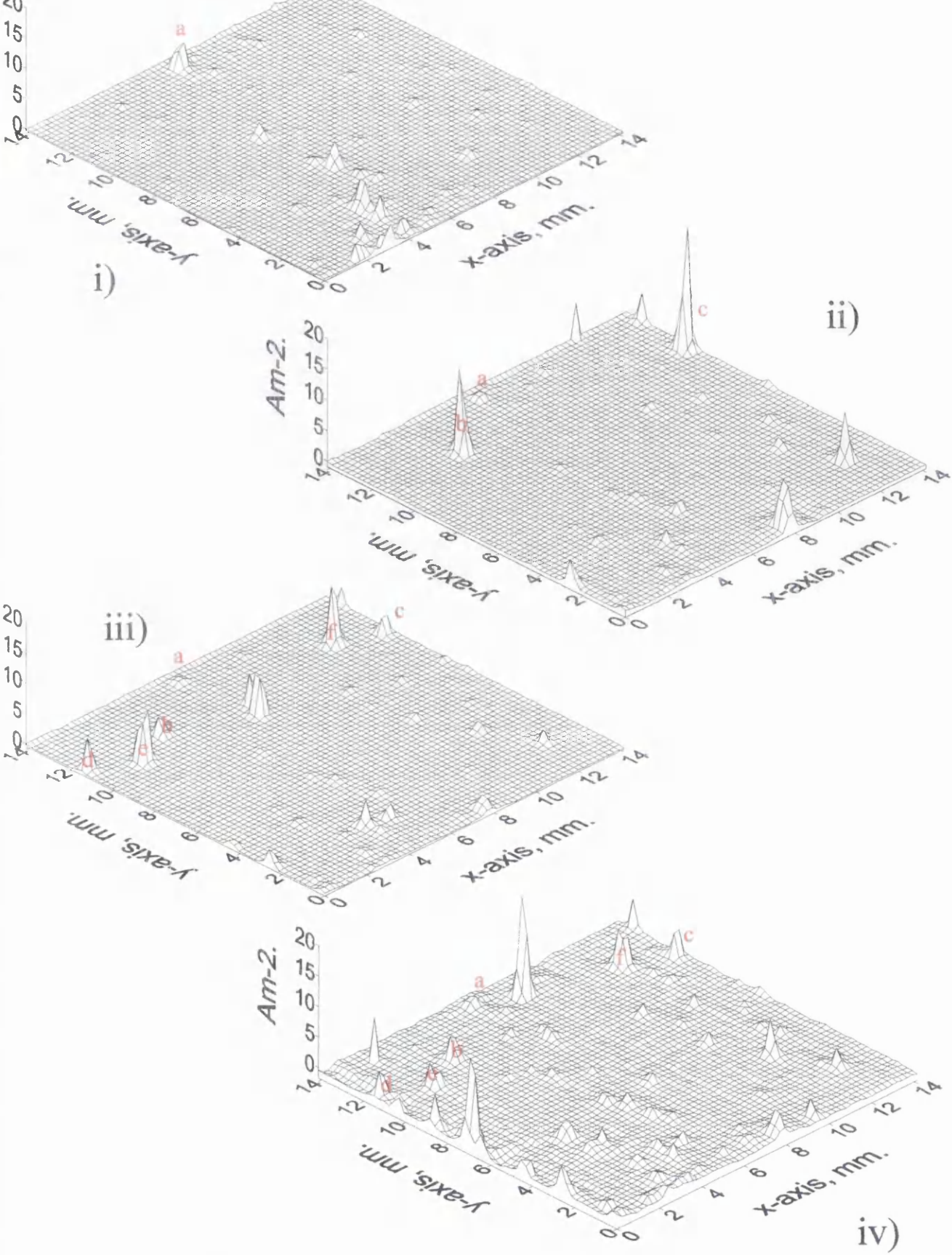

Figure 6.2: Surface plots of SVET scans for AA2024-T3 freely corroding in 3.5% w/w NaCl, after i) 0 hours, ii) 8 hours, iii) 16 hours and iv) 24 hours immersion.

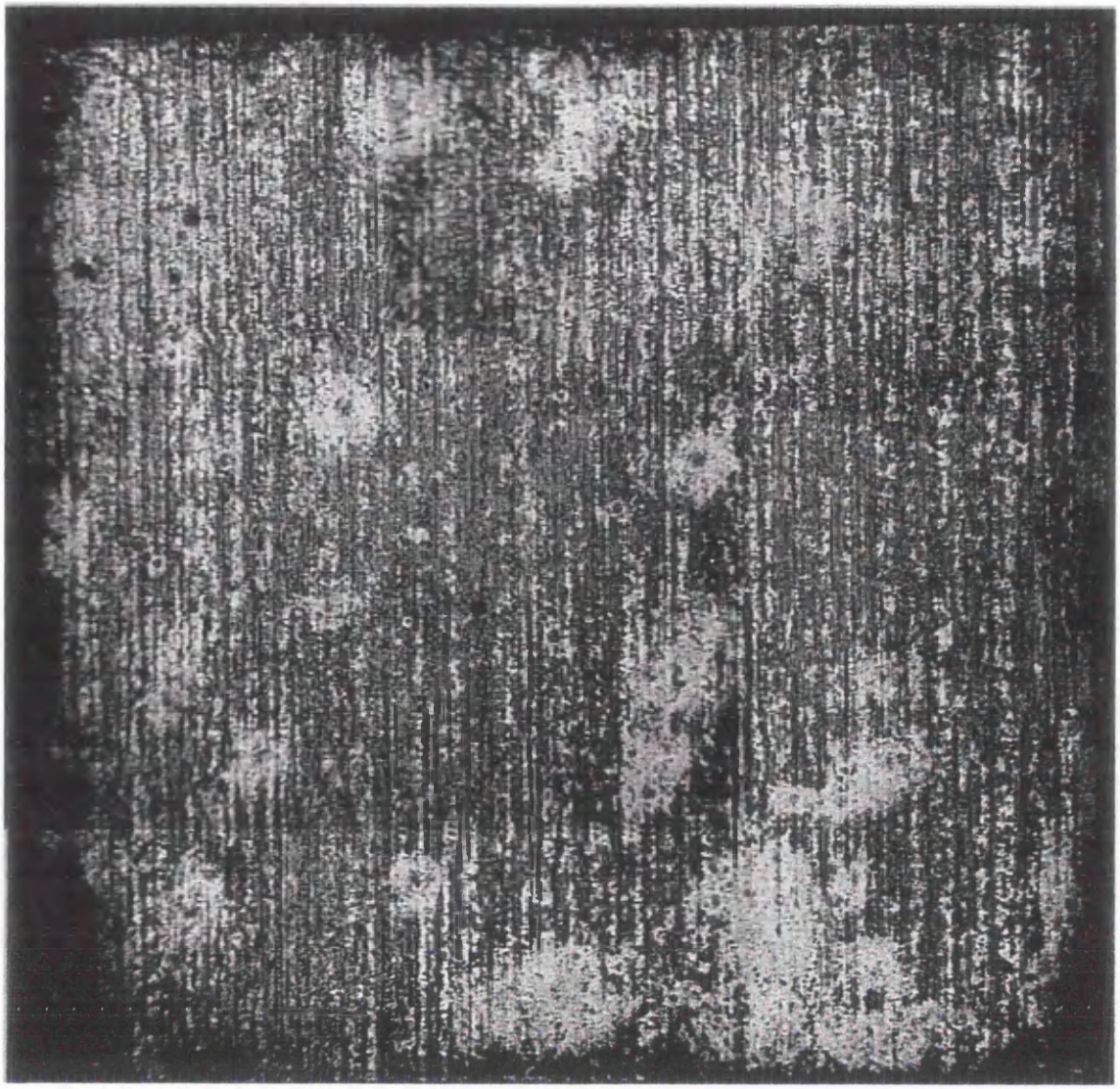

Figure 6.3: Optical micrograph of the exposed AA2024-T3 sample surface seen in figure 6.2, after 24 hours immersion in 3.5% w/w aqueous NaCl at 25°C.

took approximately 30 seconds to complete. Scans commenced at the point denoted as the origin of the corresponding current density map. It may therefore be understood from figure 6.2 that pitting corrosion becomes initiated on the alloy surface within a few seconds of electrolyte contact.

The visual appearance of the AA2024-T3 surface after 24 hours immersion is illustrated in figure 6.3. The corroded surface was covered with a large number (~20 cm^{-2}) of pits, with diameters ranging from 35 to 250 μm. Individual pits were surrounded by an approximately flat deposit of white corrosion product, which was particularly evident in the case of the larger pits where the diameter of the deposit area was in the range (0.1-0.5mm). The remainder of the AA2024-T3 surface was covered with a dark tarnish. It was observed optically, that the physical position of a pit on the surface after immersion, corresponded very closely with a peak at the same co-ordinates on the SVET potential data. Hence, peaks in the SVET potential data were taken to depict pits on the corroding surface. Due to the underlying noise level, a threshold was required to separate the noise from peaks produced by pitting on the surface. A value of 0.2 Am^{-2} was taken as the maximum value at which a detected peak could potentially be due to noise, rather than due to an anodic site on the corroding surface. Therefore, a pit is defined as any $jz_{(x,y)}$ peak above 0.2 Am^{-2}.

Following initiation, individual pits propagate for varying periods of time before passivating. Thus it may be seen from figure 6.2 that some pits remain active over an 8 hour period or longer (lettered a-f in figure 6.2) whereas many more do not. In principle, SVET data of the sort shown in figure 6.2 should allow the time-dependence of individual pitting events to be observed over two different time-scales. The first of these is the time between successive line scans, here ~30 seconds. The second is the time between area scans, here 1 hour. Using the point density shown in

figure 6.2 the current from an individual pit is typically detected in 4-5 successive line-scans. This implies a pit lifetime > 2-2.5 minutes, which is consistent with stable pitting. However, if a pit is detected in only one line scan, and not in its neighbours, then it may be concluded that the lifetime of that particular pitting event is <30 seconds, which is consistent with metastable pitting. However, at any instant the SVET probe sees only a very small fraction of the sample surface and this, together with the relatively slow rate of scan, implies that SVET will detect only a very small fraction of the total number of metastable pitting events. Typically, each SVET area scan contains only one or two $jz_{(x,y)}$ features which could be interpreted as metastable pitting, *i.e.* features with lifetime <30 sec. Figure 6.4 shows a surface plot where only the data points of the same y value are joined. This makes it easier to see peaks which only last one line of scanning, implying metastable pitting. Furthermore, the peak $jz_{(x,y)}$ values associated with these metastable pitting events are typically more than an order of magnitude lower than that associated with stable pits. Consequently, we may assume that the $jz_{(x,y)}$ distributions seen in figure 6.2 derive substantially from stable pitting events.

Anodic current density measurements:.

The total anodic current (i_a) present in each of the $j_{(x,y)}$ distribution maps exemplified in figure 6.2 was determined using equation 3.1 with a threshold (Th) current density value of 0.2 Am^{-2}. In this manner one value of J_{corr} was obtained from each hourly SVET scan. Five successive scans were carried out on bare AA2024-T3 to determine the reproducibility of the technique. J_{corr} is plotted as a function of time in figure 6.5. The coloured lines show how the anodic current density varies with time of immersion for each experiment. The black line with the circle symbol indicates the

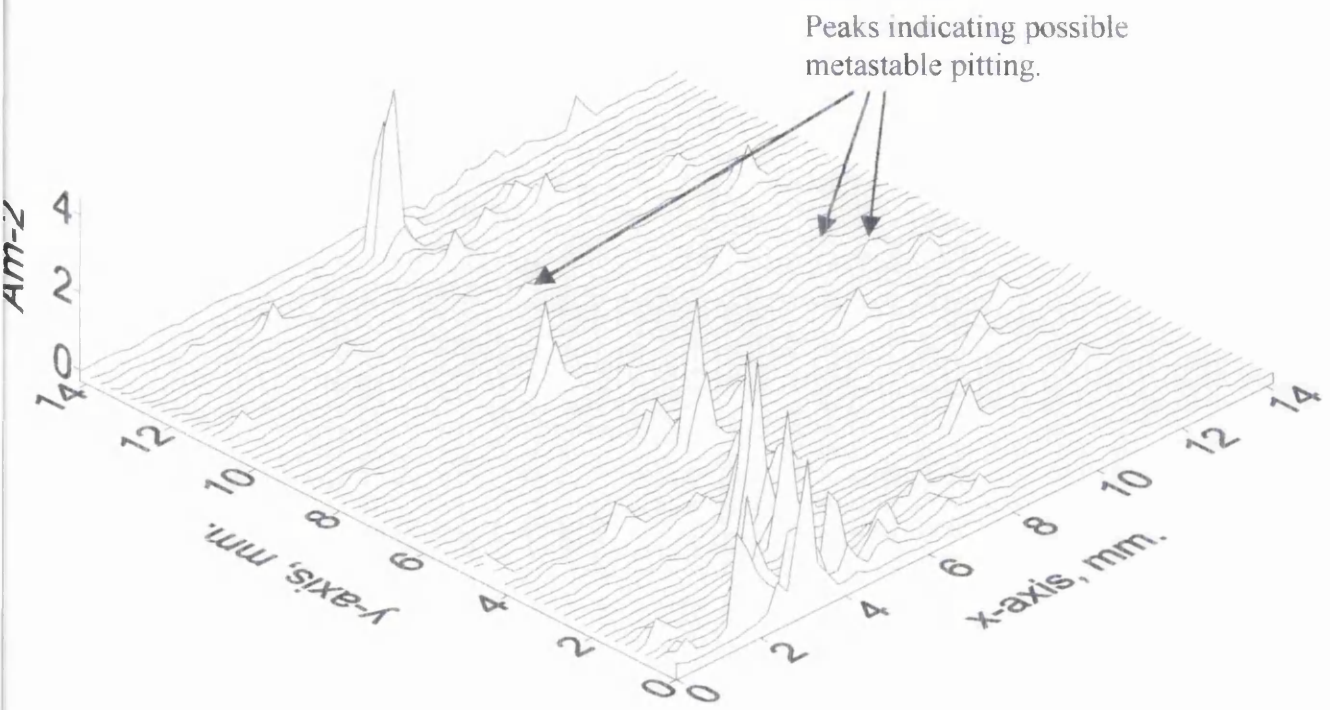

Figure 6.4: Surface plot of SVET scans for AA2024-T3 freely corroding in 3.5% w/w NaCl immediately after immersion.

average value for each hour. Figure 6.5 shows a fairly large degree of scatter in corrosion rate. Consequently, the average of the five experiments will be used to show the case of uninhibited AA2024-T3. The black line in figure 6.5 shows that J_{corr} is initially ~0.019 Am^{-2}, rising to a maximum of ~0.05 Am^{-2} after 4 hours and falling to a minimum of ~0.008 Am^{-2} after 24 hours. This decrease in anodic current density throughout the experimental period is consistent in all five uninhibited experiments, and therefore depicts a general trend in the corrosion characteristics of AA2024-T3 freely corroding in 3.5% w/w NaCl.

Figure 6.6 shows how the number density of stable pits as detected by the SVET varies with time of immersion. As shown in figure 6.5 the coloured lines indicate the five separate experiments carried out, and the black line with the circle symbols shows the average value. Since the average number density of stable pits actually increases slightly between 5 and 24 hours immersion, the implication is that, over this period, the average current associated with individual pits becomes steadily reduced.

The total quantity of charge emitted from corrosion pits (Q) over the 24 hour experimental period was calculated from J(t) using equation 3.2. The mean value of Q obtained from 5 repetitions of the 24 hour immersion experiment, using a freshly prepared AA2024-T3 sample each time, was 2026 ± 640 Cm^{-2}, which corresponds to a *teal* value of 0.189 ± 0.060 g m^{-2}.

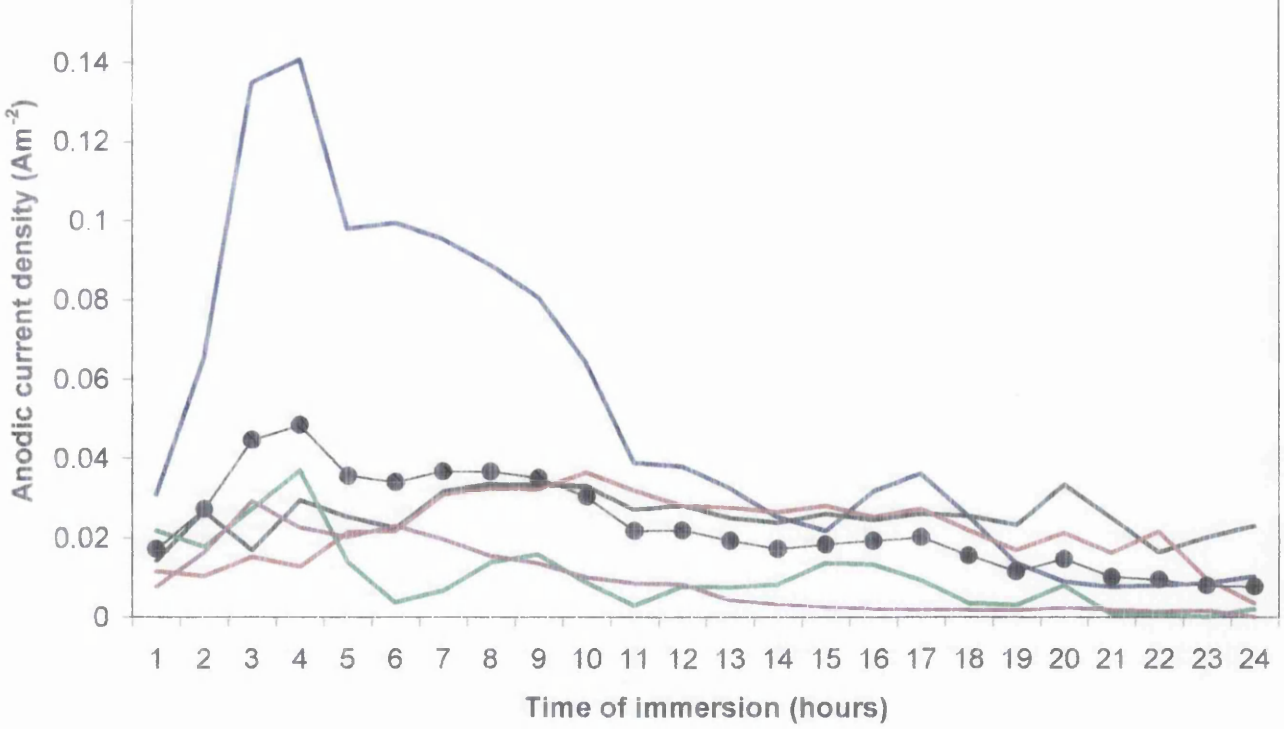

Figure 6.5: Plot of area-averaged anodic current density (J(t)) versus immersion time for AA2024-T3 freely corroding in 3.5% w/w aqueous NaCl. Coloured lines show the range of anodic current density for five separate experiments. Black line with circle symbol represents mean value.

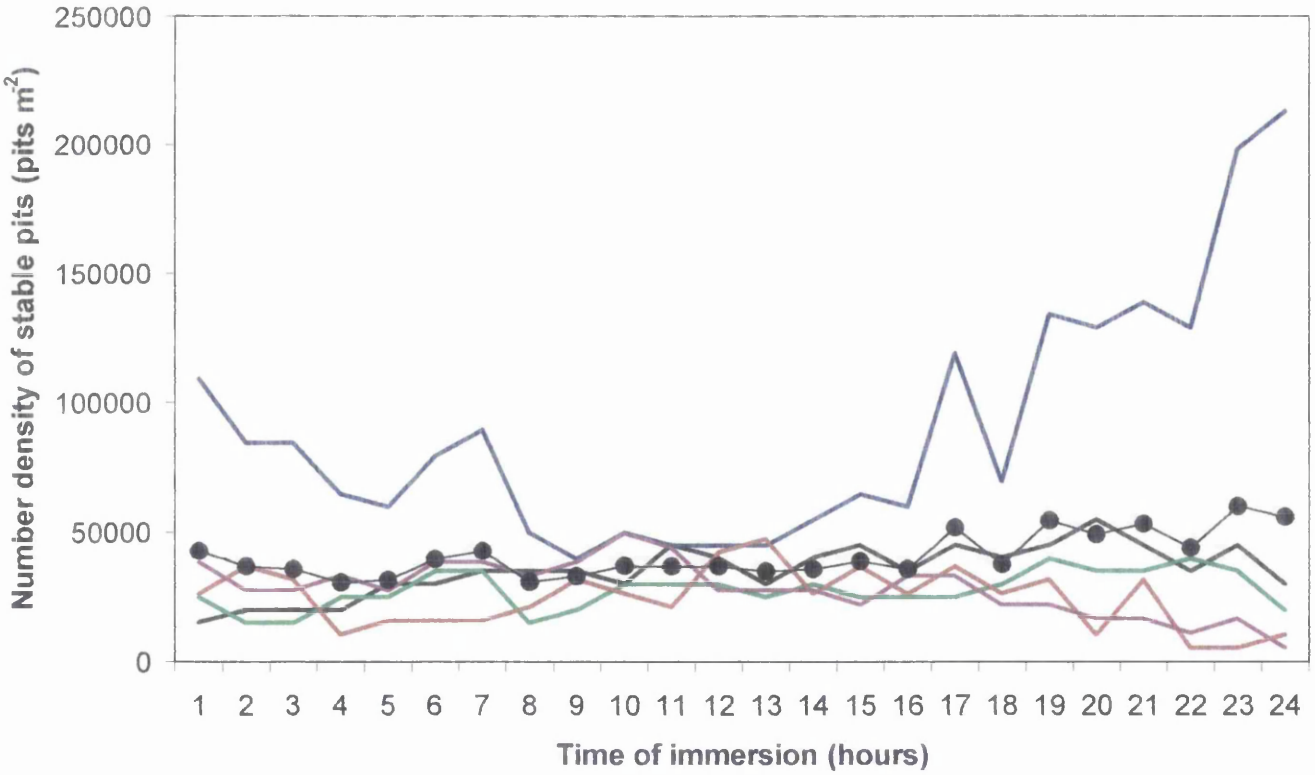

Figure 6.6: Plot of number density of stable pits versus immersion time for AA2024-T3 freely corroding in 3.5% w/w aqueous NaCl. Coloured lines show the range of number density of stable pits for five separate experiments. Black line with circle symbol represents mean value.

6.3.2: Inhibited corrosion of AA2024-T3.

A series of experiments were carried out in which AA2024-T3 samples were immersed in 3.5% aqueous NaCl in which inhibitor was already present. The inhibitors used in these experiments were Na_2CrO_4, YCl_3, $LaCl_3$ and $CeCl_3$, in concentrations varied systematically between 2.5 x 10^{-3} mol dm^{-3} and 2.5 x 10^{-5} mol dm^{-3}. In the case of Na_2CrO_4 additional experiments were carried out in which the inhibitor was added to the experimental electrolyte 5 hours after sample immersion, i.e. after stable pitting had become well established. As in the uninhibited experiment, SVET scanning was carried out immediately on immersion and at 1 hour intervals thereafter for 24 hours. Figure 6.7 shows a representative set of current density distribution ($jz_{(x,y)}$) maps obtained in the presence of 2.5 x 10^{-5} mol dm^{-3} YCl_3. Comparison of figures 6.2 and 6.7 shows how the YCl_3 inhibitor acts to progressively reduce both the number and the intensity of corrosion pits. Figure 6.8 is an example of an optical picture taken after the sample was immersed in 3.5% w/w aqueous NaCl containing 2.5 x 10^{-3} mol dm^{-3} $CeCl_3$. Comparing this to figure 6.3 it can be seen that the surface has greatly been protected by the rare earth inhibitor, however a small amount of corrosion has occurred on the right of the picture.

Figure 6.9 shows current density distribution maps in the presence of 2.5x10^{-3} mol dm^{-3} Na_2CrO_4, and comparison with figure 6.7 shows that the SVET is unable to detect surface corrosion at any time during the experiment. Time-dependent area-averaged corrosion current density (J(t)) values were obtained as before using equation 3.1. Figures 6.10a,b,c and d show plots of J(t) vs time for $CeCl_3$, $LaCl_3$, YCl_3 and Na_2CrO_4 respectively, present at the lowest (green line with solid triangle symbol) and highest (pink line with solid square symbol) experimental concentrations. The blue line with diamond symbols shows the average of five

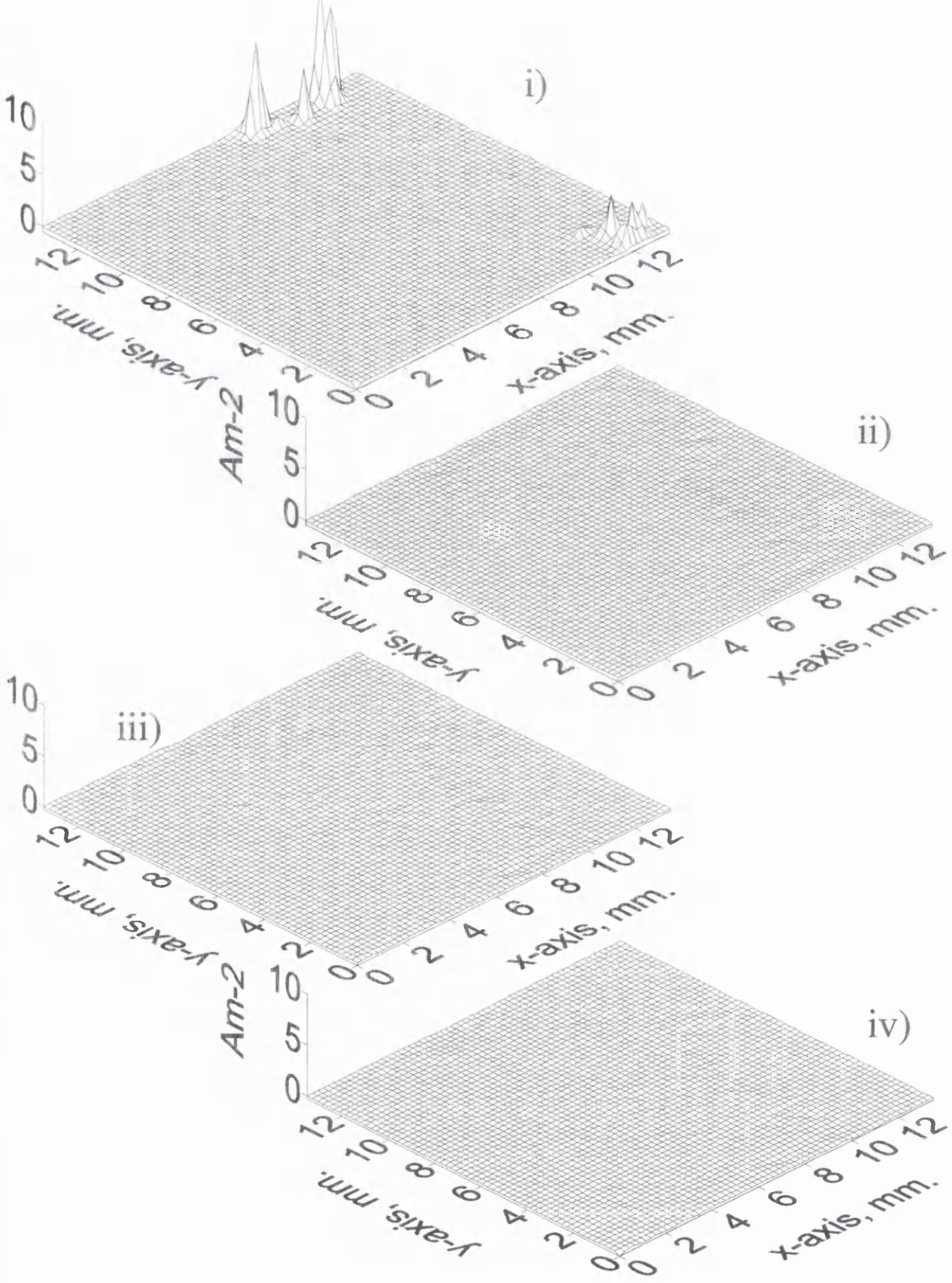

Figure 6.7: Surface plots of SVET scans for AA2024-T3 freely corroding in 3.5% w/w NaCl with 2.5 x 10^{-5} mol dm^{-3} YCl_3, after i) 0 hours, ii) 8 hours, iii) 16 hours and iv) 24 hours immersion.

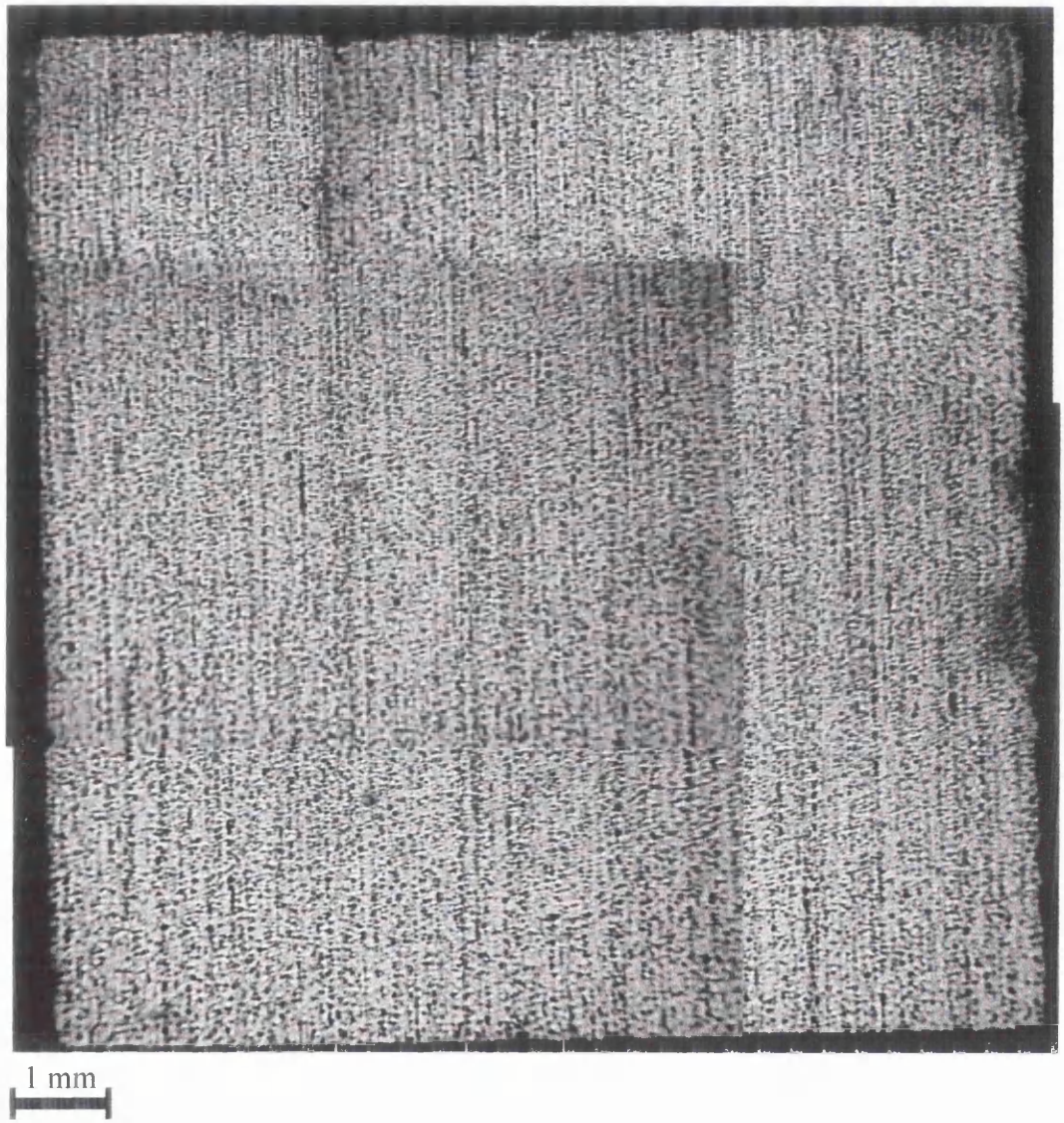

Figure 6.8: Optical micrograph of the exposed AA2024-T3 sample surface, after 24 hours immersion in 3.5% w/w aqueous NaCl with 2.5 x 10^{-3} mol dm^{-3} $CeCl_3$ added at 25°C.

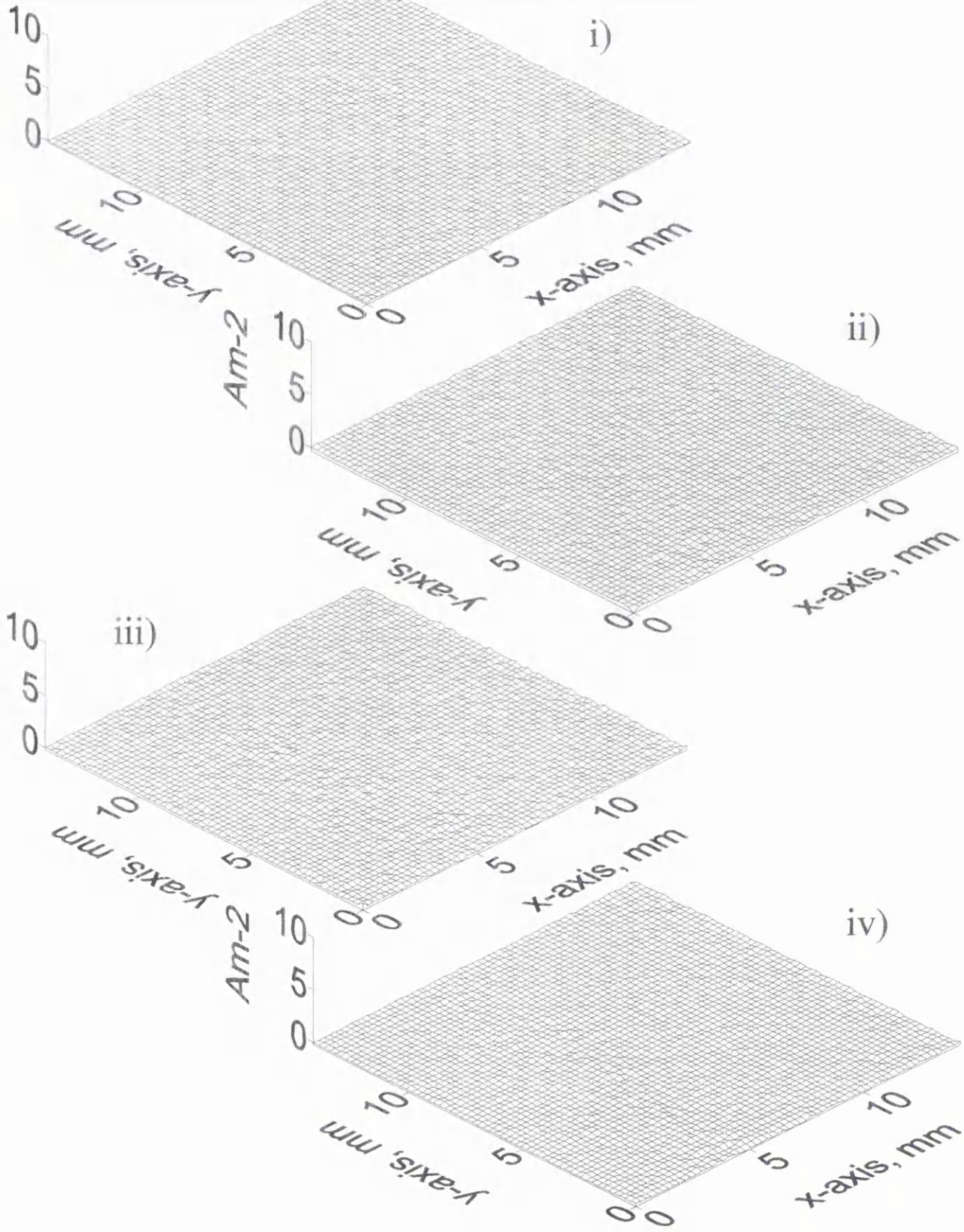

Figure 6.9: Surface plots of SVET scans for AA2024-T3 freely corroding in 3.5% w/w NaCl with 2.5 x 10^{-3} mol dm^{-3} Na_2CrO_4, after i) 0 hours, ii) 8 hours, iii) 16 hours and iv) 24 hours immersion.

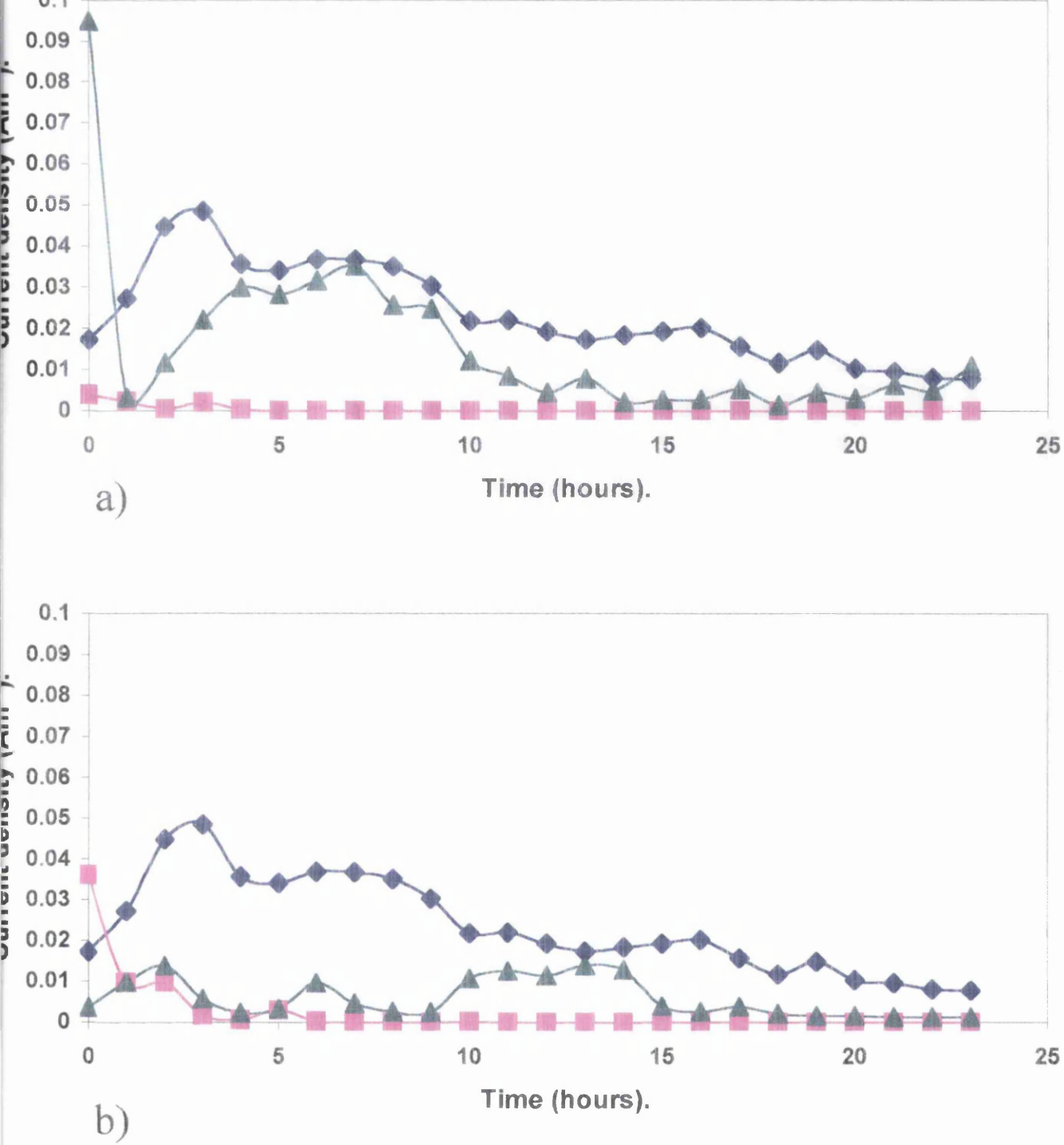

Figure 6.10: Plots of area-averaged anodic current density (J(t)) versus immersion time for AA2024-T3 corroding in 3.5%w/w aqueous NaCl. The blue line with diamond symbol shows the mean of five experiments in the absence of inhibitor. Inhibitors: a) $CeCl_3$, b) $LaCl_3$. Inhibitor concentrations: Pink with square = 2.5×10^{-3} mol dm^{-3}, Green with triangle = 2.5×10^{-5} mol dm^{-3}.

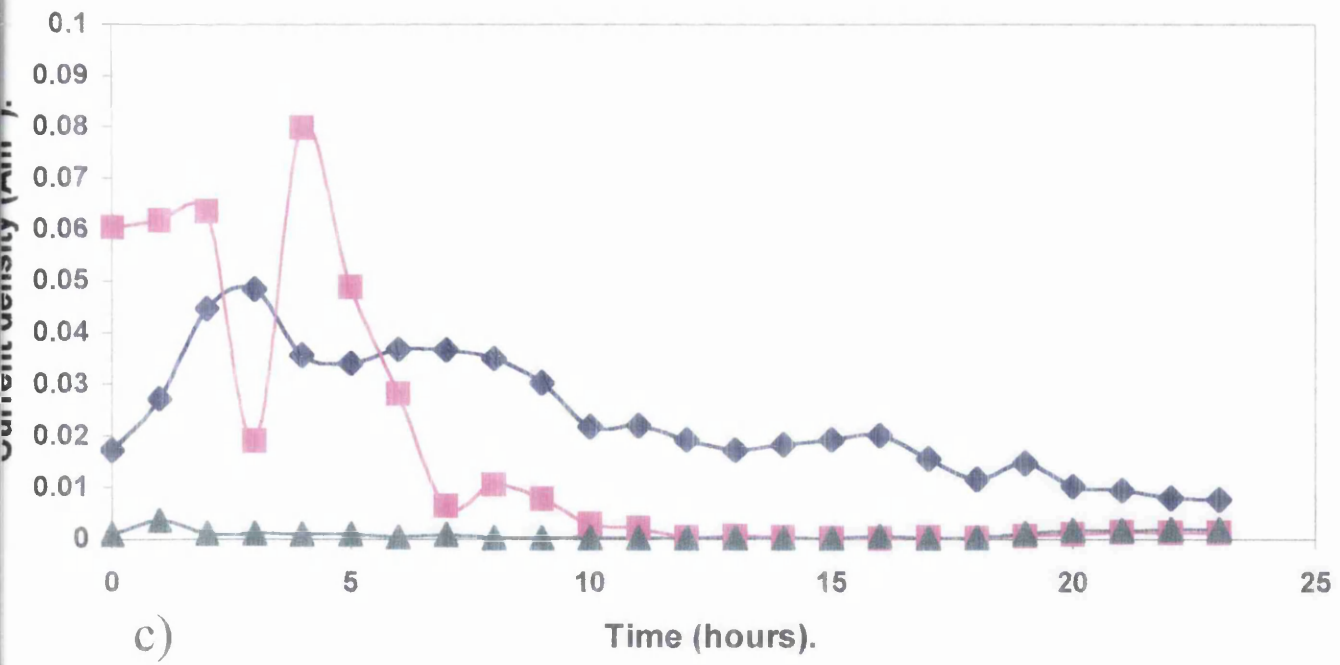

c)

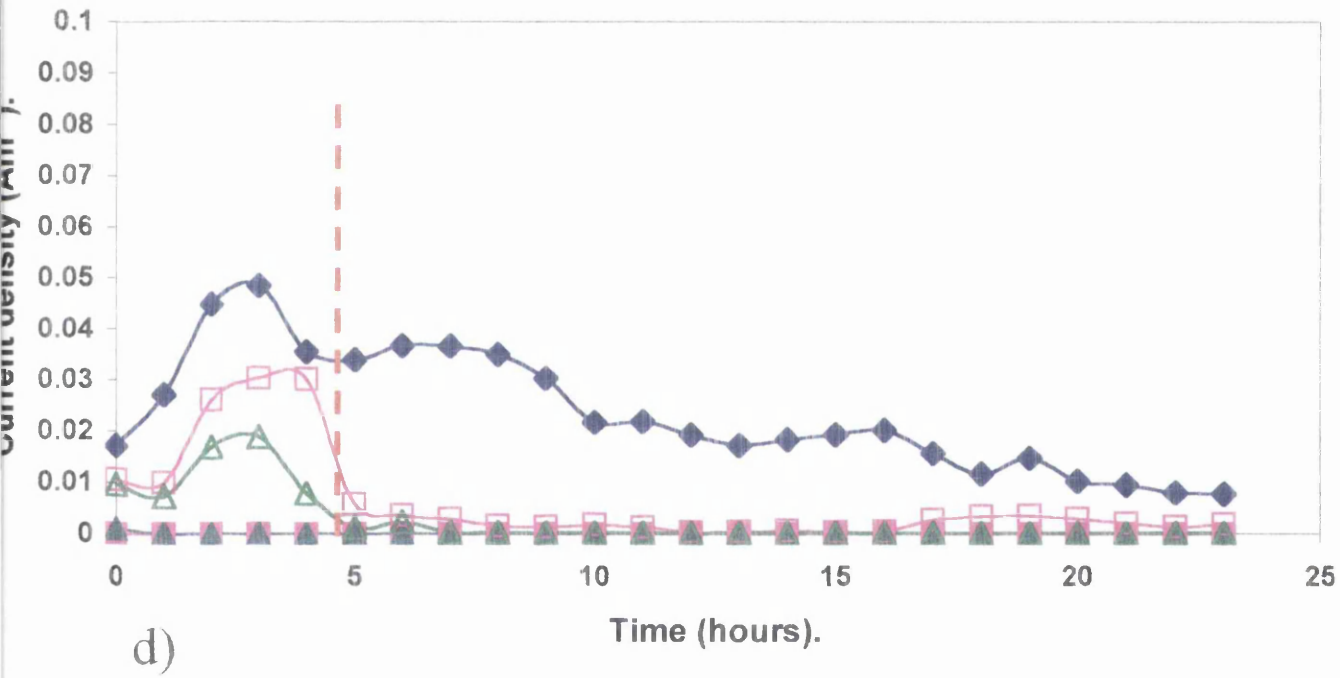

d)

Figure 6.10: Plots of area-averaged anodic current density (J(t)) versus immersion time for AA2024-T3 corroding in 3.5%w/w aqueous NaCl. The blue line with diamond symbol shows the mean of five experiments in the absence of inhibitor. Inhibitors: c) YCl_3, and d) Na_2CrO_4. Inhibitor concentrations: Pink with square = 2.5×10^{-3} mol dm^{-3}, Green with triangle = 2.5×10^{-5} mol dm^{-3}.

In d) (Na_2CrO_4 plot) the hollow symbols represent experiments where inhibitor was added after 5 hours immersion (shown with red dotted line).

uninhibited experiments. In figure 6.10d the two additional series (hollow symbols) on the plot show cases where the Na_2CrO_4 was added to the electrolyte after pitting corrosion was well established, and the red dotted line indicates the time at which the inhibitor was added.

It may be seen from figure 6.10d that when present from t=0 Na_2CrO_4 reduces the J(t) values to well below the uninhibited case at all experimental concentrations. For Na_2CrO_4 = 2.5 x 10^{-3} mol dm^{-3} J(t) is effectively zero, i.e. below the detection limit of the SVET, throughout the experimental period. However, pitting currents were detectable initially for lower Na_2CrO_4 concentrations. For example, figure 6.10d shows that Na_2CrO_4 = 2.5 x 10^{-5} mol dm^{-3} J(t) was 0.001 Am^{-2} in the initial SVET scan but fell to zero after 1 hour of immersion. Figure 6.10d also shows that when Na_2CrO_4 is added to the electrolyte after pitting corrosion is well established, it does not inhibit pitting corrosion so completely as when it is present from t=0. That is to say although J(t) is greatly reduced within minutes of adding the inhibitor to the electrolyte, at no point is surface pitting corrosion completely inhibited. All the REM chloride inhibitors were found to reduce J(t) values but not as rapidly or as completely as in the case of Na_2CrO_4. Furthermore, the degree of inhibition was found to be dependent on the concentration of REM chloride salt present. For example, figure 6.10a shows that 2.5 x 10^{-3} mol dm^{-3} $CeCl_3$ reduces the initial value of J(t) to 4 x 10^{-3} Am^{-2}, with J(t) falling to zero after 4 hours immersion. Whereas, the same figure shows that 2.5 x 10^{-5} mol dm^{-3} $CeCl_3$ scarcely reduces J(t) values at all over the first 10-12 hours of immersion, although J(t) values do fall below the uninhibited case thereafter. Figure 6.10b shows that $LaCl_3$ acts in a similar fashion to $CeCl_3$, although J(t) values are less concentration dependent. Figure 6.10c suggests that YCl_3 behaves

anomolously, producing a greater reduction in J(t) values at 2.5 x 10^{-5} mol dm^{-3} than at 2.5 x 10^{-3} mol dm^{-3}.

Thus, the data shown in figure 6.10 indicate that all the REM chloride salts inhibit the pitting corrosion of AA2024-T3 to some extent, provided they are present in sufficient concentration. However, figure 6.10 also indicates that the REM chloride salts do not typically produce so rapid or so complete an inhibition as does chromate.

The equivalent metal loss over the 24 hour experimental period was calculated using equation 3.3. The results for both uninhibited and inhibited cases are shown in figure 6.11. Figure 6.11a shows the total metal loss for $CeCl_3$ at the five experimental concentrations. These can be compared to the blue dashed line which depicts the average of the uninhibited experiments. It can be seen that at the higher concentrations $CeCl_3$ inhibits surface pitting corrosion on AA2024-T3 quite effectively, however its effectiveness deteriorates at lower concentrations. Figure 6.11b shows the total metal loss for $LaCl_3$, although it does not appear as effective as $CeCl_3$ it does follow the same trend in inhibition. Figure 6.11c shows the same information for YCl_3, as can be seen from this graph Yttrium seems to inhibit corrosion most effectively at the middle concentrations used. At the highest and lowest concentrations YCl_3 was very unpredictable, in fact at these concentrations repeat experiments showed little reproducibility with respect to the uninhibited cases and the middle concentration of YCl_3 (after repeated experiments error bars (± standard deviation on the mean) were produced at three concentrations for YCl_3). Figure 6.11d shows the results for Na_2CrO_4. It illustrates that at the highest concentration the SVET was unable to detect any surface pitting corrosion, and at the lower concentrations chromate inhibited corrosion more effectively than any of the

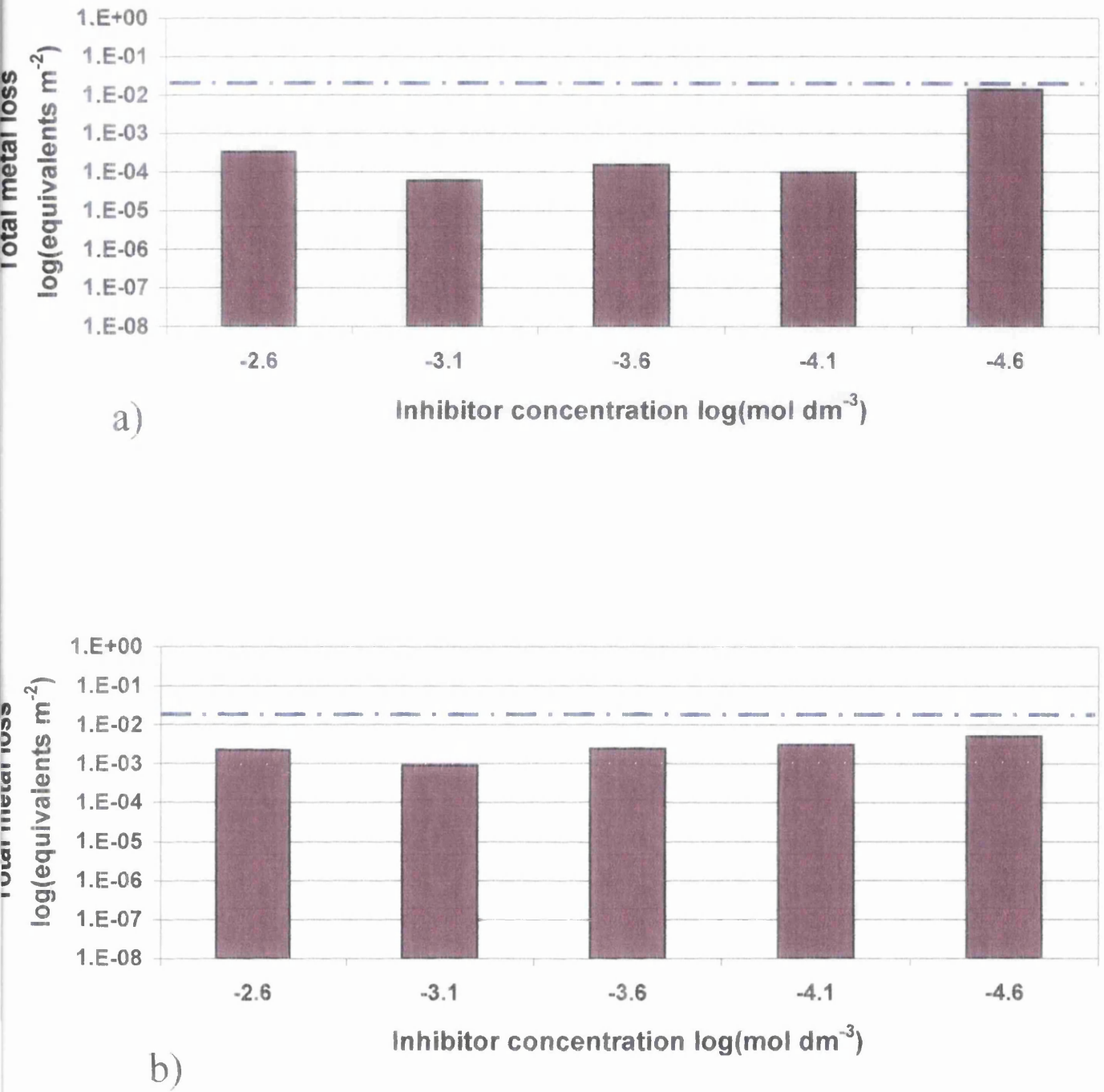

Figure 6.11: Metal loss in equivalents per square metre for AA2024-T3 corroding in 3.5%w/w aqueous NaCl at 25°C for 24 hours. The blue dashed line shows the mean of five experiments in the absence of inhibitor. Inhibitors: a) $CeCl_3$, b) $LaCl_3$,.

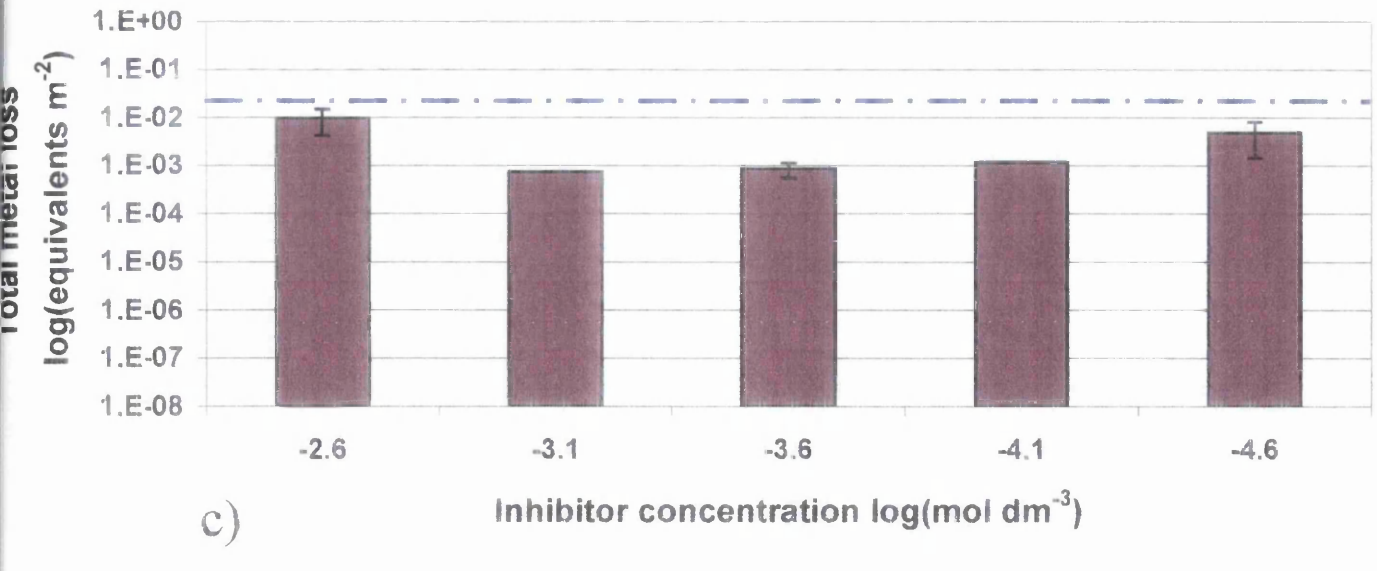

c)

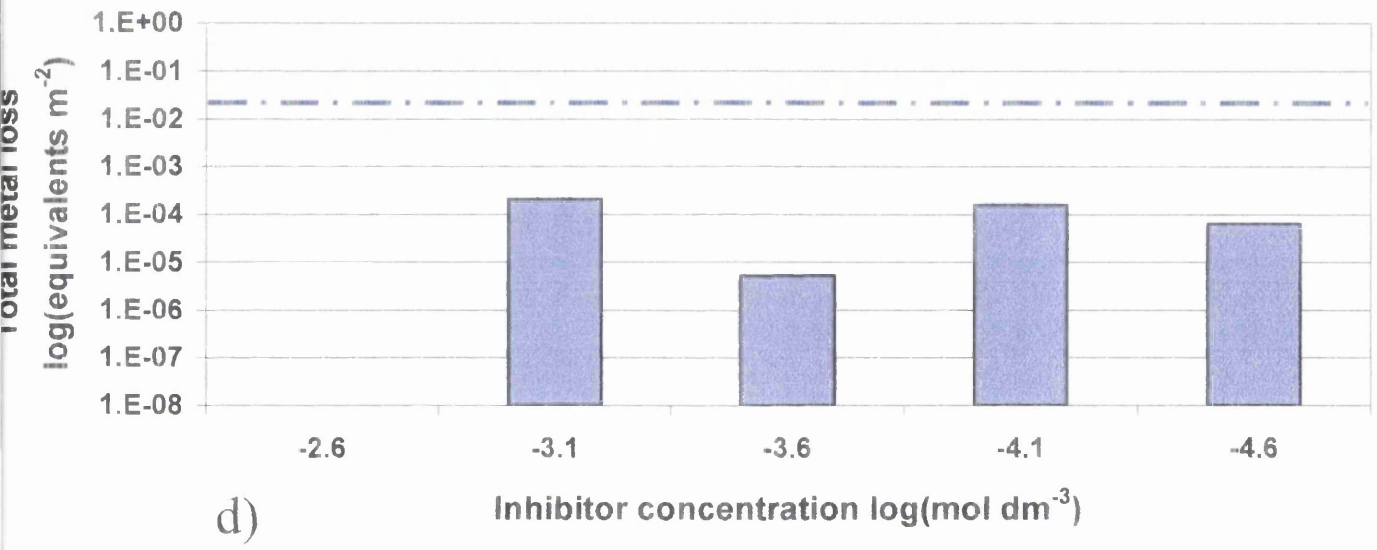

d)

Figure 6.11: Metal loss in equivalents per square metre for AA2024-T3 corroding in 3.5%w/w aqueous NaCl at 25°C for 24 hours. The blue dashed line shows the mean of five experiments in the absence of inhibitor. Inhibitors: c) YCl_3, and d) Na_2CrO_4.

other inhibitors used. It may be seen from figure 6.11 that inhibitor efficiency increases in the order $Y^{3+} \sim La^{3+} < Ce^{3+} < CrO_4^{2-}$. Furthermore, it may be seen from figure 6.10 that the principal reason for the lower efficiencies of the REM cations is the slower onset of inhibition observed with these species. That is to say, whilst the ultimate reduction in pitting current may be similar in the case of REM and chromate inhibitors, the persistence of pitting current for longer periods in the case of REM cations gives rise to significantly higher levels of metal loss. It would seem reasonable to propose that the slower onset of inhibition in the case of REM cations arises from the need for corrosion, and associated cathodic oxygen reduction, to proceed in order to allow the deposition of a REM (hydr)oxide cathodic film. In contrast chromate may act as a cathodic depolariser, producing rapid surface passivation without the requirement for significant levels of corrosion to have occurred.

Figure 6.12 shows how the number density of pits detected by the SVET varies with time of immersion for each of the inhibitors at the highest (2.5×10^{-3} mol dm^{-3}, pink line with square symbol) and lowest (2.5×10^{-5} mol dm^{-3}, green line with triangle symbol) concentrations used. The blue line with diamond symbols depicts the mean value obtained from five uninhibited experiments. The experiments from which these results were taken are the same as used for figure 6.10, hence the pink line in figure 6.12a corresponds directly to the pink line in figure 6.10a. From this it is possible to deduce that the number density of pits on a surface is not necessarily related to the anodic current density. An example of this can be seen with the lowest concentration of cerium (green lines in figures 6.10a and 6.12a). In figure 6.10a it can be seen that the anodic current density is greatly reduced after 10 hours immersion,

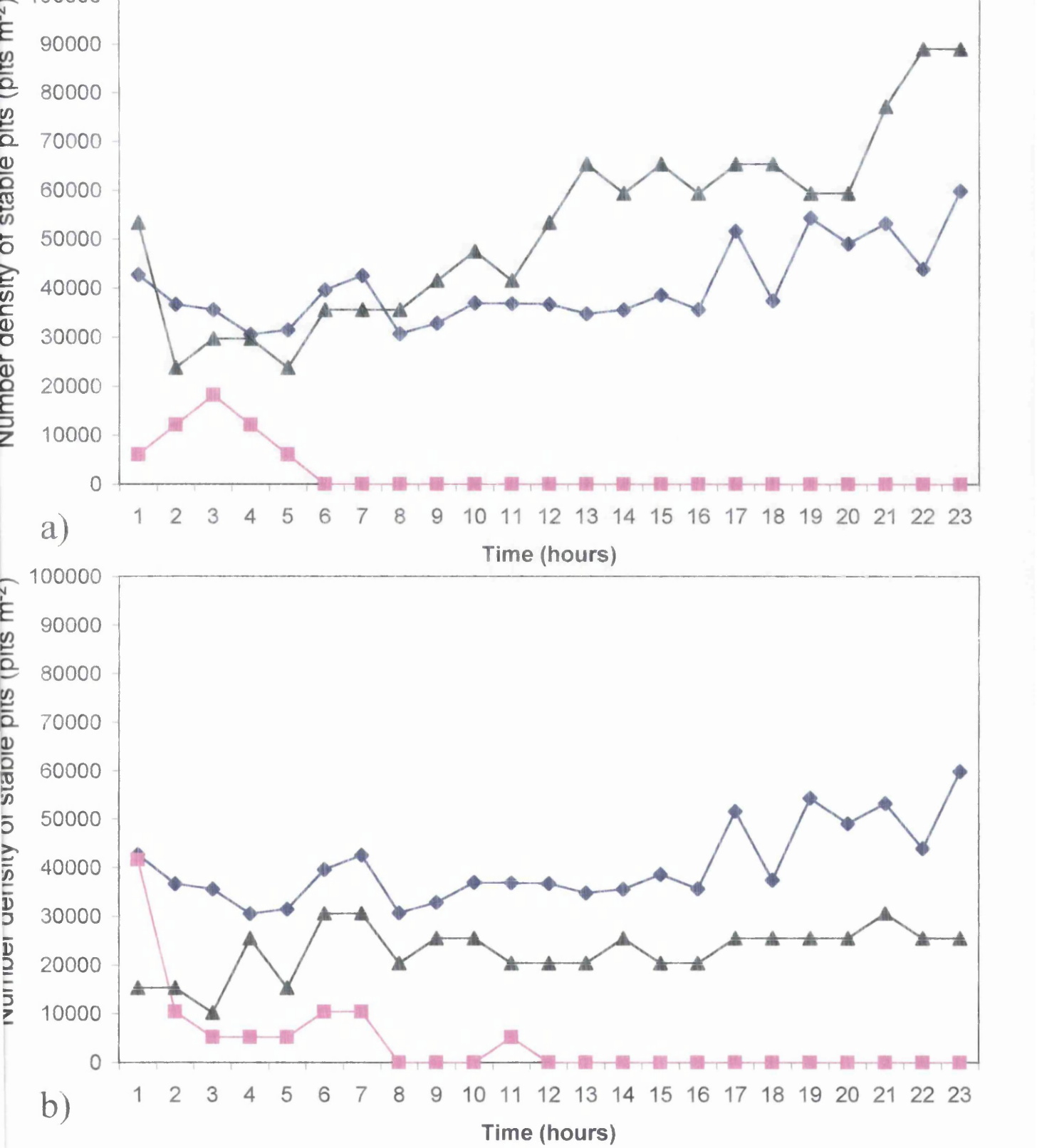

Figure 6.12: Plots of number density of stable pits versus immersion time for AA2024-T3 corroding in 3.5%w/w aqueous NaCl. The blue line with diamond symbol shows the mean of five experiments in the absence of inhibitor. Inhibitors. a) $CeCl_3$, b) $LaCl_3$. Inhibitor concentrations: Pink with square = 2.5×10^{-3} mol dm^{-3}, Green with triangle = 2.5×10^{-5} mol dm^{-3}.

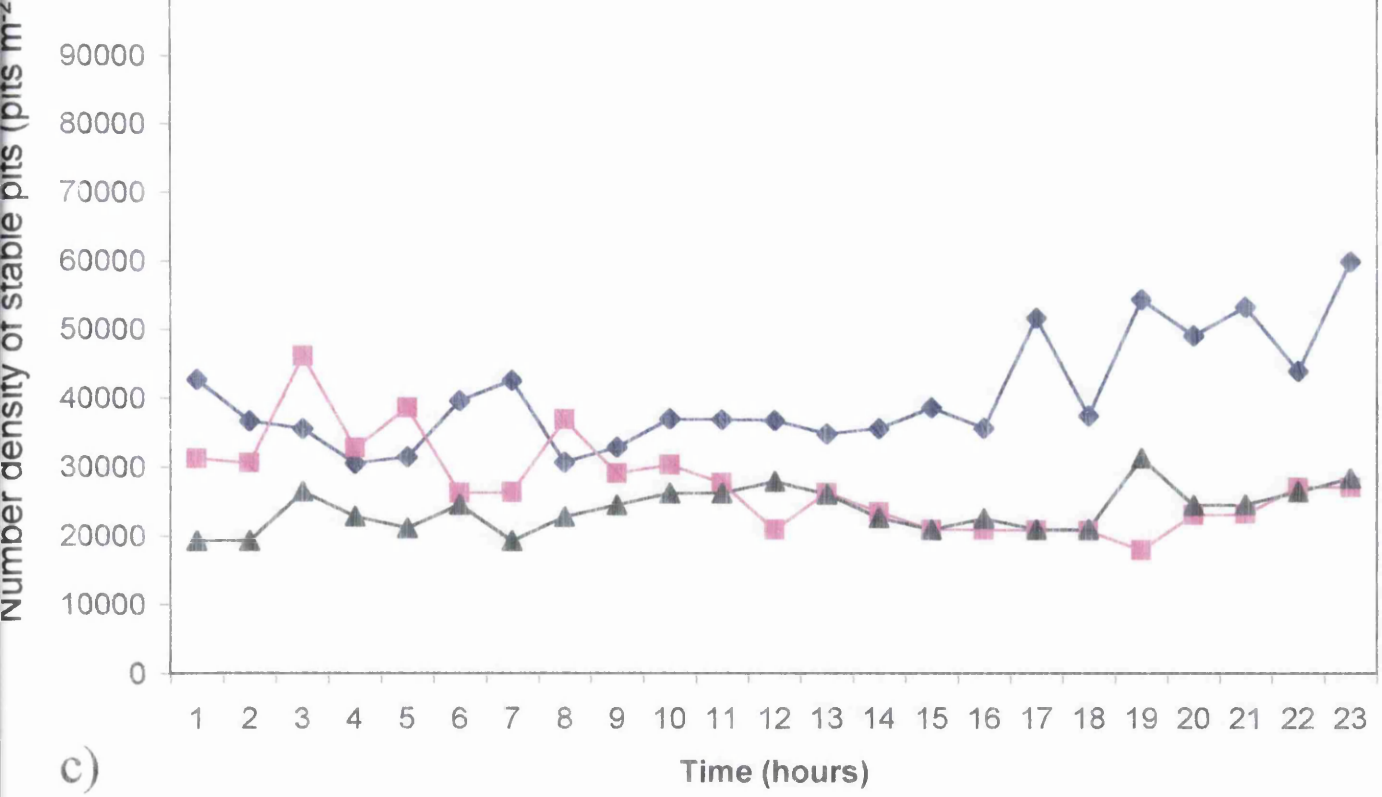

c)

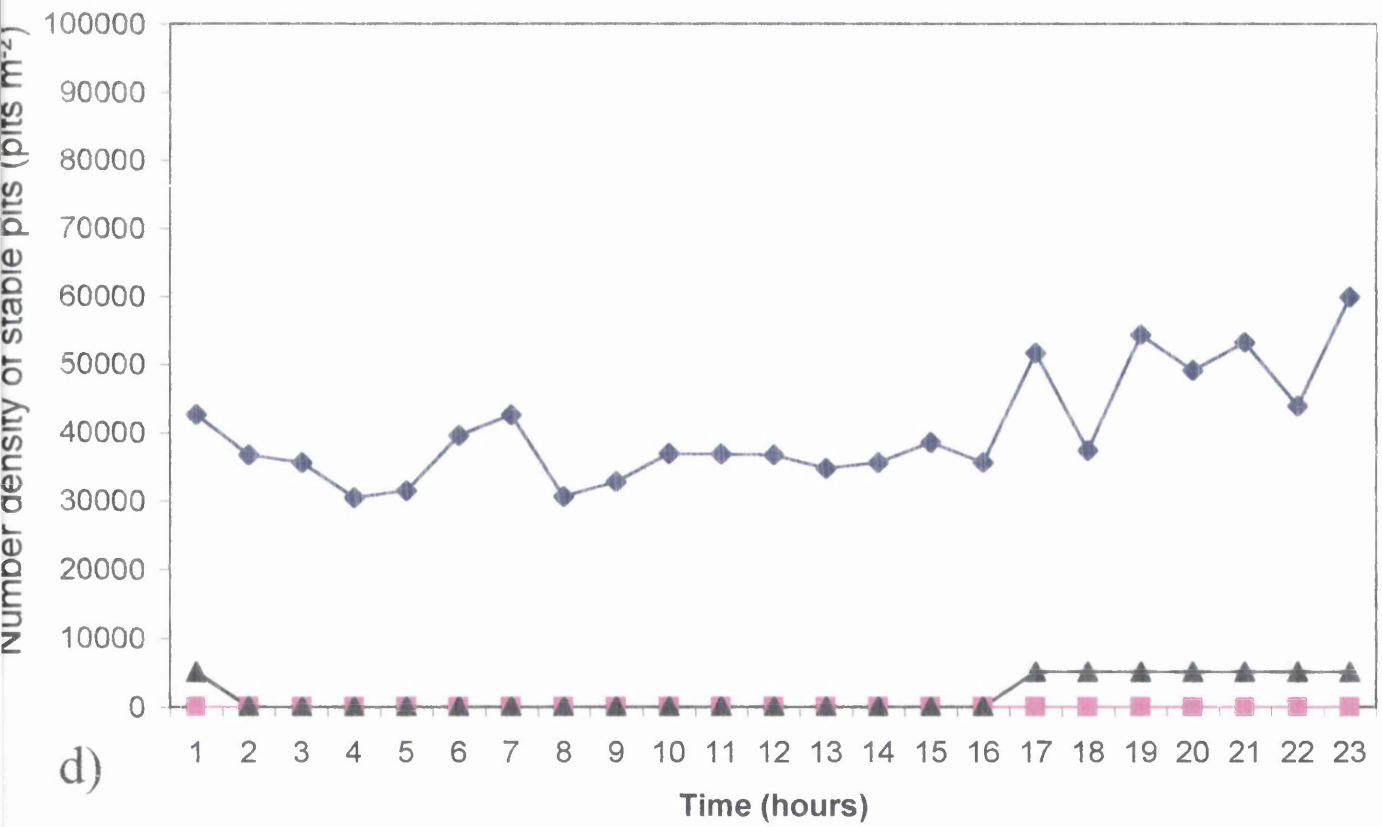

d)

Figure 6.12: Plots of number density of stable pits versus immersion time for AA2024-T3 corroding in 3.5%w/w aqueous NaCl. The blue line with diamond symbol shows the mean of five experiments in the absence of inhibitor. Inhibitors: c) YCl_3, and d) Na_2CrO_4. Inhibitor concentrations: Pink with square = 2.5×10^{-3} mol dm^{-3}, Green with triangle = 2.5×10^{-5} mol dm^{-3}.

however from figure 6.12a it can be seen that at this time the number density of pits detected increases. Other cases like this can be seen in figures 6.10c and 6.12c.

6.4: Conclusions.

It has been shown that a "thresholded" numerical integral of SVET current density data obtained from unpolarised samples of AA2024-T3 undergoing pitting corrosion in 3.5% w/w aqueous NaCl may be used to obtain a series of instantaneous values for the area-averaged anodic current density. These current density values may, in turn, be numerically integrated with respect to time in order to obtain a value for equivalent metal loss over a 24 hour period. By using such an approach it has been shown that the efficiency of chromate and trivalent REM cations as inhibitors of AA2024-T3 surface pitting corrosion increases in the order $Y^{3+} \sim La^{3+} < Ce^{3+} < CrO_4^{2-}$. It has also been shown that the principal reason for the higher efficiency of CrO_4^{2-} is that corrosion currents decay more rapidly in the presence of CrO_4^{2-} than in the presence of the REM cations[20]. However for the cases where Na_2CrO_4 was added to the electrolyte after surface pitting corrosion was well established, it was shown that the inhibition of corrosion was not as complete as for the same concentration of Na_2CrO_4 present in the electrolyte from initiation. The more rapid onset of inhibition by CrO_4^{2-} may arise from the ability of CrO_4^{2-} reduction to replace cathodic O_2 reduction, quickly generating a Cr(III) (hydr)oxide cathodic film. Alternatively, competitive adsorption of CrO_4^{2-} on the AlO_3 surface oxide may coulombically disfavour Cl^- adsorption, reducing the possibility of surface depassivation. The second possibility is consistent with the observation that CrO_4^{2-} inhibition is less complete if depassivation (pitting) has already commenced.

6.5: Reference:

[1] A. Marshall, *NACE National Conference*, Toronto, Ontario, paper-192, (1981).
[2] E.E. Abd El Aal, A. Abd El Aal and S.M. Abd El Haleem, *Anti Corrosion Methods and Materials*, **41**, 21, (1994).
[3] U.S. Public Health Service, *Toxicological Profile for Chromium, Report No ATSDR/TP 88/10*, Agency for toxic substances, U.S. Public Health Service, Washington D.C., (1989).
[4] U.S Environmental Protection Agency, "Health Assessment Document for Chromium", *Final Report*, EPA-600/8-83-014F, 21 (1984).
[5] G. Pallos and G. Wallwork, *Corrosion*, **38**, 305 (1982).
[6] H.N. McMurray, S.M. Powell and D.A. Worsley, *Corrosion*, **55**, 1040 (1999).
H.N. McMurray, S.M. Powell and D.A. Worsley, *Corrosion 99 NACE International Conference Proceedings*, San Antonio, Texas, paper 211, (1999).
[7] B.R.W. Hinton, D.R. Arnott and N.E. Ryan, *Metals Forum*, **7**, 211 (1984).
[8] B.R.W. Hinton, N.E. Ryan, D.R. Arnott and P.N. Trathan, *Corros. Australas.*, **10**, 12 (1985).
[9] D.R. Arnott, B.R.W. Hinton and N. E. Ryan, *Mater. Performance*, **26,** 211 (1987).
[10] B.R.W. Hinton and L. Wilson, *Corros. Sci.*, **29,** 967 (1989).
[11] B.R.W. Hinton, *J. Alloys and Compounds*, **180,** 15 (1992).
[12] A.J. Aldykiewicz, H. S. Isaacs and A. J. Davenport, *J. Electrochem. Soc.*, **142,** 3342, (1995).
[13] A. J. Aldykiewicz, A. J. Davenport and H. S. Isaacs *J. Electrochem. Soc.* **143,** 147 (1996).
[14] A. J. Davenport, H. S. Isaacs and M. W. Kendig, *Corros. Sci.*, **32,** 653 (1991).
[15] M. Bethencourt, F. J. Botana, M. A. Cauqui, M. Marcos, M. A. Rodriguez and J. M. RodriguezIzquierdo, *J. Alloys and Compounds*, **250,** 455 (1997).
[16] D.R. Arnott, B.R.W. Hinton and N. E. Ryan, *Corros. Sci*, **45,** 12 (1989).
[17] K.R. Baldwin, M.C. Gibson, P.L. Lane and C.J.E. Smith, *Proceedings of the 7th European Symposium on Corrosion Inhibitors*, Univ. Ferrara, N.S., Sez. V, **9**, 771 (1990).
[18] A. Perrone and O. Lotti, "*Present Status Standardisation of High – Strength Aluminium Alloys for Aerospace Applications*", *Aluminium Alloys in the Aircraft Industry – Symposium*, Technicopy Ltd, 21 (1976).
[19] C. L. Burton, L. W. Mayer and E. H. Spuhler, "*Aircraft and Aerospace Applications*", *Aluminium Design and Application*, (Ed. K. R. Van Horn) American Society for Metals, **2**, 415 (1967).
[20] S. O'Driscoll, H. N. McMurray and P. C. Morgan, "*Corrosion and Corrosion Protection*", *Proceedings of the International Symposium*, P.V. 2001-22, (Ed. J. D. Sinclair, R. P. Frankenthal, E. Kalman and W. Plieth) The Electrochemical Society, N.J, 452 (2001).

Chapter 7.

Chapter 7: Chromate inhibition of filiform corrosion on organic coated AA2024-T3 investigated using a scanning Kelvin probe.

7.1: Introduction.

Filiform corrosion (FFC), first described scientifically in 1944[1], is an atmospheric corrosion phenomenon affecting organic coated metals and producing characteristic "thread-like" deposits of corrosion product beneath the coating. Extensive studies on coated aluminium, steel and magnesium surfaces have shown that oxygen, aggressive ions such as chloride, and a high relative humidity must all be present for FFC to occur[2,3]. Filaments, each comprising a liquid filled "active head" and a "tail" of dry corrosion products, propagate from penetrative defects in the organic coating and may attain a length of several centimetres. The primary driving force for filament advancement is thought to be an oxygen concentration cell which forces anodic metal dissolution, reaction (7.1) in the case of aluminium, to occur at the leading edge and cathodic oxygen reduction, reaction (7.2), to occur at the trailing edge of the active head[2,3].

$$[Al(H_2O)_6]^{3+}{}_{(aq)} + 3e^- \rightleftharpoons Al_{(s)} + 6H_2O_{(l)} \qquad [7.1]$$

$$O_2 + 2H_2O + 4e^- \rightleftharpoons 4OH^-(aq) \qquad [7.2]$$

The absence of a bulk electrolyte, the small size of FFC features (width 0.1-0.5mm) and the high electrical resistance of organic coatings make FFC notoriously difficult to study by conventional electrochemical techniques[4,5,6]. However, recently published

developments in the scanning Kelvin probe (SKP) have shown that this non-contact, non-perturbing, technique allows spatially-resolved potential measurements to be made on metallic surfaces coated with intact insulating films and/or in contact with thin adsorbed layers of electrolyte[7,8,9,10,11,12,13,14,15]. The theory of SKP operation has been elaborated elsewhere[7,8,9,10,11], and a brief overview can be seen in section 2.2. The aim of our work has been to use SKP to carry out an investigation of the kinetics of FFC as it occurs on a model system comprising strontium chromate ($SrCrO_4$) pigmented polyvinyl butyral (PVB) coated AA2034-T3 aerospace aluminium alloy. This has been done with the intention of determining the mechanisms by which sparingly soluble chromate salts, such as $SrCrO_4$, act to inhibit FFC.

7.2: Experimental.

7.2.1: Materials.

All experiments were carried out using AA2024-T3 aluminium alloy as descibed in section 3.2.1 supplied by BAE Systems Ltd. Strontium chromate ($SrCrO_4$) pigment, primary particle size 1-3μm, was supplied as a 70% w/w suspension in xylene by Akzo Nobel UK Plc. All other chemicals were obtained from Aldrich plc in analytical grade purity. Aluminium alloy samples were cut into 35 mm square coupons and prepared as shown schematically in figure 7.1. Figure 7.1a shows how the sample was abrasively cleaned using increasingly fine grades of silica paper (400, 800, 1200 and 1600) along the rolling direction, followed by degreasing in ethanol. Figure 7.1b shows how two layers of PVC insulation tape were placed along the edge of the sample parallel to the polishing direction. This was to create a platform above the surface so that the film could be cast easily and evenly using a casting rod. The PVB solutions (15% w/w) were prepared in ethanol, and any required amount of

a) Sample abrasively polished with increasingly fine grades of silica paper, along the sample rolling direction. Then degreased using ethanol.

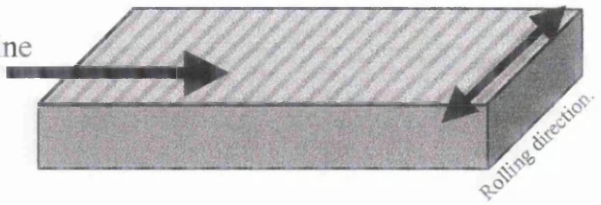

b) PVC insulation tape placed along sample edges to produce raised platform, to make casting easier. Pigmented PVB solution cast using bar.

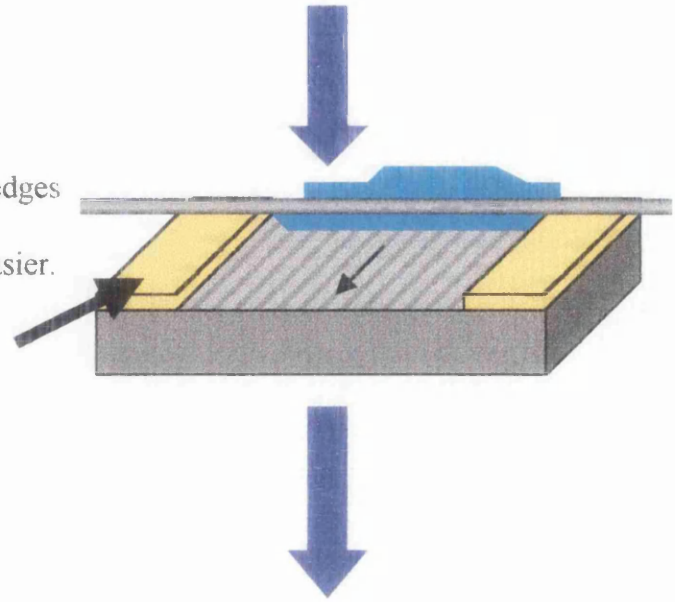

c) Pigmented PVB film left to dry in air. Result is 30μm thick film.

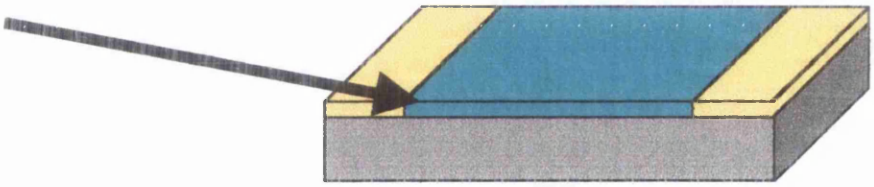

d) Filiform corrosion was initiated by applying a 1 μl volume of 0.5 mol dm^{-3} aqueous HCl along the length of a 10mm linear coating defect, scribed in the centre of PVB coated sample using a scalpel blade.

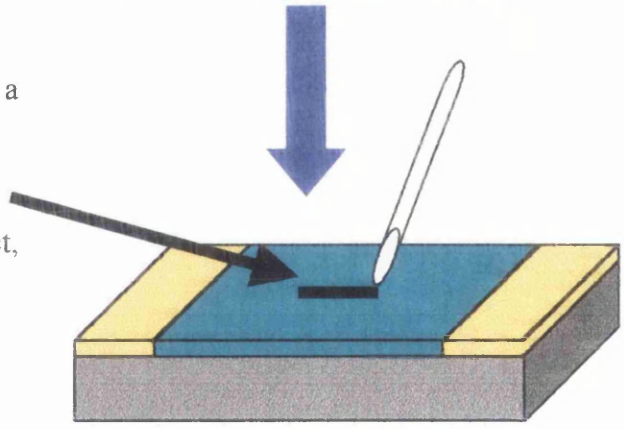

Figure 7.1: Schematic diagram showing preparation of AA2024-T3 sample prior to SKP corrosion experiments.

$SrCrO_4$ added as a dispersion in xylene, and the two mixed using a high shear blender. Figure 7.1c shows the pigmented PVB solutions after being bar cast on to the clean sample surface and allowed to dry in air. This procedure gave a dry film thickness of 30 μm as measured using a micrometer screw gauge. Figure 7.1d shows how the filiform corrosion was initiated by applying a 1 μl volume of 0.5 mol dm^{-3} aqueous HCl along the length of a 10mm linear coating defect, previously scribed in the centre of each PVB coated AA2024-T3 alloy sample using a scalpel blade. In every case, the direction of the scribe was perpendicular to the abrasive polishing direction.

7.2.2: Methods.

SKP:

Details of the SKP instrument used in this work can be found in section 2.2. The scanning reference probe consisted of a 125 μm diameter gold wire vibrated along its long axis and normal to the sample surface with amplitude 40μm and frequency 280Hz. The sample was then placed in the thermostatically controlled (20°C) stainless steel environment chamber of the SKP, maintained at a constant relative humidity of 93% by equilibration of the experimental atmosphere (air) with saturated $Na_2SO_4.10H_2O$ (aq). Repetitive scans were carried out every 3 hours on a 1 cm^2 area of the coated sample encompassing the scribe, using a data point density of 10 points per mm and a mean probe to sample height of 100 microns.

Optical microscopy:

On completion of the SKP experiment the sample was immediately scanned to obtained an optical micrograph of the surface as described in section 2.6.

7.3: Results.

Unpigmented coatings:

Repeated SKP scanning of AA2024-T3 samples, coated with unpigmented PVB films and with PVB films containing $SrCrO_4$ volume fractions (ϕ) of 0.01 to 0.05, was used to generate a series of time lapse animations showing dynamic changes in local free corrosion (E_{corr}) patterns. Figure 7.2 shows the progression of the SKP image plots (obtained using Golden Software, Surfer 6 cartography package) for the unpigmented PVB film. From figure 7.2 it can be seen that some time after initiation (~ 4 hours) FFC filament heads (dark regions) are visible along the edge of the defect, which then start to propagate perpendicular to the defect (along polishing/rolling direction). In the case of uninhibited coatings, E_{corr} values beneath the intact coating are ~ –0.2V *vs.* SHE, which is consistent with the coated aluminium surface existing in a substantially passive state. In the head region of propagating filaments E_{corr} values fall to ~ –0.5V *vs.* SHE indicating local depassivation. However, E_{corr} values in the filament tail (light region) are ~ 0.1V *vs.* SHE, indicating local superpassivation. These potential relationships are perhaps more easily seen in figure 7.3, which shows the time-dependent E_{corr} distribution along the axis of filament propagation for an individual filament. In figure 7.3 the active head is seen as a 1 mm long region of E_{corr} < -200 mV *vs.* SHE which shifts from left to right *i.e.* away from the penetrative defect, with increasing time. The tail region of the filament, which is seen to develop as the head moves away from the defect, exhibits E_{corr} values which are significantly more positive than those associated with the intact coating. Figure 7.2b shows an optical micrograph of the sample on completion of the SKP experiment, it shows very good correlation with the image plots obtained from the SKP data.

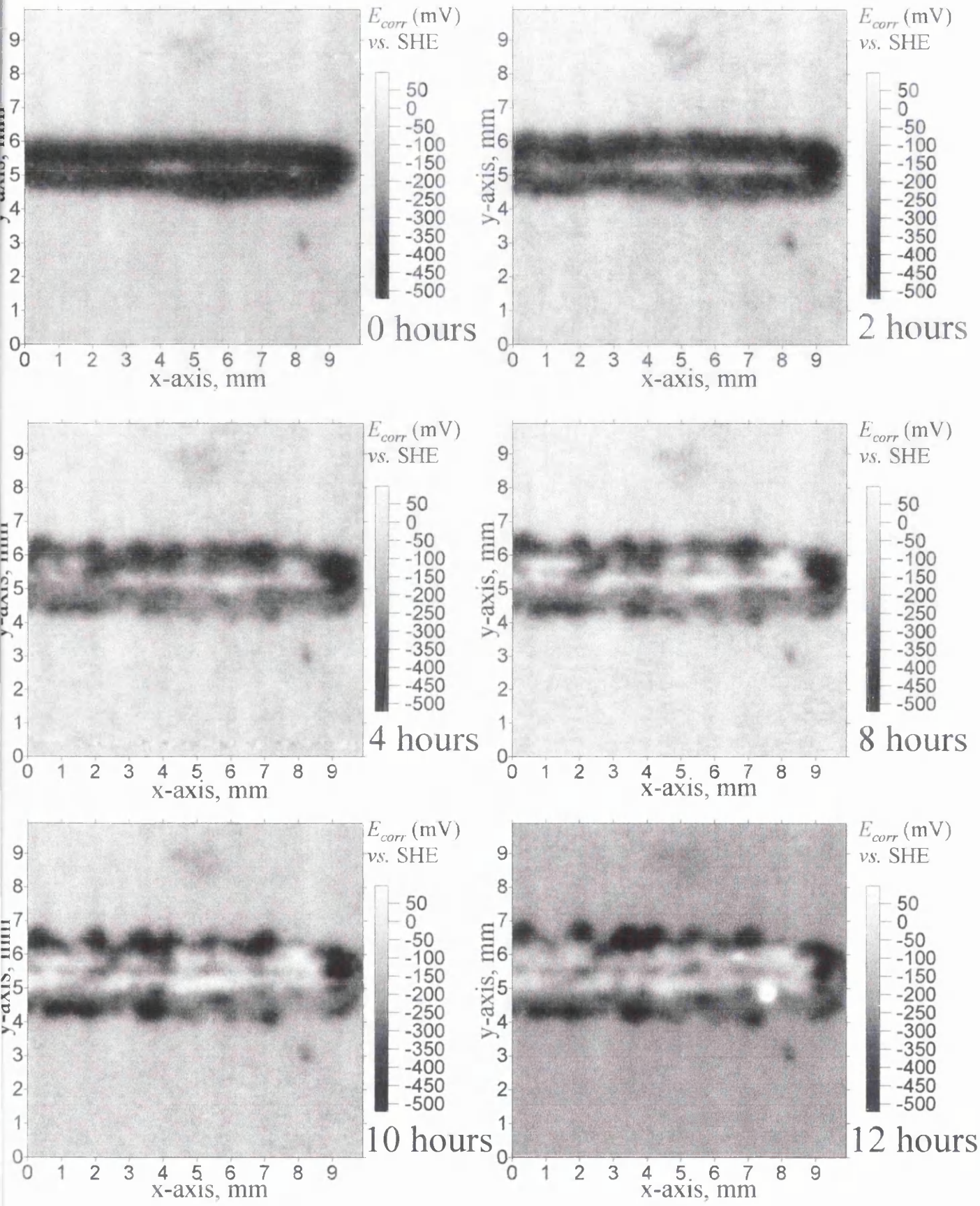

Figure 7.2: Image plots of SKP scans for AA2024-T3 coated with 30μm thick PVB film in 93% relative humidity at 20^{0}C, being initiated with 1μl volume of 0.5 mol dm^{-3} aqueous HCl .

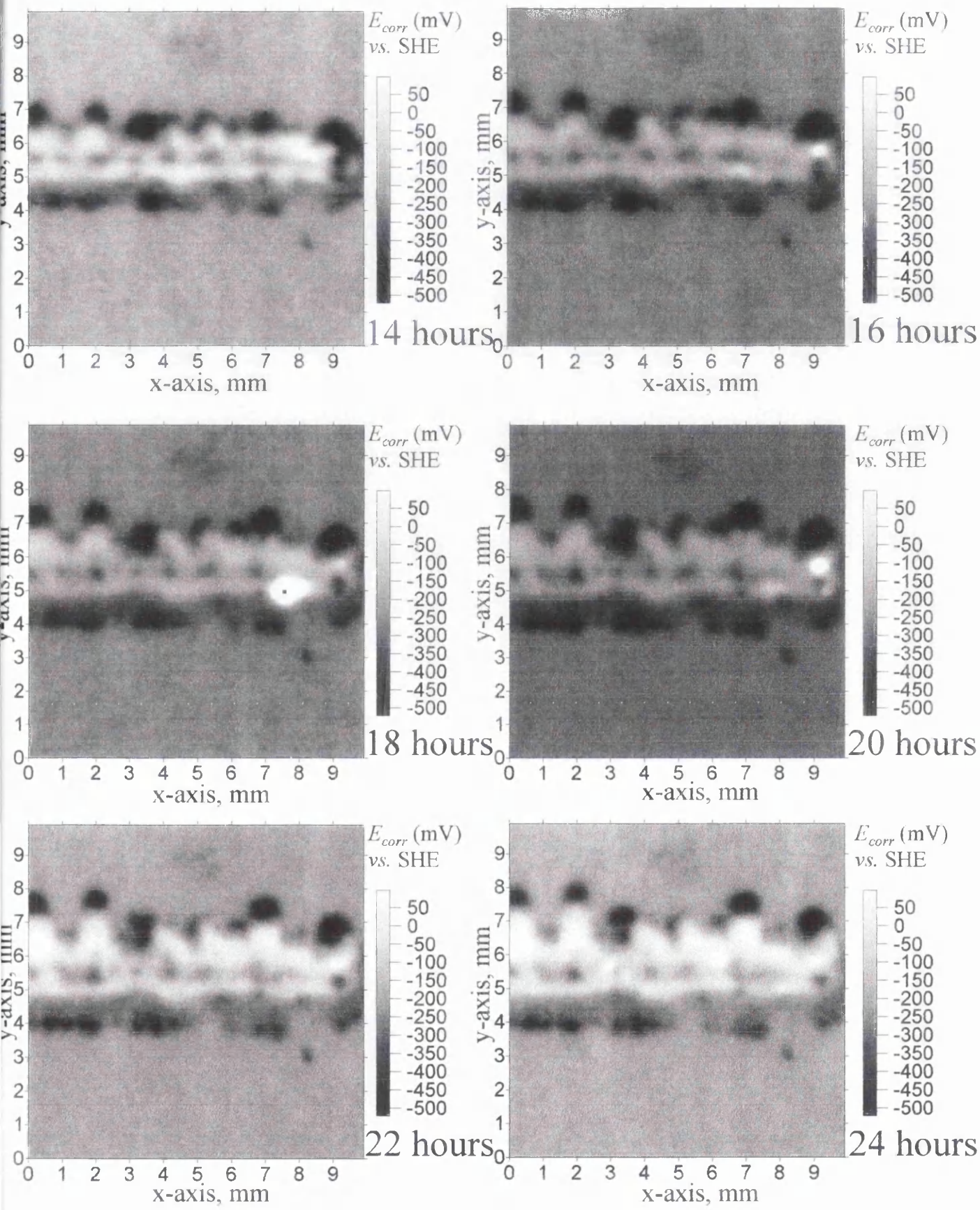

Figure 7.2: Image plots of SKP scans for AA2024-T3 coated with 30μm thick PVB film in 93% relative humidity at 20^{0}C, being initiated with 1μl volume of 0.5 mol dm^{-3} aqueous HCl .

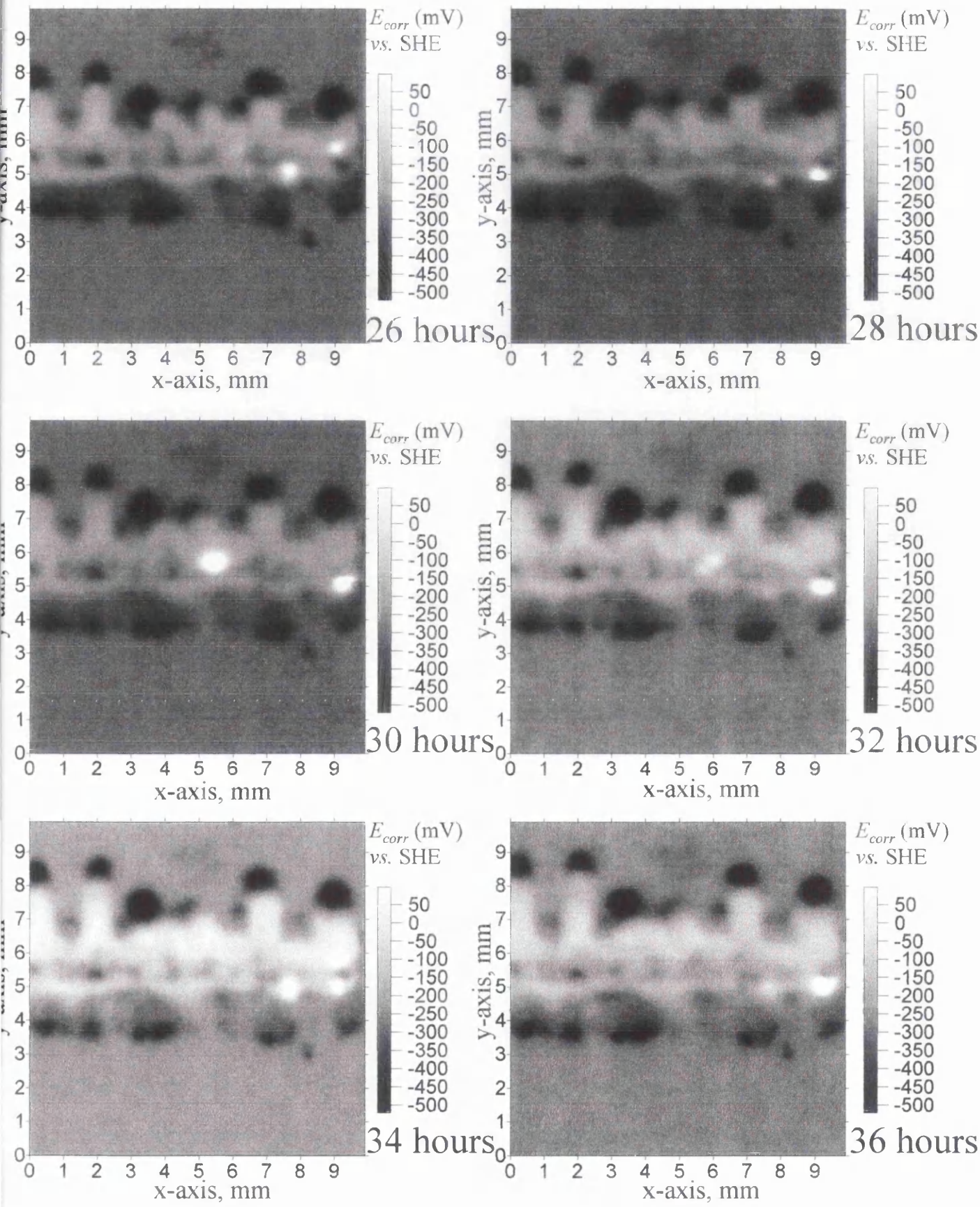

Figure 7.2: Image plots of SKP scans for AA2024-T3 coated with 30μm thick PVB film in 93% relative humidity at 20^0C, being initiated with 1μl volume of 0.5 mol dm^{-3} aqueous HCl.

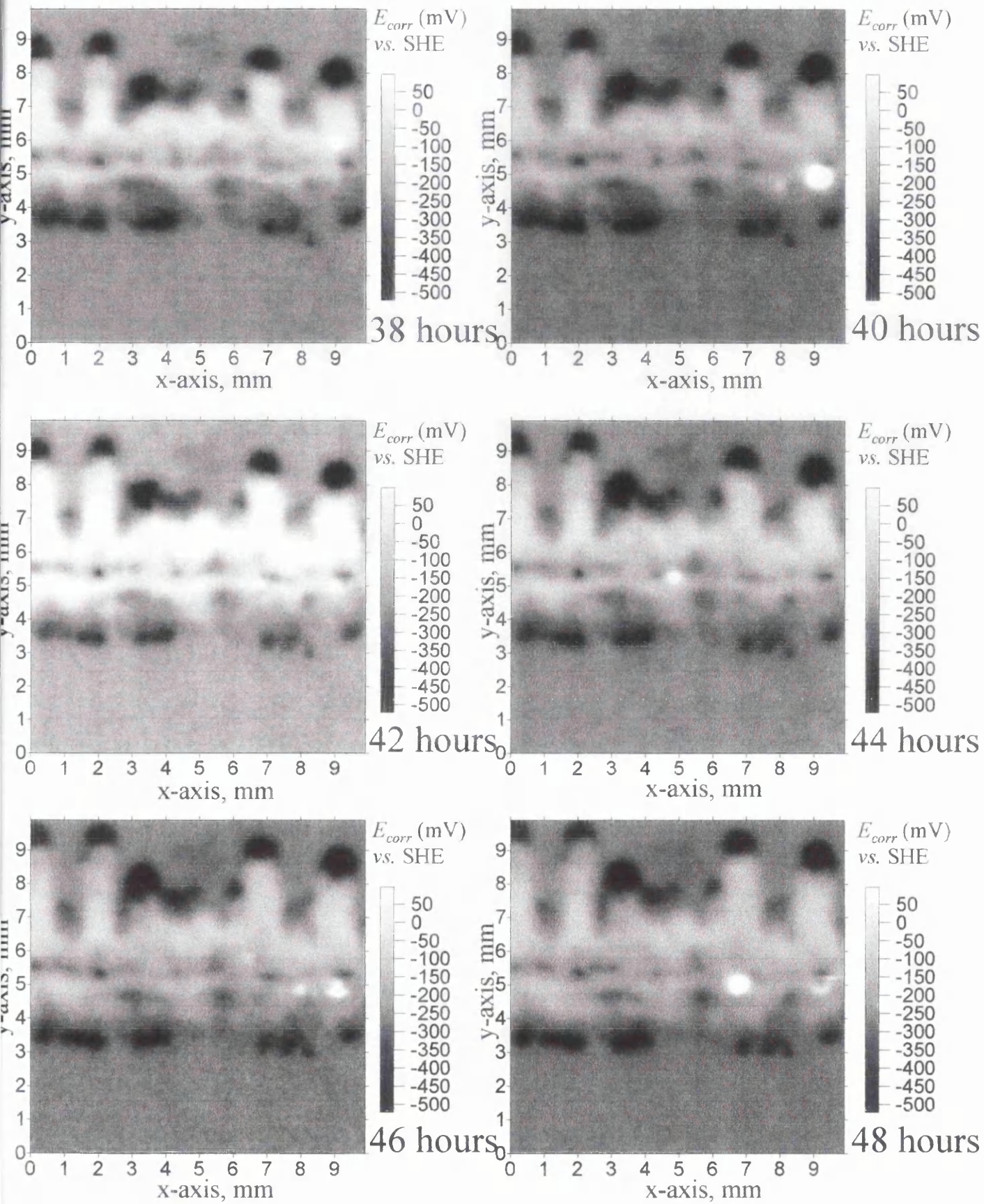

Figure 7.2: Image plots of SKP scans for AA2024-T3 coated with 30μm thick PVB film in 93% relative humidity at 20^0C, being initiated with 1μl volume of 0.5 mol dm^{-3} aqueous HCl .

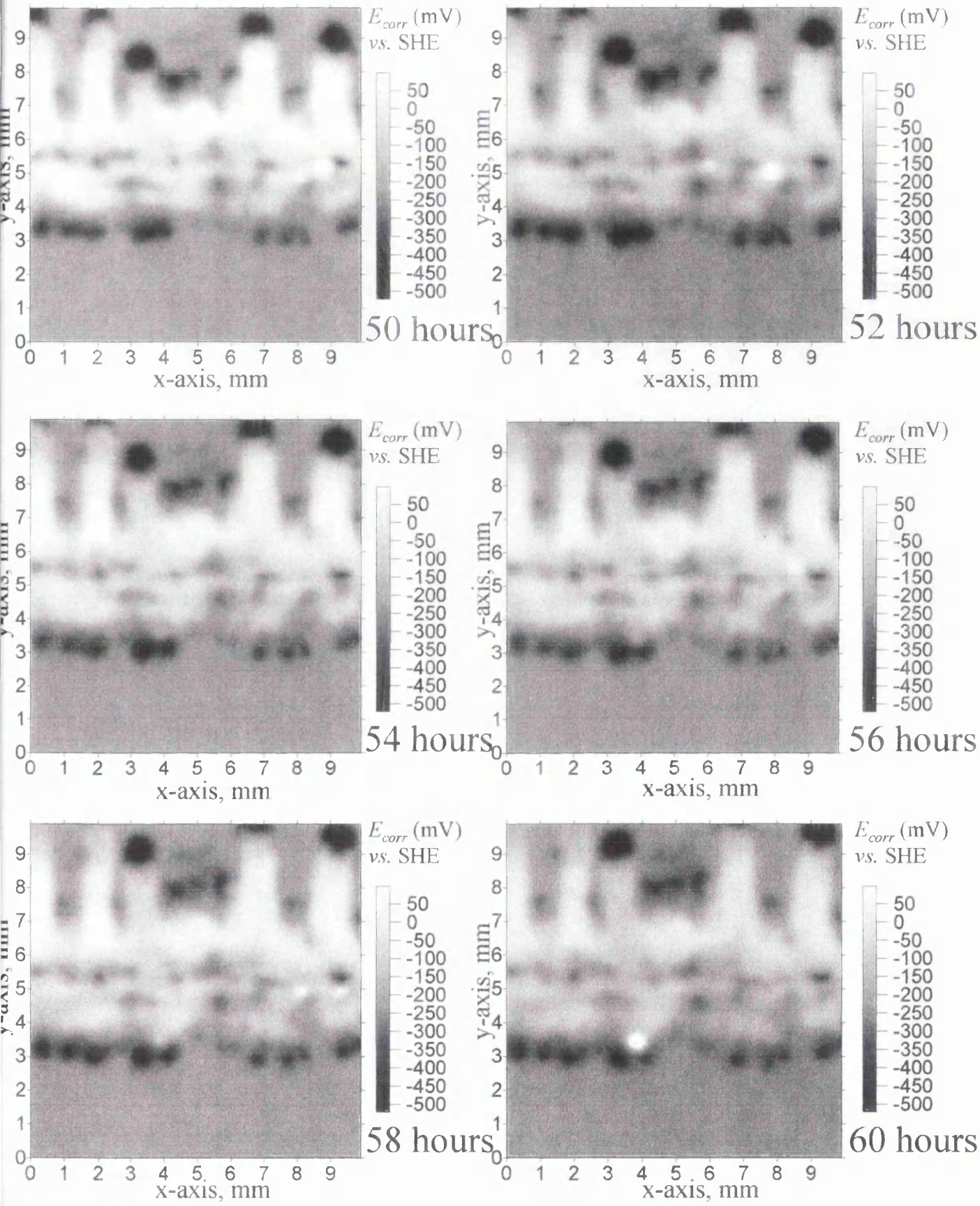

Figure 7.2: Image plots of SKP scans for AA2024-T3 coated with 30μm thick PVB film in 93% relative humidity at 20°C, being initiated with 1μl volume of 0.5 mol dm^{-3} aqueous HCl.

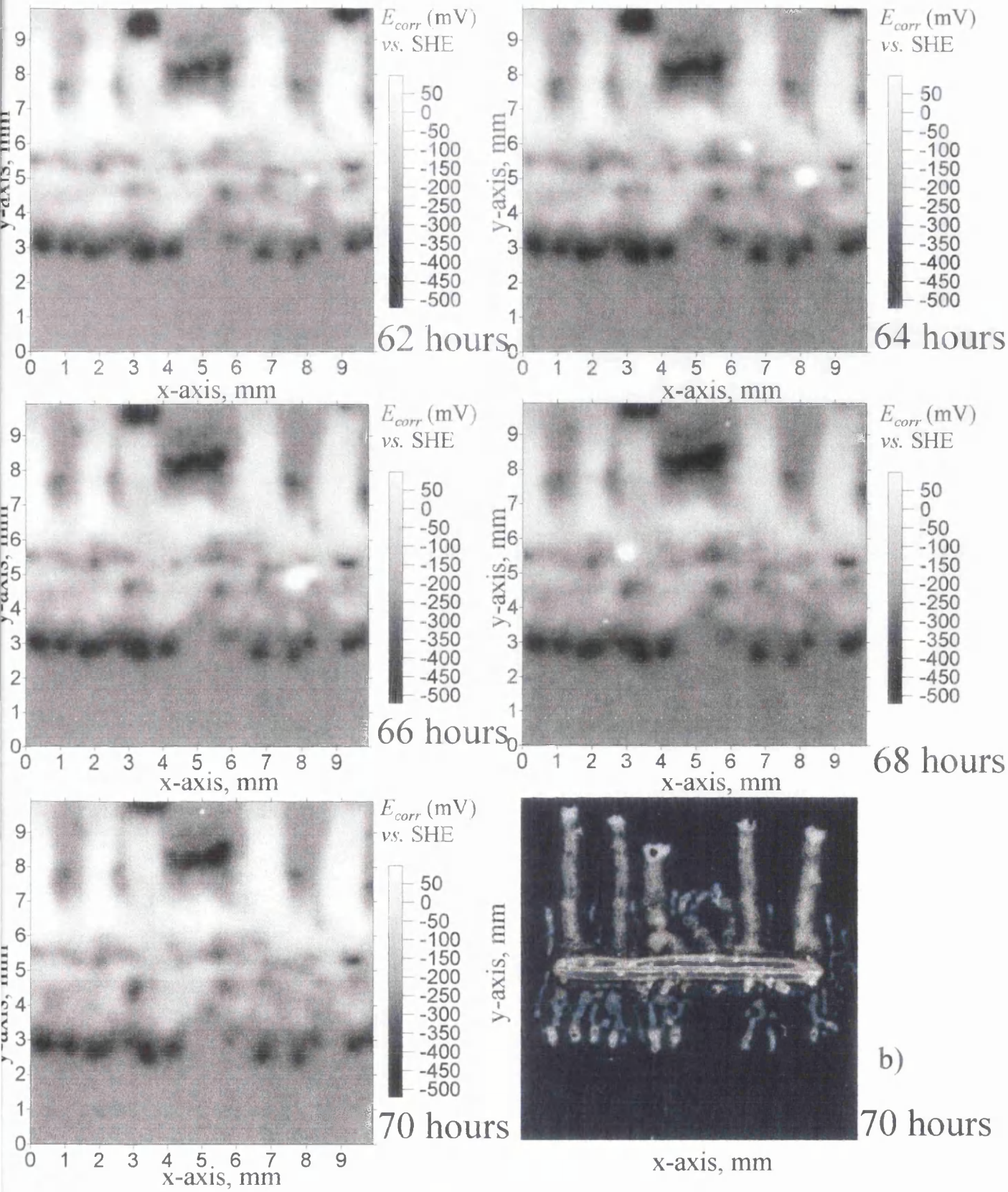

Figure 7.2: Image plots of SKP scans for AA2024-T3 coated with 30μm thick PVB film in 93% relative humidity at 20^{0}C, being initiated with 1μl volume of 0.5 mol dm^{-3} aqueous HCl.

b) Optical picture of sample after completion of experiment .

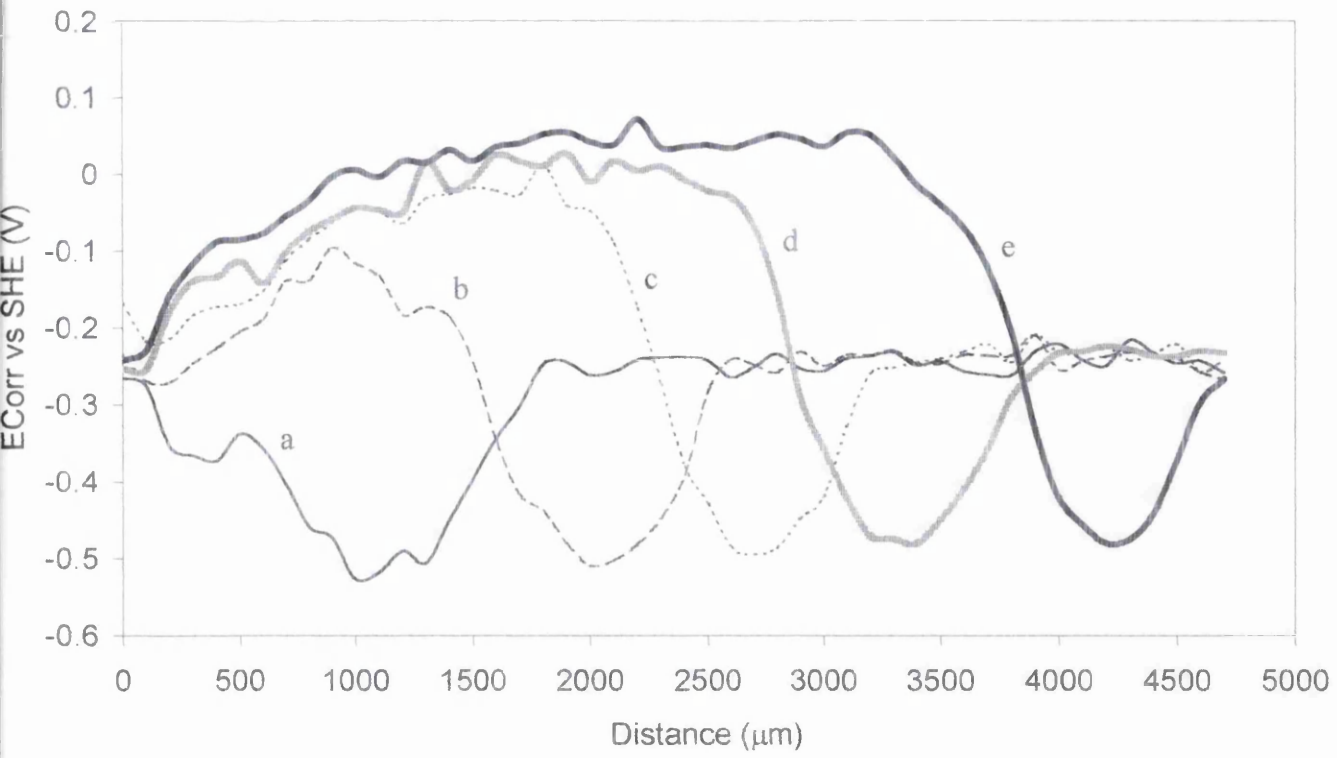

Figure 7.3: E_{corr} - distance profiles for a representative FFC filament on PVB / AA2024-T3, measured centrally along the axis of propagation for time = a) 8 hours, b) 18 hours, c) 28 hours d) 36 hours and e) 46 hours.

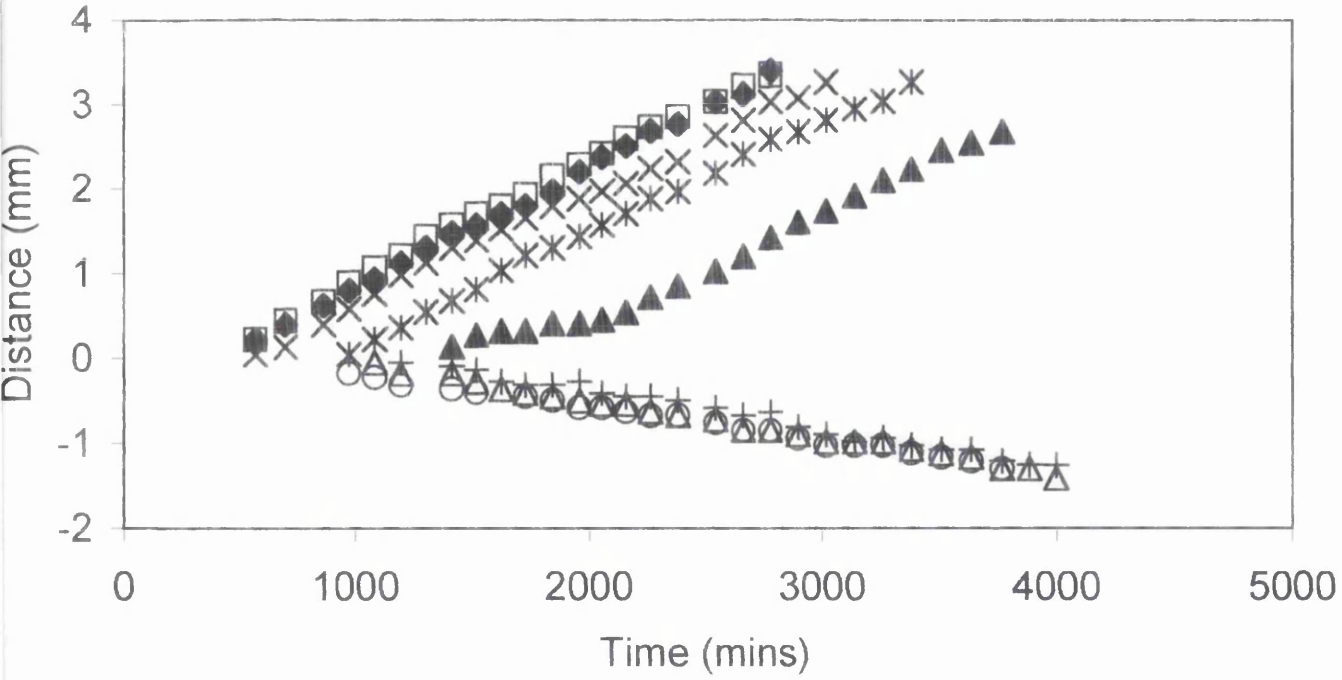

Figure 7.4: Distance - Time profiles for a selection FFC filaments on PVB / AA2024-T3, as detected by SKP, after being initiated using 1 μl of 0.5 M aqueous HCl.

The digital nature of the data obtained in individual SKP scans allows a detailed analysis of the instantaneous E_{corr} distributions associated with FFC filaments. Furthermore, the time-dependent progress of filaments may be quantified by comparing the spatial distribution of E_{corr} values between successive scans. This was achieved by determining the distance travelled by a filament in a given time, using the 'map digitise' function described in section 3.3.4. For unpigmented coatings, the position of filiform heads in any scan may be determined by locating the associated E_{corr} minima. Plotting the position of individual E_{corr} minima over time, as shown in figure 7.4, shows that on average filaments propagate at a constant speed of 1.3 ± 0.2 μm min^{-1} along the rolling direction and do not intersect.

However, this approach suffers from two difficulties. Firstly, the labour involved in measuring a large number of filaments. Secondly, the inevitable subjectivity involved in estimating the exact extent of filament progress. In an alternative approach, the extent of FFC may be quantified automatically by computing the delaminated area from each instantaneous E_{corr} distribution map. As in section 3.3.3 Surfer 6 cartography software is used, however in this case it is to calculate the fractions of the scanned area which have E_{corr} values which are displaced positive or negative of the background by an amount ≥0.1V. The sum of the assigned head areas (negative displacement) and tail areas (positive displacement) therefore provides the total delaminated area at a given time. The results obtained for an unpigmented coating are shown in figure 7.5. After an initial period of 400 min, representing a "delay time" required for the FFC corrosion cell to become established, the tail area increases at a rate of 0.0126 mm^2 min^{-1}, while head area decreases at a rate of 0.0021 mm^2 min^{-1}. This results in the growth of total delaminated area at a rate of 0.0105 mm^2 min^{-1}.

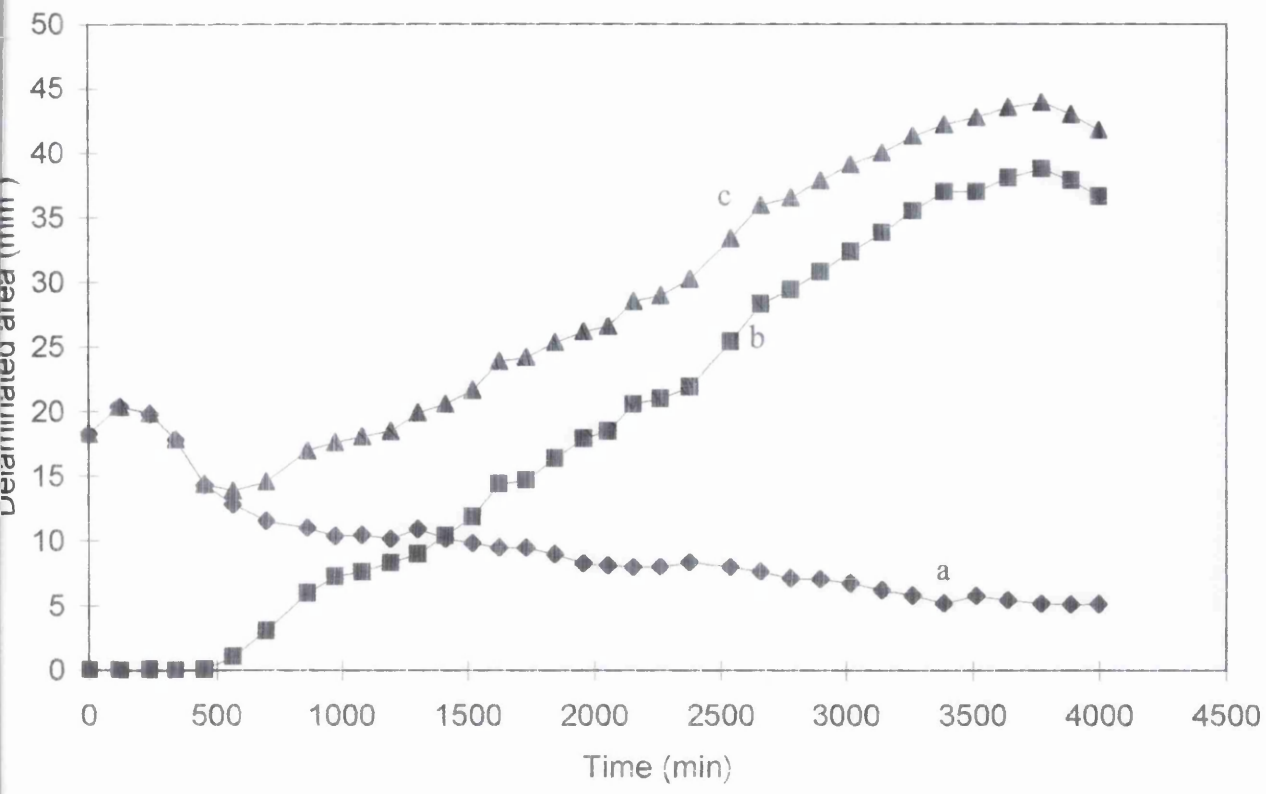

Figure 7.5: Delaminated area - time profile for FFC filaments on PVB / AA2024-T3, as detected by SKP, after being initiated using 1 μl of 0.5 M aqueous HCl. For a) filament head, b) filament tail, and c) total delaminated area.

Coatings pigmented with $SrCrO_4$:

Figure 7.6 shows representative E_{corr} distributions, observed 50 hours after initiation, for samples of varying ϕ. Figures 7.6a-6d show that, as the $SrCrO_4$ content of the PVB coating is increased from ϕ = 0.01 to ϕ = 0.05 so the extent of filament propagation decreases significantly and that E_{corr} values measured beneath the intact coating also decrease. Figure 7.7 shows scanned images of the same samples after completion of the SKP experiments. As can be seen the pigmented coatings are progressively more yellow in colour as expected for $SrCrO_4$. The pictures also correspond well with the images obtained from the SKP data. This shift in potential is perhaps more clear in figure 7.8. This shows E_{corr} distributions along the axis of filament propagation for individual filaments which have advanced an equal distance from the coating defect. It may be seen from figure 7.8 that E_{corr} values measured beneath the intact coating decrease from –0.2V to –0.5V *vs.* SHE, as ϕ increases from zero to 0.02. However, samples prepared with $0.02 < \phi \geq 0.05$ showed no further decrease in intact coating E_{corr} values. Figure 7.8 also shows that E_{corr} values measured in the head region of propagating filaments are substantially independent of coating $SrCrO_4$ content and remain similar to the uninhibited case, *ie.* ~ –0.5V *vs.* SHE. In contrast, E_{corr} values in the filament tail region are strongly influenced by $SrCrO_4$ levels and are shifted downwards from the uninhibited case to ~ –50 mV for ϕ = 0.02.

For $SrCrO_4$ pigmented coatings, because of the observed similarity between background and filament head E_{corr} values, the progress of the filament is most easily quantified by measuring the increase in length of the filament tail region. Such an analysis shows that filament velocity decreases progressively as ϕ is increased, approaching zero for $\phi > 0.05$, as can be seen in figure 7.9.

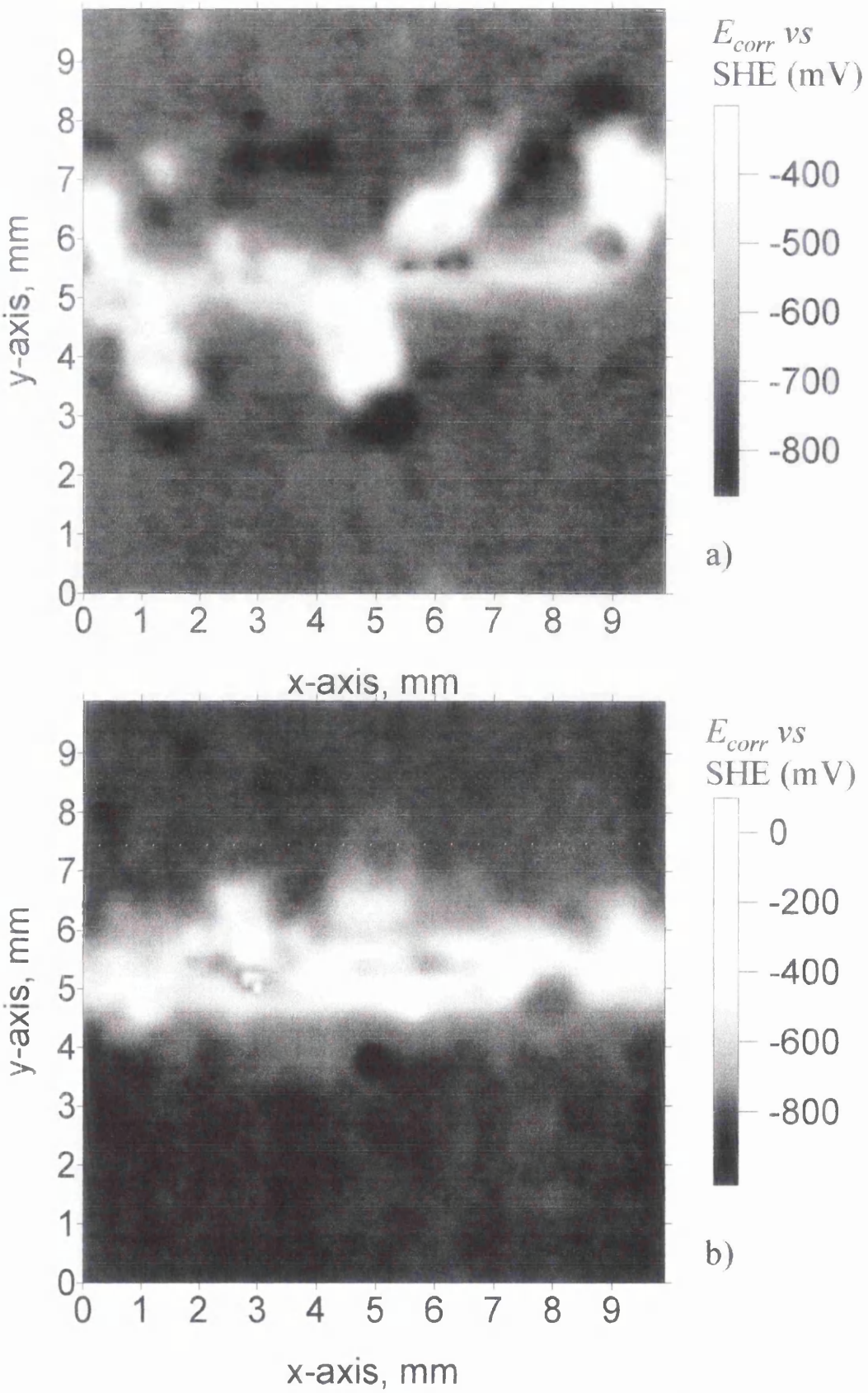

Figure 7.6: Image plots of SKP scans for AA2024-T3 50 hours after initiation with 1μl volume of 0.5 mol dm^{-3} aqueous HCl in 93% relative humidity at 20^0C. Coating $SrCrO_4$ pigment volume fraction, ϕ_{sc} = a) 0.01, b) 0.02, c) 0 035 and, d) 0.05.

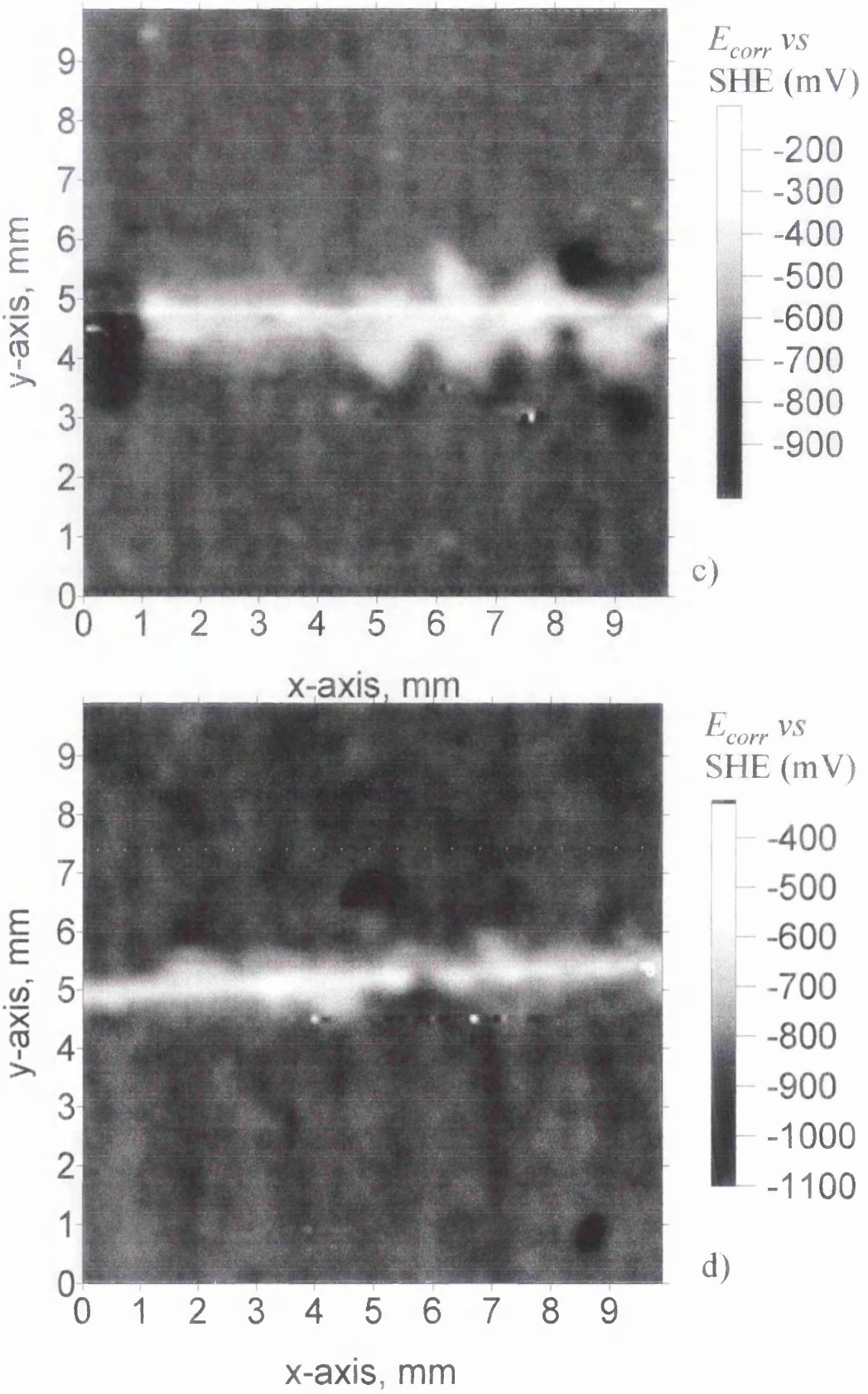

Figure 7.6: Image plots of SKP scans for AA2024-T3 50 hours after initiation with 1µl volume of 0.5 mol dm^{-3} aqueous HCl in 93% relative humidity at 20^0C. Coating $SrCrO_4$ pigment volume fraction, ϕ_{sc} = a) 0.01, b) 0.02, c) 0.035 and, d) 0.05.

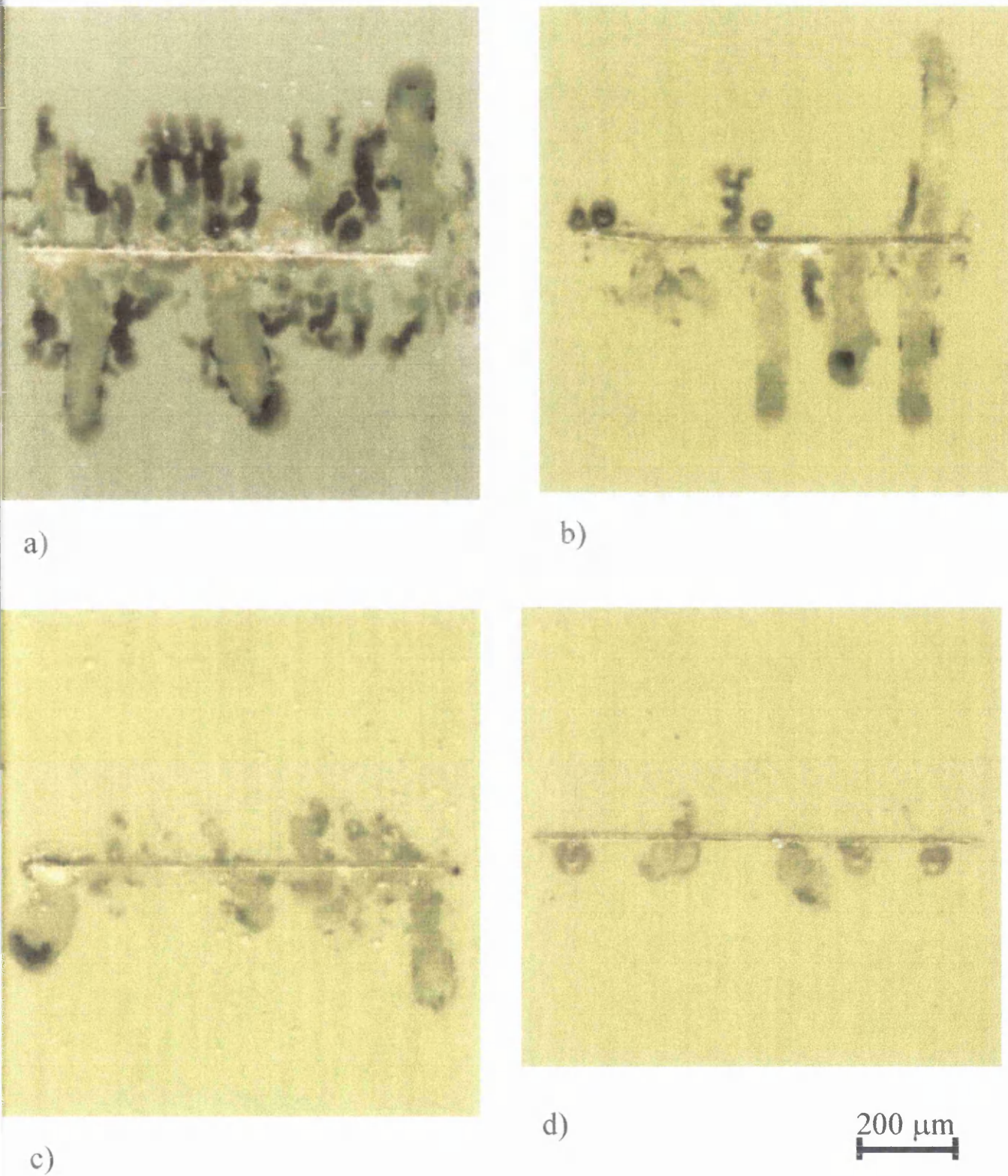

Figure 7.7: Optical images of coated sample after completion of SKP experiment. Coating $SrCrO_4$ pigment volume fraction, ϕ_{sc} = a) 0.01, b) 0.02, c) 0.035 and, d) 0.05.

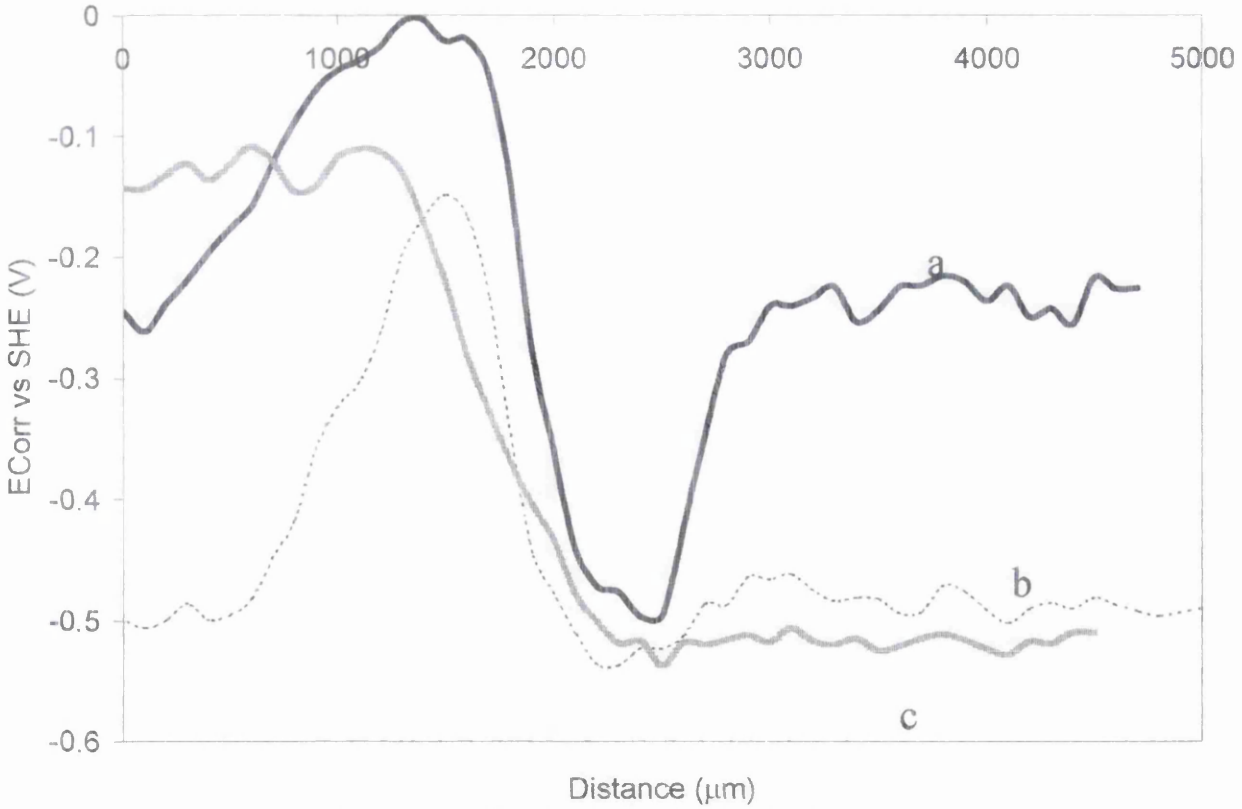

Figure 7.8: E_{corr} - distance profiles for individual FFC filaments on PVB / AA2024-T3, measured centrally along axis of propagation. Coating $SrCrO_4$ pigment volume fraction, ϕ_{sc} = a) 0, b) 0.01 and b) 0.02.

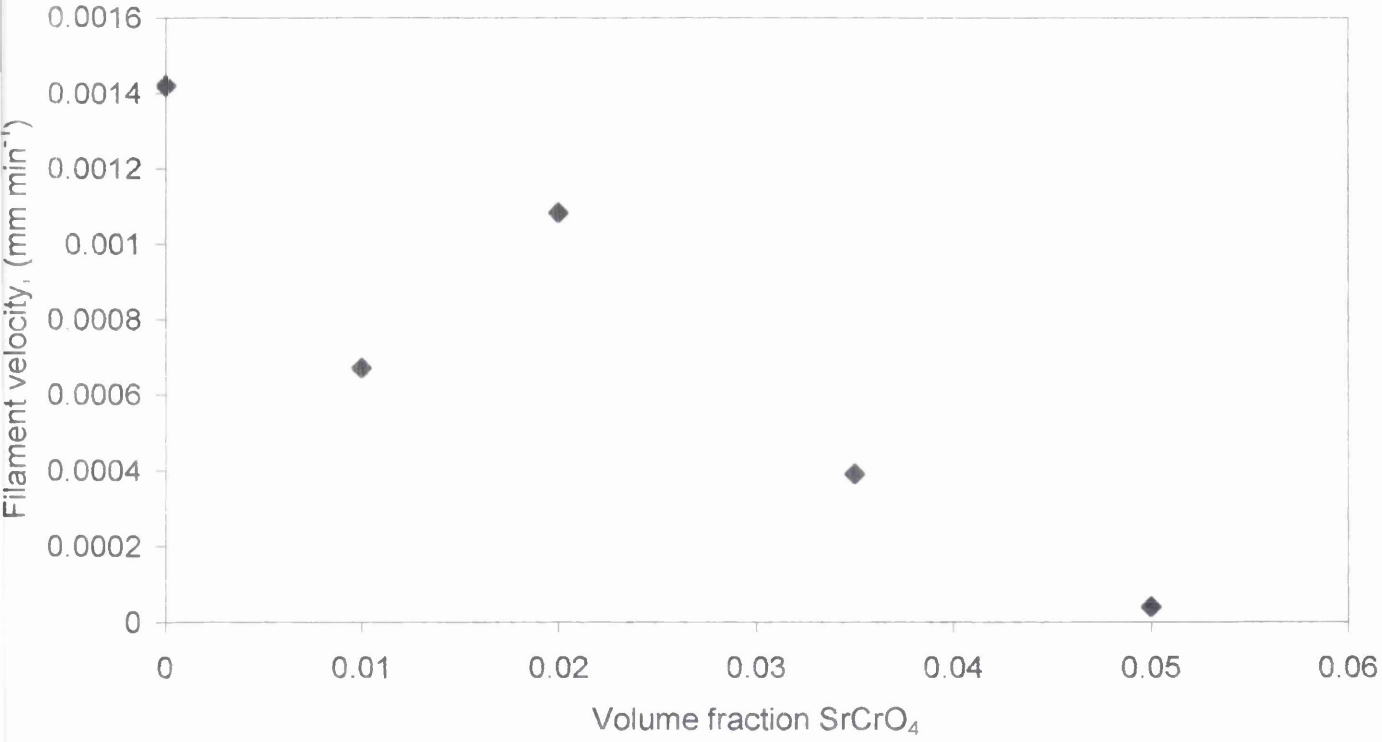

Figure 7.9: Plot of filament velocity against pigment volume fraction of $SrCrO_4$ in PVB coating.

Once again, the similarity of filament head and intact coating E_{corr} values in the case of $SrCrO_4$ pigmented coatings makes head, area and hence total delaminated area, difficult to determine. Consequently, for pigmented coatings tail area is used as a measure of FFC propagation. Using this approach, the influence of $SrCrO_4$ pigment levels on FFC delamination kinetics is shown in figure 7.10. It may be seen from figure 7.10 that the rate of tail area growth is approximately linear and that rate decreases progressively with increasing ϕ. This effect is summarised in figure 7.11, which shows FFC delamination rate, as determined from the slope of tail area-time data, as a function of ϕ.

7.4: Discussion.

When in equilibrium with air at 93% relative humidity the exposed aluminium alloy surface will be covered with an adsorbed aqueous film[7]. Furthermore, prior exposure to aqueous HCl will have resulted in production of $AlCl_3$ and Al(III) hydroxychloride salts ($Al(OH)_2Cl$ and $Al(OH)Cl_2$) at the exposed metal surface. These salts may then dissolve in the adsorbed humidity film to produce an aqueous electrolyte capable of supporting the electrochemical reactions of corrosion. Reactions 7.1 and 7.2 are generally believed to be localised in the FFC corrosion cell as shown schematically in figure 7.12, which also shows the relationship to (uninhibited) E_{corr} profile. Filament head pH values may be <pH2 as a result of Al^{3+} aquo-cation hydrolysis[2,3]. Filament tail pH values may be >pH10[2,3]. The reduced E_{corr} values observed in the filament head region are consistent with the substantial dissolution of the pre-existing passive oxide film on the surface of the aluminium matrix[16]. The high E_{corr} values observed in the filament tail region are consistent with the presence of a thick aluminium-rich (hydr)oxide film. However, entrapment of aluminium hydroxychloride salts in the

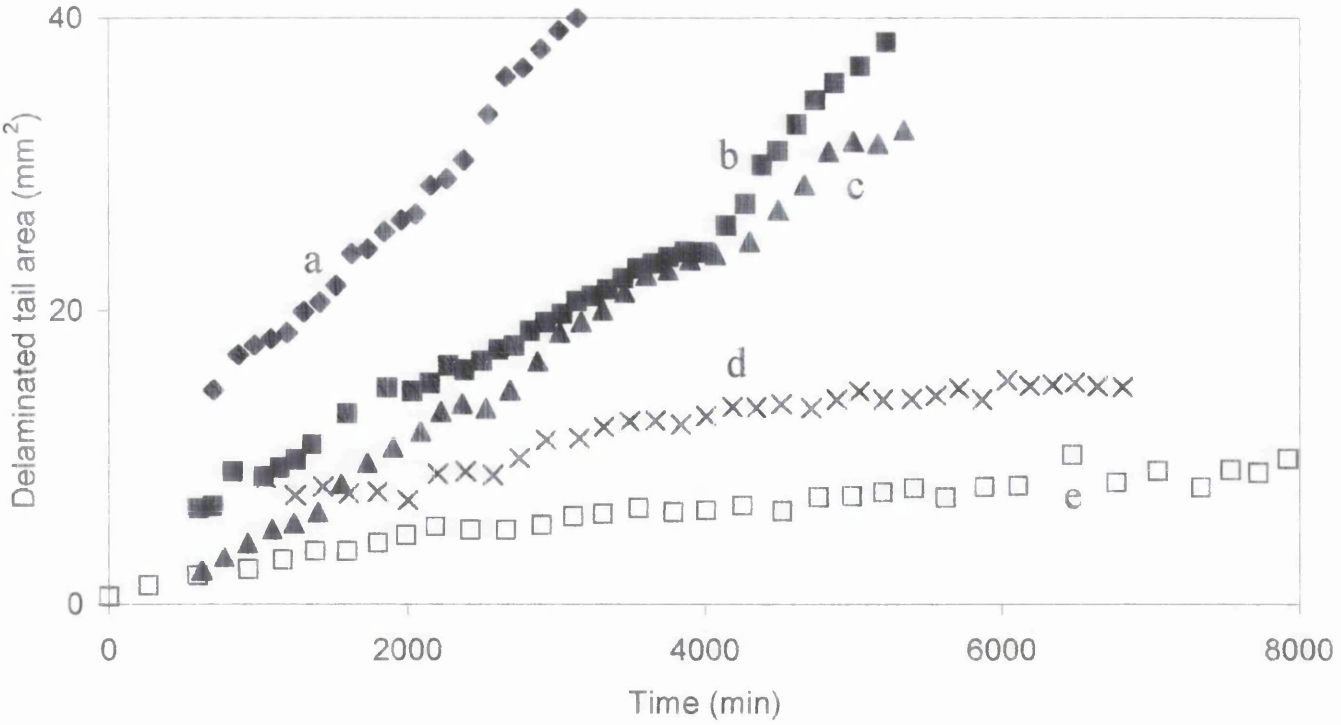

Figure 7.10: Plot of tail area against pigment volume fraction of $SrCrO_4$ in PVB coating.

For, a)$\phi = 0$, b)$\phi = 0.01$, c)$\phi = 0.02$, d)$\phi = 0.035$, and e)$\phi = 0.05$.

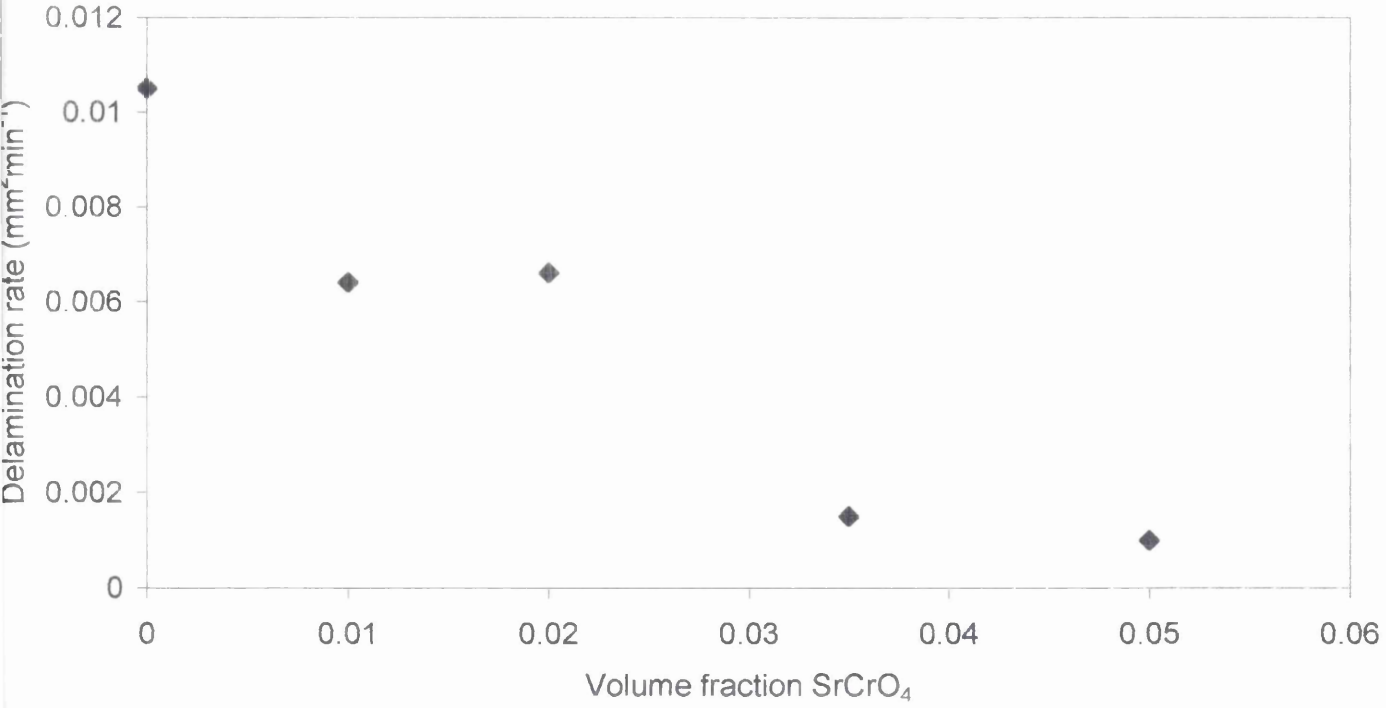

Figure 7.11: Plot of tail delamination rate against pigment volume fraction of $SrCrO_4$ in PVB coating.

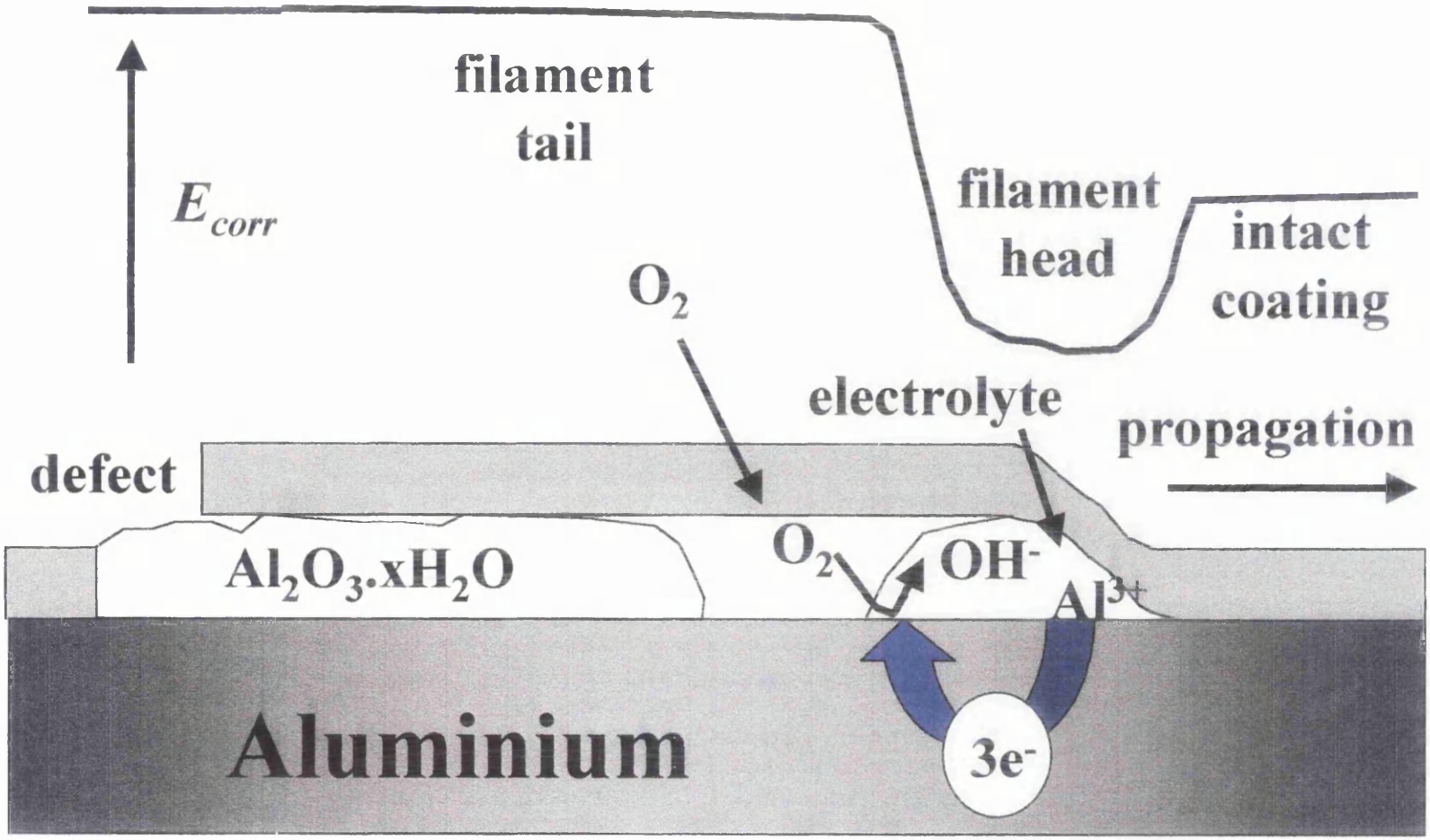

Figure 7.12: Schematic correlation between E_{corr} distribution and filiform corrosion cell.

tail region is also possible and the resulting depletion of head-electrolyte may account for the slow decrease in head area seen in figure 7.12[15].

The solubility product of $SrCrO_4$ is 3.6×10^{-5} mol^2 dm^{-6} at 15^{0}C[17]. Thus, when the PVB coating contains dispersed $SrCrO_4$, Sr^{2+} cations and CrO_4^{2-} anions may diffuse into the FFC cell electrolyte. The absence of any anodic shift in E_{corr} values suggests that $SrCrO_4$ does not significantly increase the polarisation of anodic processes occurring in the filament head region. This is probably due to the relatively high solubility of dichromate ($Cr_2O_7^{2-}$) salts and Cr^{3+} cations (the reduction product of $Cr_2O_7^{2-}$) at the low pH values and high chloride concentrations prevailing at the FFC cell anode site. Conversely, the cathodic shift in E_{corr} values in the filament tail region suggests that $SrCrO_4$ does increase the polarisation of cathodic processes occurring at sites in the filiform corrosion cell, where the local pH is high enough for relatively insoluble $Cr(OH)_3$ and basic Cr(III)Cr(VI) salts to be the predominant CrO_4^{2-} reduction products. It has been shown that, for AA2024-T3, reaction (7.2) occurs mainly on $CuMgAl_2$ and (Cu,Fe,Mn,)Al_6 intermetallic particles and also on Cu which has been replated onto the surface of the Al matrix following corrosion-driven particle dealloying[18]. It has also been shown that the rate of reaction (7.2) on (Cu,Fe,Mn,)Al_6 and Cu is reduced by ~ 1 order of magnitude in the presence of 10^{-2} mol dm^{-3} CrO_4^{2-} [18].

The observation that E_{corr} values in the intact coating region may be decreased by ~ 0.3V in the presence of $SrCrO_4$ implies that electrochemical interaction between CrO_4^{2-} and the AA2024-T3 surface may take place before FFC delamination has occurred. This begs the question as to whether such interactions play any role in forestalling FFC. It has been proposed that a portion of reaction 7.2 may occur in a

zone preceding the FFC filament head[19,20]. However, the spatial resolution of our SKP instrument is insufficient to confirm whether or not this is the case.

7.5: Conclusions.

Filiform corrosion filaments on organic coated AA2024-T3 aluminium alloy may be detected using SKP by imaging changes in local free corrosion potential (E_{corr}). The presence of in-coating $SrCrO_4$ dispersions substantially reduced the rate of FFC-driven coating delamination, which becomes zero for $SrCrO_4$ volume fractions ≥0.06. Increasing $SrCrO_4$ volume fraction produces little or no change in filament head E_{corr} values, but significantly depresses E_{corr} values in the filament tail and undelaminated surface. This suggests an increased polarisation of cathodic oxygen reduction occurring at sites where the local pH is high enough for insoluble Cr(III) salts to be the predominant CrO_4^{2-} reduction product.

7.6: Reference:

[1] C. F. Sharman, *Nature*, **153,** 621 (1944).
[2] R.T. Ruggieri and T. R. Beck, *Corrosion*, **39,** 452 (1983).
[3] A. Bauista, *Prog. Org. Coatings*, **28,** 49, (1996).
[4] A. T. A. Jenkins and R. D. Armstrong, *Corrosion Sci.*, **38**, 1147 (1996).
[5] V. Poulain and J. P. Petitjean, *Electrochim. Acta*, **41,** 1223 (1996).
[6] J. M. C. Mol, B. R. W. Hinton, D. H. Van der Weijde, J. H. W. De Wit and S. Van der Zwaag, *J. Mater. Sci.*, **35,** 1629 (2000).
[7] S. Yee, R. A. Oriani and M. Stratmann, *J. Electrochem. Soc.*, **138,** 55 (1991).
[8] M. Stratmann, H. Streckel and R. Feser, *Corrosion Sci.*, **32,** 467 (1991).
[9] M. Stratmann, R. Feser and A. Leng, *Electrochim. Acta*, **39,** 1207 (1994).
[10] W. Furbeth and M. Stratmann, *Fresenius J. Anal. Chem.*, **353,** 337 (1995).
[11] A. Leng, H. Streckel and M. Stratmann, *Corrosion Sci.*, **41,** 547 (1999).
[12] W. Furbeth and M. Stratmann, *Prog. Org. Coatings*, **39,** 23 (2000).
[13] W. Schmidt and M Stratmann, *Corrosion Sci.*, **40,** 1441 (1998).
[14] C. Chen and F. Mansfeld, *Corrosion Sci.*, **39,** 409 (1997).
[15] G. Williams, H. N. McMurray, D. Hayman and P. C. Morgan, *PhysChemComm.*, **6,** 1 (2001).
[16] E. Deltombe, C. Vanleugenhaghe and M. Pourbaix in *Atlas of Electrochemical Equilibria in Aqueous Solutions,* ed. M. Pourbaix, Pergamon Press, London, 168 (1966).
[17] *Electrochemica Data*, D. Dobos, Editor, Elsevier, Oxford, 226 (1975).
[18] G. O. Ilevbare and J. R. Scully, *J. Electrochem. Soc.*, **148,** 196 (2001).
[19] W. Funke, Prog. Org. Coate. **9**, 29 (1981).
[20] M. J. Schofield, J. D. Scantlebury, G. C. Wood and J. B. Johnson, *8th. Int. Congr. Metall. Corros.*, **2,** 1047 (1981).

Conclusions:

1. Surface preparation is significant in determining the pattern and intensity of pitting corrosion on AA2024. In the cases were the surface was polished with a slurry of 5μm alumina paste, the highest anodic activity recorded was 20 Am^{-2} after only 8 hours immersion. However, when the surface was polished to a 1μm diamond paste mirror finish, the highest anodic activity recorded was halved to 10 Am^{-2} after 10 hours immersion.

2. Pits formed on the surface of AA2024 after 24 hours immersion in 3.5% aqueous NaCl are not hemispherical in nature, but take the form of many openings to the surface connected by tunnels.

3. The rates of pitting corrosion on AA2024 are determined by the area concentration of intermetallic particles. By halving the area percentage of particles from 3% to 1.5%, the amount of aluminium lost through pitting corrosion, as determined by the SVET, more then halved from 0.07 gm^{-2} to $0.03gm^{-2}$ after 24 hours immersion in 3.5% aqueous NaCl.

4. Intermetallic particles act as cathodic sites. In SVET studies of samples exhibiting a non-uniform distribution of intermetallic particles, cathodic activity was focused at the sites of highest particle concentration.

5. In SKP studies of filiform corrosion, filaments were found to preferentially propagate along the samples rolling direction, i.e. along the direction of

intermetallic particle elongation. This finding is consistent with cathodic oxygen reduction occurring on intermetallic particles and de-alloyed intermetallic particles. Thus, the orientation of the intermetallic particles determines the direction of the filament propagation.

6. Rare earth chlorides (Ce^{3+}, La^{3+} and Y^{3+}) are effective inhibitors of pitting corrosion on AA2024. The efficiency of these trivalent cations increases in the order $Y^{3+} \sim La^{3+} < Ce^{3+}$.

7. Chromate ($NaCrO_4$) was a more effective inhibitor of pitting corrosion than REM chlorides. This greater efficiency appears to result from a more rapid onset of inhibition. At a concentration of 2.5×10^{-3} M/l in 3.5% aqueous NaCl, chromate completely inhibits pitting corrosion within the first hours immersion. Whereas cerium, lanthanum and yttrium take 4, 8 and 24 hours respectively to completely inhibit pitting corrosion.

Future work:

On completion of the thesis I was made aware that the T number designated to the two types of sample supplied (i.e. AA2024-T3 and AA2024-T351) was not correct. The sample described in this thesis as 3mm thick AA2024-T3 is actually AA2024-T351, and the sample described as a cube of AA2024-T351 is AA2024 (no designation). This is because the cube sample has not been through any of the processes described in table 1.2, because of this the two samples are completely different in structure. However, it would be possible to treat the cube sample in such a way as to make the two samples comparable. This would mean in any results obtained from SVET experiments on these samples, could be directly compared to each other.

With more time and the correct equipment, it would be possible to map the surface of these samples to show the distribution and composition of intermetallic particles. This would give a more complete picture as to the surface composition, and may help in determining which type of particle (if any) contributes the most to surface pitting corrosion.

Using the SVET and SKP, there are may avenues available for future work, some suggestions are. Investigating further how surface preparation for both SVET and SKP influences corrosion. Also any number of inhibitors can be investigated both with SVET and SKP.